UNIVERSIDADE FEDERAL DE MINAS GERAIS

Escola de Engenharia

Programa de Pós-Graduação em Engenharia de Estruturas

Debora Francisco Lalo

NUMERICAL MODELING AND EXPERIMENTAL CHARACTERIZATION OF CONICAL-LAMINATED ELASTOMERIC BEARINGS SUBJECTED TO DIFFERENT MODES OF LARGE MULTIAXIAL STRAINS – AN APPLICATION OF DIC TECHNIQUE IN BIAXIAL STRAINING

Belo Horizonte

2020

Debora Francisco Lalo

NUMERICAL MODELING AND EXPERIMENTAL CHARACTERIZATION OF CONICAL-LAMINATED ELASTOMERIC BEARINGS SUBJECTED TO DIFFERENT MODES OF LARGE MULTIAXIAL STRAINS – AN APPLICATION OF DIC TECHNIQUE IN BIAXIAL STRAINING

Dissertation presented to the Postgraduate Program in Structural Engineering (PROPEEs) of the Universidade Federal de Minas Gerais (UFMG), being part of the requirements for the "Philosophical degree in Structural Engineering".

Advisor: Prof. Dr. Marcelo Greco

Belo Horizonte
2020

Lalo, Debora Francisco.
L212n Numerical modeling and experimental characterization of conical-laminated elastomeric bearings subjected to different modes of large multiaxial strains - An application of DIC technique in biaxial straining [recurso eletrônico] / Debora Francisco Lalo. - 2020.
1 recurso online (257 f. : il., color.) : pdf.

Orientador: Marcelo Greco.

Tese (doutorado) - Universidade Federal de Minas Gerais, Escola de Engenharia.

Apêndices: f. 239-257.

Bibliografia: f. 221-238.
Exigências do sistema: Adobe Acrobat Reader.

1. Engenharia de estruturas - Teses. 2. Elastômeros - Teses. 3. Método dos elementos finitos - Teses. I. Greco, Marcelo. II. Universidade Federal de Minas Gerais. Escola de Engenharia. III. Título.

CDU: 624(043)

Ficha catalográfica elaborada pelo bibliotecário Reginaldo César Vital dos Santos CRB/6 2165
Biblioteca Profº Mário Werneck, Escola de Engenharia da UFMG

UNIVERSIDADE FEDERAL DE MINAS GERAIS

PROGRAMA DE PÓS-GRADUAÇÃO EM ENGENHARIA DE ESTRUTURAS

PROPEEs UFMG

ATA DA DEFESA DE TESE DE DOUTORADO EM ENGENHARIA DE ESTRUTURAS Nº: 74 DA ALUNA DEBORA FRANCISCO LALO PEREIRA.

Às **14:00** horas do dia **25** do mês de **junho** de **2020**, reuniu-se, totalmente por videoconferência para atender aos novos protocolos de distanciamento social adotados pelo governo federal e pela prefeitura de Belo Horizonte, que integram medidas para combater o avanço da pandemia de Covid-19, provocada pelo novo coronavírus, a Comissão Examinadora indicada pelo Colegiado do Programa em **20 de maio de 2020**, para julgar a defesa da Tese de Doutorado intitulada **"Numerical Modeling and Experimental Characterization of Conical-Laminated Elastomeric Bearings Subjected to Different Modes of Large Multiaxial Strains - an Application of DIC Technique in Biaxial Straining"**, cuja aprovação é um dos requisitos para a obtenção do Grau de DOUTOR EM ENGENHARIA DE ESTRUTURAS na área de ESTRUTURAS .

Abrindo a sessão, o Presidente da Comissão, **Prof. Dr. Marcelo Greco**, após dar a conhecer aos presentes o teor das Normas Regulamentares passou a palavra à candidata para apresentação de seu trabalho. Seguiu-se a argüição pelos examinadores, com a respectiva defesa da candidata. Logo após, a Comissão se reuniu, sem a presença da candidata e do público, para julgamento e expedição do resultado final.

Prof. Dr. Marcelo Greco - DEES - UFMG (Orientador)
Prof. Dr. Estevam Barbosa de Las Casas - DEES - UFMG
Prof. Dr. Felício Bruzzi Barros - DEES - UFMG
Prof. Dr. Marcilio Alves - USP
Profa. Dra. Katia Lucchesi Cavalca Dedini - UNICAMP

Pelas indicações acima, a candidata foi considerada APROVADA, conforme pareceres em anexo.
O resultado final foi comunicado publicamente à candidata pelo Presidente da Comissão.
Nada mais havendo a tratar, o Presidente encerrou a reunião e lavrou a presente ATA, que será assinada por todos os membros participantes da Comissão Examinadora. Belo Horizonte, 25 de junho de 2020.

Observações:

1. A aprovação da candidata na defesa da Tese de Doutorado não significa que a mesma tenha cumprido todos os requisitos necessários para obtenção do Grau de Doutor em Engenharia de Estruturas;
2. Este documento não terá validade sem a assinatura e carimbo do Coordenador do Programa de Pós-Graduação.

Documento assinado eletronicamente por **Marcelo Greco**, **Membro**, em 26/06/2020, às 10:10, conforme horário oficial de Brasília, com fundamento no art. 6º, § 1º, do Decreto nº 8.539, de 8 de outubro de 2015.

Documento assinado eletronicamente por **Katia Lucchesi Cavalca Dedini**, **Usuário Externo**, em 26/06/2020, às 12:59, conforme horário oficial de Brasília, com fundamento no art. 6º, § 1º, do Decreto nº 8.539, de 8 de outubro de 2015.

Documento assinado eletronicamente por **Marcilio Alves**, **Usuário Externo**, em 26/06/2020, às 15:12, conforme horário oficial de Brasília, com fundamento no art. 6º, § 1º, do Decreto nº 8.539, de 8 de outubro de 2015.

Documento assinado eletronicamente por **Felicio Bruzzi Barros**, **Membro de comissão**, em 29/06/2020, às 12:05, conforme horário oficial de Brasília, com fundamento no art. 6º, § 1º, do Decreto nº 8.539, de 8 de outubro de 2015.

Documento assinado eletronicamente por **Estevam Barbosa de Las Casas**, **Diretor(a)**, em 29/06/2020, às 18:21, conforme horário oficial de Brasília, com fundamento no art. 6º, § 1º, do Decreto nº 8.539, de 8 de outubro de 2015.

A autenticidade deste documento pode ser conferida no site https://sei.ufmg.br/sei/controlador_externo.php?acao=documento_conferir&id_orgao_acesso_externo=0, informando o código verificador **0160855** e o código CRC **346E4D5F**.

Referência: Processo nº 23072.216155/2020-70 SEI nº 0160855

ACKNOWLEDGMENTS

First of all, I would like to pay my special regards to God for guiding me, enlightening and giving me enough strength to move forward with my goals and not be discouraged by difficulties.

I wish to acknowledge the support and great love of my husband, Felipe. He gave me unconditional support and knew how to act patiently in the most difficult moments of this journey. In addition, I thank my parents for giving me education and values that were essential for my personal and intellectual growth.

I would like to thank my advisor, Marcelo Greco, and recognize his invaluable assistance and friendship. His comments and suggestions were essential for improving this work.

I truly appreciate the physical and technical contribution of Vibtech company. Without their support and funding, this project could not have reached its goal.

I wish to express my deepest gratitude to the mechanical department of the Saarland University and the entire team of professor Stefan Diebels. In particular the attention and support given by Selina and Joachim during equal biaxial experimental tests.

I am also very grateful to the Group of Solid Mechanics and Structural Impact (GMSIE) from USP-POLI, directed by professor Marcílio Alves. In addition, I would like to express my gratitude to the professors, Gilmar Batalha, Rafael Celeghini and Demétrio Jackson for the valuable suggestions and contributions.

I wish to extend my special thanks to the mechanical department of University Center of FEI to allow me conduct additional experimental tests that were essential to the development of this work. I also would like to thank the professor Sergio Delijaicov for the important contributions and indications that have led towards the success of this study.

Finally yet importantly, I would like to express my thanks to all those who, in some way, allowed this Dissertation to materialize.

“If you double the number of experiments you do per year you’re going to double your inventiveness.” – Jeff Bezos

ABSTRACT

Elastomeric components are essential in engineering field since they isolate vibration, reduce noise, accommodate oscillatory movements and allow misalignment between axes. Their mechanical properties can vary according to a specific condition, enabling their applications be subjected to large deformations under multiaxial loading. Since their constitutive relations are highly nonlinear and different for each pure mode of deformation, experimental tests for each mode must be performed in order to obtain the proper law which describes the behavior of this type of material. In this context, the framework of this study is to develop a methodology based on Digital Image Correlation (DIC) applied in biaxial straining under large deformations to calibrate the rubber computational modeling by Finite Element Method (FEM) according to prototype tests when subjected to a very complex deformation mode. Thus, the validation of the adopted methodology has as focus of study a conical rubber spring used in suspensions of the railway industry and which is produced by an engineering company. Since the material approaches incompressibility, different shape functions were adopted to describe the fields of pressure and displacements according to the finite element hybrid formulation. The biaxial experiments were performed in a cruciform machine and the applied methodology was validated through a classical bulge test. Despite the low biaxiality degree, reasonable results were obtained to nominal strain levels higher than 300%, with the proposed methodology. Initially, the correlation between axial and radial stiffness under pre-compression was obtained by experimental tests in prototypes and virtual modeling developed through a curve fitting procedure. Next, aiming to compare the material responses and investigate its mechanical behavior under different multiaxial loading conditions, the constitutive parameters were accurately adjusted through an optimization algorithm implemented in Python® program language for Abaqus®, which calibrates the virtual model according to the prototype test data. Final results pointed to a change in material behavior when subjected to radial loading due to friction between rubber pads and metal parts as well as due to pre-compression effects. In order to take this effect into account a subroutine for adaptive remeshing and mesh mapping solution was implemented. Finally, an analytical solution for radial stiffness was proposed taking into account the shape factor and compression modulus of the rubber component.

Keywords:

Elastomers; Hiperelastic Models; Biaxial Extension; DIC; Conical Rubber Spring.

RESUMO

Os componentes elastoméricos são essenciais na engenharia, pois isolam a vibração, reduzem ruídos, acomodam movimentos oscilatórios e permitem o desalinhamento entre os eixos. Suas propriedades mecânicas podem variar de acordo com uma condição específica, permitindo que suas aplicações sejam submetidas a grandes cargas multiaxiais. Como suas relações constitutivas são altamente não-lineares para cada modo puro de deformação, testes experimentais devem ser realizados para obtenção da lei apropriada que descreva o comportamento desse tipo de material. Nesse contexto, o presente estudo visa desenvolver uma metodologia baseada em Correlação de Imagens Digitais para grandes extensões biaxiais e calibração da modelagem computacional da borracha pelo Método dos Elementos Finitos de acordo com testes em protótipo quando submetidos a um modo de deformação muito complexo. A validação da metodologia adotada tem como foco de estudo uma mola cônica utilizada em suspensões de veículos ferroviários, produzida por uma empresa de engenharia. Como o material se aproxima da incompressibilidade, diferentes funções de forma foram adotadas para descrever os campos de pressão e de deslocamentos de acordo com a formulação híbrida de elementos finitos. Os experimentos biaxiais foram realizados no modo cruciforme e a metodologia aplicada foi validada através de um *bulge test* clássico. Apesar do baixo grau de biaxialidade, os resultados obtidos foram aceitáveis para níveis de deformação superiores a 300%, com a metodologia proposta. Inicialmente, a correlação entre rigidez axial e radial sob pré-compressão foi obtida por testes em protótipos e modelagem virtual desenvolvida através de um procedimento de ajuste de curvas. Em seguida, com o objetivo de comparar as respostas dos materiais e investigar seu comportamento mecânico sob diferentes condições de carregamento multiaxial, os parâmetros constitutivos foram ajustados por meio de um algoritmo de otimização implementado em linguagem de programação Python® para Abaqus®, que calibra o modelo virtual de acordo com os dados de teste. Os resultados finais apontaram uma mudança no comportamento do material quando submetido a carga radial devido ao atrito entre as camadas de borracha e as peças metálicas, bem como devido aos efeitos de pré-compressão. Para considerar este efeito, foi implementada uma sub-rotina para remalhamento adaptativo. Por fim, foi proposta uma solução analítica para rigidez radial, levando em consideração o fator de forma e o módulo de compressão do componente de borracha.

Palavras-chave:

Elastomeros; Modelos Hiperelásticos; Extensão Biaxial; DIC; Mola Cônica de Borracha.

LIST OF FIGURES

LIST OF TABLES

ACRONYMS

FEM – Finite Element Method

FE – Finite Element

FEA - Finite Element Analysis

DIC – Digital Image Correlation

NR – Natural Rubber

SR – Synthetic Rubber

IRHD – International Rubber Hardness Degrees

SH – Shore Hardness

1D – One-dimensional

2D – Two-dimensional

3D – Tree-dimensional

ZOI – Zone Of Interest

SSD – Sum of Squared Differences

LED – Light Emitting Diode

CMOS – Complementary Metal-Oxide Semiconductor

GRG – Generalized Reduced Gradient

VBA – Visual Basic for Applications

LSM – Least Squares Method

DC – Direct Current

AW – Added Weight

CPS4 – 4-node bilinear plane stress quadrilateral element

S4R – 4-node doubly curved thin shell element with reduced integration and hourglass control

CAX8H – 8-node biquadratic quadrilateral axisymmetric element with hybrid formulation

CAX4 – 4-node bilinear axisymmetric quadrilateral element

CAX4H – 4-node bilinear quadrilateral axisymmetric element with hybrid formulation

CAX3 – 3-node linear triangle axisymmetric element

C3D8RH – 8-node linear hex element with hybrid formulation

C3D10I – 10-node tetrahedron with an improved surface stress formulation

CAD – Computer Aided Design

ALLAE – Total artificial strain energy

ALLSE – Total elastic strain energy

MMFD – Modified Method of Feasible Directions

CONTENTS

APPENDICES

1

INTRODUCTION

1.1 Project Background

Road and railway vehicles must comply with a large spectrum of objectives including noise reduction, ride enhancement, dynamic behavior and/or handling improvement while reducing costs. The use of bushing elements can reduce the wear of the components in a mechanism by using their energy absorption capacity to decrease transmitted vibrations (LUO *et al.*, 2013; SEBESAN *et al.*, 2015). Therefore, laminated elastomeric bearings arranged in a conical shape, which is usually known as conical rubber spring, became a very important suspension component used between the frame and the axle for railway vehicles. The elastomeric bushings are essential in this type of application since they isolate vibration, reduce noise, accommodate oscillatory motions and allow axes misalignments (LUO *et al.*, 2001).

The main problem regarding elastomeric materials are the time consuming and costly experiments conducted in a trial and error methodology to obtain the mechanical behavior of complex shape components during the product development process. This happens due to complex constitutive laws for rubber-like materials under multiaxial loading, making it difficult to implement a computational simulation procedure. At Vibtech, an engineering company which produces rubber-like material components, some difficulties have been found concerning Finite Element (FE) modeling and strong divergence appeared when correlation between numerical simulation and experimental tests in prototypes was tried. For this reason, a partnership was made with this company in order to obtain all information regarding the conical rubber spring, experimental tests and design complexity.

In Finite Element Analysis (FEA) involving rubbers, some experiments should be performed in order to assess the material constitutive law. Thus, for this reason the elastomers physical testing often requires experiments in multiple strain states under certain loading conditions.

Several material models are available in the most common computational codes, but at least uniaxial and equal biaxial stretching tests are required to fit the model accurately and to extract material parameters (HARIHARAPUTHIRAN and SARAVANAN, 2016; LALO and GRECO, 2017; SASSO *et al.*, 2008). The uniaxial testing can be performed in a standard tensile machine which is easily accessible, but on the other hand the equal biaxial extension is much more complex and difficult to implement (MILLER, 2004a). In situations where the elastomer is highly constrained, a volumetric compression test may be requested in order to determine the bulk behavior, but if the material is considered to be almost incompressible the third basic invariant is constant and, hence, does not contribute to the stored energy (ZIMMERMANN and STOMMEL, 2013a).

The main strain states are simple tension, pure shear and simple compression. For experimental reasons that will be discussed further on, the compression test will be replaced by the equal biaxial extension, which is much more complex than the simple compression experimental test. Thus, in order to have a more accurate material model, the Author developed an innovative and more efficient way of computing stress-strain relations based on biaxial extension to obtain the compressive strain and consequently the force-displacement relationship obtained by FEA necessary to determine the conical rubber spring stiffness.

The biaxial experimental tests were performed in the “Technische Mechanik” lab from Saarland University and consisted of a classical cruciform device controlled by four step engines symmetrically triggered and headed according to a high performance embedded controller, during a sandwich doctorate cooperation project. The biaxial deformation was captured in the center of the specimen through GOM Correlate®, a free Digital Image Correlation (DIC) and evaluation software. A bulge test was also conducted, but data were evaluated in the VIC-3D® software from correlated solutions, since the calibration pattern was related to this software.

The main concern about this methodology development was to obtain by computational simulation the stiffness response due to changes in design such as the number of elastomeric layers, the cone tilt angle and the rubber thickness without having to build new prototypes.

The contact surfaces were also studied using the FE commercial software Abaqus® to represent the interaction between rubber and metal parts.

1.2 Objectives

The main focus of the present Dissertation is to develop a methodology to correlate the FE modeling of a conical rubber spring with the prototype experimental data under different multiaxial deformation loads.

The methodology was applied to evaluate the axial and radial stiffness under pre-compression of a real component in some certain working load conditions, where the final FE model has to be able to describe the real mechanical behavior of complex rubber bushings and to work effectively in the simulation.

In order to reach the proposed objective some steps were performed:

- For the purpose of fitting material models in FEA, the elastomers physical experiments were performed in uniaxial simple tension and simple compression which could also be represented by the equal biaxial extension test;

- Since the equal biaxial extension is one of the most challenging tests and is highly discussed in the literature concerning the accuracy of the uniform deformation region, a new method for obtaining the nominal stress-strain relationship was proposed. The validation was conducted by numerical simulations and biaxial extension experiments, which were treated according to the proposed methodology for large strains;

- An optimization algorithm was implemented in Python program language for Abaqus® in order to obtain the material parameters from FE simulations accurately adjusted according to the prototype test data. In the case of radial deflection, the optimization algorithm was implemented aiming to calibrate the responses considering the effects of a vertical pre-compression load. In addition, a subroutine for adaptive remeshing and

mesh mapping solution was implemented to regenerate the distorted mesh and to account the material constitutive behavior changes over the solution process;

- Finally, an analytical solution for radial deflection when the component is in the pre-compression free condition was developed based on simple rubber bushing geometries.

The effectiveness of the proposed approaches applied for the present Dissertation were demonstrated through the comparison with results obtained from the FE model and prototypes tests. From the final results, the main challenges involved in the finite element hyperelasticity simulation of rubber-like material real components under different cases of multiaxial loading and pre-compression could be stated.

1.3 Problem statement

Since new products development has always been increasing, several efforts have been focused on reducing time and costs. As the usual prototype-construction is generally very expensive and time-consuming, numerical simulation tools like the finite element method should become more reliable.

Even though a number of materials are available, elastomers play an important role in the product properties definition since it fulfills a wide range of functional tasks. Their typical applications are related to vibration damping, acoustic insulation, sealing, coupling, tires, consumer goods and so on. The high elasticity, considerable durability and the ability to support large deformations under external forces are their basic characteristics (EYERER *et al.*, 2008; GENT, 2012).

In railway industry the rubber springs are very useful, since they accommodate oscillatory motions and allow axes misalignments. They are located in the primary suspension, between the bogie frame and the axle box. Although a wide range of geometries can be found in order to fulfill user requirements, the conical rubber spring is one of the most used designs, since it acts as a universal damping and guiding element (LUO *et al.*, 2001; SEBESAN *et al.*, 2015). It consists of rubber pads bonded on its inner and outer metal surfaces layers conically arranged.

Thus, it is worth mentioning that this component needs to combine high stiffness for axle-guiding and an optimally vertical rigidity due to damping purposes.

Besides the conical rubber spring, the most common rubber components are subjected to different multiaxial loading cases in the real working conditions. For this reason, choosing a proper material model to be implemented in the numerical simulations is necessary to better describe the component behavior under each loading case (CHEVALIER *et al.*, 2001).

Since rubbers are materials that exhibit nearly incompressible behavior and often experience high strains in service, their strain states are usually very complex. Thus, their mechanical behavior should be defined based on strain energy potentials formulated according to the hyperelasticity theory. They are a mixture of tension, compression and shear with a very small amount of volume change.

The strain energy density function (W) defines the strain energy stored in the material per unit of reference volume. This function depends on the principal stretches or invariants of the strain tensor and it is directly linked to the material's stress-strain relationship which depends on a series of parameters (material constants) (LALO and GRECO, 2017). Therefore, in order to assess the rubber-like material constitutive law, some experiments should be performed for input data into curve fitting procedures for the Finite Element Analysis (FEA).

Several published works related to rubber bushing have been extensively researched since last decades. The first studies have been performed by Adkins and Gent (1954), who found a formulation to predict the stiffness variation according to the bushing length for four principal modes of deflection termed: torsional, axial, radial and tilting. Hill (1975a; b; 1977) performed studies related to the radial deformations of bonded cylindrical rubber bush mountings and its pre-compression effect. Petek and Kicher (1987) experimentally investigated the nonlinear behavior of a shear bushing with conical ends focusing on the axial quasi-static load/deflection properties.

In addition to the empirical bushing models, constitutive modeling through FEA has also been studied. Despite the main challenges about computational efforts and time-consuming process, Morman and Pan (1988) performed studies comparing the closed-form analytical equations developed for the application in the design of elastomeric components and simulation response

through FEA. They argued that the closed-form equations should not provide accurate results in case of more complicated geometries and complex boundary conditions.

Besides the studies presented above, Horton *et al.* (2000a; b) and Horton and Tupholme (2006) derived more accurate expressions for annular rubber bush mountings subjected to radial loading and tilting deflection based on the classical theory of elasticity. In the meantime, Luo *et al.* (2001) obtained the stress state of a simplified conical rubber spring by FEA according to the von Mises criterion. They compared the prototype experimental data with simulations, but only focusing on strength and durability of metal parts of the system. Kadlowec *et al.* (2003) performed studies in which annular bushings were subjected to radial, torsional and coupled radial-torsional modes of deformation. They compared the elastic bushing response obtained experimentally with finite element results. As far as the torsional mode was concerned, Horton and Tupholme (2005) derived new closed-form expressions for the torsional stiffness of spherical rubber bush mountings in the two principal modes of angular deformation. Despite the reasonably agreement of some analytical relationships, there have been some limitations in the use of closed-form equations, not being possible to cover all the real situations.

Thus, since the last ten years the modeling of rubber components through the finite element method has been increasingly used. Gil-Negrete *et al.* (2006) predicted the dynamic stiffness of filled rubber isolators using a finite element (FE) code. Olsson (2007) presented a method to analyze the dynamic behavior of rubber components under radial loading by considering an overlay of viscoelastic and elastoplastic finite element models. Gracia *et al*. (2010) studied two types of filled rubber industrial components subjected to several loads using FE analysis with the overlay model. In more recent studies, Tobajas *et al.* (2016) compared six hyperelastic models to simulate the behavior of a rubber used in automotive engines. Finally, Lee *et al.* (2017) proposed a hybrid method based on FEA and empirical modeling to obtain the hysteresis of suspension rubber bushings and predict the dynamic stiffness without performing iterative experiments and avoiding high computational costs.

Since the rubber properties for FEA should be defined from experimental data, Seibert and his co-workers (2014) studied an optimized specimen's shape through biaxial extension to calibrate the hyperelastic material parameters for the simulation of an engine mount placed in a car under multiaxial loading. Furthermore, Kaya *et al.* (2016) simulated the behavior of a vehicular rubber bushing using FEA and performed the shape optimization to redesign its geometry and to meet

the target static stiffness curve. Lalo and Greco (2017) compared the rubber bushing behavior extracted experimentally with hyperelastic models based on shore hardness and uniaxial extension.

At this point, it is worth mentioning that this Dissertation should be of value not only to the rubber industries, but also to the description of certain biomaterials, including soft tissues, cells and the DNA, which can be represented by hyperelastic models (FUNG, 1993; 1994). This happens since the biological molecules are mainly long chains of covalently bonded carbon and hydrogen atoms witch can be modeled by entropic elasticity (TRELOAR, 1975). Some research have shown that pathological soft tissues show different elastic behavior, as compared to healthy tissues. For example, the cancerous tissue is 3–7 times stiffer than the normal tissue (KROUSKOP *et al.*, 1998). Diabetes can increase the stiffness of the soft tissues of feet, causing pain in the region of the heel (ZHENG *et al.*, 2000). Nowadays with the overwhelming advance in 3D printing technology some breakthroughs in biomaterials (JAMMALAMADAKA and TAPPA, 2018; LIU and LI, 2018) and hyperelastic metamaterials (BODAGHI *et al.*, 2017; MANSOURI *et al.*, 2018) have been made. Recent studies have also been related to the hyperelastic bone (ALLURI *et al.*, 2018; JAKUS *et al.*, 2016), a 3D-printed synthetic material in which consists of an intricate latticework, designed to support the growth and regeneration of the new bone.

Based on the apparent extent of earlier works in modeling rubber-like materials, it is possible to state that the hyperelastic constitutive models predefined in finite element codes can be able to simulate geometry-independent components. However, some challenges need to be overcome when dealing with different multiaxial loading cases under large strains. In this situation, the present work seeks to develop a methodology based on curve fitting procedures for the main pure modes of deformation and optimization algorithms to characterize the hyperelastic constitutive model according to the applied multiaxial loading. Although the loading directions are axial and radial, the complex geometry of the component results in multiaxial modes of deformation on the rubber pads. According to the final results, it will be shown that special care should be taken when the load direction is changed and the previous characterization cannot be valid anymore.

Therefore, the wide range of hyperelastic materials application justifies a high research interest in their characterization through experimental techniques and in the study of accurate constitutive models able to describe their particular behavior.

1.4 Manuscript organization

The organization of this Dissertation will be done as follows:

- In the present chapter one, some introductory considerations were made in order to emphasize the relevance of the theme, considering the justifications, objectives and organization of the text.

- The second chapter presents a brief literature review about the rubber general characteristics (molecular structure, manufacturing process and mechanical properties). It also describes the hyperelastic constitutive relations and the experimental tests for fitting the material stress-strain curves into the FEA. An explanation about the conical rubber spring characteristics, geometry and applications is also approached in this chapter.

- In the third chapter the methods adopted to achieve the proposed objectives are presented. It contains the laboratory apparatus description and how the different rubber tests had been performed. The FE methodology used for all the structural calculation involved in this project is also explained in this chapter, including a brief description about the boundary conditions adopted.

- The fourth chapter shows the uniaxial and equal biaxial experimental results and its correlation with FEA. A comparison between equal biaxial and simple compression test considering both an oily and rough surface is also presented. Only for knowledge, a hardness test of the rubber is shown in this chapter. In addition, as for prototype tests, its experimental results and respective correlation with FEA based on data fitting and optimization algorithms can be found in this chapter together with the analytical solution developed for radial stiffness when the component is subjected free of pre-compression.

- The fifth and last chapter is addressed to the final conclusions about the applicability of the implemented methods and final results obtained. This chapter also suggests recommendations and proposals for future work.

2

LITERATURE REVIEW

2.1 Rubber general characteristics

Rubber is a collective name for a large group of materials with different chemical compositions but similar molecular structure and mechanical properties. The name “rubber” was originated from the pencil erasing property, since it could be used to erase or "rub out" mistakes made with a pencil. In the 18th century, it started to be used in the manufacturing of suspenders and straps. Many products were impregnated with rubber to make them waterproof, but its performance was still poor and used to cause major changes in products due temperature variation. Then, in 1839 Charles Goodyear discovered accidentally the vulcanization process, making the rubber an elastic material capable of preserving its characteristics over a wide temperature range (HANHI *et al.*, 2007). The fact that all rubbers are highly elastic polymers, that is, their shapes are recovered after being stretched or deformed, justifies the origin of the more descriptive name elastomer.

The common physical properties measured in rubber compounds include hardness, ultimate tensile strength, ultimate elongation, rebound resilience, aging resistance, tear resistance, weather resistance and fatigue resistance.

A very important process called vulcanization converts the plastic raw elastomeric material into a solid with elastic consistency. The vulcanization is a chemical process where the long molecular chains are linked together and thereby a stable and highly elastic matrix is formed. In general, the cross linking is enabled by a small amount of sulfur that is mixed with the plastic raw material. When the mixture is heated to about 150°C, the vulcanization process starts and cross-links are formed, connecting the molecular chains (CHEN *et al.*, 2017).

After vulcanization process, a flexible, resistive, three-dimensional chain is constructed, and then the material has an established structure and shape, becoming a soft, elastic solid. Its deterioration also becomes significantly slower, being able to be accelerated when exposed to ultraviolet radiation (GENT, 2012).

According to Morton (MORTON, 2013), rubber formulations are not simple and they are generally composed of a base rubber, fillers/oil system and a curing agent for vulcanization process. In general, the materials added in the rubber composition can be classified into the main following categories:

- Elastomers: The basic component of the rubber, selected in order to obtain the final physical properties of the product. It can be rubber alone, rubber-oil masterbatches, rubber-carbon black, reclaimed rubber, or thermoplastic elastomers.
- Processing Aids: Materials used to modify the rubber during mixing or during the processing steps. They are useful to help extrusion, calendering or molding operation.
- Vulcanization Agents: These materials are necessary for vulcanization in natural rubber. Without the chemical crosslinking reactions involving these agents, no improvement in the physical properties of the elastomers can occur.
- Accelerators: These ingredients reduce the vulcanization time (cure time) by increasing the rate of chemical reactions between compound molecules. In most cases the mechanical properties of the products are also improved.
- Accelerator Activators: They react with the accelerators in order to obtain maximum benefits from the acceleration process. Since they increase vulcanization rates, they are able to improve the final product's properties.
- Age-Resistors (Antidegradants): Antioxidants, antiozonants and other materials used to reduce aging processes in vulcanizates. They work by slowing the deterioration of rubber products, in which occur through reactions with an environment that causes damage to elastomer integrity, such as oxygen, ozone, light, heat, radiation, among others.
- Fillers: These materials are used to reinforce or modify physical/mechanical properties, to transmit processing properties and/or to reduce costs.

- Softeners: These materials when added to the rubber aid the molecules to interact better with each other within the blend. They promote higher elasticity, adhesion or replace a portion of rubber hydrocarbon without loss of physical properties.

Additional components may include colors, antioxidants, adhesion agents, flame retardant agents, blowing aids, abrasives and many other special process-enhancing chemical additives. Every component of a rubber formulation may affect its physical properties, where the mixing and curing process is also critical to define. Changes to improve one compound property may affect other properties, positively or negatively (DICK, 2014).

2.1.1 Molecular structure

Rubber is a collective term for macromolecular substances of natural (Natural Rubber - NR) or synthetic origin (Synthetic Rubber - SR), which are amorphous and composed by long molecular chains.

The rubber structure is composed of isoprene which is polymerized to give the polyisoprene polymer. The isoprene polymerization may follow either of two pathways: cis-polymerization (Figure 2-1a) or trans-polymerization (Figure 2-1b). The rubber formed from cis-polymerization is called cis-polyisoprene or Natural Rubber. Similarly, the rubber formed from trans-polymerization is called Synthetic Rubber (SHANKS and KONG, 2013).

(a) (b)

Figure 2-1: Rubber molecular structure (a) Cis (b) Trans.
Source: Shanks and Kong (2013)

Natural rubber is prepared from latex which is a colloidal solution of rubber in water. It has elastic properties and undergoes long range reversible extension even if relatively small force is applied to it.

Synthetic Rubber is an artificial rubber which is used as a substitute for the natural one. It is a by-product of petroleum and obtained by polymerization or polycondensation of unsaturated monomers. A wide range of different synthetic rubbers have emerged, reflecting the various different applications they are required.

The elastic properties of elastomers stem from a few crosslinks between the molecular chains (Figure 2-2) which are generated by crosslinking reactions between the macromolecules.

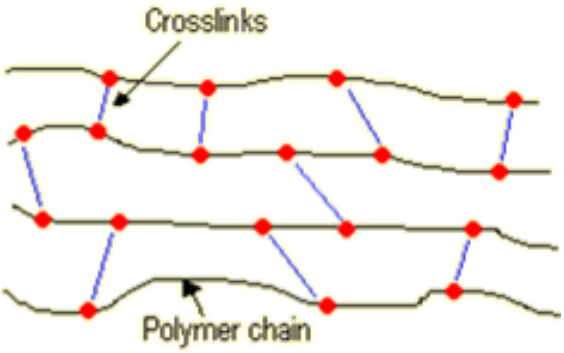

Figure 2-2: Elastomer structural diagram.
Source: Tomanek (1993)

The elasticity is derived from the ability of long molecular chains to stretch and to orient themselves at the straining direction. Thus, it is possible they reconfigure themselves to distribute an applied stress. The covalent cross-linkages ensure that the elastomer will return to its original configuration after the stress is removed. As a result of this extreme flexibility, elastomers can reversibly extend from 5% to 700%, depending on the specific material. These all are possible because the repeated molecular units in the polymer can rotate freely about the bonds joining the units. Without the cross-linkages or with short uneasily reconfigured chains, the applied stress would result in a permanent deformation (WHITE *et al.*, 2009).

Since the deformation is related to the straightening of chains, there is little volume change under an applied stress. Hence, it is possible to say that elastomers are nearly incompressible.

Reinforcing fillers such as carbon-black are added in order to increase the material stiffness and for some applications, to increase the resistance to wear. Carbon-black consists of very small particles of carbon (20nm – 50nm) that are mixed into the raw rubber base before vulcanization. The filler and the elastomeric material are not chemically joined. They are separate phases in the vulcanized rubber connected only by the cross-links. The rubber phase forms a continuous network, and the filler material forms agglomerates inside the rubber network. The material is thus a two-phase material made from constituents with completely different mechanical properties (DICK, 2014). Figure 2-3 better illustrates the carbon-black-filled rubber microstructure.

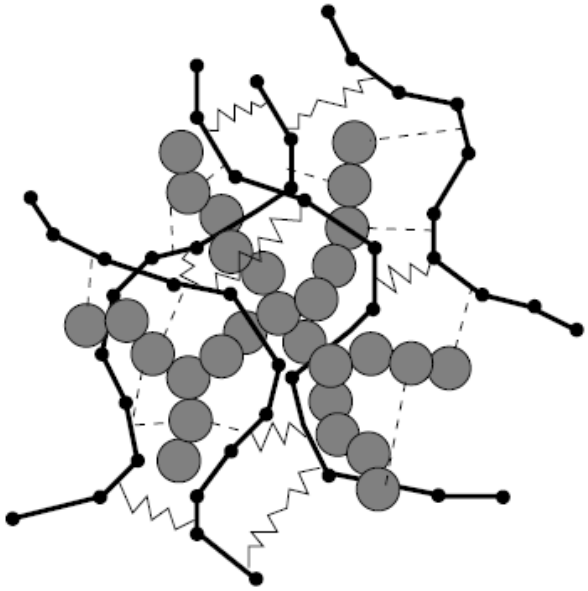

Figure 2-3: Microstructure for a carbon-black-filled vulcanized rubber. Grey circles: carbon-black particles. Solid lines: polymer chains. Zigzag and dashed lines: crosslinks.
Source: Olsson (2007)

Currently more than 42 standard commercial grades of carbon black are available to the rubber compounder. Some rubber formulations will use more than one grade of carbon black to balance the compound performance properties, adding further to the complexity (DICK, 2014).

Some fillers which do not impart the black coloration to the rubber can also be found, they are known as white fillers and are divided into non-reinforcing fillers and reinforcing fillers. Both are used to increase the viscosity of the vulcanizates, but non-reinforcing fillers can cause a

decrease in the mechanical quality of the material (generally for cost reduction) whereas reinforcing fillers provide hardness gain and mechanical resistance, among other important properties (MORTON, 2013). The main and most commonly used substances known as white fillers are: kaolins, calcium carbonates, hydrated silica and the silicates.

2.1.2 Manufacturing process

Vulcanized polymers are generally not used without compounding. Various additives like curing additives, protective system, reinforcing agents, cheapeners and other process aids have to be mixed to the polymer to make a coherent homogenous mass of all these ingredients

Due to the partly elastic nature and very high viscosity of rubber, power intensive sturdy machinery like mixing mills or internal mixers is necessary to achieve the mixing of additives into the polymer. The ingredients are in form of liquids, solid powders or solid agglomerates.

The mixing of solid raw materials into the polymer occurs in phases. During subdivision, large lumps or agglomerates are several times broken down into smaller aggregates at controlled temperatures for suitable incorporation into the rubber.

The ingredients incorporation is a very slow process. After an intensive mixing, the agglomerates and particles moves from one point to another increasing the randomness of the mixture. The powdery mass is compacted in another machine and then fed to the internal mixer.

Vulcanization and shaping are combined in the so-called molding process. The rubber filler mix is inserted into the mold cavity and heated to the appropriated temperature. Afterwards, the vulcanization process begins. The curing time is dependent on the temperature, the unit size and the appropriate heat is transferred to the unit. Engineering applications are often composed of both rubber and steel. The attached steel parts are used to connect the rubber unit to other structures or to increase the stiffness of the unit. It is possible to attach steel parts to the rubber material in the molding process. The steel parts are bonded, very efficiently, to the rubber.

The bond can be stronger than the rubber material itself in the sense that a rupture in a manufactured rubber-steel unit usually occurs in the rubber and not at the bonding surface between rubber and steel.

2.1.3 Mechanical properties

The most prominent feature of vulcanized rubbers is the elastic property. The ability to store large amounts of strain energy and to release most of it during unloading phase is a primary function. However, the more filler is mixed in the compound, the less elastic and stiffer becomes the material.

Another rubber characteristic is the large difference between shear modulus and bulk modulus. An example is a typical carbon-black-filled vulcanized rubber where the shear modulus (around 1MPa) is much lower than the bulk modulus (around 2000MPa). The large volumetric stiffness compared to the shear stiffness indicates a nearly incompressible behavior (FREAKLY and PAYNE, 1978).

Although rubber is a highly elastic material, it is not perfectly elastic. A difference is always observed between the loading and the unloading curves in a stress-strain diagram. This phenomenon is referred to as hysteresis, and is illustrated in Figure 2-4.

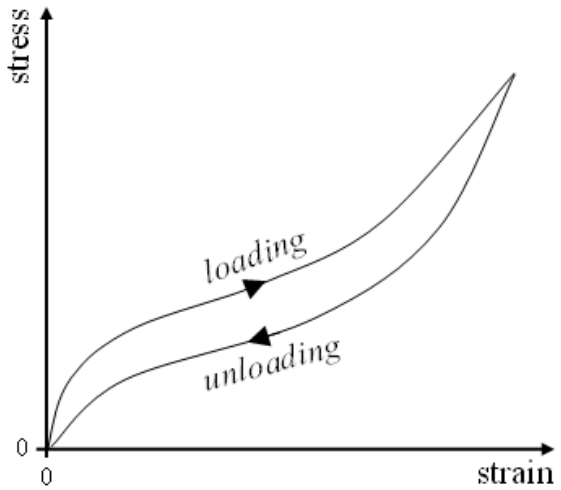

Figure 2-4: Hysteresis curve for natural rubber.
Source: Adapted from Shanks and Kong (2013)

The enclosed area by the loading and unloading curves represents energy dissipated mainly as heat. For free vibrations this phenomenon causes the amplitude decrease, and for this reason its property is therefore termed as damping capacity. In cyclic loading, the stress softening (or Mullin's effect) is another phenomenon which has to be considered and will be discussed further in this Dissertation.

The filler phase has a very small stress strength capacity as compared to the rubber phase. They can be regarded as rigid inclusions embedded in the rubber matrix. Consequently, stress and strain in the rubber phase of filled elastomeric units will reach higher levels than an unfilled unit. The maximum elongation will also be affected and it will be decreased by adding fillers. This effect due to filler adding on the rubber phase is called strain amplification. According to Chen *et al.* (2013) the rubber stiffness is classified by a hardness value. It is measured by an indentation test with three different shapes of indenter: spherical, conical or cylindrical. In the experimental test, a constant force is applied and the vertical displacement of the indenter's tip is measured.

There are two standard test methods used for measuring the rubber hardness: the IRHD (International Rubber Hardness Degrees) and the SH (Shore Hardness). The tests scales are almost identical for rubbers in the range of 30-80 IRHD where most rubbers mixes belong. The hardness test gives an indirect measure of the elastic modulus. This is sometimes the only value available for the material modulus. The relationship between the elastic modulus "*E*" and hardness in terms of shore scale is indicated in Figure 2-5 (ISO 7619-I, 2010; ISO 7619-II, 2010).

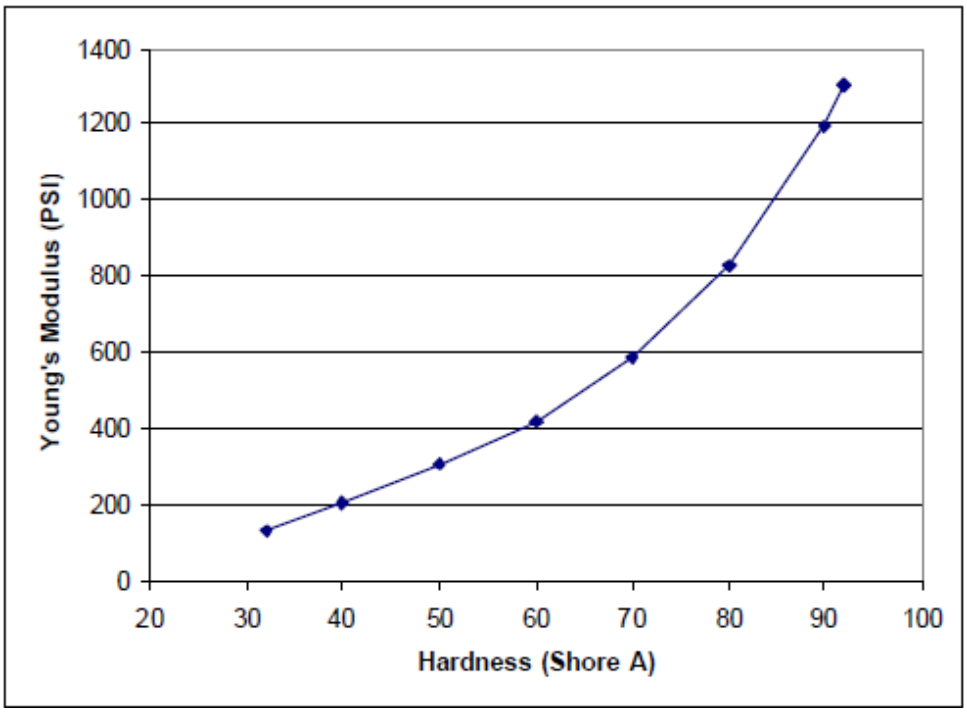

Figure 2-5: Relationship between the elastic modulus E and the shore hardness SH.
Source: Adapted from Göbel (1978)

The temperature is an important factor as well. When the polymer is below glass transition (T_g) temperature, there is insufficient thermal energy to overcome the activation energy for segmental motions and it will be glassy, that is a hard and relatively brittle state. If the temperature of a polymer is above Tg, segmental motions will occur and the polymer will exhibit an elastomeric behavior. When the temperature is within the glass transition range the polymer will be predominately viscoelastic. Thus, to obtain an effective elastomer, the polymer should be at a temperature higher than its T_g. Elastomeric performance at ambient temperatures (20–25 ºC) effectively requires Tg in the range of -70 to -20 ºC for an effective instantaneous reversible response to occur (GENT, 2012; SHANKS and KONG, 2013).

According to Figure 2-6 it is possible to see the expected results for a tensile test considering the three states of a polymer: glassy, crystalline and rubbery.

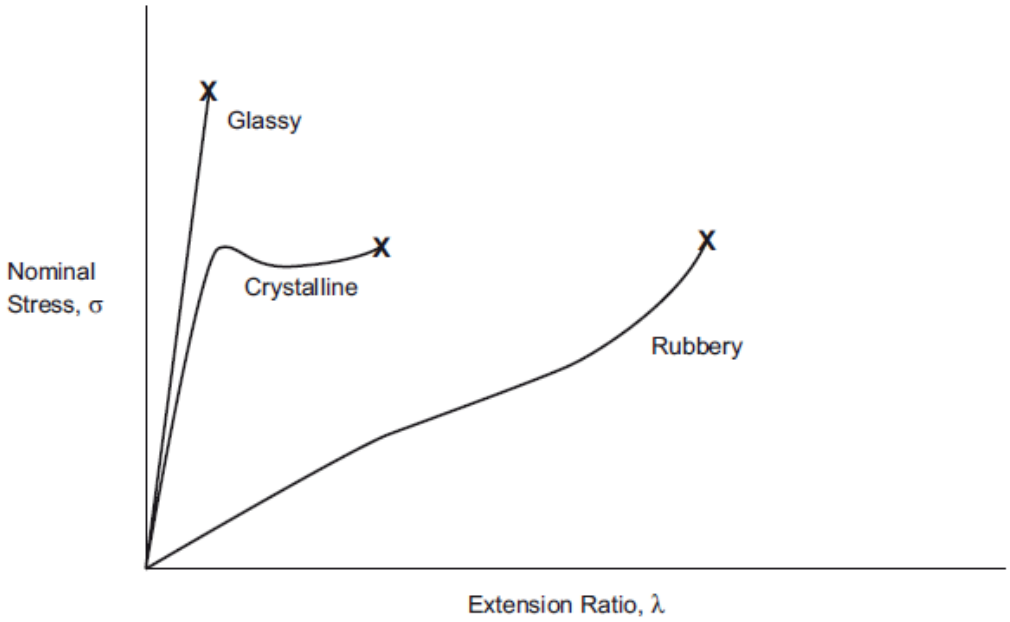

Figure 2-6: Stress-strain curves for a polymer in its three physical states: glassy, crystalline and rubbery.
Source: Gent (2012)

When the polymer becomes crystalline, it undergoes a series of changes until it reaches the rupture, such as: elastic deformation, yielding, plastic flow, necking, strain hardening and rupture (GENT, 2012).

2.2 Rubber nonlinear elasticity

In this section, a brief overview of the basic equations which describe the response of an incompressible isotropic nonlinear elastic material is provided. As the presented theory is focused on incompressible materials, a more general description of the nonlinear elasticity encompassing volume changes can be found in the works of (BORST *et al.*, 2012; CRISFIELD, 2000; HOLZAPFEL, 2000; OGDEN, 1984).

In continuum mechanics, the finite strain theory (also called large deformation theory) deals with deformations in which both rotations and normal strains are arbitrarily large. In this case, the undeformed and deformed configurations of the continuum are significantly different and a

clear distinction has to be made between them. This is commonly the case of elastomers, plastically-deforming materials and biological soft tissues.

Based on a constitutive law, an ideal material model can be described and the predictions of this law should provide an accurate approximation to the actual behavior of a real material (HOLZAPFEL, 2000)

The hyperelastic constitutive models are able to describe the behavior of nearly incompressible materials that exhibit instantaneous elastic response up to large strains. They are expressed in terms of a strain energy density function (W) which defines the strain energy stored in the material per unit of reference volume. This function depends on the principal stretches or invariants of the strain tensor and it is directly linked to the material's stress-strain relationship which depends on a series of parameters (material constants). In order to determine these constants, the nominal stress-strain data obtained from experimental tests are required to fit most models theoretical behavior available (BORTOLI *et al.*, 2011).

Based on hyperelasticity theory, the mechanical behavior of elastomers, foams and many biological tissues can usually be defined. Since elastomers are materials that exhibit nearly incompressible behavior and undergo large strains in service, its states of strain are usually very complex (LALO and GRECO, 2017). They are a mixture of traction, compression and shear with a very small amount of volume change.

This class of material still represents an elastic material, which means that it will return to its original form after the applied effort is removed. The main difference to the linear elastic material is that the hyperelastic stress-strain relationship derives from the function W and not from a constant factor. This definition says nothing about the Poisson's ratio, but since the material is nearly incompressible, the Poisson's ratio is considered to be close to 0.5 (JAKEL, 2010).

Several mathematical constitutive theories for hyperelastic large-strain response in quasi-static conditions and without irreversible strain phenomena have been extensively studied since last decades and are basically defined in two main theories: phenomenological or micromechanical.

The phenomenological models capture the overall behavior of some polymers and fit their experimental data with reasonable accuracy aiming to minimize computational effort. The first representative formulations were developed in the works of Mooney (1940) and Rivlin (1948a; b). The authors' approach was based on the strain invariants and in the concept that the material is isotropic and incompressible. Later, Rivlin and Saunders (1951) have proposed a new constitutive model, currently known as Mooney-Rivlin. In the 90s, Yeoh (1990; 1993) proposed a model by truncating the polynomial series to the first invariant and added more terms in order to increase accuracy. The simplest form of Rivlin's strain energy function is the Neo-Hookean model, based only on the first term (YEOH, 1993). The phenomenological models can also be formulated in terms of principal stretches as in Valanis and Landel (1967), and Ogden (1972).

On the other hand, the micromechanical models are based on statistical mechanics to capture the network evolution of cross-linked polymer chains and to predict the three-dimensional material response. These models can be applied to unusual polymers types, being first studied in the works of Flory and Rehner (1943), James and Guth (1943), Treloar (1943a; b; 1946) and Wang and Guth (1952). Latter, other classical models such as van der Waals proposed by Kilian *et al*. (1986), Arruda-Boyce (1993) and Gent (1996) were developed and nowadays are implemented in the most common FEA commercial software packages.

Additional documentation on this research topic including other theories and conditions can also be found in Al Akhass *et al.* (2014), Beda (2007), Cao *et al.* (2017), Carroll (2011), Destrade and Ogden (2010), Destrade *et al*. (2017), Drozdov (2007), Horgan (2015), Lambert-diani and Rey (1999) and Veronda *et al.* (1970).

Initially, an introduction to the nonlinear continuum mechanics is approached and following the hyperelastic constitutive relations assigned to rubbers will be discussed.
This Dissertation will focus on the constitutive models which have been implemented into the most common computational codes (ANSYS INC., 2014; MSC, 2016; SIMULIA, 2016). A quick review of the different models (Polynomial, Neo Hooke, Mooney–Rivlin, Yeoh, Ogden, Arruda–Boyce, Gent and van der Waals) will be given in the next sections, showing their characteristic formulations and how they are able to fit experimental data of uniaxial and equal biaxial extension tests.

Thus, after data fitting it is possible to simulate the mechanical behavior of a hyperelastic component into FEA codes and verify how simulations data are comparable to experimental ones.

2.2.1 Description of deformation and motion

To describe deformation properties of a body it is necessary to find the relation between the initial (not deformed) and final (deformed) positions. For a generic material point "*P*" in the body, the initial position will be the reference configuration of this elastic body (R_0) and its position vector "$\boldsymbol{X}$" is relative to an arbitrary chosen origin. Application of mechanical forces deforms the body, so that the initial point from $\boldsymbol{X}$ occupies a new position vector "$\boldsymbol{x}$" in the deformed configuration which is denoted by R_t (Figure 2-7). The reference system orientation is such that the loading directions for all cases are parallel to the Cartesian coordinate axes (PANCHERI and DORFMANN, 2012). The reference configuration can be denoted by material or Lagrangian coordinates and the deformed configuration by spatial, current or Eulerian coordinates (MAL and SINGH, 1991).

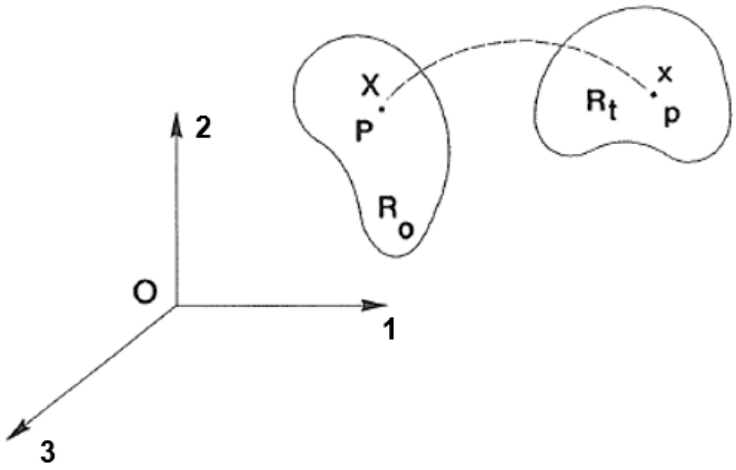

Figure 2-7: Representation of a generic material point "*P*" from the reference to deformed configuration.

Source: Adapted from Mal and Singh (1991)

Thus, the motion of a body can be described by a transformation function φ, defined according to the coordinates (X_1, X_2, X_3) from the vector $\boldsymbol{X}$ and (x_1, x_2, x_3) from the vector $\boldsymbol{x}$ at time "t" (DOGHRI, 2000):

$$\boldsymbol{x} = \varphi(\boldsymbol{X}, t)\ ; \qquad \boldsymbol{X} = \varphi^{-1}(\boldsymbol{x}, t) \tag{2-1}$$

Equation (2-1) can be interpreted as a mapping function which relates the reference configuration to the deformed configuration and describes the body motion.

This deformation is completely described by the second-order Cartesian tensor "$\boldsymbol{F}$" called deformation gradient tensor and defined by:

$$\boldsymbol{F} = \nabla \boldsymbol{x} \tag{2-2}$$

where ∇ denotes the gradient operator with respect to $\boldsymbol{X}$. The Cartesian components of $\boldsymbol{F}$ are $F_{lK} = \partial x_l / \partial X_K$, where $l = 1, 2, 3$ and $K = 1, 2, 3$.

Since $\boldsymbol{x} = \boldsymbol{X} + \boldsymbol{u}$ where $\boldsymbol{u}$ is the displacement, the deformation gradient can also be given by:

$$\boldsymbol{F} = 1 + \frac{\partial \boldsymbol{u}}{\partial \boldsymbol{X}} = \boldsymbol{I} + \nabla \boldsymbol{u}\ ; \qquad \text{where } \boldsymbol{I} \text{ is the identity tensor} \tag{2-3}$$

From the undeformed and deformed length relationships of an infinitesimal fiber of material, the expressions for infinitesimal volume variation in both configurations can be defined by the mixed product calculation (DOGHRI, 2000; OGDEN, 1984):

$$dV = d\boldsymbol{X}_1 . (d\boldsymbol{X}_2 \times d\boldsymbol{X}_3) = (d\boldsymbol{X}_1, d\boldsymbol{X}_2, d\boldsymbol{X}_3) \tag{2-4}$$

$$dv = d\boldsymbol{x}_1 . (d\boldsymbol{x}_2 \times d\boldsymbol{x}_3) = (d\boldsymbol{x}_1, d\boldsymbol{x}_2, d\boldsymbol{x}_3) \tag{2-5}$$

Thus, the volumetric relationship between both configurations is derived as follows:

$$dv = (\boldsymbol{F} . d\boldsymbol{X}_1, \boldsymbol{F} . d\boldsymbol{X}_2, \boldsymbol{F} . d\boldsymbol{X}_3) = |\boldsymbol{F}| dV \tag{2-6}$$

The determinant of $\boldsymbol{F}$ is called the functional determinant or the Jacobian[1] "J", which must be greater than zero for a continuous deformation to be physically possible. If the material is considered incompressible, $J = 1$, that is, the initial volume is equal to the final volume.

$$J = \det[F_{lK}] = |\boldsymbol{F}| > 0 \tag{2-7}$$

From equation (2-2), it is possible to see that the transformation of all infinitesimal line elements in the neighborhood of the material points is described by the values of the $\boldsymbol{F}$ at that point. However, the general motion of a line element consists of rigid translation and/or rotation, as well as a deformation caused by the material stretching containing the line element (MAL and SINGH, 1991).

From the statement above, the displacement of a body has two components: a rigid-body motion and a deformation. The rigid-body motion consists of a simultaneous translation and rotation of the body without changing its shape or size, and deformation on the other hand, implies the change in shape and/or size of the body from an initial or undeformed configuration to a current or deformed configuration.

Since $\boldsymbol{F}$ is asymmetric and the major interest is in the deformational properties of the solid, it is necessary to identify and separate out the part of $\boldsymbol{F}$ that describes the rigid translation and rotation of the element. Thus, this can be accomplished as the deformation gradient can be decomposed according to the unique polar decomposition (BORST *et al.*, 2012):

$$\boldsymbol{F} = \boldsymbol{R}.\boldsymbol{U} = \boldsymbol{V}.\boldsymbol{R} \tag{2-8}$$

where $\boldsymbol{R}$ is a proper orthogonal rotation tensor, and $\boldsymbol{U}$ and $\boldsymbol{V}$ are positive-definite and symmetric tensors. They are known as the right and left stretch tensors[2] respectively.

[1] Relates the factor by which the components of **F** expand or shrink volumes near P.

[2] The terms right and left means that they are to the right and to the left of the rotation tensor R, respectively.

The tensors $\boldsymbol{U}$ and $\boldsymbol{V}$ have the same three real positive eigenvalues λ_1, λ_2 and λ_3 (principal stretches) and three mutually orthogonal eigenvectors, which are the principal directions of the deformation defined according to a rotation followed by stretches.

Since the stretch tensors measure the material length variation, two new strain measurements can be defined by calculating the squared length of an infinitesimal fiber of material in the reference and current configurations:

$$d\boldsymbol{x}^2 = (\boldsymbol{F}d\boldsymbol{X})^2 = d\boldsymbol{X}^T.\boldsymbol{F}^T.\boldsymbol{F}.d\boldsymbol{X} = d\boldsymbol{X}^T.\boldsymbol{C}.d\boldsymbol{X} \tag{2-9}$$

$$d\boldsymbol{X}^2 = (\boldsymbol{F}^{-1}d\boldsymbol{x})^2 = d\boldsymbol{x}^T.(\boldsymbol{F}.\boldsymbol{F}^T)^{-1}.d\boldsymbol{x} = d\boldsymbol{x}^T.\boldsymbol{B}^{-1}.d\boldsymbol{x} \tag{2-10}$$

Thus, through the decomposition of $\boldsymbol{F}$, it is possible to have a very important strain measure for hyperelastic constitutive models, which is called Cauchy-Green strain tensor. This tensor is symmetrical and is subdivided into two strain tensors known as: right and left Cauchy-Green strain tensor, respectively represented by equations (2-11) and (2-12).

$$\boldsymbol{C} = \boldsymbol{F}^T.\boldsymbol{F} = \boldsymbol{U}^T.\boldsymbol{R}^T.\boldsymbol{R}.\boldsymbol{U} = \boldsymbol{U}^2 \tag{2-11}$$

$$\boldsymbol{B} = \boldsymbol{F}.\boldsymbol{F}^T = \boldsymbol{V}.\boldsymbol{R}.\boldsymbol{R}^T.\boldsymbol{V}^T = \boldsymbol{V}^2 \tag{2-12}$$

Therefore, it was clearly shown that $\boldsymbol{C}$ was defined according to the reference configuration while $\boldsymbol{B}$ according to the current configuration.

From the eigenvalues of $\boldsymbol{C}$ or $\boldsymbol{B}$, the squared principal stretches λ_i^2 $(i = 1,2,3)$ can be computed with their respective invariants I_1, I_2 and I_3 based on the tensor $\boldsymbol{C}$ (HOLZAPFEL, 2000):

$$I_1 = tr\,\boldsymbol{C} = {\lambda_1}^2 + {\lambda_2}^2 + {\lambda_3}^2 \tag{2-13}$$

$$I_2 = \frac{1}{2}(tr\,\boldsymbol{C})^2 - \frac{1}{2}(tr\,\boldsymbol{C}^2) = {\lambda_1}^2.{\lambda_2}^2 + {\lambda_2}^2.{\lambda_3}^2 + {\lambda_3}^2.{\lambda_1}^2 \tag{2-14}$$

$$I_3 = |\mathbf{C}| = J^2 = {\lambda_1}^2.{\lambda_2}^2.{\lambda_3}^2 \tag{2-15}$$

Thus, it is possible to show that the transformation of the line element from $\boldsymbol{X}$ to $\boldsymbol{x}$ is due to compression if $\lambda_i < 1$ or stretching if $\lambda_i > 1$ along the principal axes of $\boldsymbol{U}$, as follows:

$$x_1 = \lambda_1 . X_1 \; ; \qquad x_2 = \lambda_2 . X_2 \; ; \qquad x_3 = \lambda_3 . X_3 \tag{2-16}$$

where X_1, X_2 and X_3 are rectangular Cartesian coordinates that identify material particles in the unstressed reference configuration, x_1, x_2 and x_3 are the corresponding coordinates after deformation with respect to the same axes, and the coefficients λ_1, λ_2 and λ_3 are positive constants, referred to as the principal stretch ratios of the deformation.

Since the mechanical experimental tests applied in the characterization of rubber-like materials are performed in pure deformation modes, the Cauchy-Green strain tensors are already obtained in a principal coordinate system:

$$\boldsymbol{C} = \boldsymbol{B} = \begin{bmatrix} {\lambda_1}^2 & 0 & 0 \\ 0 & {\lambda_2}^2 & 0 \\ 0 & 0 & {\lambda_3}^3 \end{bmatrix} \tag{2-17}$$

2.2.2 Finite strain measures

Since elastomers deals with deformations in which strains and/or rotations are very large, the undeformed and deformed configurations of the continuum are significantly different, requiring a clear distinction between them, and recalling to the finite strain theory.

From the concept of Cauchy-Green strain tensors and their respective stretches, some classical measurements applied in the finite strain theory could be developed according to the Seth-Hill family (SETH, 1961), which for one-dimensional (1D) case is defined as follows (GRECO and DA COSTA, 2012):

$$\varepsilon_m = \frac{1}{m}(\lambda^m - 1) \qquad : m \in \mathbb{R} \setminus \{0\} \tag{2-18}$$

$$\varepsilon_m = ln(\lambda) \qquad : m = 0 \tag{2-19}$$

The above strain measurement ε_m can also be generalized from 1D to 3D (three-dimensional), resulting in a strain tensor $\boldsymbol{E}_m$.

$$\boldsymbol{E}_m = \frac{1}{m}(\boldsymbol{U}^m - \boldsymbol{I}) = \frac{1}{m}\left(\boldsymbol{C}^{m/2} - \boldsymbol{I}\right) \qquad : m \in \mathbb{R} \setminus \{0\} \tag{2-20}$$

$$\boldsymbol{E}_m = \ln(\boldsymbol{U}) \qquad : m = 0 \tag{2-21}$$

where m is intrinsically related to the strain measure adopted. This strain measure must be invariant for rotational motions, that is, rigid body rotations cannot generate strains (GRECO and DA COSTA, 2012). Some classical strain tensors are described according to the different values of m:

- Green-Lagrange strain tensor: This tensor is written based on the reference configuration and does not account for rigid body motions by subtracting the identity tensor $\boldsymbol{I}$.

$$\boldsymbol{E}_{m=2} = \frac{1}{2}(\boldsymbol{U}^2 - \boldsymbol{I}) = \frac{1}{2}(\boldsymbol{C} - \boldsymbol{I}) \tag{2-22}$$

- Euler-Almansi strain tensor: This tensor also disregards rigid body motions, but unlike Green-Lagrange, the strain measurements are written in the current configuration.

$$\boldsymbol{E}_{m=-2} = \frac{1}{2}(\boldsymbol{I} - \boldsymbol{U}^{-2}) = \frac{1}{2}(\boldsymbol{I} - \boldsymbol{C}^{-1}) \tag{2-23}$$

According to Seth (1961) the Green and Almansi strain tensors can be special cases of a more general strain measures.

- Biot strain tensor: This tensor corresponds to the nominal strain measurement. It is a linear tensor and corresponds to the engineering strain, also known as Cauchy tensor.

$$\boldsymbol{E}_{m=1} = (\boldsymbol{U} - \boldsymbol{I}) \tag{2-24}$$

- Hencky strain tensor: This tensor corresponds to the true strain measurement and is written in a logarithmic scale.

$$\boldsymbol{E}_{m=0} = \ln(\boldsymbol{U}) \tag{2-25}$$

- Hyperbolic strain tensor: This tensor is also known as Swainger and is based on linear displacement gradients in the deformation state (SETH, 1961).

$$\boldsymbol{E}_{m=-1} = (\boldsymbol{I} - \boldsymbol{U}^{-1}) \tag{2-26}$$

From Figure 2-8 it is worth noting that all strain measures presented in the graph tend to the same value for infinitesimal stretching measures ($\lambda \approx 1$). As the stretching increases or decreases, the results diverge significantly. This explains how important is the strain measure when dealing with a large strain regime.

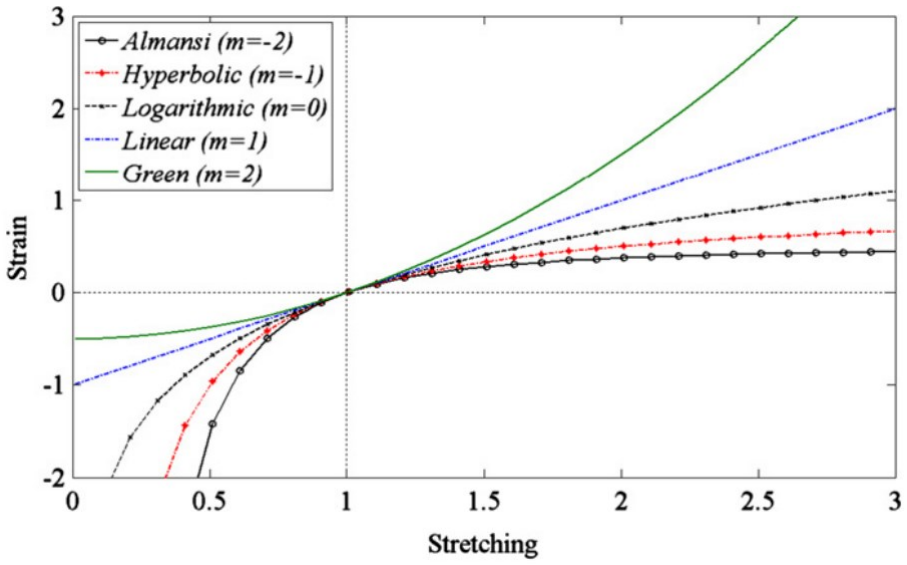

Figure 2-8: Strain-stretching curves for the classical strain measures

Source: Greco and Da Costa (2012)

2.2.3 Stress measures

Mechanical stress is defined as a measurement of forces density per unit of area, represented by each point of the continuum body as a second order tensor. As there are several ways to

measure strain, there are also several ways to measure stress. For each type of strain measure, there is an energy conjugate stress pair σ_m, which is associated to the constant m and stretch λ (GRECO and DA COSTA, 2012).

In the case of large deformations, it is of great interest to deal with material geometry in the reference configuration. For this reason, the nominal stress σ_N measures are very useful, since it is directly conjugate to the linear strains. The classical strain–stress energy conjugate pairs are presented in Table 2-1:

$$\sigma_m = \sigma_N . \lambda^{(1-m)} \tag{2-27}$$

Table 2-1: Strain–stress energy conjugate pairs
Source: Adapted from Greco and Da Costa (2012)

	m	Symbol	Strain measure	Stress pair
Almansi	-2	ε_A	$1/2(1-\lambda^{-2})$	$\sigma_A = \sigma_N . \lambda^3$
Hyperbolic	-1	ε_H	$(1-\lambda^{-1})$	$\sigma_H = \sigma_N . \lambda^2$
Logarithmic	0	ε_L	$ln(\lambda)$	$\sigma_L = \sigma_N . \lambda$
Linear	1	ε_N	$(\lambda - 1)$	$\sigma_N = (N/A)$
Green	2	ε_G	$1/2(\lambda^2 - 1)$	$\sigma_G = \sigma_N . \lambda^{-1}$

In order to better represent the physical meaning of some stress measures, a circular cylindrical bar is considered. The current value of the tension force will be F, while the cross section area will be A and a for the initial and final configurations, respectively. As the nominal stresses are related to the reference configuration it will be denoted as σ_N, while the Cauchy stresses (σ_L), also known as true stresses or even logarithmic stresses, are related to the current configuration.

$$\sigma_N = \frac{F}{A}; \qquad \sigma_L = \frac{F}{a}; \qquad F = \sigma_N . A = \sigma_L . a \tag{2-28}$$

Then, considering an infinitesimal area da and the outward normal vector $\boldsymbol{n}$ on R_t, and an infinitesimal area dA with the outward normal vector $\boldsymbol{N}$ on R_0, it is possible to generalize the relations obtained in equation (2-28) to multiaxial stress states. In this context, Nanson's formula, see Ogden (1984), becomes a very interesting relationship:

$$\boldsymbol{F}^{T}.\boldsymbol{n}\,da = J.\boldsymbol{N}\,dA \tag{2-29}$$

remembering that $\boldsymbol{F}$ is the deformation gradient tensor and J its determinant.

As long as Cauchy stress is a second order tensor ($\boldsymbol{\sigma_L}$) defined with respect to the current configuration, it can be written in terms of traction forces $\boldsymbol{t}$ for uniaxial extension at time t:

$$\boldsymbol{t}(\boldsymbol{x},t,\boldsymbol{n}) = \boldsymbol{\sigma_L}^{T}(\boldsymbol{x},t).\boldsymbol{n} \tag{2-30}$$

From equations (2-29) and (2-30), a new expression for the traction force can be found:

$$\boldsymbol{t}\,da = (\boldsymbol{\sigma_L}^{T}.\boldsymbol{n})\,da = (J.\boldsymbol{\sigma_L}^{T}.\boldsymbol{F}^{-T}).\boldsymbol{N}\,dA \tag{2-31}$$

Thus, the expression $(J.\boldsymbol{\sigma_L}^{T}.\boldsymbol{F}^{-T})$ represents the first Piola-Kirchhoff stress $\boldsymbol{P}$, and its transpose the nominal stress $\boldsymbol{\sigma_N} = \boldsymbol{P}^{T} = J.\boldsymbol{F}^{-1}.\boldsymbol{\sigma_L}$.

If the traction per unit of area is designated by $\boldsymbol{t}(\boldsymbol{x},t,\boldsymbol{n})$ and $\boldsymbol{T}(\boldsymbol{X},t,\boldsymbol{N})$ in the current and reference configurations, respectively, it is possible to have the extension from 1D to 3D as follows:

$$(\boldsymbol{\sigma_L}^{T}.\boldsymbol{n})\,da = (\boldsymbol{P}.\boldsymbol{N})\,dA\ ; \qquad \begin{matrix}\boldsymbol{t} = \boldsymbol{\sigma_L}^{T}.\boldsymbol{n} \\ \boldsymbol{T} = \boldsymbol{P}.\boldsymbol{N} = \boldsymbol{\sigma_N}^{T}.\boldsymbol{N}\end{matrix} \tag{2-32}$$

It is worth noting that vectors $\boldsymbol{t}$ and $\boldsymbol{T}$ have the same directions.

One of the main difficulties of the first Piola-Kirchhoff stress tensor is its unsymmetry, which results in very complex constitutive equations. For this reason, another important symmetric stress tensor which is conjugate with Green-Lagrange strains was developed. It is named as second Piola-Kirchhoff and designated by $\boldsymbol{S}$.

To solve the symmetry problem, the traction forces should be transferred from deformed configuration to the initial configuration through the inverse of the deformation gradient tensor.

$$\boldsymbol{S} = J.\boldsymbol{F}^{-1}.\boldsymbol{\sigma_L}.\boldsymbol{F}^{-T} = \boldsymbol{\sigma_N}.\boldsymbol{F}^{-T} \quad (2\text{-}33)$$

From the definition of the classical strain tensors and consequently, through the constitutive equations of the deformable material it is possible to relate each stress tensor according to the respective conjugate pair of strain.

2.2.4 Hyperelastic constitutive relations

The quantifiers of stress-strain responses are related through laws, which are called constitutive laws. How they relate to each other depends on the material behavior and its application (ALI *et al.*, 2010). In general, the behavior of materials can be listed according to models which can include one or more behaviors, such as: elasticity, hyper/hypoelasticity, viscoelasticity, plasticity, viscoplasticity, among others.

In order to obtain the constitutive relationships for hyperelastic materials specially applied to isotropic and incompressible materials, the definitions of nonlinear elasticity for the large strain regime must be developed.

In the theory of hyperelasticity, the work done by body forces and surface tractions is all stored as elastic energy, for a time independent deformation. As already mentioned in the beginning of this chapter, the strain energy density is denoted by "W" and represents the work done by the stress when deforming a unitary volume from domain R_0 to domain R_t. For homogeneous materials, W depends on the deformation gradient and for this reason it will be used the notation $W = W(\boldsymbol{F})$.

Since $\boldsymbol{F} = \boldsymbol{R}.\boldsymbol{U}$ and $\boldsymbol{C} = \boldsymbol{F}^T.\boldsymbol{F} = \boldsymbol{U}^2$ from the polar decomposition and according to the principle of material objectivity[3], the rotation matrix $\boldsymbol{R}$ reduces to the identity matrix $\boldsymbol{I}$, so the energy W can also be written in terms of the strain tensor $\boldsymbol{C}$ (DOGHRI, 2000):

[3] The objectivity requires that the stored energy is unchanged when the body is subject to an arbitrary rigid motion in the configuration R_t.

$$W(\boldsymbol{F}) = W(\boldsymbol{C}) \tag{2-34}$$

Recalling that $\boldsymbol{C}$ is symmetric, so $\boldsymbol{C}^T = \boldsymbol{C}$. The energy function W depends on the principal invariants of $\boldsymbol{C}$. These are denoted by I_1, I_2 and I_3 as a function of principal stretches according to equations (2-13), (2-14) and (2-15) already presented in the previous section.

Therefore, the energy function of an unconstrained, isotropic and elastic material can be derived as a function of the right Cauchy-Green strain invariants I_1, I_2 and I_3, or even in terms of the principal stretches λ_1, λ_2 and λ_3 (OGDEN, 1984; VALANIS and LANDEL, 1967). If the energy is a symmetric function of the principal stretches, it can be rewritten as:

$$W(\lambda_1, \lambda_2, \lambda_3) = W(\lambda_2, \lambda_1, \lambda_3) = W(\lambda_1, \lambda_3, \lambda_2) \tag{2-35}$$

Since the material is considered to be incompressible, a single scalar constraint called $h = (\boldsymbol{F})$ should be taken into account, and its time derivation $\dot{h}$ equals zero (DOGHRI, 2000):

$$\dot{h} = \frac{\partial h}{\partial \boldsymbol{F}} . \dot{\boldsymbol{F}} = 0 \tag{2-36}$$

where $\dot{\boldsymbol{F}}$ means the deformation gradient rate.

Based on this assumption the expression for strain energy rate ($\dot{W}$) can be formulated according to derivative chain rule in terms of $\dot{h}$.

$$\dot{W} = \frac{\partial W}{\partial \boldsymbol{F}} . \dot{\boldsymbol{F}} - p . \frac{\partial h}{\partial \boldsymbol{F}} . \dot{\boldsymbol{F}} \tag{2-37}$$

where p is treated as a Lagrange multiplier related to the volume change.

Thus, providing that $\dot{W} = \boldsymbol{\sigma_N} . \dot{\boldsymbol{F}}$, it is possible to derive the stress accounting for the compressibility constraint.

$$\boldsymbol{\sigma_N} = \frac{\partial W}{\partial \boldsymbol{F}} - p . \frac{\partial h}{\partial \boldsymbol{F}} \tag{2-38}$$

Since for rubber-like materials it is common to adopt the incompressibility constraint, it is considered that: $h(\boldsymbol{F}) = J - 1 = 0 \ \therefore J = 1$. According to Ogden (1984) $\partial J/\partial \boldsymbol{F} = J.\boldsymbol{F}^{-T}$, and then, the second part of the equation (2-38) is rewritten according to the chain rule:

$$\boldsymbol{\sigma_N} = \frac{\partial W}{\partial \boldsymbol{F}} - p.\boldsymbol{F}^{-T} \tag{2-39}$$

Then, equation (2-39) can be read in the component form:

$$\sigma_{N_{iK}} = \frac{\partial W}{\partial F_{iK}} - p.F_{Ki}^{-1}\,; \qquad i,K = 1,2,3 \tag{2-40}$$

where it is possible to note the switch of indices with respect to the gradient deformation tensor.

In some cases, it may be useful to work in the current configuration using the Cauchy stress tensor (CRISFIELD, 2000). Thus, considering the Nanson's formula showed in equation (2-29) the connection between the symmetric second-order Cauchy stress $\boldsymbol{\sigma_L}$ and the nominal stress $\boldsymbol{\sigma_N}$ is obtained:

$$\boldsymbol{\sigma_L} = J^{-1}.\boldsymbol{F}.\boldsymbol{\sigma_N} \tag{2-41}$$

Since for an incompressible material $J = 1$, equation (2-41) gives:

$$\boldsymbol{\sigma_L} = \boldsymbol{F}\frac{\partial W}{\partial \boldsymbol{F}} - p.\boldsymbol{I}\,; \qquad \sigma_{L_{ij}} = F_{iK}\frac{\partial W}{\partial F_{jK}} - p.\delta_{ij} \tag{2-42}$$

where $\boldsymbol{I}$ is the identity tensor and δ_{ij} the Kronecker delta. The first terms in $\boldsymbol{\sigma_N}$ and $\boldsymbol{\sigma_L}$ are related to the deviatoric[4] part of stress, while p in the second term to the hydrostatic[5] part of stress which is associated with the incompressibility condition (CHEVALIER *et al.*, 2001).

[4] The deviatoric stress is related to shape change and it is what's left after subtracting out the hydrostatic stress.

[5] The hydrostatic stress is related to volume change.

The stress tensor $\boldsymbol{\sigma_L}$ can also be written is terms of Cauchy-Green strain tensor $\boldsymbol{C}$, by the following relation:

$$\frac{\partial W}{\partial \boldsymbol{F}} = 2.\boldsymbol{F}^T.\frac{\partial W}{\partial \boldsymbol{C}}\ ; \qquad \boldsymbol{\sigma_L} = 2.\boldsymbol{F}\frac{\partial W}{\partial \boldsymbol{C}}.\boldsymbol{F}^T - p.\boldsymbol{I} \tag{2-43}$$

It's worth mentioning that the Lagrange multiplier p is not given by the constitutive model, but instead it can be obtained from solving the boundary value problem together with the incompressibility constraint.

From this point, according to the Cayley-Hamilton theorem, the tensor $\boldsymbol{C}$ can be derived in terms of its invariants as follows:

$$\boldsymbol{C}^3 - I_1\boldsymbol{C}^2 + I_2\boldsymbol{C} - I_3\boldsymbol{I} = 0 \tag{2-44}$$

As already mentioned in section 2.2.1, the experiments for elastomers are performed in pure modes of deformation. For this reason, the tensor $\boldsymbol{C}$ is already obtained in the principal directions and analytical solutions can be derived. From this assumption and equation (2-44) the constitutive relation for a hyperelastic isotropic material is given based on strain invariants (MANSOURI *et al.*, 2016; MARCKMANN and VERRON, 2006):

$$\boldsymbol{\sigma_L} = 2\frac{\partial W}{\partial I_1}\mathbf{C} - 2\frac{\partial W}{\partial I_2}\mathbf{C}^{-1} - p\mathbf{I} \tag{2-45}$$

or in terms of its components in the principal directions:

$$\sigma_{L_i} = 2\lambda_i^2\frac{\partial W}{\partial I_1} - \frac{2}{\lambda_i^2}\frac{\partial W}{\partial I_2} - p\ ; \qquad i = 1,2,3 \tag{2-46}$$

For the energy function determination, Valanis and Landel (1967) and Ogden (1984) stated that stress deformation relation in terms of the extension ratios is more appropriate than the strain invariants. Hence, the Cauchy stress components in terms of principal stretches is given by:

$$\sigma_{L_i} = \lambda_i.\frac{\partial W}{\partial \lambda_i} - p\ ; \qquad i = 1,2,3 \tag{2-47}$$

where σ_{L_i} are the eigenvalues of $\boldsymbol{\sigma_L}$. Similary, the specialization of equation (2-47) gives the principal Nominal stresses:

$$\sigma_{N_i} = \frac{\partial W}{\partial \lambda_i} - p.{\lambda_i}^{-1}\,; \qquad i = 1,2,3 \tag{2-48}$$

Note that the transformation between the principal components of $\boldsymbol{\sigma_N}$ and $\boldsymbol{\sigma_L}$ reduces to $\sigma_{L_i} = \lambda_i.\sigma_{N_i}$, with no summation over i.

When the incompressibility constraint $J = 1$ is applied $I_3 = {\lambda_1}^2.{\lambda_2}^2.{\lambda_3}^2 = 1$, and the stretch in the third direction is expressed as:

$$\lambda_3 = {\lambda_1}^{-1}.{\lambda_2}^{-1} \tag{2-49}$$

This means that only two of the principal stretches are independent, so the strain energy can be defined by a symmetric function of the stretches λ_1 and λ_2 as follows:

$$\widetilde{W}(\lambda_1, \lambda_2) = W\left(\lambda_1, \lambda_2, {\lambda_1}^{-1}.{\lambda_2}^{-1}\right) \tag{2-50}$$

Using equation (2-50) in (2-47) the principal stress differences are given:

$$\sigma_{L_1} - \sigma_{L_3} = \lambda_1.\frac{\partial \widetilde{W}}{\partial \lambda_1}\,; \qquad \sigma_{L_2} - \sigma_{L_3} = \lambda_2.\frac{\partial \widetilde{W}}{\partial \lambda_2} \tag{2-51}$$

where one note that the scalar "p" has been eliminate, and $\widetilde{W}$ is an arbitrary function of λ_1 and λ_2. For consistency with the classical theory, $\widetilde{W}$ must satisfy a series of conditions (SASSO *et al.*, 2008):

$$\begin{cases} \widetilde{W}(1,1) = 0 \\ \dfrac{\partial \widetilde{W}}{\partial \lambda_1}(1,1) = \dfrac{\partial \widetilde{W}}{\partial \lambda_2}(1,1) = 0 \\ \dfrac{\partial^2 \widetilde{W}}{\partial \lambda_1 \partial \lambda_2}(1,1) = 2\mu \\ \dfrac{\partial^2 \widetilde{W}}{\partial \lambda_1^2}(1,1) = \dfrac{\partial^2 \widetilde{W}}{\partial \lambda_2^2}(1,1) = 4\mu \end{cases} \tag{2-52}$$

where μ is the shear modulus of the material in the reference configuration.

If the deformation is applied to a thin sheet of material (a common situation experimentally) then a plane stress condition is applied, and the stress normal to the plane of the sheet, $\sigma_3 = 0$. Then, equation (2-51) can be simplified as follows:

$$\sigma_{L_1} = \lambda_1 . \frac{\partial \widetilde{W}}{\partial \lambda_1} \; ; \qquad \sigma_{L_2} = \lambda_2 . \frac{\partial \widetilde{W}}{\partial \lambda_2} \tag{2-53}$$

There are several special cases of tests which are important from the experimental point of view. These are simple tension, equal biaxial extension and pure shear, which are going to be discussed later.

When the material compressibility is a concern, it is necessary to split out the deviatoric (represented with "superscript bar") and volumetric terms of the strain energy function, represented by W_d and W_b respectively. As a result, the volumetric term is a function of the volume ratio J only.

$$W = W_d(\overline{I_1}, \overline{I_2}) + W_b(J) \tag{2-54}$$

$$W = W_d\left(\overline{\lambda_1}, \overline{\lambda_2}, \overline{\lambda_3}\right) + W_b(J) \tag{2-55}$$

where the deviatoric principal stretches and invariants are respectively defined as:

$$\overline{\lambda_p} = J^{-1/3} . \lambda_p \; ; \qquad p = 1,2,3 \tag{2-56}$$

$$\overline{I_1} = J^{-2/3} . I_1 \; ; \qquad \overline{I_2} = J^{-4/3} . I_2 \tag{2-57}$$

Thus, the first and second deviatoric strain invariants "I_1" and "I_2" derived from equations (2-13) and (2-14) can be rewritten as:

$$\overline{I_1} = \bar{\lambda}_1^2 + \bar{\lambda}_2^2 + \bar{\lambda}_3^2 \tag{2-58}$$

$$\bar{I}_2 = \bar{\lambda}_1^{(-2)} + \bar{\lambda}_2^{(-2)} + \bar{\lambda}_3^{(-2)} \tag{2-59}$$

The particular models of the strain energy functions will be discussed in the next sections, as they determine whether stretch ratios or invariants are going to be used.

2.2.4.1 Neo-Hookean model

Treloar (1943a; b) proposed the so-called neo-Hookean material model based on molecular chain statistics theory. This is the simplest physically based constitutive model for rubbers since it was derived only in terms of the first invariant ($\bar{I}_1$). It can also be formulated by truncating the power series of a polynomial equation (RIVLIN, 1948a; b) and has the following simple form:

$$W = C_{10}.(\bar{I}_1 - 3) + \frac{1}{D_1}(J-1)^2 \tag{2-60}$$

where, C_{10} is a material parameter obtained from experimental data for deviatoric part and D_1 is related to the compressibility ratio. Then, the initial shear modulus "μ_0" and bulk modulus "K_0" are given by:

$$\mu_0 = 2.C_{10}\,; \qquad K_0 = 2/D_1 \tag{2-61}$$

Even though the phenomenological and statistical theories were formulated from quite different premises they are considered equivalent. This model can be a good starting point for the analysis, knowing just the constant shear modulus. However, the strains should be limited up to 30-40% in uniaxial extension and up to 80-90% in shear deformation, according to the commercial software packages guidelines (ANSYS INC., 2014; MSC, 2016; SIMULIA, 2016).

2.2.4.2 Mooney-Rivlin model

The Mooney-Rivlin model is very useful to describe the stress-strain nonlinear response at large values of stretch. It is a phenomenological model and was derived by Rivlin and Saunders (1951) in a full polynomial form as an infinite series of the first and the second deviatoric

principal invariants $\overline{I_1}$ and $\overline{I_2}$. The compressibility degree can be accounted by adding the terms of D_k in the hydrostatic part of the W equation:

$$W = \sum_{i,j=0}^{N=\infty} C_{ij}.(\overline{I_1} - 3)^i.(\overline{I_2} - 3)^j + \sum_{k=1}^{N=\infty} \frac{1}{D_k}(J-1)^{2k} \tag{2-62}$$

In this case, C_{ij} are the material constants for a "N^{th}" order with $C_{00} = 0$. The values of D_k can be estimated from volumetric test data, but if the material is considered to be almost incompressible, $D_k \to 0$.

The higher the value of N, the better the response to the exact solution. Nevertheless, it may cause numerical difficulties when fitting the material constants and requires enough data to cover the entire range of the aimed deformation. For this reason, high values of N is not usually recommended.

The first order of this model ($N = 1$) was originally developed by Mooney (1940) and is represented by the equation (2-63). However, since its approximation is linear it can be valid only for small deformations (RIVLIN and SAUNDERS, 1951).

$$W = C_{10}.(\overline{I_1} - 3) + C_{01}.(\overline{I_2} - 3) + \frac{1}{D_1}(J-1)^2 \tag{2-63}$$

The parameters C_{ij} are generally determined from experimental data and they can be related to μ_0 similar to that of the Neo-Hookean form. Thus, μ_0 and K_0 are defined by the following equation:

$$\mu_0 = 2.(C_{10} + C_{01})\,; \qquad K_0 = 2/D_1 \tag{2-64}$$

As a general guideline, the two-term form can be applied for tensile strains up to 90-100%, despite this, the stiffening effects usually presented at large strains are not taken into account. Compression behavior may also not be well characterized with only the two-term model (CRISFIELD, 2000; MSC, 2010).

2.2.4.3 Yeoh model

Yeoh (1990; 1993) introduced a phenomenological model dependent only on the first strain invariant $\overline{I_1}$ in the deviatoric part of W. Since it is based on a polynomial form but neglects the second invariant $\overline{I_2}$, the Yeoh model can be also called as reduced polynomial model and has the general form:

$$W = \sum_{i=1}^{N} C_{i0}.(\overline{I_1} - 3)^i + \sum_{k=1}^{N} \frac{1}{D_k}(J-1)^{2k} \tag{2-65}$$

Thus, μ_0 and K_0 are given by:

$$\mu_0 = 2.C_{10}\,; \qquad K_0 = 2/D_1 \tag{2-66}$$

According to Yeoh (1993) the terms containing $\overline{I_2}$ were eliminated from the equation since its variation in the sensitivity of W function is negligible if compared to $\overline{I_1}$. Thus, it is possible to improve the model's ability when predicting the behavior of deformation states over a large strain range even when limited test data is available.

The Yeoh model is commonly considered with $N = 3$, and the upturn of the stress-strain curve can be captured. This model is generally applied in the characterization of carbon-black filled rubbers and has a good fit over a large strain range, being able to simulate various modes of deformation even with limited data, reducing consequently the requirements on material testing (RENAUD *et al.*, 2009). However, caution needs to be exercised when applying this model for deformations involving low strains (YEOH, 1996).

2.2.4.4 Ogden model

Proposed by Ogden (1972), this is also a phenomenological model and is based on the principal stretches rather than strain invariants. This model has been found to be effective for very large strains and it is written as:

$$W = \sum_{i=1}^{N} \frac{\mu_i}{\alpha_i} . (\bar{\lambda}_1^{\alpha_i} + \bar{\lambda}_2^{\alpha_i} + \bar{\lambda}_3^{\alpha_i} - 3) + \sum_{k=1}^{N} \frac{1}{D_k} (J-1)^{2k} \tag{2-67}$$

where μ_i and α_i are real material parameters, being positive or negative and satisfying the condition for μ_0 and K_0 given by:

$$\mu_0 = \frac{1}{2} \sum_{i=1}^{N} \mu_i . \alpha_i \; ; \qquad K_0 = 2/D_1 \tag{2-68}$$

If a two-term expansion ($N = 2$) is applied with $\alpha_1 = 2$ and $\alpha_2 = -2$, it coincides with the 2 parameter Mooney-Rivlin form for typical values of $\mu_1 = 2.C_{10}$ and $\mu_2 = -2.C_{01}$. If N is set to 1 with $\alpha_1 = 2$ and $\mu_1 = \mu_0 = 2.C_{10}$, it degenerates to the Neo-Hookean form (CRISFIELD, 2000).

As in the polynomial Rivlin series, there is no limitation on N, but although high values of N is able to provide better results, it may cause numerical difficulties when fitting the material constants. For this reason, a value of $N > 3$ is not usually recommended (OGDEN *et al.*, 2004).

Although this model is more computationally expensive, it provides a good data fitting and thereby, is more accurate since it is directly based on the principal stretch ratios. This model is able to capture upturn (stiffening) of stress-strain curve but attention should be paid to not use this model with limited test data (e.g. just uniaxial tension) (OGDEN *et al.*, 2004).

2.2.4.5 Arruda-Boyce model

Proposed by Arruda and Boyce (1993), this model was developed based on a statistical treatment of the non-Gaussian chains, in which the volume element is represented by a cubic containing eight chains emanating from the center along to its corners as in Figure 2-9. This is the reason why it is also known as the eight-chain model.

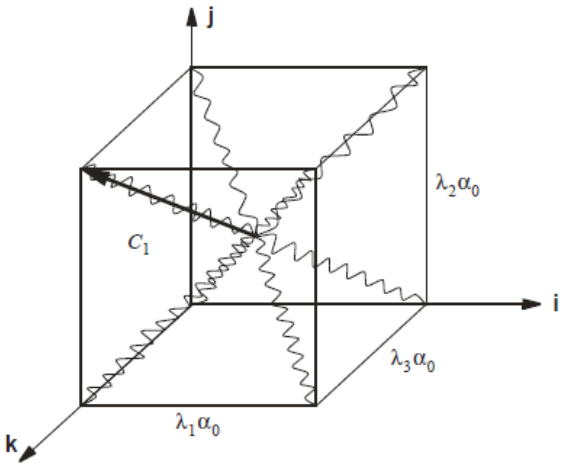

Figure 2-9: Eight Chain Network in stretched configuration

Source: MSC (2005)

where α_0 is the cube dimension with an unstretched network.

As this model represents the physics of network deformation, they are called micro-mechanical models and can be described as follows:

$$W = \mu \sum_{i=1}^{5} \frac{C_i}{\lambda_L^{2i-2}} . (\bar{I}_1^i - 3^i) + \frac{1}{D}\left(\frac{J^2-1}{2} - ln\, J\right) \tag{2-69}$$

where the material constants C_i are predefined functions of the limiting network stretch "λ_L" as it follows:

$$C_1 = \frac{1}{2}; \quad C_2 = \frac{1}{20}; \quad C_3 = \frac{11}{1050}; \quad C_4 = \frac{19}{7000}; \quad C_5 = \frac{519}{673750} \tag{2-70}$$

Although the material constants are predefined functions of the λ_L, it is possible to observe that the Arruda-Boyce model is equivalent to the Yeoh with $N = 5$. On the other hand, if λ_L becomes infinite, the Arruda-Boyce model tends to the Neo-Hookean form. The physical meaning of λ_L is that it corresponds to the stretch at which stress starts to increase without limit.

In the Arruda-Boyce model, the material parameter μ is defined as:

$$\mu = c.k.\Theta \tag{2-71}$$

which it is a function of the chain density "c", the Boltzmann's constant 'k", and temperature "Θ".

Thus, K_0 is related to D according to the expression (2-72):

$$K_0 = 2/D \tag{2-72}$$

The original equation is based on the inverse Langevin[6] function as this function represents an expanded series and λ_L can be less pronounced (TØMMERNES, 2014).

According to Arruda and Boyce (1993), this model is unique since it is able to provide great accuracy for multiple modes of deformation based only on the standard uniaxial tensile test.

2.2.4.6 Gent model

The Gent form was proposed by Gent (1996) and it is also a micromechanical model. Similar to Arruda-Boyce model, it is based on the concept of limiting network stretch and its constitutive relation is proposed as follows:

$$W = -\frac{EI_m}{6}.ln\left(1 - \frac{\overline{I_1} - 3}{I_m}\right) + \frac{1}{D}\left(\frac{J^2 - 1}{2} - ln\,J\right) \tag{2-73}$$

where the constant "E" is the initial elastic modulus, in which for incompressible materials, is $3\mu_0$, and I_m is the limiting value of $(\overline{I_1} - 3)$, analogous to λ_L for Arruda-Boyce.

If the natural logarithm is expanded, this expression will be equivalent to the Yeoh model, but in this case the coefficients will be predefined functions of I_m.

---

[6] Generally used when studying an idealized paramagnetic material in statistical mechanics. In this case, by using the statistical mechanics considerations, the work of deformation is proportional to the entropy change on stretching the chains from the unstretched state.

The constant EI_m is independent of the molecular length, and hence of the crosslinking degree. This model is attractive due to its simplicity, but yet captures the main behavior of a network of extensible molecules over the entire range of possible strains (GENT, 1996).

The initial bulk modulus can be obtained based on the same relation as in Arruda-Boyce form. Thus, it is quite clear that there are many similarities between the Gent and Arruda-Boyce models.

2.2.4.7 Van der Waals model

This model was developed by Kilian (1981) and is based on van der Waals interactions between the chains of a molecular network. It is also a micromechanical model and its strain energy equation is described as follows:

$$W = \mu\left[-(\lambda_m^2 - 3)(ln(1-\eta)+\eta) - \frac{2}{3}a\left(\frac{1}{2}I_l - \frac{3}{2}\right)^{\frac{3}{2}}\right] \tag{2-74}$$

$$\eta = \sqrt{\frac{I_l - 3}{\lambda_m^2 - 3}}; \qquad I_l = (1-\beta)I_1 + \beta I_2 \tag{2-75}$$

where: μ, λ_m, a and β are material parameters. The variables a and λ_m are invariant parameters, but a express the interactions between the chains and is hard to be obtained, while λ_m is the maximum elongation possible. The parameter β controls the curvature changes of the stress-strain curve for different modes of deformation exhibited by the material. If $\beta = 0$ the strain energy function will be dependent only on the first invariant I_1 (KILIAN, 1981; KILIAN *et al.*, 1986).

2.2.4.8 Valanis-Landel hypothesis

Valanis and Landel (1967), based on several experimental data, postulated that the strain energy "W" for a incompressible isotropic material can be split out according to the sum of separate functions of the principal stretches, which can be expressed in the following form:

$$W(\lambda_1, \lambda_2, \lambda_3) = w(\lambda_1) + w(\lambda_2) + w(\lambda_3) \tag{2-76}$$

where the function "w" is a scalar value and due to the symmetry condition obtained by equation (2-35), has the same form for each of the principal stretches.

If the material is incompressible, the three principal stretches are not independent and equation (2-76) can be rewritten:

$$\widetilde{W}(\lambda_1, \lambda_2) = W\left(\lambda_1, \lambda_2, {\lambda_1}^{-1}.{\lambda_2}^{-1}\right) = w(\lambda_1) + w(\lambda_2) + \overline{w}(\lambda_1.\lambda_2) \tag{2-77}$$

where the argument of the function $\overline{w}$ is $\lambda_1.\lambda_2$, i.e. $\overline{w}(\lambda_1.\lambda_2) = w\left({\lambda_1}^{-1}.{\lambda_2}^{-1}\right) = w(\lambda_3)$.

Equation (2-53) using the formulation of equation (2-77) for $\widetilde{W}$, gives:

$$\sigma_1 = \lambda_1 w'(\lambda_1) + \lambda_1.\lambda_2.\overline{w}'(\lambda_1.\lambda_2) \tag{2-78}$$

$$\sigma_2 = \lambda_2 w'(\lambda_2) + \lambda_1.\lambda_2.\overline{w}'(\lambda_1.\lambda_2) \tag{2-79}$$

where, for convenience of notation, the superscript $'$ is used to indicate differentiation with respect of the argument of the function concerned.

2.3 Mullins effect

The Mullins effect is a phenomenon resulting from load-induced changes to constitutive response exhibited by some hyperelastic materials. This property generally occurs in filled and non-filled rubber-like materials and has been investigated intensively by Mullins and his co-workers, for this reason it is referred to as the ‘‘Mullins effect" (MULLINS, 1969).

The effect is most evident during cyclic loading, where the unloading response is more compliant than the loading behavior. Thus, if the elastomer is loaded up to a determined strain level and after that is completely unloaded to a zero stress during several cycles, a phenomenon called stress softening changes the structural properties from cycle to cycle, which occurs due to the effect of stress relaxation. According to Mullins (1969), the initial stress-strain curve

obtained from the first strain of an elastomer is unique and cannot be retraced. Through cyclic tests in a NR-MPC with carbon black, Mullins also concluded that the major relaxation occurs at the first deformation, decreasing over the course of the cycles until the response becomes stable for strain levels below that the maximum which was initially requested. However, if the elastomer is taken to a new higher strain, structural properties will change significantly again and the result will be an irreversible and instantaneous softening of the material, which causes a hysteresis in the stress-strain response.

Bergström and Boyce (1999) performed uniaxial cyclic compression tests on chloroprene rubbers with different quantities of carbon black, and they realized that the higher the concentration of this filler in the rubber compound, the greater its stiffness and relaxation, that is, the more evident will be the Mullins effect. They also considered different temperature ranges in some strain levels and observed great dependence of this factor on the stress-strain curves.

One example of this behavior is well represented in the paper of Diani *et al*. (2009), where cyclic uniaxial tension tests were performed on a sulfur-vulcanized SBR filled with 50 phr of N220 carbon-black. According to Figure 2-10 the stress-strain responses of two samples are illustrated: one sample was submitted to a simple uniaxial tension test, while another one was submitted to a cyclic uniaxial tension test with the maximum stretching increasing every 5 cycles.

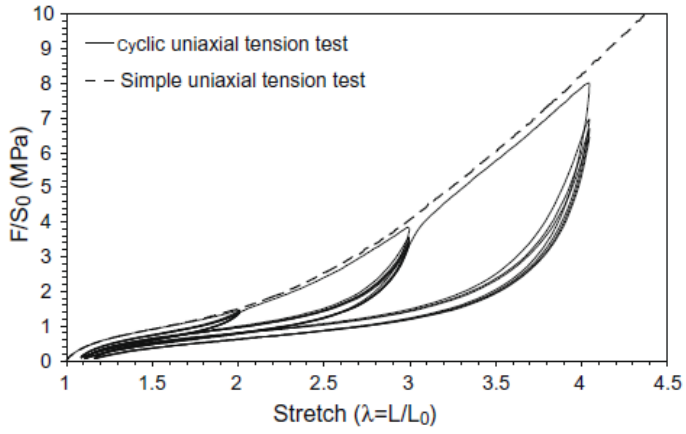

Figure 2-10: Stress–strain responses of a 50 phr carbon-black filled SBR submitted to a simple and cyclic uniaxial tension test.

Source: Diani *et al*. (2009)

Attempting to explain the stress relaxation phenomenon, researchers have proposed various physical interpretations, such as, chains rupture at the interface between rubber and fillers (BLANCHARD and PARKINSON, 1952), slip of molecules (HOUWINK, 1956), breakage of filler structure (KRAUS *et al.*, 1966), chain slack (HANSON *et al.*, 2005), among others, but its molecular origins still remains unresolved (CLOUGH *et al.*, 2016).

The Mullins effect is also reported in the literature for other states of deformation such as: uniaxial compression, simple shear and equibiaxial extension (AMIN *et al.*, 2002; JOHNSON and BEATTY, 1995; LI *et al.*, 2008; MARS and FATEMI, 2004; NÉMETH *et al.*, 2005), as well as hydrostatic tension (DORFMANN, 2003). Anyway, it is still not clear which mechanical quantity pilots the Mullins effect.

Although a number of constitutive models have been proposed to describe this effect (DARGAZANY and ITSKOV, 2013; DORFMANN and OGDEN, 2004; DROZDOV and DORFMANN, 2001; LU and WANG, 2017), one famous example is the work done by Ogden and Roxburgh (1999), which is implemented in several commercial FE computational codes. It consists in a pseudo-elastic model based on the theory of incompressible isotropic elasticity modified by the incorporation of a single continuous parameter, interpreted as a damage parameter η. This variable represents the material damage due to deformation and controls the material properties, so that the material response is governed by an energy function for unloading and subsequent reloading different from that obtained at the initial state. Thus, it is no longer appropriate to assign W as a stored elastic energy, since part of it is dissipated as damage. Therefore, it can be stated that:

$$\frac{\partial W}{\partial \eta}(\boldsymbol{F}, \eta) = 0 \tag{2-80}$$

Equation (2-80) determines the evolution of η during the deformation process, where it may be in the active or inactive state and varies continuously. In the idle state $\eta = 1$ and the material will have an elastic behavior according to the energy function $W(\boldsymbol{F}, \eta)$. When η is active, it behaves elastically based on a new potential energy function $(\mathbf{F}, \eta(\mathbf{F}))$.

The Ogden-Roxburgh model derives from the deviatoric part in the energy density function, and exhibits history dependence under certain conditions as in the following form:

$$W_d\left(\overline{\lambda_1},\overline{\lambda_2},\eta\right) = \eta.\widetilde{W}_d\left(\overline{\lambda_1},\overline{\lambda_2}\right) + \phi(\eta) \tag{2-81}$$

where $\phi(\eta)$ is the damage function written in terms of the damage variable "η", and that are expressed as:

$$\eta = 1 - \frac{1}{r} erf\left(\frac{W_d^m - W_d}{m + \beta W_d^m}\right) \tag{2-82}$$

being the damage function implemented in the commercial software Abaqus® in the following form:

$$\varphi(\eta) = (m + \beta W_d^m) erf^{-1}\left(r(1-\eta)\right) - W_d^m \tag{2-83}$$

where r,m and β are material parameters obtained from cyclic experimental tests, W_d^m is the maximum value of W_d and erf means error function (SIMULIA, 2016).

The variable η varies continuously during the material deformation process to satisfy condition $0 < \eta \leq 1$. When $\eta = 1$, $\varphi\ (\eta = 1) = 0$ and the material deformation state is at a point on the hyperelastic initial curve, not accounting for the Mullins effect (OGDEN and ROXBURGH, 1999; SIMULIA, 2016).

Although the Ogden-Roxburgh is a phenomenological model, its parameters are related to particular physical aspects of the stress-strain response. At the microscopic level, the stress softening is generally interpreted as being due to damage caused by the loading and viscoelastic effects, since in filled rubber there can be additional contributions to the mechanical hysteresis from filler particles debonding from each other or from the polymer chains (OGDEN and ROXBURGH, 1999).

It should be clear that the Mullins effect does not address the dependence of dynamic stiffness on dynamic strain amplitude (generally called the Payne effect or the Fletcher-Gent effect).

2.4 Fletcher-Gent effect

The Fletcher-Gent effect proposed by Fletcher and Gent (1953), involves a non-linearity in the dynamic stress-strain behavior and it becomes more pronounced with the presence of rubber fillers, generally one of the many kinds of carbon black, as shown by Payne and Whittaker (1971). It is also known as Payne effect due to the scientist who made extensive studies of the phenomenon, e. g. Payne (PAYNE, 1962, 1963).

By this phenomenon, the dynamic stiffness decreases with increasing dynamic amplitude and the linear viscoelastic theory is naturally unable to deal with this effect. This phenomenon is observed under cyclic loading conditions in the range of 0.1% up to 50% strain amplitudes, and is related to a dependence of the viscoelastic storage modulus[7] on the amplitude of the applied strain (KRAUS, 1984; LION, 2005; RENDEK and LION, 2010; ULMER, 1996).

The experimental tests performed by Lion *et al*. (2003) implied that the storage modulus strongly decreased as a function of the strain amplitude, but on the other hand, increasing frequencies lead to an increase in the modulus (Figure 2-11).

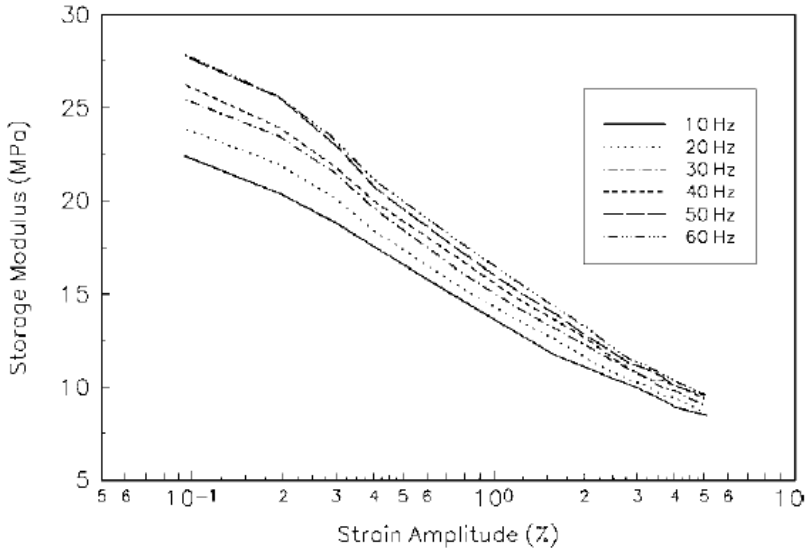

Figure 2-11: Experimental data of the storage modulus.
Source: Lion *et al*. (2003)

[7] The storage modulus in viscoelastic materials measures the stored energy associated with the elastic properties.

The Fletcher-Gent effect is usually denoted as a plastic effect (MIEHE and KECK, 2000). It can be attributed to irreversible slip processes between the filler particles and their plastic deformations. For this reason, it can also be characterized using friction models, like Gregory (1985), Coveney *et al*. (1995) and Kaliske and Rothert (1998).

The constitutive relations of this phenomenon should be applied when it is necessary to predict the frequency and/or amplitude-dependent dynamic stiffness, as well as damping behavior of rubber bushings, automotive tires and other products (GIL-NEGRETE *et al.*, 2006; LION *et al.*, 2003). Since this Dissertation deals with static stiffness for multiaxial loadings it was not implemented in this work, but it is an important topic to be discussed for the future ones.

2.5 Fitting curve experimental tests

When fitting hyperelastic material models in mechanical analysis software, it is desirable to set experimental data for multiple strain state, so that the material model can effectively analyze the elastomer behavior that occur in numerical simulations. Each mode of deformation put the material into a particular strain state. Thus, in order to represent the elastomer behavior in such a defined state, individual experimental tests are performed aiming to achieve pure strain states and as a result, the material parameters for constitutive models can be sufficiently defined.

For almost incompressible elastomers, the main strain states are simple tension, pure shear and simple compression. Nevertheless, as there is friction between the test specimen surface and the equipment contacting platens, the simple compression test should to be replaced by an equivalent biaxial extension. Therefore, the specimen is completely free to expand laterally, which in fact does not occur during the compression test due to friction, and the surface friction strains create an undefined strain state (MILLER, 2004a). The typical behavior of the three main stress-strain curves appropriate for input the material into fitting routines are shown in Figure 2-12.

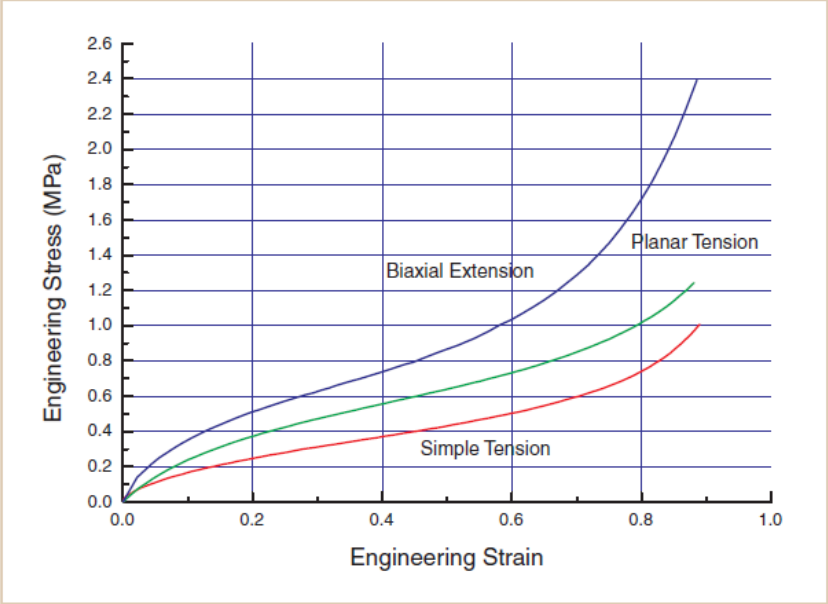

Figure 2-12: Typical stress strain curves for input into fitting the material.
Source: Miller (2004a)

The nearly incompressible behavior of elastomers is such that the Poisson's ratio is close to 0.5. If an elastomer is considered constrained in service, exactly how close to 0.5, it may be critical to predict the hydrostatic stresses. Then, since Poisson's ratio cannot be measured in the lab with sufficient precision, a volumetric compression test may be needed in situations where the elastomer is slightly compressible or highly constrained, and consequently, the bulk behavior can be determined (MILLER, 2004a).

The hyperelastic material models can represent a surface that contains the stress response for all of the various combinations of strains. When the material model is calibrated, the surface is defined. Each individual experiment defines a line on the surface (Figure 2-13) where, to adequately define the entire surface, experiments in several strain states are performed so as to crisscross the surface and force it to represent the actual material.

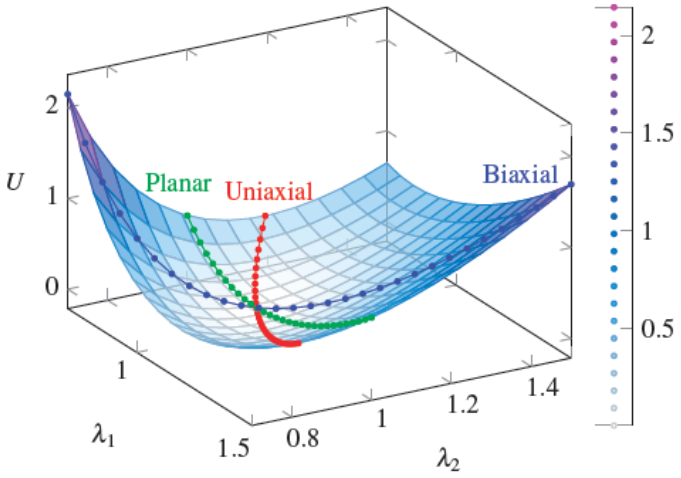

Figure 2-13: Hyperelastic energy surface with three testing paths.
Source: Miller (MILLER, 2004b)

It is very important that the experiments should be performed at reasonable strain levels according to the application. If the applied strains are much different than those that the part will experience, the material properties can be changed and the obtained response becomes unrealistic for the application of interest. In addition, to evaluate the structural condition of a component in service, the stress-strain curves should be derived by cycling the material until its properties are stabilized. This happens due to Mullins effect (DIANI, FAYOLLE and GILORMINI, 2009).

2.5.1 Simple Tension Strain State

Simple tension experiments are widely used for elastomers. It corresponds to an elongation in one direction accompanied by free contraction in the other two Cartesian directions. To achieve a pure strain state, the specimen must be much longer in the stretching direction than in the other dimensions. As a result, the lateral constraint associated with specimen thinning will be eliminated.

Despite some standard test methods for rubbers in simple tension, such as ASTM D412 (2016), it is not mandatory to use the dogbone shape in the sample if a failure oriented experiment is not required (MILLER, 2004a). Notwithstanding, depending on the magnitude in which the component is subjected, it turns needful to experiment the sample under high levels of strain

and the dogbone shape becomes interesting from the point of view of this condition, since it avoids the earlier tearing effect.

In this experimental test, the real length should be comprised between the clamp edges. It is worth noting that the specimen straining cannot be measured close to the clamps, as the pure tension strain state occurs away from them. An example of a strain measuring device required for the test is shown in Figure 2-14.

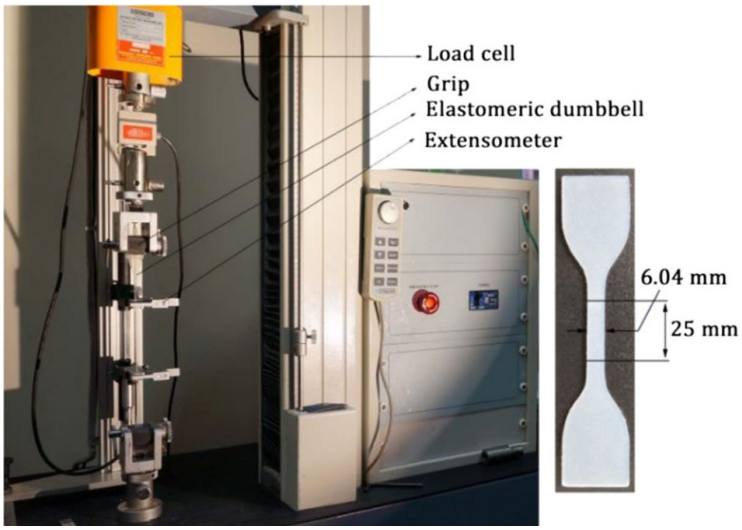

Figure 2-14: Simple tension experiment device.

Source: Mansouri *et al.* (2016)

Particularizing that $J = 1$ and $\sigma_2 = \sigma_3 = 0$ according to Figure 2-15, the corresponding principal stretches are given by:

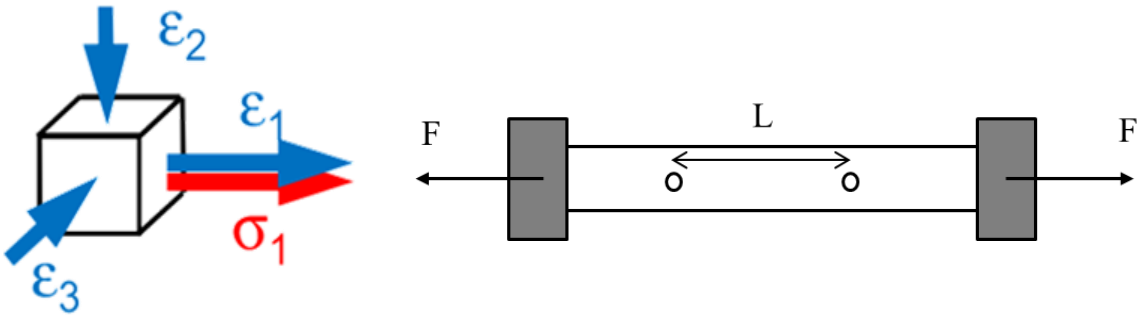

Figure 2-15: Stress-strain state of a thin sheet under uniaxial extension.

Source: Adapted from Jakel (2010)

$$\lambda_1 = \lambda_U \; ; \qquad \lambda_2 = \lambda_3 = {\lambda_U}^{-1/2} \tag{2-84}$$

$$I_1 = {\lambda_U}^2 + \frac{2}{\lambda_U} \; ; \qquad I_2 = 2\lambda_U + \frac{1}{{\lambda_U}^2} \tag{2-85}$$

By attempting these boundary conditions, the parameter p from equation (2-46) will result in:

$$p = \frac{2}{\lambda_U}\frac{\partial W}{\partial I_1} - 2\lambda_U \frac{\partial W}{\partial I_2} \tag{2-86}$$

Thus, the uniaxial Cauchy stress σ_{L1} will be:

$$\sigma_{L1} = 2\left({\lambda_U}^2 - \frac{1}{\lambda_U}\right)\left(\frac{\partial W}{\partial I_1} + \frac{1}{\lambda_U}\frac{\partial W}{\partial I_2}\right) \tag{2-87}$$

Appling the Valanis-Landel hypothesis, the energy in equation (2-77) can be rewritten only in terms of principal stretches, such as:

$$\begin{aligned} &\bar{W}(\lambda_U) = \widetilde{W}\left(\lambda_U, {\lambda_U}^{-\frac{1}{2}}\right) = w(\lambda_U) + w\left({\lambda_U}^{-\frac{1}{2}}\right) + \bar{w}\left({\lambda_U}^{\frac{1}{2}}\right) \\ &\bar{W}(\lambda_U) = w(\lambda_U) + 2w\left({\lambda_U}^{-1/2}\right) \end{aligned} \tag{2-88}$$

and the principal stress components, making use of equation (2-53), are:

$$\sigma_{L1} = \lambda_U \cdot \frac{\partial \bar{W}(\lambda_U)}{\partial \lambda_U} = \lambda_U . w'(\lambda_U) - {\lambda_U}^{-1/2} . w'({\lambda_U}^{-1/2}) \; ; \qquad \sigma_2 = \sigma_3 = 0 \tag{2-89}$$

The corresponding nominal stress is $\sigma_{N1} = \sigma_{L1}/\lambda_U$, as already discussed in section 2.2.4.

2.5.2 Equal-biaxial Strain State

Unfortunately, only uniaxial-tensile data do not fulfill the requirements to characterize the material with sufficiently accuracy, especially for those applications with multiaxial loading (KEERTHIWANSA *et al.*, 2018). Although biaxial extension is essential for data-fitting, there

is not any standard with proper directives to conduct this test. This happens due to complexity of the tests and of the mathematical models required for defining the highly nonlinear material behavior.

Equal-biaxial tension tests were initially developed in order to represent the strain state of pure compression. Even though this state can also be achieved by a simple uniaxial compression test, it is inaccurate because small amounts of friction generated between rubber specimen and metal surfaces cause a mixed state of compressive, shear and tensile strain (DAY and MILLER, 2000). The friction can also vary as the compressive load increases, and even for small levels of friction the deviation from the pure uniaxial compressive strain state causes significant measurement errors. For this reason, by adopting a suitable equal-biaxial testing fixture it is possible to obtain a pure compressive strain accurately, eliminating the errors due to friction.

In general, the most commonly methods used for biaxial tests are: straining a circular specimen radially, biaxial extension of a thin square sheet or bulge tests. Initially, the first studies have been conducted concerning the bubble shape and tearing pattern in an inflated latex rubber sheet clamped around its circumference by Flint and Naunton (1937). Next, Treloar (1944), Hart-Smith and Crisp (1967) and Schmidt and Carley (1975) developed devices for bulge tests aiming to characterize the stress-strain relations for rubber in a two-dimensional (2D) extension.

As far as biaxial strain distributions are concerned, Rivlin and Saunders (1951), introduced tests in a thin square sheet in order to produce a pure homogeneous deformation. Later, based on this approach, Obata *et al*. (1970), Arenz *et al.* (1975) and, Jones and Treloar (1975) implemented experimental tests trying to predict the relation between stress and strain when applying the theory of elasticity over the entire region of strain invariants (I_1, I_2).

Then, from the 21st century, several variants of the experimental approaches to the biaxial straining in elastomers have been developed based on these initial concepts and which nowadays are aided by Digital Image Correlation (DIC). The bulge test technique consists in the expansion of a thin elastomeric sheet using air/hydraulic pressure as illustrated in the Figure 2-16. The main disadvantage of this approach is the difficulty of controlling the strain in the center as the balloon shape increases. Also, the sheet thickness needs to be much thinner than its circumference and it is necessary to deal with two synchronized digital cameras to capture the strain range. Some implementations can be seen in Reuge *et al.* (2001), Nguyen *et al.* (2004),

Genovese *et al.* (2006), Selvadurai (2006), Feichter *et al.* (2007), Meunier *et al.* (2008), Sasso *et al.* (2008), Jerrams *et al.* (2012), Lăzărescu *et al.* (2012), Çakmak *et al.* (2014), Mansouri *et al.* (2016), Keerthiwansa *et al.* (2018).

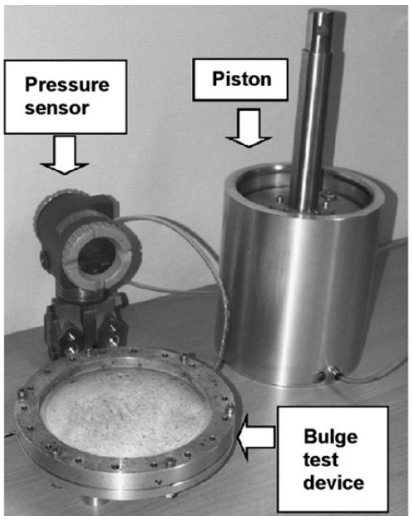

Figure 2-16: Bulge test apparatus for equal biaxial inflation of the rubber sheet.
Source: Meunier *et al.* (2008)

In the case of a square sheet, the specimen is gripped around its perimeter and stretched with multiple arms or cable bearing systems according to Figure 2-17. This experiment has been used with great success by several investigators, and has the advantage of elastomer deformations be examined in unequal biaxial deformation states. However, the stress calculation has been one of the main difficulties in this approach and, for this reason, is still being studied. Some biaxial testing device implementations can be found in Chevalier *et al.* (2001), Batra *et al.* (2005), Fujikawa *et al.* (2010), Johlitz and Diebels (2011), Pancheri and Dorfmann (2012), Jerrams *et al.* (2012), Chen *et al.* (2013) Zhao *et al.* (2013), Fujikawa *et al.* (2014), Seibert *et al.* (2014), Avanzini and Battini (2016), Hariharaputhiran and Saravan (2016).

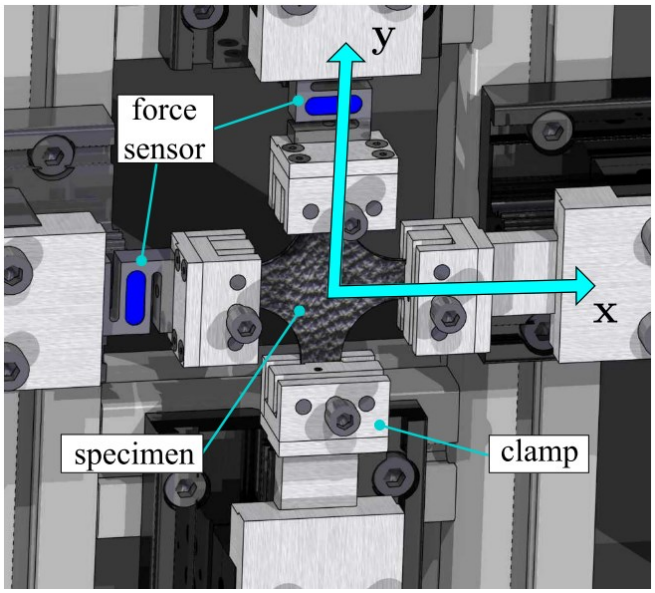

Figure 2-17: Biaxial tensile test apparatus for a square thin sheet specimen.
Source: Seibert *et al*. (2014)

In addition to the implementations cited above, some low-cost and easy mounting fixture devices have been developed to be coupled with a universal tensile machine. Most of these fixture devices consist of four scissor arms at 45 degrees to the axis of the machine, as shown in Figure 2-18 (ADEEL *et al.*, 2012; SHAHZAD *et al.*, 2015; VENKATESH and MURTHY, 2012). Other fixture devices have also been proposed in Bhatnagar *et al*. (2007) and Barroso *et al*. (2012). More recently, Medellín and La Peña (2017) studied different fixture designs in order to identify their advantages and disadvantages as well as their behavior under loading. From 3D printed models, they evaluated the kinetic behavior of each fixture and proposed a new design, but despite the correct deformation, some improvements regarding the manufacturing process, clamping edges and accuracy should be performed.

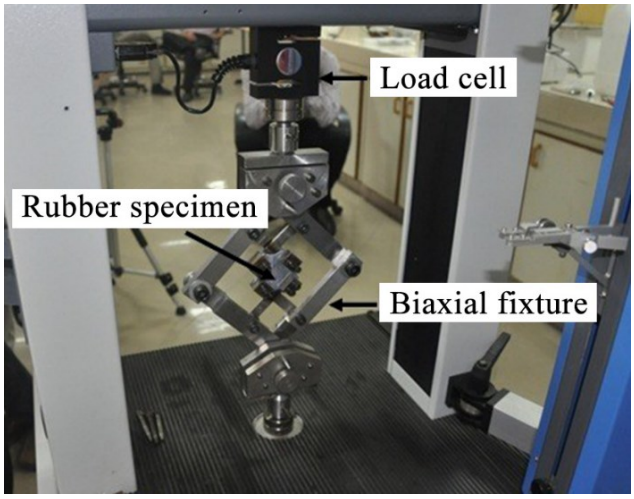

Figure 2-18: Fixture device to produce equal biaxial strains in a square thin sheet specimen. Source: Shahzad *et al*. (2015)

Finally, for the radial extension of a circular plate, the grips are moved radially outward by pulling with thin flexible cables which are redirected around pulleys to a common loading plate as shown in Figure 2-19 (DAY and MILLER, 2000). This type of equal biaxial rig gives a better control of the strains, since there is little influence of the geometry on the stress state in the center of the sample. In spite of its complex construction and difficulty of implementation, a very recent study conducted by Robinson *et al*. (2019) could build in-house this type of test, just assembling the apparatus to a single uniaxial testing machine. Most of the parts were obtained from 3D printing, which enabled its implementation (see Figure 2-20).

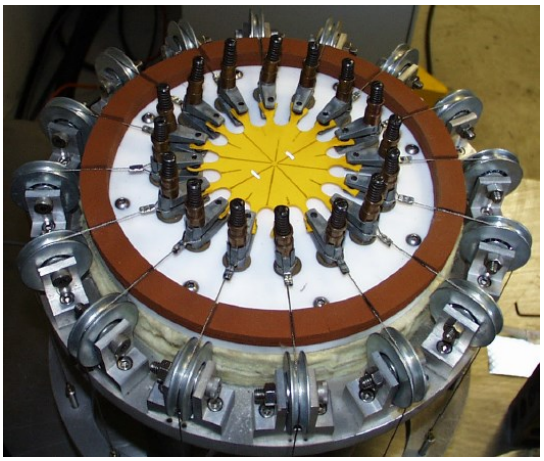

Figure 2-19: Biaxial tensile test apparatus for a circular specimen stretched radially. Source: Day and Miller (2000)

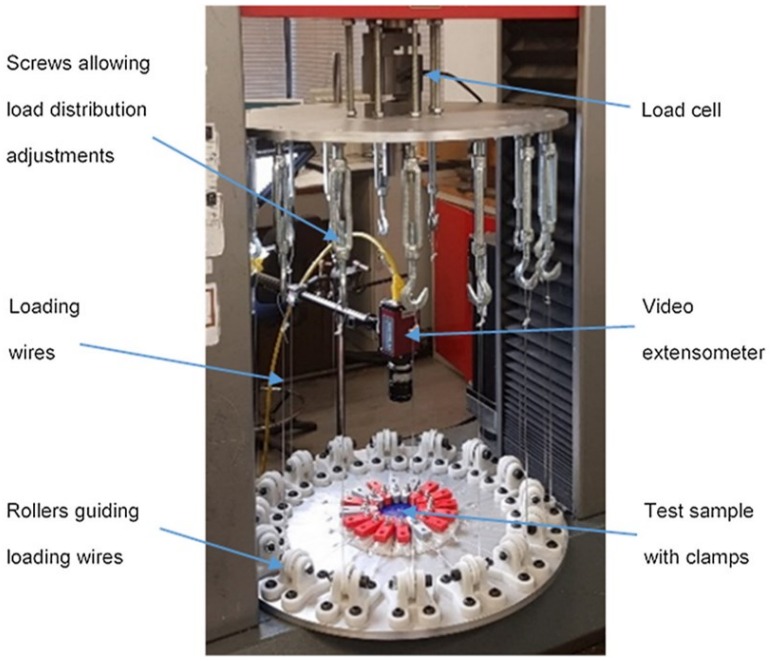

Figure 2-20: Circular biaxial tensile test apparatus coupled with uniaxial machine.
Source: Adapted from Robinson *et al.* (2019)

As long as $\sigma_3 = 0$ for the biaxial extension, it is possible to derive the principal stretches based on Figure 2-21:

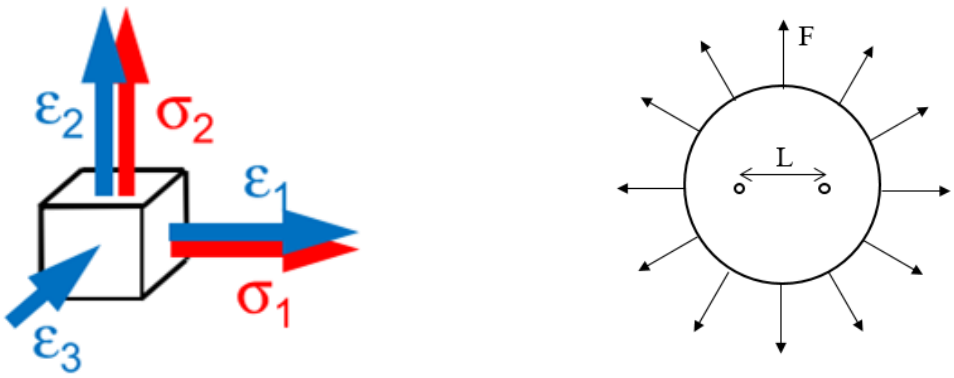

Figure 2-21: Stress-strain state of a thin sheet under biaxial extension.
Source: Adapted from Jakel (2010)

$$\lambda_1 = \lambda_2 = \lambda_B \; ; \qquad \lambda_3 = \frac{1}{{\lambda_B}^2} \tag{2-90}$$

$$I_1 = 2{\lambda_B}^2 + \frac{1}{{\lambda_B}^4}\ ; \qquad I_2 = {\lambda_B}^4 + \frac{2}{{\lambda_B}^2} \tag{2-91}$$

Thus, recalling equation (2-46), the parameter p will result in:

$$p = \frac{2}{{\lambda_B}^4}\frac{\partial W}{\partial I_1} - 2{\lambda_B}^4\frac{\partial W}{\partial I_2} \tag{2-92}$$

and the Cauchy stress will be $\sigma_{L1} = \sigma_{L2}$ according to equation (2-93):

$$\sigma_{L1} = \sigma_{L2} = 2\left({\lambda_B}^2 - \frac{1}{{\lambda_B}^4}\right)\left(\frac{\partial W}{\partial I_1} + {\lambda_B}^2\frac{\partial W}{\partial I_2}\right) \tag{2-93}$$

Appling the Valanis-Landel hypothesis, the energy in equation (2-77) can be rewritten only in terms of principal stretches, such as:

$$\overline{\overline{W}}(\lambda_B) = \widetilde{W}(\lambda_B, \lambda_B) = 2w(\lambda_B) + \overline{w}\left({\lambda_B}^2\right) \tag{2-94}$$

and the principal stress components, making use of equation (2-53), are:

$$\sigma_{L1} = \sigma_{L2} = \frac{\lambda_B}{2}.\frac{\partial\overline{\overline{W}}(\lambda_B)}{\partial\lambda} = \lambda_B.w'(\lambda_B) + {\lambda_B}^2.\overline{w}'({\lambda_B}^2)\ ; \qquad \sigma_3 = 0 \tag{2-95}$$

where the superscript $'$ on $\overline{w}$ indicates differentiation with respect to the argument ${\lambda_B}^2$ and $\sigma_{N1} = \sigma_{N2} = \sigma_{L1}/\lambda_B$

Since the objectives herein do not involve the need for unequal biaxial straining, the mechanical aspects of the experimental approach can be greatly simplified. The biaxial tests conducted by the author will be described in more detail in Chapter 3. Particularly at this chapter, some of the original contributions of this Dissertation will be detailed.

2.5.3 Pure Shear Strain State

Pure shear deformation occurs when a thin rectangular sheet is stretched along the 1-direction, free to contract in the secondary direction and no deformation at a third direction. Since elastomers are nearly incompressible, a state of pure shear exists in the specimen at an inclined angle of 45 degrees regarding the stretching direction (TIMOSHENKO, 1970).

Treloar (1943c) was the first to conduct pure shear experiments on a thin sheet of rubber. Afterwards, Rivlin (1948b) applied surface forces necessary to produce simple shear in a cuboid of either compressible or incompressible material. From this study, Rivlin and Saunders (1951) extracted load-deformation relations obtained for pure shear to predict the results of simple extension tests. In 1964, Mooney reported a series of measurements using a hollow cylinder rather than a sheet of rubber aiming to increase the shear beyond 200% reached in flexometer[8] (MOONEY, 1964).

Many recent researches have been developed over the last years, mainly with regard to the rotational effects that relate pure shear and simple shear (DESTRADE *et al.*, 2012; MOREIRA and NUNES, 2013; NUNES, 2011; RITTO and NUNES, 2015; THIEL *et al.*, 2019). Notwithstanding, several studies have been conducted to show that uniaxial and biaxial fitted models are able to reproduce the planar shear behavior correctly (BAASER and NOLL, 2009; CHEN *et al.*, 2013; CHEVALIER and MARCO, 2002; MEUNIER *et al.*, 2008; SASSO *et al.*, 2008; SEIBERT *et al.*, 2014). According to Seibert *et al*. (2014) all achievable deformations are within uniaxial and biaxial curves, and by performing a biaxial tensile test it is possible to capture a larger area in the invariant plane.

The specimen used in this type of experiment should be much shorter in the direction of stretching than its width, thus its thinning will only occur in the thickness direction resulting in a pure shear state. According to Miller (2004a), based on FEA of a specimen geometry, the width must be at least 10 times wider than the length in the stretching direction, being the experiment very sensitive to this ratio.

---

[8] It is a device used to measure the motion range of various joints around the body. It is also able to test the flexibility of materials.

This experimental test is based on a rectangular sheet under tension at its plane normal to the clamped edges according to Figure 2-22. An optical strain measuring device can be used to measure the strain away from the clamp edges, where there is in fact a pure strain state.

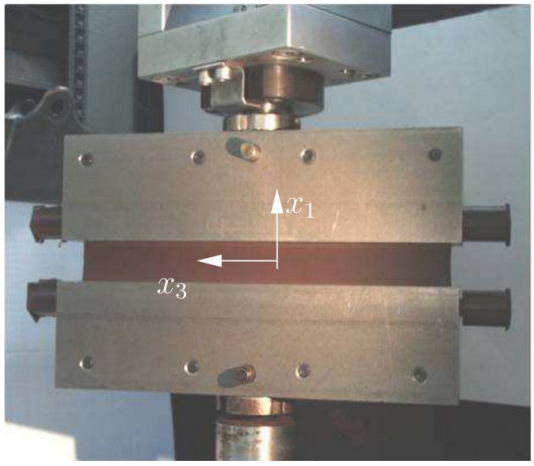

Figure 2-22: Pure shear experiment device.

Source: Baaser and Noll (2009)

In the case of planar shear the thickness contraction was considered in the 2-direction as shown in Figure 2-23, and consequently $\sigma_2 = 0$. As a result, the principal stretches can be written as follows:

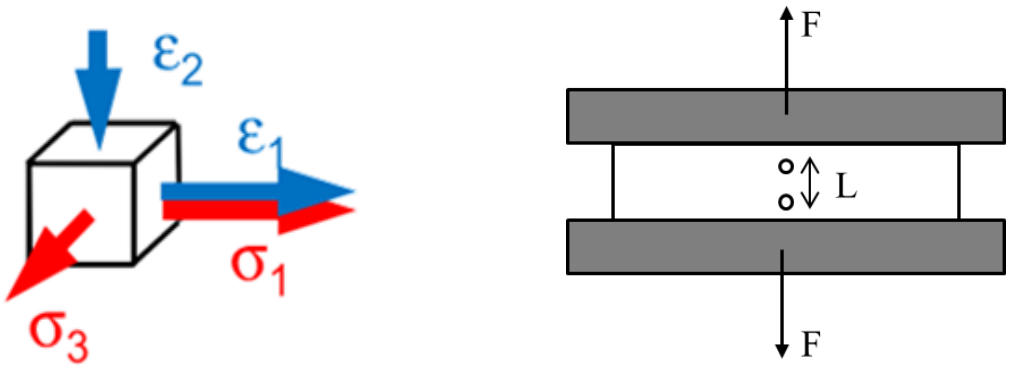

Figure 2-23: Stress-strain state of a thin sheet under planar shear.

Source: Adapted from Jakel (2010)

$$\lambda_1 = \lambda_S\,; \qquad \lambda_2 = {\lambda_S}^{-1}; \qquad \lambda_3 = 1 \tag{2-96}$$

$$I_1 = {\lambda_S}^2 + \frac{1}{{\lambda_S}^2} + 1\,; \qquad I_2 = I_1 \tag{2-97}$$

Thus, recalling equation (2-46), the parameter p will result in:

$$p = \frac{2}{{\lambda_S}^2}\frac{\partial W}{\partial I_1} - 2{\lambda_S}^2\frac{\partial W}{\partial I_2} \tag{2-98}$$

and the Cauchy stresses σ_{L1} and σ_{L3} are written respectively as:

$$\sigma_{L1} = 2\left({\lambda_S}^2 - \frac{1}{{\lambda_S}^2}\right)\left(\frac{\partial W}{\partial I_1} + \frac{\partial W}{\partial I_2}\right) \tag{2-99}$$

$$\sigma_{L3} = 2\left(1 - \frac{1}{{\lambda_S}^2}\right)\left(\frac{\partial W}{\partial I_1} + {\lambda_S}^2\frac{\partial W}{\partial I_2}\right) \tag{2-100}$$

Appling the Valanis-Landel hypothesis, the energy in equation (2-77) can be rewritten only in terms of principal stretches, such as:

$$\ddot{W}(\lambda_S) = \widetilde{W}\left(\lambda_S, {\lambda_S}^{-1}\right) = w(\lambda_S) + w\left({\lambda_S}^{-1}\right) \tag{2-101}$$

and the principal stress components, making use of equation (2-53), are:

$$\sigma_{L1} = \lambda_S.\frac{\partial \ddot{W}(\lambda_S)}{\partial \lambda_S} = \lambda.w'(\lambda_S) - \lambda^{-1}.w'({\lambda_S}^{-1})\,; \qquad \sigma_2 = 0 \tag{2-102}$$

where again the superscript $'$ indicates differentiation with respect to the argument of the function w. From equation (2-51) the component σ_{L3} is:

$$\sigma_{L3} = -{\lambda_S}^{-1}.w'\left({\lambda_S}^{-1}\right) - \overline{w}'(\lambda_1\lambda_2) \tag{2-103}$$

evaluated at $\lambda_1 = \lambda_S$ and $\lambda_2 = {\lambda_S}^{-1}$. Just as the other deformation modes $\sigma_{N1} = \sigma_{L1}/\lambda_S$ and $\sigma_{N3} = \sigma_{L3}/\lambda_S$.

2.5.4 Volumetric Compression

When the material cannot be assumed to be incompressible, the volumetric properties should be included in the model predictions. The compressibility degree has a high effect on the mechanical behavior of rubbers, and this property is intimately related to the rubber packing density. It can be quantified by the bulk modulus assigned by the variable K; when the problem is effectively almost incompressible, this variable tends to very high values, being solved by a penalty procedure, in which the pressure variables act as Lagrange multipliers to force the condition of incompressibility (AL AKHRASS *et al.*, 2014).

The first studies as for rubber compressibility started with rubber blocks being compressed by two steel plates (GENT and LINDLEY, 1959; HOLOWNIA, 1971; 1972). However, when Holownia (1972) varied carbon black content to measure bulk modulus he found problems in the field of compliant-surface bearings owing to fluid-film dependency behavior while rubber was used. Then, in 1975, Holownia proposed a thick mild steel cylinder into which the rubber sample was placed, such that the radial displacements could be constrained. With this method he obtained great accuracy ($\pm 3\%$ maximum error) in the measuring of K (HOLOWNIA, 1975). Afterwards, other authors conducted studies regarding the reliability of this approach (CROCKER and DUNCAN, 2001; PENG *et al.*, 1994).

Some important results concerning the change in volume of a natural rubber can be found in the works Mott *et al.* (2008). Then, based on the Digital Image Correlation (DIC) technique, Le Cam and Toussaint (2008; 2009) captured the volume variation of a stretched sample. They performed studies on both natural and synthetic rubbers, unfilled and filled with carbon black. In more recent studies, Zimmermann and Stommel (2013a) analyzed the mechanical behavior of a reinforced natural rubber under hydrostatic pressure and showed insufficient outcome quality when a nearly incompressible material is assumed in simulations. In (2013b), they evaluated the influence of different filler types and filler contents on the hydrostatic compression behavior of natural rubber. They also performed cyclic uniaxial tensile tests to take the stress softening and determine the influence of previous loading on the compression behavior. Ilseng *et al*. (2015), tested six different elastomer compounds under cyclic volumetric compression and verified no significant stress softening between the volumetric compression cycles. On the other hand, Gehrmann *et al*. (2017) found the cyclic evolution of the bulk

modulus for a technical ethylene propylene diene rubber (EPDM) by using cyclic volumetric compression tests.

Nowadays, the usual way of conducting a volumetric compression test involves the application of stress to the sample at one direction only. The sample is a small cylinder of material constrained in a rigid container and compressed by a piston as shown in Figure 2-24. The stresses generated on the sides are lower than those observed at the top and the bottom. Thus, the stress field is close to a hydrostatic state (quasi-hydrostatic state). Because the bulk modulus is much higher than the shear modulus, the deviatoric part of the stress will be much smaller than the hydrostatic, and for this reason it can be neglected (CROCKER and DUNCAN, 2001).

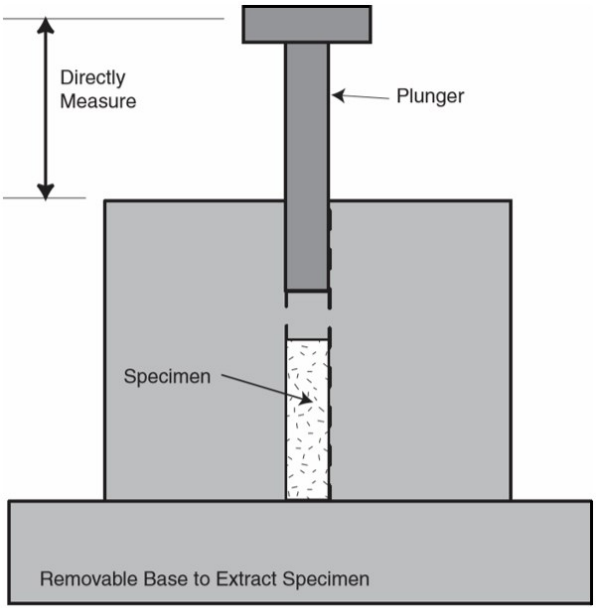

Figure 2-24: Volumetric compression experiment scheme.
Source: Miller (2004b)

According to Miller (2004a), during the compression test the actual displacement is very small, and for this reason, great care must be taken to not measure the container stiffness. The bulk modulus is obtained through the initial slope of the resulting stress-strain function. Just to have a notion, this value is typically two or three orders of magnitude greater than the shear modulus for elastomers.

The relation between initial bulk modulus (K_0) and shear modulus (μ_0) is given by the Poisson's ratio (ν) according to the equation (2-104) derived from the theory of elasticity (LOVE, 1982). Based on this equation some representative values can be considered as follows in Table 2-2. As a guide, typical unfilled elastomers have ν in the range of 0.4995 to 0.49995 and filled elastomers in the range of 0.490 to 0.497 (SIMULIA, 2016).

$$\nu = \frac{3K_0 - 2\mu_0}{6K_0 + 2\mu_0} = \frac{3K_0/\mu_0 - 2}{6K_0/\mu_0 + 2} \tag{2-104}$$

Table 2-2: Compressibility degree according to Poisson's ratio
Source: Adapted from Simulia (2016).

K_0/μ_0	Poisson's ratio
10	0.452
20	0.475
50	0.490
100	0.495
1000	0.4995
10000	0.49995

The bulk modulus is a material constant which defines the material resistance to volume change when subjected to compression loading. Consequently, it is a function of volumetric strain and can be expressed as a derivative of the pressure-strain curve (OGDEN, 1984). Nevertheless, as these are experimental results it turns appropriated to define the bulk modulus in an incremental form, such that:

$$K_{inc}^{i} = \frac{dp}{d\varepsilon_v} = \frac{\Delta p}{\Delta \varepsilon_v} = \frac{p^{i+1} - p^{i}}{{\varepsilon_v}^{i+1} - {\varepsilon_v}^{i}} \tag{2-105}$$

where i represents the sequential number of the experimental points; p and ε_v are respectively the pressure on the sample and volumetric strain.

In the experimental tests, the compression load is applied evenly over the piston's contact surface, such that p can be easily calculated through the force "F" exerted on the piston.

$$p = \frac{F}{A_p} \tag{2-106}$$

where A_p is the piston area in contact with the button sample.

Since the diameter of the cylindrical sample remains constant during the compression, the volumetric strains can be derived as follows:

$$\varepsilon_v = \frac{V_0 - V}{V_0} = \frac{h_0 - h}{h_0} \tag{2-107}$$

In this case, V and h are respectively the volume and height of the button sample at the instant of measurement, while V_0 and h_0 are the initial volume and height.

Since rubber-like materials are considered isotropic, hydrostatic stresses act equally in all directions, so that this state can be written according to Figure 2-25.

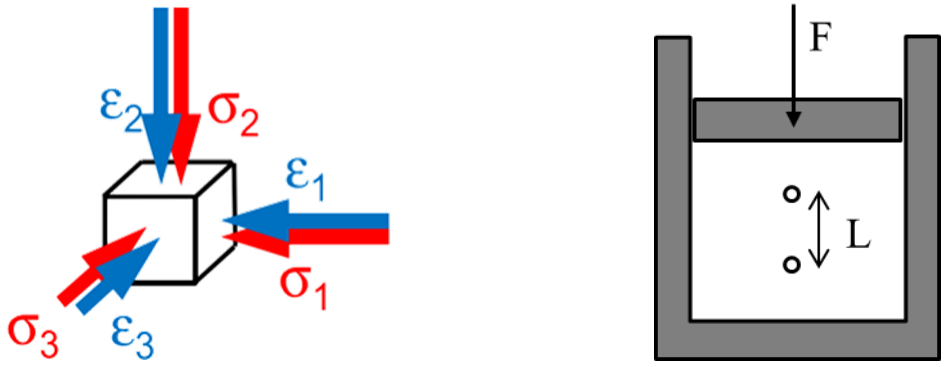

Figure 2-25: Stress-strain state under hydrostatic compression.
Source: Adapted from Jakel (2010)

$$\lambda_V = \lambda_1 = \lambda_2 = \lambda_3 \tag{2-108}$$

$$I_1 = 3{\lambda_V}^2 ; \qquad I_2 = 3{\lambda_V}^4 ; \qquad I_3 = {\lambda_V}^6 = J^2 \tag{2-109}$$

$$J = {\lambda_V}^3 < 1 \tag{2-110}$$

$$p = \sigma_1 = \sigma_2 = \sigma_3 \tag{2-111}$$

In this situation $\sigma_1; \sigma_2; \sigma_3$ means the representation of both Cauchy or nominal stresses.

2.6 Conical rubber spring

Conical rubber springs, or just conical springs, are used as vibration isolators combining the function of primary damping and axle linkage in a single component. This kind of spring is one of the main objectives of study in the present Dissertation.

As a universal damping and guiding element, the conical spring needs to combine all the properties required: high stiffness for axle-guiding and an optimally vertical rigidity for damping purposes.

Its design is compact and light, making it easy for retrofitting. It consists of one or several conically arranged elastomeric layers bordered by adequately molded metallic components, the conical metallic molded parts should provide a separation between the various elastomeric layers as shown in Figure 2-26.

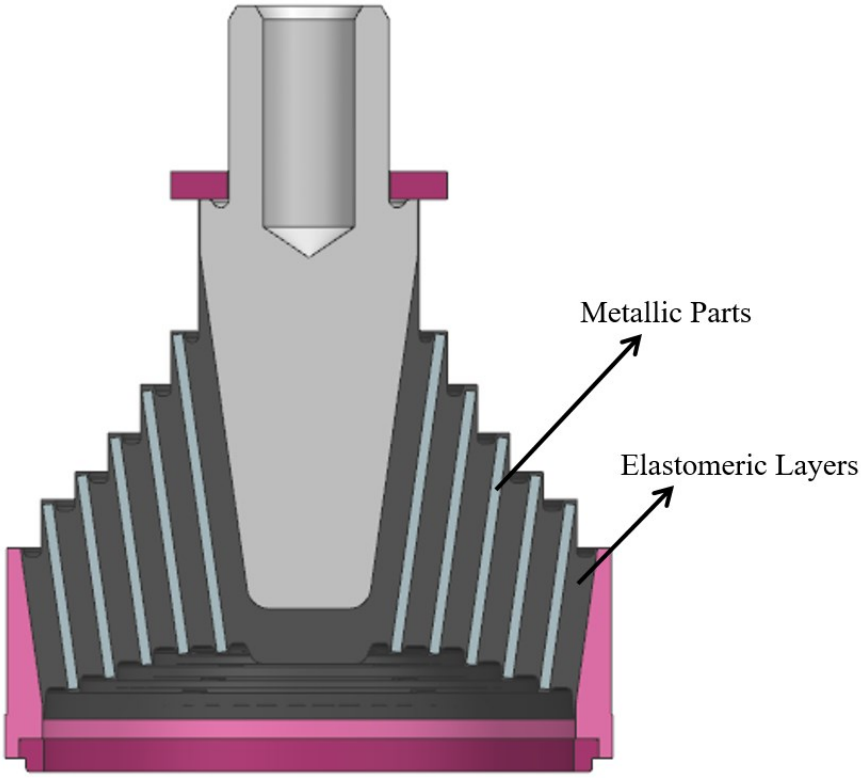

Figure 2-26: Conical rubber spring design.
Source: Author modeling as a courtesy from Vibtech manufacturer

The conical spring application and its performance depend on the number of elastomeric layers, the cone tilt angle and the selection of an optimum elastomeric compound. As the rubber is in both compression and shear when loaded, the conical springs allow for considerable excursion and have a progressive characteristic curve.

They are generally used in the railway industry in order to comply with comfort and environmental demands. Some conical springs are even fitted with bump stops that help to absorb shock loads without causing permanent damage. Its assembly between wheels and bogie frame is illustrated according to Figure 2-27.

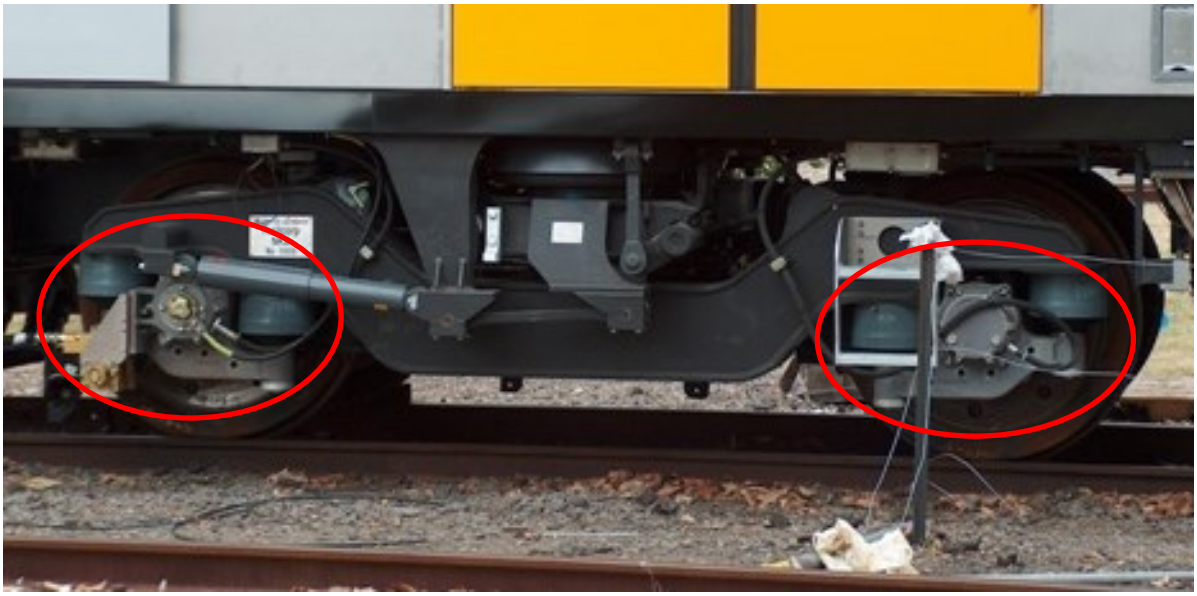

Figure 2-27: Conical rubber spring assembly.

Source: Adapted from Rail Motor Society (2017)

3

MATERIALS AND METHODS

3.1 Sample details and experimental apparatus for rubber characterization

In order to reach the main objectives proposed in the present Dissertation, samples of natural rubber reinforced with carbon-black have been prepared from the same batch of raw material to conduct a series of uniaxial and equal biaxial extension tests. In order to avoid the Mullins effect (see section 2.3), five loading cycles were performed prior to each test. The rubber compound used in characterization tests is a confidential formulation produced by Vibtech company, since it is the elastomeric material presented in the laminated bearings of the conical rubber spring.

The uniaxial stretching tests have been performed in a standard tensile machine according to ASTM D412 (2016).

For the case of equal biaxial deformation mode, two different methodologies have been studied: stretching the elastomeric sample in a cruciform device and blowing the sample according to the classical bulge test method. Both methodologies have been coupled with Digital Image Correlation (DIC) technique, allowing measurements in real time of strain levels on the surface of the deformed specimen. Just as a comparison, the compression test was also carried out varying the friction levels between rubber and metal surfaces (from rough to oily surface).

The rubber shore hardness was extracted from five circular samples with at least 6 mm in thickness according to ASTM D2240 (2015). The average hardness value was 47 Shore A, as depicted in Figure 3-1.

Figure 3-1: Rubber shore hardness test on a type A durometer

Other experimental tests regarding tear resistance (ASTM D624, 2012), deterioration under high temperatures (ASTM D573-04, 2015), adhesion to rigid substrates (ASTM D429, 2014), compression set in air or liquid media (ASTM D395, 2018), resistance to outdoor weathering (ASTM D1171, 2018), impact resilience (ASTM D2632, 2015) and vulcanization characteristics from rheometer (ASTM D2084, 2019) have been conducted to ensure the rubber quality. Because these results are confidential to Vibtech company and they are not in the scope of the Dissertation, they will not be present here.

3.1.1 Strain field measurement with DIC technique

The DIC technique is a way of collecting data that does not involve contact between the object studied and the measurement method. Data acquisition is done through photography, which is digitally stored and analyzed through mathematical formulation according to an algorithm capable of extracting the physics of the underlying deformation processes (SUTTON *et al.*, 2009).

During DIC analysis a reference image should be fixed (generally the one free of deformation). In the reference image, a sub-area called Zone Of Interest (ZOI) is defined, and then a series of other images can be evaluated from the reference one. The full-field measurement information

can be described by random speckle patterns artificially applied through, for example, an ink able to adhere to the surface without interfering the mechanical properties of the material under study. These speckles consist of describing discrete image areas, which can be determined with subpixel accuracy by analyzing the image information. Figure 3-2 shows how ZOI is defined and how it matches the next image in a deformed configuration based on a determined speckle pattern (CHEVALIER *et al.*, 2001; MOREIRA, 2015).

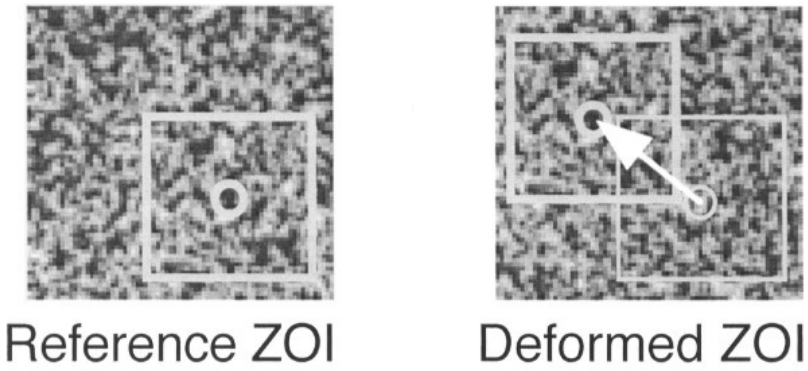

Figure 3-2: ZOI in the initial and 'deformed' image for a two-dimensional configuration. Source: (CHEVALIER *et al.*, 2001)

The displacement field is analyzed by a correlation function, which is defined by a subset size. The subset size controls the ZOI to track the displacement between images. It should be large enough to ensure that there is a sufficiently distinctive pattern contained in the area used for correlation. This function understands that deformed configuration is like a copy of the reference image in which the point of interest has been displaced.

A classic correlation function can be described according to the Sum of Squared Differences (SSD) of the pixel values, where smaller values represent better similarity. Thus, the correlation function can act as a similarity score, checking the possible matches at several locations, as follows (CORRELATED SOLUTIONS, 2009):

$$C(x,y,u,v) = \sum_{i,j=-n/2}^{n/2} \left(I(x+i,y+j) - I^*(x+u+i,y+v+j)\right)^2 \tag{3-1}$$

where C is the correlation function; x and y pixel coordinates from reference image; u and v the displacements; and n the subset size. The image before motion (I) is related to $(x+i, y+j)$, while the image after motion (I^*) is related to $(x+u+i, y+v+j)$.

For a 2D test, only one camera is necessary to be used, but when the test is in a 3D system, two cameras should be synchronized each other in order to take the out of plane deformations. In addition, illumination through Light Emitting Diode (LED) and camera tripod are requested to an accurate data acquisition. During the experiment, the speckle pattern deforms with the surface and is captured by the camera, which is connected to the computer. In this case, the image acquisition can be done automatically, using a programming for the camera to be triggered with each deformation performed by the device.

In this work, the deformation of the measuring field was mapped with a CMOS (Complementary Metal-Oxide Semiconductor) camera, Manta G-235B®, from Allied Vision Technologies GmbH®. It is important to emphasize, that the measuring field stayed stationary in the center during the entire experiments herein conducted and the corresponding force values were stored in a file at the same time of each picture in the deformed configuration, ensuring data synchronization.

3.1.2 Uniaxial stretching tests

According to ASTM D412 (2016), measurements for tensile stress, tensile strength and ultimate elongation should be performed on specimens that have not been pre-stressed, and rubbers should be compared only when tested under the same conditions. The periods of extension and recovery must be controlled in order to avoid residual deformation and to obtain comparable results.

The experimental uniaxial tensile tests were performed on a dual column tabletop testing system (Instron 5567) coupled with a maximum capacity 5kN load cell. Two different approaches of strain measurement have been performed: clip gauges (extensometers) coupled with the machine and DIC (Figure 3-3 (a) and (b) respectively) capable of measuring large displacements. The specimens analyzed were submitted to three mechanical traction tests under a 500 mm/min displacement rate and the final curve was obtained from tests average.

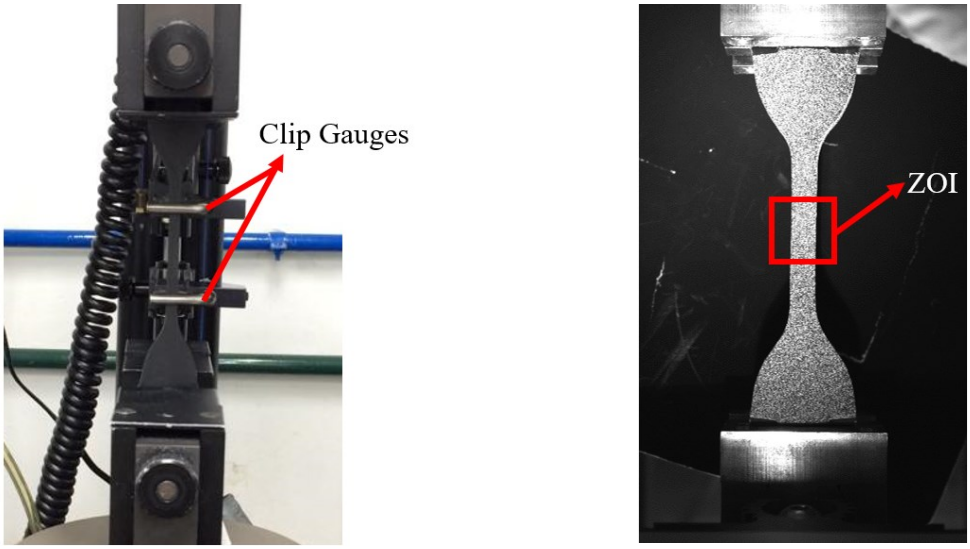

(a) (b)

Figure 3-3: Uniaxial extension test. (a) Instron clip gauges (b) DIC speckle pattern

According to ASTM D412 (2016), the two grips clamped on the dumbbell shape specimen in Figure 3-3 (a) are called bench marks and are used to calculate the strain in the central area. On the other hand, the strain field of Figure 3-3 (b) will be computed by GOM Correlate®, a free DIC and evaluation software. The samples adopted in the experimental tests have been cut off from a 2mm thick flat sheet, with a width of 6mm on the reduced section where the distance between each bench mark is equal to 25mm as illustrated in Figure 3-4.

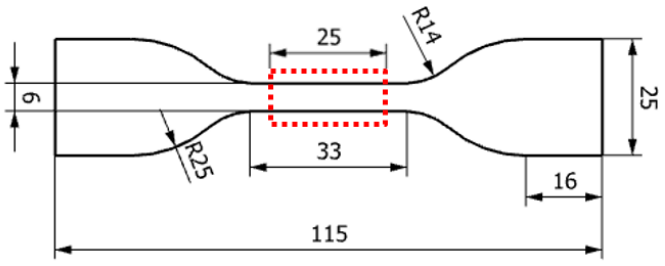

Figure 3-4: Dumbbell shape specimen dimensions according to ASTM D412 (2016).

3.1.3 Equal biaxial stretching tests

As already mentioned, to accurately determine the material constants for a hyperelastic material model, the nominal stress-strain relationships under equal biaxial extension should be considered in addition to that under uniaxial extension.

Since this type of deformation mode has no technical standard which guides the experimental tests, several approaches describing nominal stress-strain measurements have been developed over the years (for more details see section 2.5.2). From this standpoint, the present work conducted equal biaxial experimental tests seeking to compare the implementation in two main different devices: cruciform extension and bulge tests.

It is very important to highlight the need to obtain results for high strain levels. This condition is imposed due to the high deformations in which the studied component is subjected, otherwise the material parameters obtained may become unrealistic for the application of interest. The experiments were carried out in the "Technische Mechanik" lab from Saarland University but the author of the current Ph.D. Dissertation has introduced some contributions in the post processing results aiming to reach accurate results for high strain levels.

3.1.3.1 Cruciform extension test

The equal biaxial tensile tests of this project were all conducted in an in-house development of the "Technische Mechanik" lab. The machine was outfitted with four diametrically opposed step engines controlled by linear actuators arranged in a cruciform manner, according to Figure 3-5. The force measurement was computed by two force sensors (one in each axis) in a range up to 200N. Just like in the tensile test, three samples were evaluated under a 500mm/min displacement rate and the final curve was obtained from tests average. The strain field was captured every 2mm of displacement between clamps through images obtained by a device-triggered digital camera connected to the real-time controller Compact RIO® (cRIO). The code environment was implemented in the software LabView® from National Instruments®. More details concerning the apparatus configuration can be found in (JOHLITZ and DIEBELS, 2011; SEIBERT *et al.*, 2014).

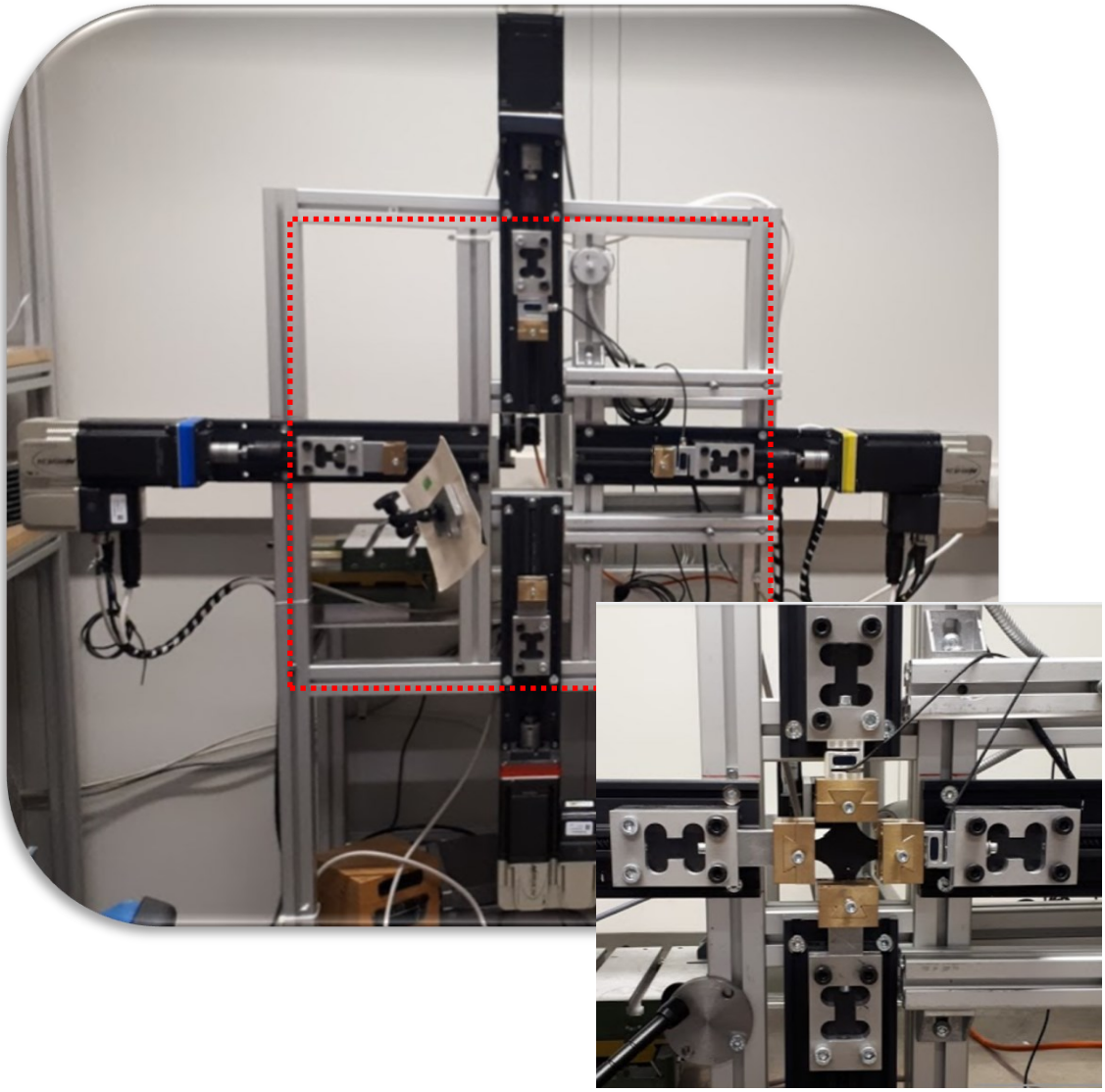

Figure 3-5: Testing device and clamping details

The design of the specimen suitable for biaxial testing should present uniform stress/strain distributions at the central zone. Moreover, geometrical features should provide height levels of strain before failure. Based on (SEIBERT *et al.*, 2014) two types of samples were adopted according to the machine fitting settings. As illustrated in Figure 3-6, each arm of the specimen should be parallel to the particular center line. The clamping region has to be a square of $12.5mm$ of width, and the average thickness was $t = 2.22$mm for both samples.

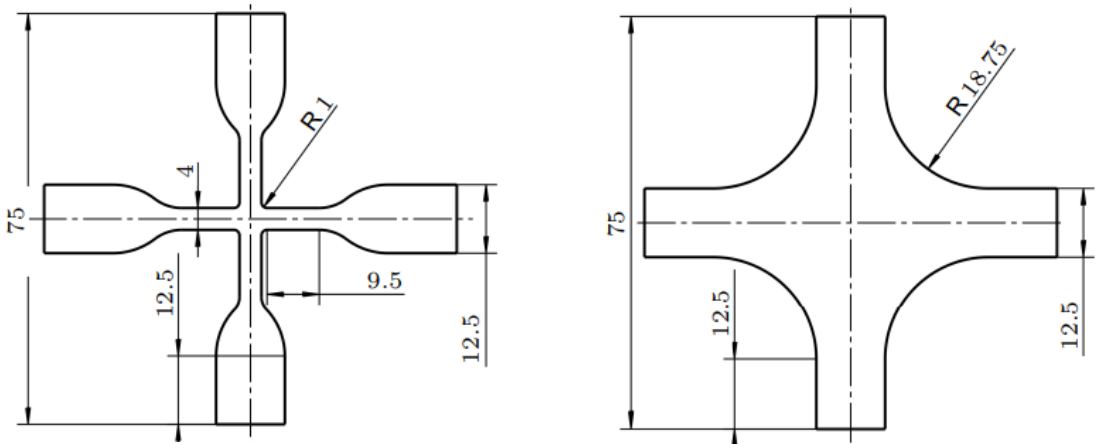

(a) (b)

Figure 3-6: Sample geometries: (a) Type: A; (b) Type: B

In order to have the corrected dimensions for the carbon black vulcanized rubber samples, special molds were developed and manufactured in house as shown in Figure 3-7.

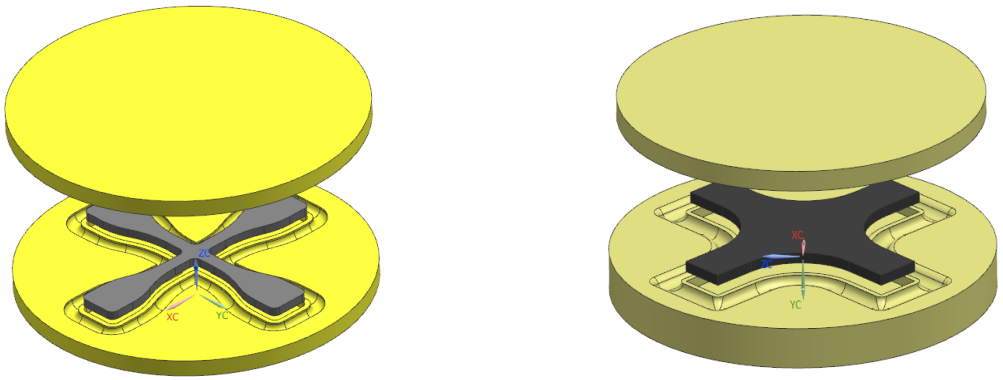

(a) (b)

Figure 3-7: Sample mold design: (a) Type: A; (b) Type: B

In this experiment, the optical setup was composed by only one high-resolution digital camera due the fact that the deformation field occurs in the plane. For the post-processing analysis, GOM correlate® software was used for strain computation, and ZOI area was described through a surface component. In the software approach, square facets are like square image fragments determined with subpixel accuracy by analyzing the image information. Figure 3-8 illustrates surface component with square facets for sample A and sample B respectively. For both samples the facet size was 15 pixels and point distance 16 pixels as depicted in Figure 3-9.

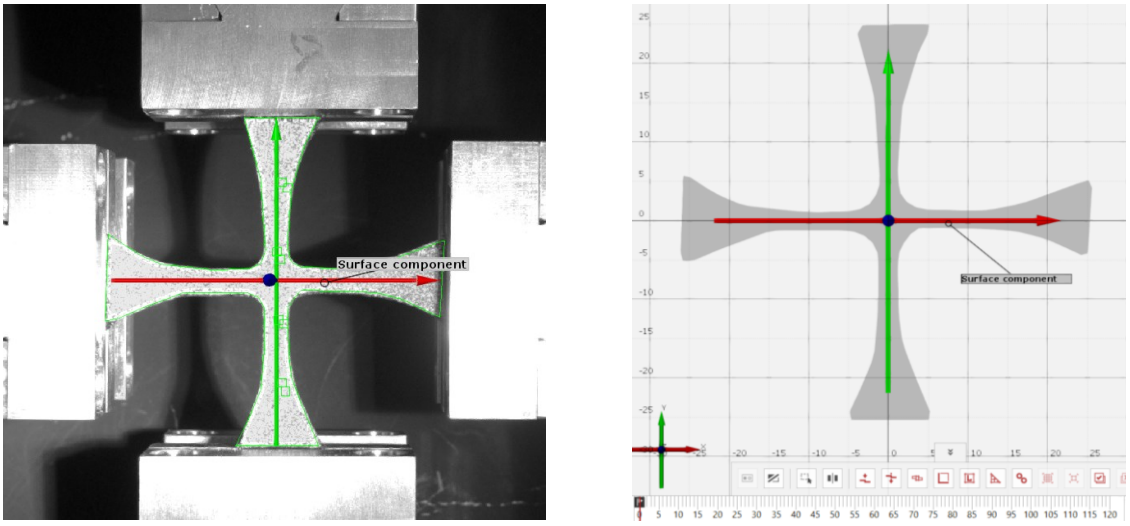

(a)

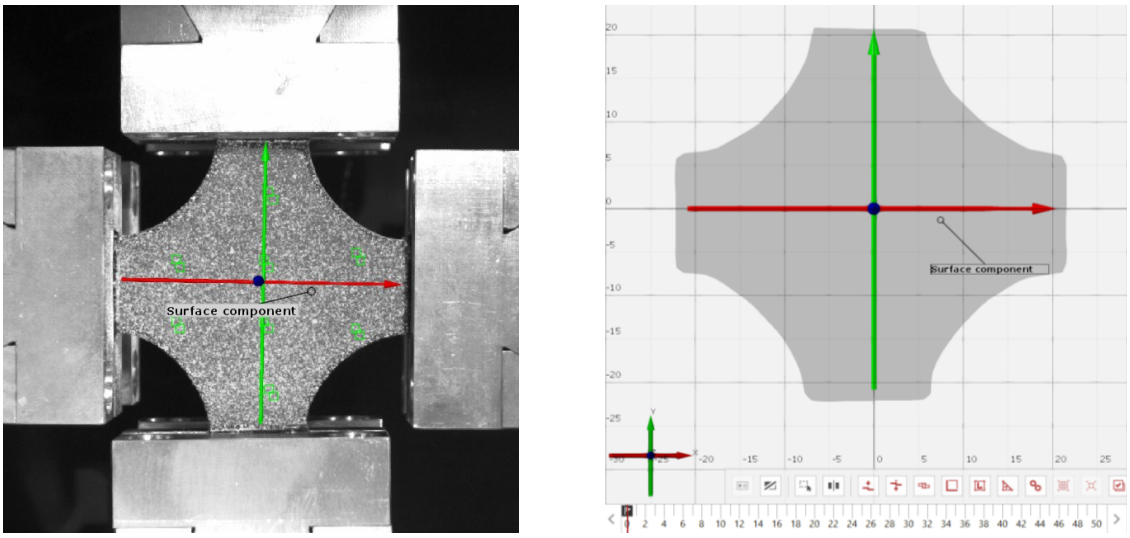

(b)

Figure 3-8: Surface component based on square facets computation. (a) Type: A; (b) Type: B

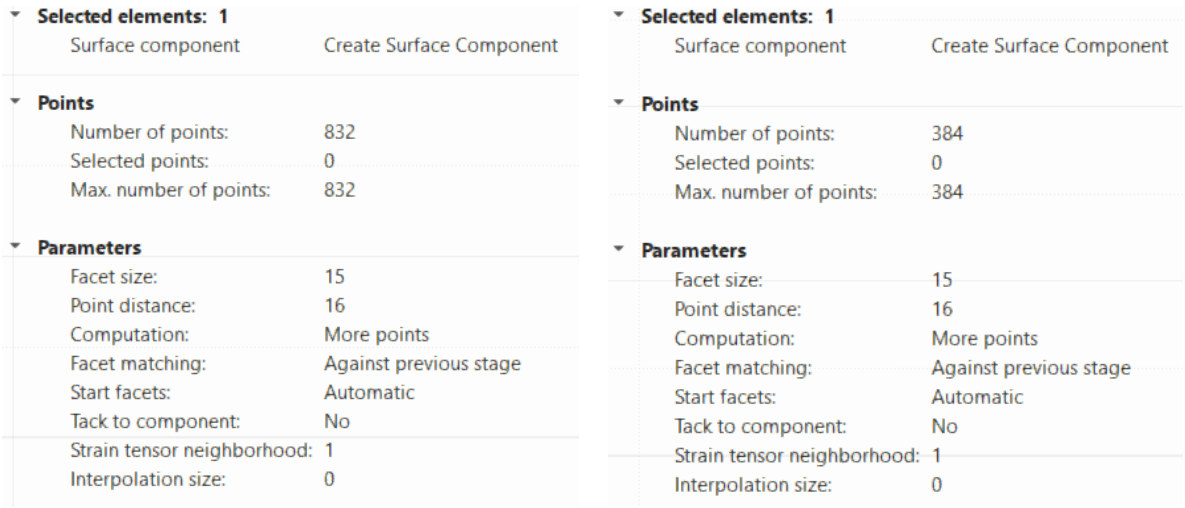

(a) (b)

Figure 3-9: Surface component parameters. (a) Type: A; (b) Type: B

Since the aim of this study is to precisely measure the nominal stress-strain relationships of industrial rubber materials for multiaxial deformation, the biaxial response should be calculated based only on uniform-deformation region. The main problem of this assumption is the uncertainty concerning the determination of the stress state in the central area of the specimen. The total force measured by the load cells differs substantially from the load transferred to the central area depending on details of the gripping system and sample shape. Then, recent research has been implementing optimization algorithms coupled with FEA aiming to extract accurate material parameters from force-displacement experimental data (AVANZINI and BATTINI, 2016). But, the main problem of this approach is the influence of gripping method when displacement is accounted between them.

Thus, the author of the present Dissertation implemented a simpler and more effective way of computing stress around uniform region in the specimen, just employing an inverse method which combines strain field obtained from DIC and FEA. In this approach, it is not necessary several iterations like optimization methods, and its effectiveness is regardless sample shape and gripping system. More details about this methodology will be described in section 3.3.2 and final results will be compared to bulge tests in section 4.3.2.

3.1.3.2 Bulge test

The bulge test methodology adopted in this project basically consists of clamping a thin rubber disc between two clamping flanges. In the implemented bulge test, the specimen assumes a "balloon like" shape when it is inflated with air pressure.

The equal biaxial inflation tests have also been performed at "Technische Mechanik" lab and the equipment was essentially composed by a lower flange with a small central hole to introduce the air pressure, and an upper flange with an internal diameter large enough to let the specimen expand avoiding any border effect. In this type of experiment, a thin rubber disc is blocked between lower and upper clamping flanges along its external circumference. Then, it is inflated by a compressed air from the inner side of the specimen until it assumes a spherical shape. In the device used, the compressed air was controlled by a compact and accurate pressure regulator, GIESA GmbH - DR10, according to the settings implemented in a LabView® environment, up to a maximum pressure of 1 bar. The change in pressure state inside the bulge chamber was measured by a 4-20 mA pressure transducer (Sensortechnics GmbH - CTE8010GV7). This means that the transducer receives a 4-20 mA Direct Current (DC) input signal from the device, where 4 mA is equivalent to the zero pressure value and 20 mA means that the pressure is equal to 10 bar. Data synchronization could be ensured through a cRIO-controller able to integrate the information from digital cameras and pressure transducer connected to the bulge chamber. The process flow and how information were all connected can be better understood through Figure 3-10.

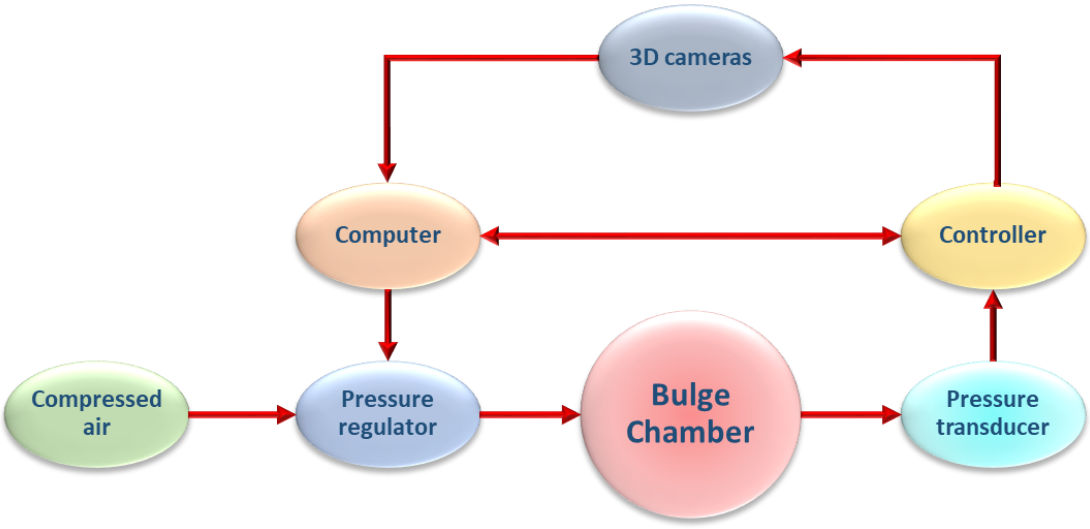

Figure 3-10: Bulge test connected devices

The specimens were disks of initial diameter $D_0 = 50mm$ and average thickness $t = 2.31mm$. Because these dimensions are in accordance with the thin-walled spherical pressure vessel theory, that is $D_0/t \geq 20$, this assumption could be adopted and the tensional state of the specimen could be obtained by force equilibrium due to stress and pressure. According to equation (3-2) the principal Cauchy stresses in the bulged thin film are calculated through the relationship between applied pressure, radius of curvature, and thickness (XIAN, 2015).

$$\sigma_{L1} = \sigma_{L2} = \frac{P.R}{2.t} = \frac{P.R}{2.t_0.\lambda_3} \tag{3-2}$$

where P is the pressure inside the bulge, R the radius on the top of the balloon, t is the thickness at the instant of acquisition, t_0 is the initial value of thickness and λ_3 is the stretch along the thickness direction. Since the thickness is much smaller than the other two planar dimensions, σ_3 is negligible and plane stress condition can be considered.

From pure geometry, the relationship between deflection height (δ), rubber sheet width (a) and curvature radius (R) can be written according to Figure 3-11.

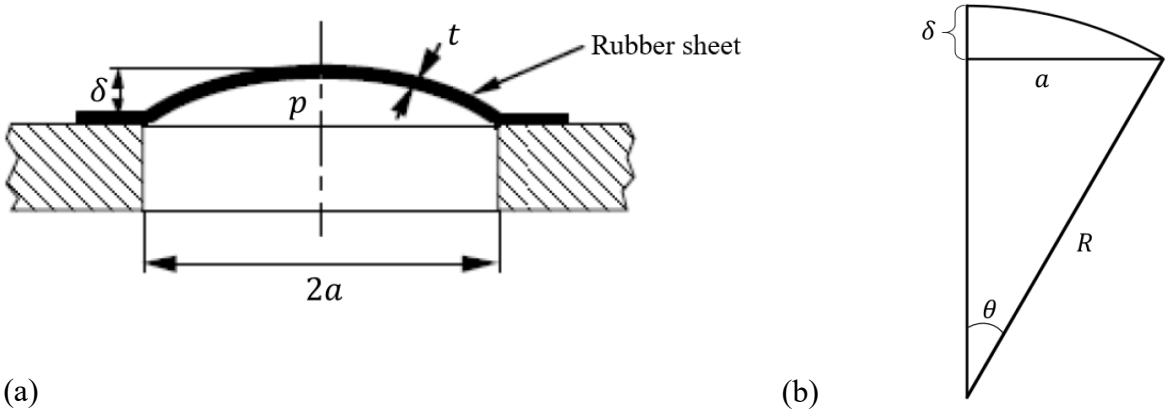

(a) (b)

Figure 3-11: Schematic representation of bulge test and its parameters. (a) Rubber sheet cross section; (b) Geometry relations.
Source: Adapted from Eijden (2008)

From Figure 3-7 (b) it is possible to note that R can be rewritten in terms of rubber sheet width a and deflection apex, δ.

$$R^2 = a^2 + (R - \delta)^2 \rightarrow R = \frac{a^2 + \delta^2}{2.\delta} \quad (3\text{-}3)$$

The optical setup was composed by two high-resolution 3D stereo camera system which delivers precise 3D coordinates based on triangulation and random speckle patterns. Based on this stochastic approach, the VIC-3D software was used to measure and visualize 3D measurements of shape, displacement, and strain based on the principle of DIC.

The cameras should be calibrated and mounted on a moveable arm in order to maintain a good focal distance during the inflation of the specimen. The developed bulge test with an undeformed specimen is shown in Figure 3-12.

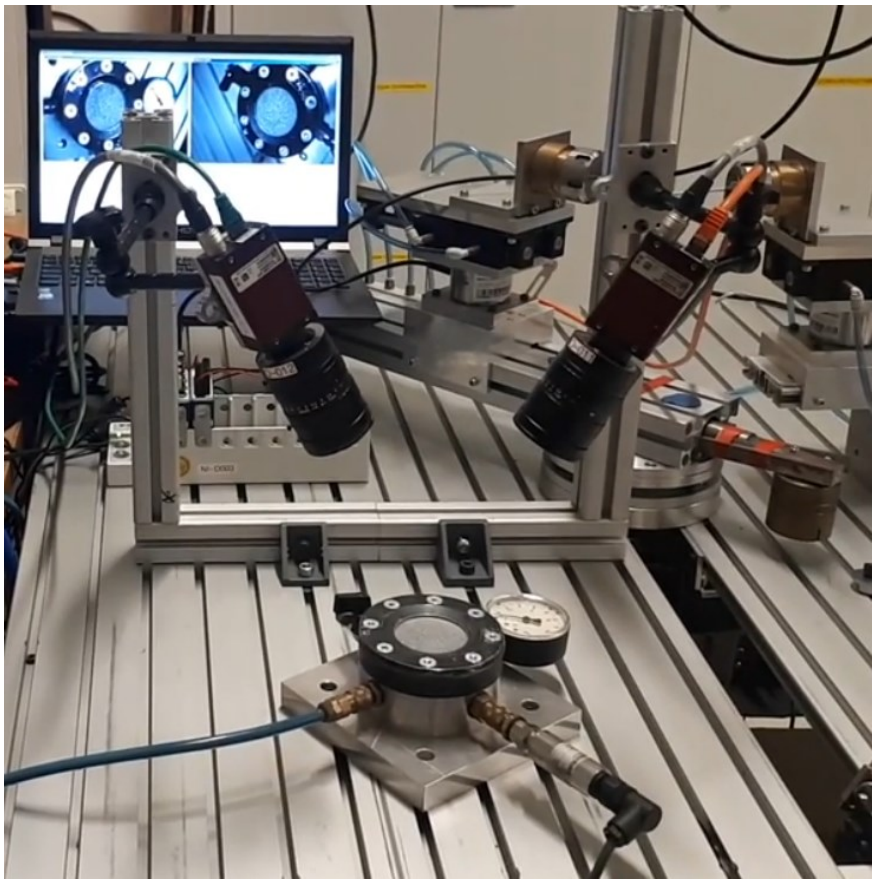

Figure 3-12: Bulge device with an undeformed specimen

As the out-of-plane surface can only be described by two cameras, they should be synchronized each other. During the calibration process, parameters are calculated together through a

calibration plate with a known distance between points (in this case, 5mm). Then, the synchronized images are used to fully calibrate the system according to a calibration target.

In this method, each camera acquires target images separately which are used to calculate intrinsic parameters for the cameras. For each image, a determined number represents the value of total points extracted (0 for failed images). The position of these points are computed and displayed during the extraction. According to Figure 3-13 it is possible to note the three hollow orientation dots labeled with different colors. When all image analysis is complete, the final calibration will be computed. There is a maximum score that validates the calibration (the lower the score, the better the calibration). If the score is higher than the limit, any outlying images will be discarded and the calibration computed again. Notwithstanding, if there are not enough images within the target, the calibration cannot be performed.

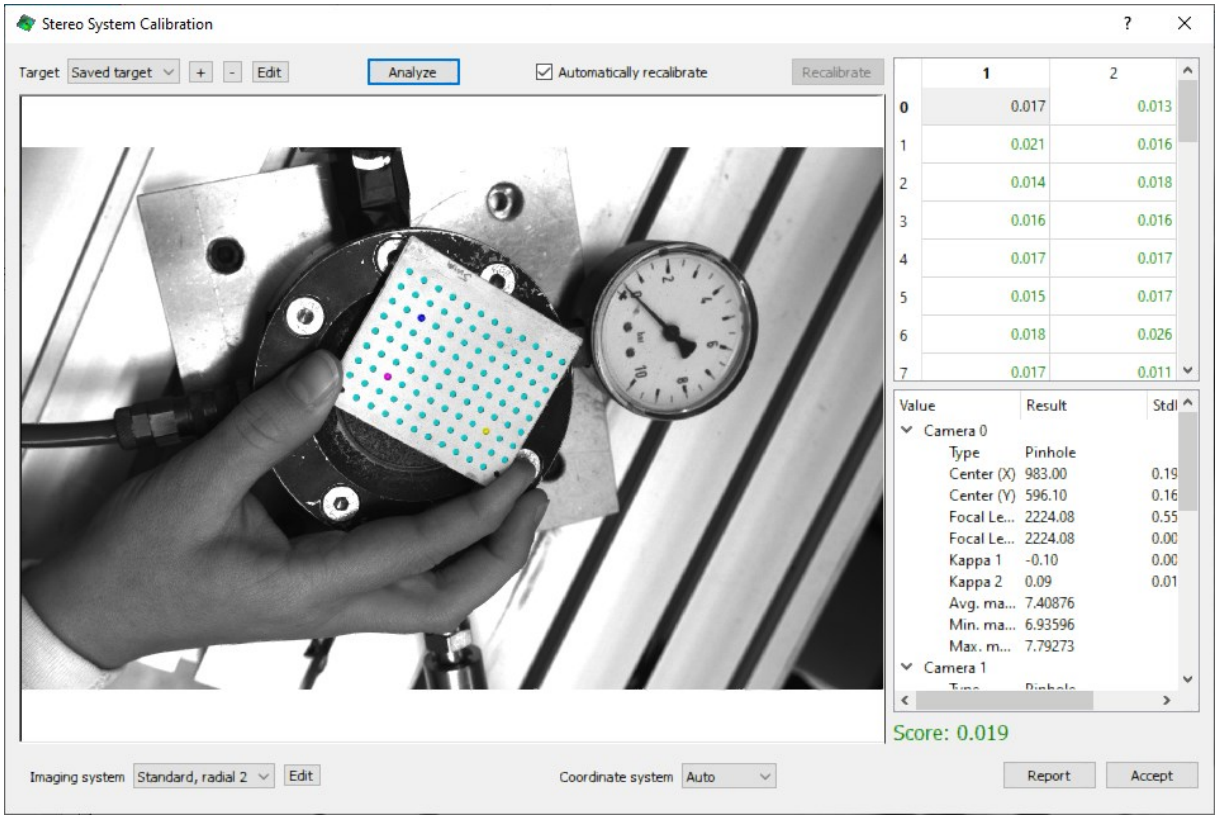

Figure 3-13: Stereo system calibration process and score

The final score presented in Figure 3-13 corresponds to the average error (in pixels) between the position where a target point was found in the image, and the theoretical position where the

mathematical calibration model places the point. Good scores are displayed in green, whereas bad scores in red.

After calibration process, data acquisition for the bulge test could be started. In the experiment, pressure range was increased approximately every 0.02bar, and from this moment a couple of images were taken from each camera synchronized with the pressure. In the post-processing, VIC-3D requires a subset and step size defined from a ZOI which can be seen in Figure 3-14.

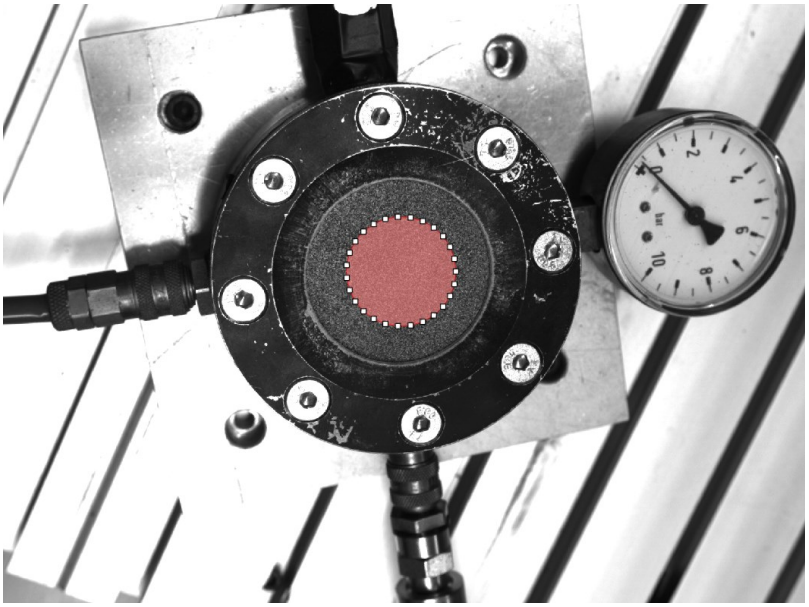

Figure 3-14: ZOI definition based on specimen size

From Figure 3-15 it is worth noting that the chosen value of subset size returns a very low uncertainty interval and consequently an accurate pattern.

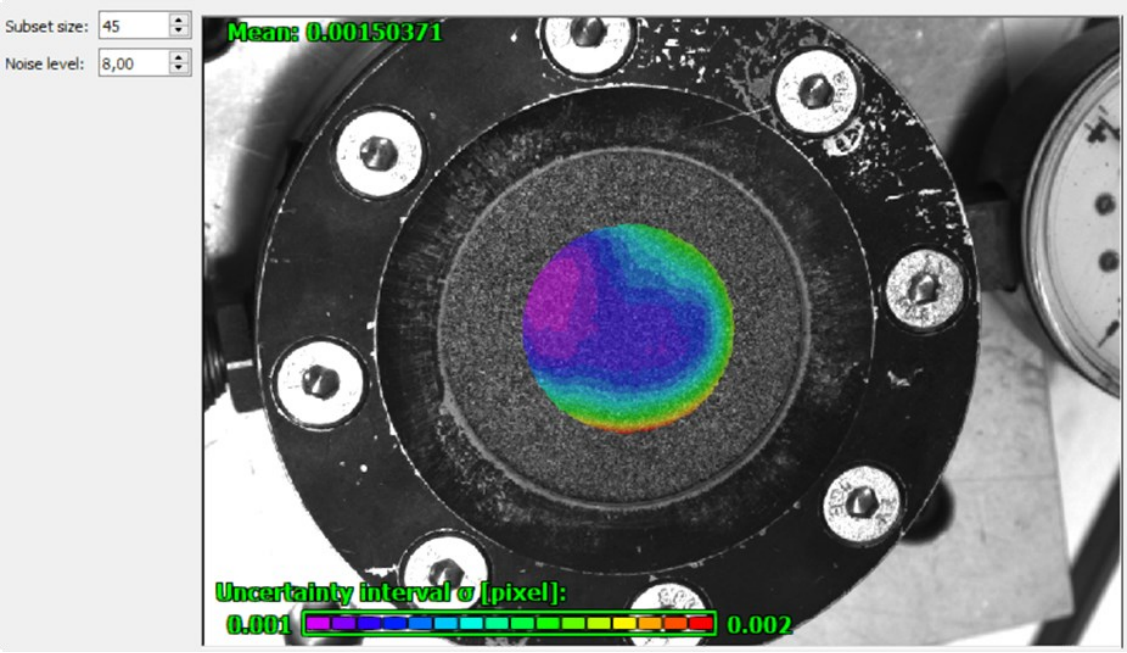

Figure 3-15: Uncertainty interval defined according to subset size

Unlike subset size, smaller values of step size return more accurate results. This happens, because step size controls the points spacing which are analyzed during correlation. On the other hand, the lower the step size the more computational efforts are necessary, and analysis time varies inversely with the square of the step size. As an example, if a step size of 1 is chosen, a correlation analysis is performed at every pixel inside ZOI, but it will take 25 times longer to analyze than a step size of 5. In this consensus, a step size of 5 was adopted, and it as able to give accurate results without destroying the surface during the analysis.

The final stress-strain curves were calculated by considering the average results obtained from several points inside a radius of 6mm around the dome as in Figure 3-16.

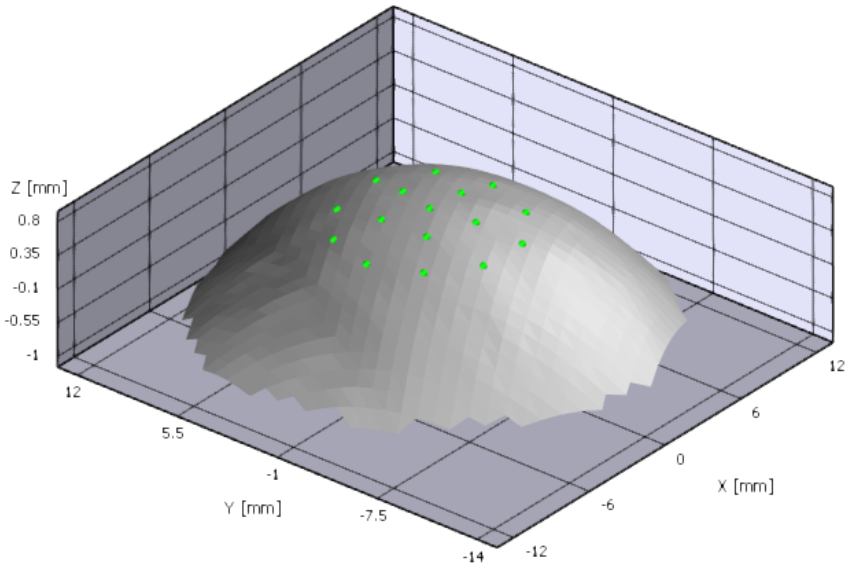

Figure 3-16: Evaluated points for bulge test stress-strain response

3.1.4 Simple compression tests

The compression tests conducted herein this project were performed according to ASTM D575-91 (2018), but taking into account some changes regarding friction between rubber and metal plates. This kind of test is very useful to compare stiffness of rubber materials in compression although the surface treatment can really affect final results. The experiment was carried out on the same machine as tensile tests (Instron 5567), but between rubber surfaces and machine plates two very different conditions of friction were evaluated: rough, with a coarse P60 sandpaper and oily, with a HD 68 hydraulic oil.

The force was applied under a deflection rate of 12 mm/min until the sample reaches 50% of strain. The sample consists of a cylinder with a diameter of approximately 28mm and a height of 12mm. The undeformed position is shown in Figure 3-17.

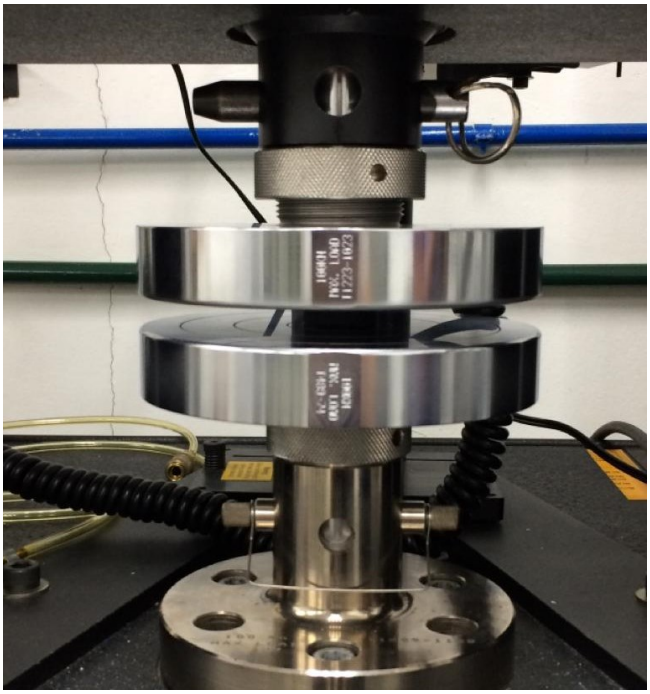

Figure 3-17: Undeformed cylindrical specimen for compression test

3.2 Conical rubber spring experimental tests

The conical rubber spring consists of rubber and metal armatures. It is placed on primary suspensions between the axle and the bogie frame, allowing the transmission of longitudinal traction/braking loads and transverse guidance loads, as well as the vertical flexibility (SEBESAN *et al.*, 2015). It must fulfill with the requirements of the standard NF EN 13913 (2004) for rubber based parts.

The bogie is the key element in wheel-rail contact. It is equipped with two axles connected to a frame by eight springs. In order to have a better understanding, a schematic example of the B23 bogie from Alstom is illustrated in Figure 3-18. The weight of each spring should be the lightest as possible and must not exceed 15.5kg.

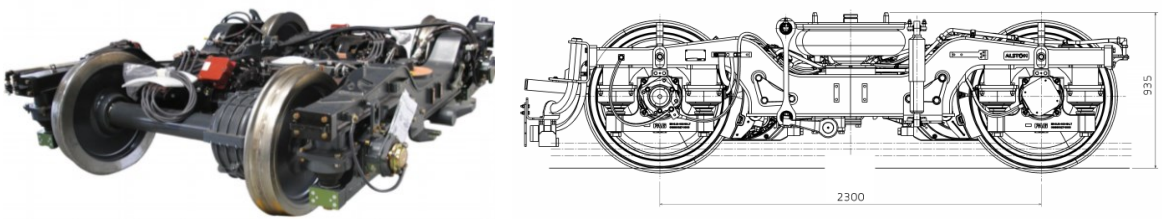

Figure 3-18: B23 Alstom bogie with conical rubber spring suspension
Source: Adapted from Alstom (2015)

Regarding the nature of the elastomer mixtures no condition is imposed, but its formulation shall be identical to the mixtures used for manufacturing the parts which successfully went through the qualification procedure.

The vulcanization characteristic curve should be in accordance with standard NFT 43-015 (1996) or ISO 6502 (2016), and the mechanical characteristics on test pieces in conformity with standard NFT 46-002 (1988) or ISO 37 (2011). All the prototype experimental tests have been performed at Vibtech, with the Dissertation author accompaniment.

3.2.1 Static vertical loads

The vertical loads per spring are described according to Table 3-1. The speeds of measurement must be in agreement with the prescriptions of the technical standard NF EN 13913 (2004).

Table 3-1: Vertical loads per spring according to AW (Added Weight).
Source: Adapted from NF EN 13913 (2004).

		Load cases	Function	Minimum load [kN]	Average load [kN]	Maximum load [kN]
Tare	AW0	-	10%	16.0	20.0	23.0
Normal load	AW1	4pers/m^2	25%	21.5	26.0	30.6
	AW2	6pers/m^2	50%	24.0	29.5	35.1
	AW3	8pers/m^2	15%	27.5	33.3	39.1
Crush load	AW4	-	-	30.0	36.5	43.0

The AW loading refers to the weight added to a vehicle to simulate passenger load, where:

- AW0 simulates an empty car;
- AW1 – AW3 simulates a load with some seated and some standing passengers;
- AW4 simulates a train with a crush load (the maximum number of passengers that can possibly travel in the railcar, standing and sitting).

The maximum load must be supported by the spring without any damage for this last one.

3.2.2 Static axial stiffness

The conical spring should present a static vertical stiffness of 650 N/mm ± 15 %. The testing machine is illustrated according to Figure 3-19, where two power screws are the responsible for executing the translational motion in order to compress the spring through a metal block controlled by a load cell. The procedure used to measure the static axial stiffness should be performed by the following methodology:

- Application of two preload cycles from 0 to AW3 - $AW3_{max}$;
- During the 3rd cycle from 0 to AW3 - $AW3_{max}$, recording of the load/deflexion curve;
- On the curve corresponding to the increasing loads, calculation of the stiffness between $AW0_{min}$ and $AW2_{min}$, then between $AW0_{max}$ and $AW2_{max}$.

Figure 3-19: Assembly for the axial stiffness test

3.2.3 Height under load

After static axial stiffness measurement, application of a fourth cycle from 0 to $AW3_{max}$ should be performed. Then, on the curve corresponding to the decreasing loads, and after a stabilization of 15 seconds under AW0, the height under load is recorded.

Under a vertical load of AW0, the conical spring should present a height under load "h" of 154 mm, as shown in Figure 3-20. Adjustment, if necessary, should be done by a maximum of two shims. These shims must be sticked to prevent any disassembly.

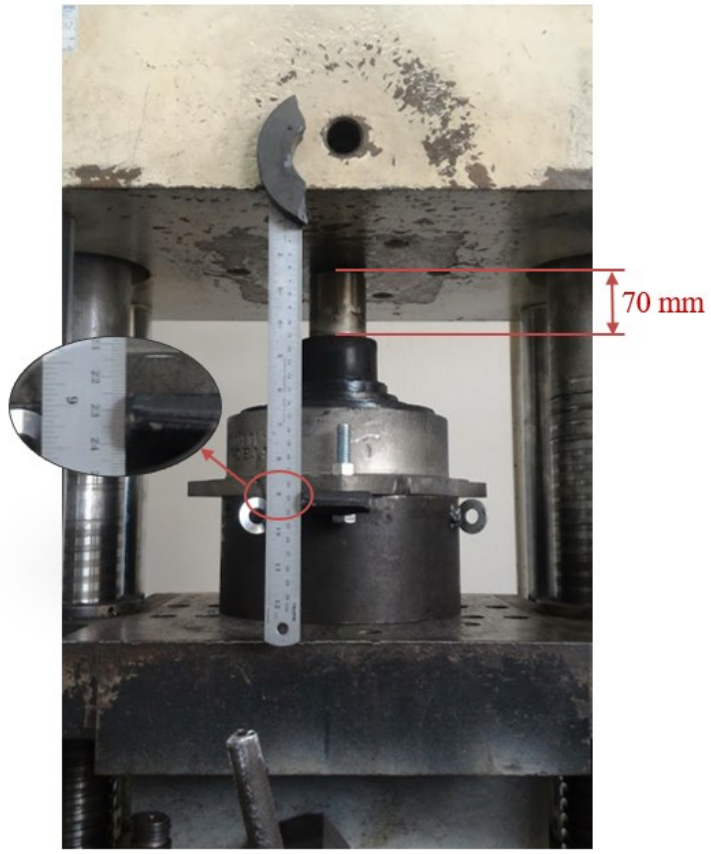

Figure 3-20: Assembly for the high under load measurement

3.2.4 Static radial stiffness

The conical spring should present a static radial stiffness of 5600 N/mm ± 15 % under a preload equivalent to the tare load AW0 which is set according to Figure 3-21. After preload the position is changed as shown in Figure 3-22, where a punch emulates the radial load. The procedure to measure the static radial stiffness, under vertical load, should be performed by the following methodology:

- Application of a vertical preload F_{zi} (N);
- Application of two preload cycles from -6 to 6mm;
- During the 3rd cycle from -6 to 6mm, recording of the load/deflection curve;
- Calculation of the stiffness pick to pick.

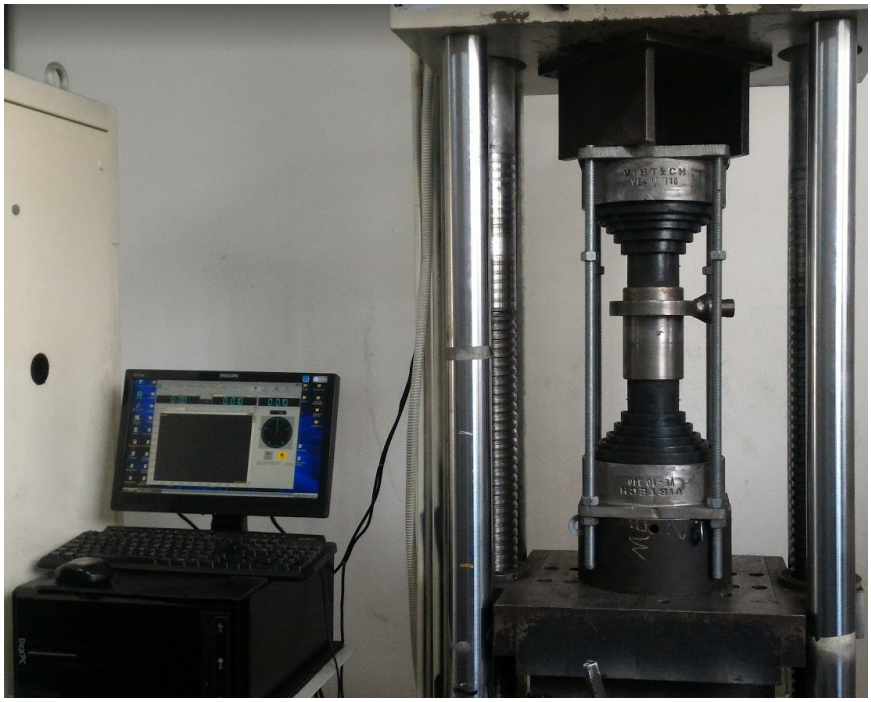

Figure 3-21: Assembly for a preload equivalent to AW0, performed before radial stiffness test

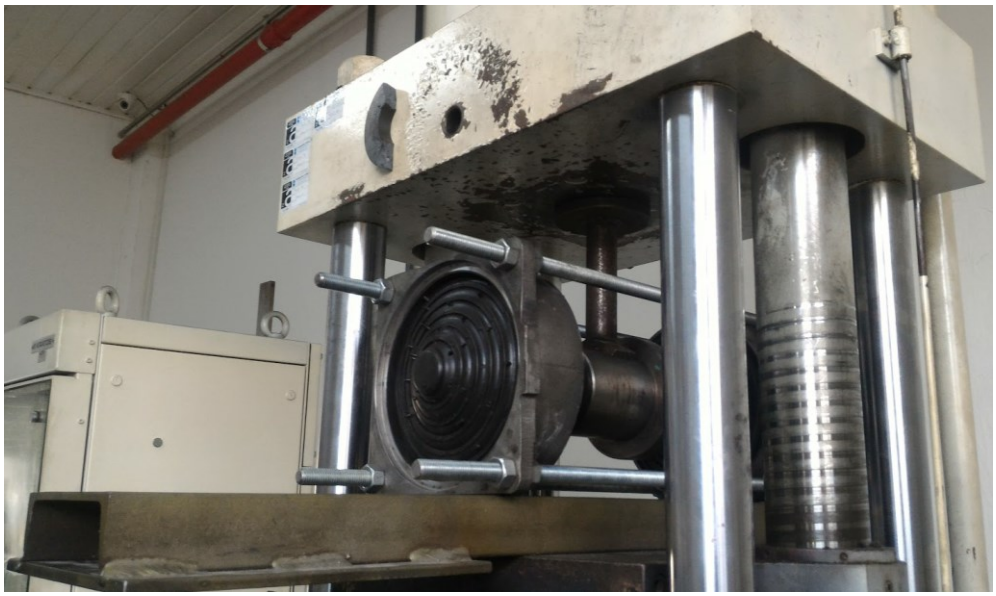

Figure 3-22: Assembly for the radial stiffness test

3.3 Finite element method for analysis correlation

The finite element method is a popular tool for designing elastomeric components. This numerical method is able to approximate the stress-strain behavior of rubber components based on a theoretical material model.

In order to correlate the hyperelastic material properties with experimental data many static tests procedures and constitutive expressions for FEM have been developed over the years – for a brief review see Beda (2014) and Marckmann and Verron (2006). Thus, based on classical hyperelastic theories it was possible to analyze the stress-strain response obtained by means of uniaxial and equal-biaxial stretching tests with the numerical models implemented in the commercial software Abaqus®. All simulation involved in this project were run in an Intel (R) Core (TM) i7-7700k 4-Core @ 4.20GHz processor with 32GB of RAM memory and a GeForce GTX 1060 6GB graphics card.

A curve fitting method was implemented through a Visual Basic for Applications - VBA® code aiming to minimize the relative and absolute errors by a Generalized Reduced Gradient (GRG) optimization algorithm.

The exactness of the material parameters was validated through a finite element analysis of each specimen type and compared with experimental data. From the obtained parameters, axial and radial stiffness of the component were evaluated, but in order to match the prototype numerical results with experimental tests final parameters were obtained by a pattern search optimization method implemented in Python® and Abaqus® scripting interface. This method was proposed by (HOOKE and JEEVES, 1961) and does not require a gradient calculation. It examines points near the current point by perturbing design variables until an improved point is found, and then follows the favorable direction until no more design improvement is possible. The convergence is detected according to a Step Size Reduction Factor until the step-length is sufficiently small or when a maximum number of runs are reached.

Since the nature of the objective function is unknown a priori, this optimization algorithm is a well-suited method for the curve fittings obtained by FEA. The optimization process coupled with finite element simulation is depicted in Figure 3-23. The design variables change

automatically throughout the process and the force-displacement curve depends on the material parameters for accounting the error.

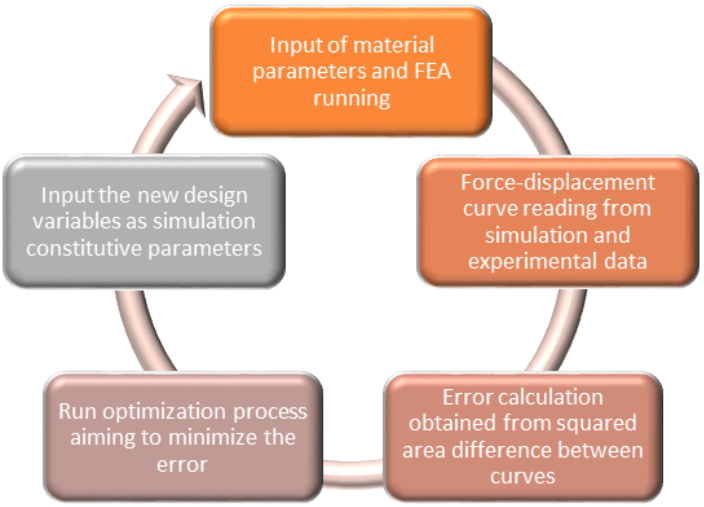

Figure 3-23: Process automation implemented for material parameters definition in prototype.

3.3.1 Data fitting routines for material model calibration

The most common procedure used in numerical computation is the Least Squares Method (LSM) based on a single process of evaluating simultaneously all the parameters of a model. Initially, the hyperelastic constants definition were performed in the Abaqus® environment through an input source selection area as shown in Figure 3-24.

Abaqus® executes the least squares method to determine the best curve for each constitutive model, where for each "n" stress-strain pair that make up the test data, the following relative error "Er" is minimized (SIMULIA, 2016):

$$Er = \sum_{i=1}^{n} (1 - T_i^{th}/T_i^{test})^2 \tag{3-4}$$

where T_i^{test} is the stress value from the test data and T_i^{th} is the theoretical stress from the fitted curve.

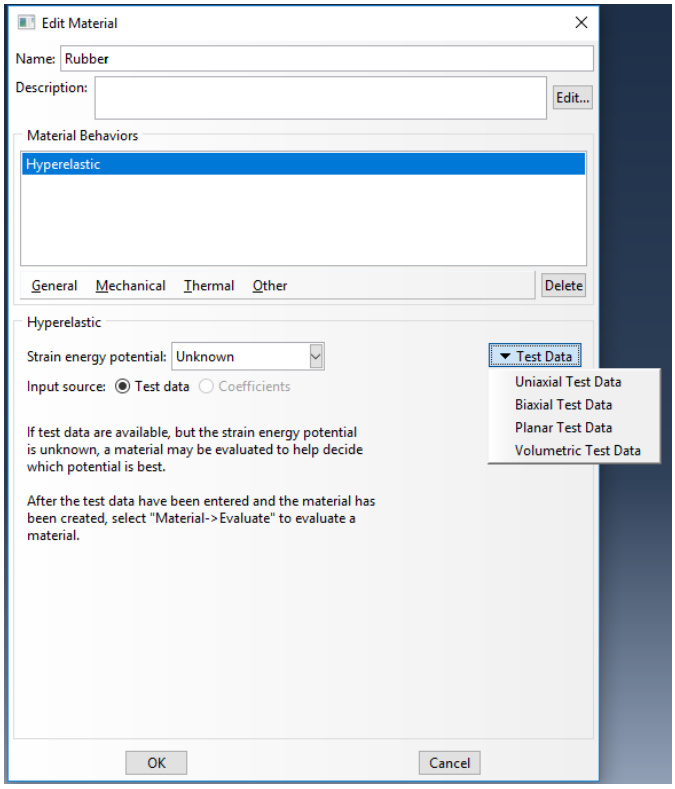

Figure 3-24: Material definition area for experimental test data input and evaluation at Abaqus®.

Another way to define the best curve fitting, but is not implemented at Abaqus® environment, is by accounting the absolute error "Ea". This measurement, can be interesting since it expresses how far the theoretical curve T_i^{th} is from the experimental values T_i^{test}. It basically takes into account the difference between expected and actual values as follows:

$$Ea = \sum_{i=1}^{n} \left| T_i^{test} - T_i^{th} \right| \tag{3-5}$$

The theoretical stresses are defined for each pure deformation mode based on the assumption of full incompressibility. Then, pure deviatoric part can be conveniently rewritten for each hyperelastic model as a function of the elongation and/or invariants of the strain experimental data. From this point, T_i^{th} equations are derived for uniaxial, biaxial and planar shear as follows (SIMULIA, 2016):

- Polynomial strain energy potential

The hyperelastic polynomial form can be fitted by Abaqus® up to order $N = 2$. Although Mooney-Rivlin is a formulation based on polynomial form, Abaqus® names it as a case of $N = 1$, where the higher-order coefficients are set to zero.

$$T_U = 2(1 - \lambda_U^{-3})\big[C_{10}.\lambda_U + C_{01} + 2C_{20}.\lambda_U(\bar{I}_1 - 3) + C_{11}\big(\bar{I}_1 - 3 + \lambda_U(\bar{I}_2 - 3)\big) + 2C_{02}(\bar{I}_2 - 3)\big] \tag{3-6}$$

$$T_B = 2(\lambda_B - \lambda_B^{-5})\big[C_{10} + C_{01}.\lambda_B^2 + 2C_{20}(\bar{I}_1 - 3) + C_{11}\big(\lambda_B^2(\bar{I}_1 - 3) + (\bar{I}_2 - 3)\big) + 2C_{02}.\lambda_B^2(\bar{I}_2 - 3)\big] \tag{3-7}$$

$$T_S = 2(\lambda_S - \lambda_S^{-3})[C_{10} + C_{01} + 2(C_{20} + C_{11} + C_{02})(\bar{I}_1 - 3)] \tag{3-8}$$

where the subscripts U, B, S corresponds to uniaxial, biaxial and planar shear respectively.

- Reduced polynomial strain energy potential

The hyperelastic reduced polynomial form can be fitted by Abaqus® up to order $N = 6$. In the case of $N = 3$ the formulation becomes identical to the Yeoh model and for $N = 1$ the Neo-Hookean model is retained.

$$T_U = 2(\lambda_U - \lambda_U^{-2}).\sum_{i=1}^{N} iC_{i0}(\bar{I}_1 - 3)^{i-1} \tag{3-9}$$

$$T_B = 2(\lambda_B - \lambda_B^{-5}).\sum_{i=1}^{N} iC_{i0}(\bar{I}_1 - 3)^{i-1} \tag{3-10}$$

$$T_S = 2(\lambda_S - \lambda_S^{-3}).\sum_{i=1}^{N} iC_{i0}(\bar{I}_1 - 3)^{i-1} \tag{3-11}$$

- Ogden strain energy potential

Like reduced polynomial, the hyperelastic Ogden form can be fitted by Abaqus® up to order $N = 6$.

$$T_U = \sum_{i=1}^{N} \frac{2\mu_i}{\alpha_i}\left(\lambda_U^{\alpha_i-1} - \lambda_U^{-1/2.\alpha_i-1}\right) \quad (3\text{-}12)$$

$$T_B = \sum_{i=1}^{N} \frac{2\mu_i}{\alpha_i}\left(\lambda_B^{\alpha_i-1} - \lambda_B^{-2.\alpha_i-1}\right) \quad (3\text{-}13)$$

$$T_S = \sum_{i=1}^{N} \frac{2\mu_i}{\alpha_i}\left(\lambda_S^{\alpha_i-1} - \lambda_S^{-\alpha_i-1}\right) \quad (3\text{-}14)$$

- Arruda-Boyce strain energy potential

$$T_U = 2\mu(\lambda_U - \lambda_U^{-2}).\sum_{i=1}^{5} \frac{iC_i}{\lambda_L^{2i-2}}(\bar{I}_1)^{i-1} \quad (3\text{-}15)$$

$$T_B = 2\mu(\lambda_B - \lambda_B^{-5}).\sum_{i=1}^{5} \frac{iC_i}{\lambda_L^{2i-2}}(\bar{I}_1)^{i-1} \quad (3\text{-}16)$$

$$T_S = 2\mu(\lambda_S - \lambda_S^{-3}).\sum_{i=1}^{5} \frac{iC_i}{\lambda_L^{2i-2}}(\bar{I}_1)^{i-1} \quad (3\text{-}17)$$

- Van der Waals energy potential

$$T_U = \mu(1 - \lambda_U^{-3}).\left(\frac{1}{1-\eta} - \alpha\sqrt{\frac{\bar{I}-3}{2}}\right)[\lambda_U(1-\beta)+\beta] \quad (3\text{-}18)$$

$$T_B = \mu(\lambda_B - \lambda_B^{-5}).\left(\frac{1}{1-\eta} - \alpha\sqrt{\frac{\bar{I}-3}{2}}\right)[1-\beta+\beta\lambda_B^2] \quad (3\text{-}19)$$

$$T_S = \mu(\lambda_S - \lambda_S^{-3}).\left(\frac{1}{1-\eta} - \alpha\sqrt{\frac{\bar{I}-3}{2}}\right) \quad (3\text{-}20)$$

As already mentioned, the specimens' response for each deformation mode was initially computed by testing the classical strain energy potential forms through Abaqus® data fitting routine using LSM. Hence, the constitutive models which best fit the experimental curves were evaluated with more accuracy by GRG optimization algorithm, taking into account the minimization of both relative and absolute error, as well as equivalent number of experimental points.

The author of the current Ph.D. Dissertation applied this original procedure due to lack of adjustment in some regions of the curve. When data are fitted simultaneously for all experiments, the number of stress-strain pairs should be equivalent, otherwise the experiment with higher number of points may have a greater weight in error accounting. In addition, if only relative error is computed, the error distribution between theoretical and experimental curves cannot be uniform and most of the total error can be concentrated in a specific region of the entire curve, resulting in a high lack of accuracy in that region.

The hyperelastic models which best fit experimental data simultaneously, being stable in all strain ranges, were Arruda-Boyce and Yeoh (see section 4.2). For this reason, these models were implemented in a VBA® code at Excel® environment. As an example, the graphical interface for Arruda-Boyce model is depicted in Figure 3-25. The model can be chosen by the dropdown menu, while the scrollbar is used to evaluate the constants influence on the theoretical curve and the optimization process can be run by pressing the solve parameters button. For implementation of other constitutive models, the only difference will be in material parameters and stress equations inside routine calculation.

Figure 3-25: Arruda-Boyce data fitting implementation by GRG optimization algorithm

3.3.2 Material parameters validation through FEA

The validation of hyperelastic models with experimental data has been done by modeling the test specimens in FE environment. Based on Arruda-Boyce and/or Yeoh coefficients obtained from an accurate data fitting, the simulation was performed to predict the correct stress-strain relation for simple tension and equal biaxial test in Abaqus®.

Since the in-plane experiments (uniaxial and cruciform biaxial) have the rubber thickness significantly lower than its width and length, the plane stress condition could be adopted. In plane stress elements the material is free to deform in the thickness direction and for this reason, special treatment on the volumetric behavior was not necessary. This is the only condition in which the element can be formulated by a fully integrated pure displacement method instead of hybrid formulation (details of hybrid formulation in Appendix A) and/or reduced integration.

In general, an analysis with hybrid element will be more computationally expensive than an analysis using a regular displacement-based element. Although reduced integration is an interesting option for shell elements, it may cause serious mesh dependency problems, especially in biaxial extension, due to a high artificial strain energy introduced by hourglass modes in coarser meshes. The author has also carried out a research about this effect, which is described in the Appendix B.

To represent the rubber samples stretching in plane, symmetry models were performed for each type of experiment. The mesh was composed of 4-node bilinear plane stress quadrilateral elements (CPS4) and the refinement was good enough to evaluate de stress-strain behavior in the area of interest. The specimen modeling and boundary conditions for each experiment is represented in Figure 3-26.

For the case of biaxial extension in a cruciform specimen, the developed methodology initially considered a uniform stress distribution around the whole central region of the specimen, and the adopted width for calculating the initial area is shown in Figure 3-27. Based on this assumption it was possible to obtain an initial guess for FEA data fitting. Thus, from this first simulation in both samples, the stress-strain uniform region size could be evaluated, as well as the reaction forces acting around this small region.

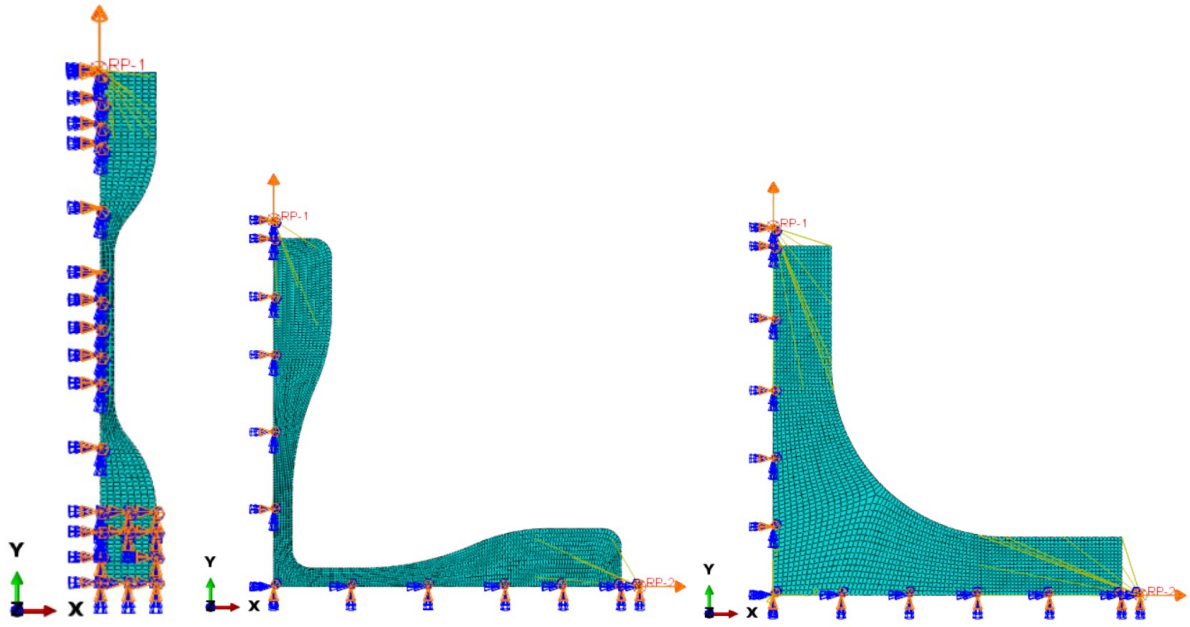

(a) (b) (c)

Figure 3-26: Specimen finite element modeling according to in plane experiments. (a) uniaxial extension; (b) cruciform biaxial: Type A; (c) cruciform biaxial: Type B

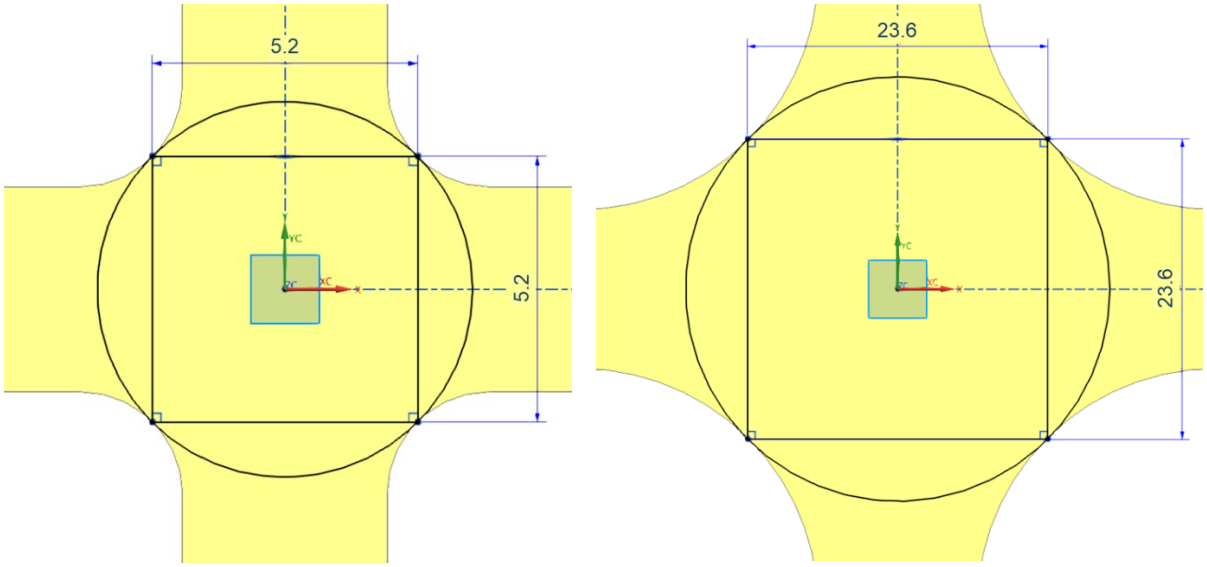

(a) (b)

Figure 3-27: Width dimensions for area initial guess in the biaxial experiment. (a) Type A; (b) Type B.

The reaction forces were obtained for each 1mm stretching increment over the analysis, which was set as analysis time period according to the number of each experiment acquisition. Just as validation, the uniform area (A_{un}) can also be calculated from equation (3-21) regardless analysis time period. The graph depicted in Figure 3-28 shows that uniform area remains constant during the simulation and the difference between time points is neglectable. The maximum displacement in sample A was 120mm and in sample B, 50mm. It is worth remembering that a very refined mesh around biaxial extension should be considered, mainly if biaxiality degree is small. Therefore, it is possible to verify the responses change node by node and extract the correct uniform region in the experiment with its respective force relation.

$$A_{un}^{i} = {RF^{i}}/{\sigma_{N}^{i}} \tag{3-21}$$

where RF is extracted from numerical simulation and corresponds to the total reaction force in the uniform area. The superscript "i" means the current time period in the analysis.

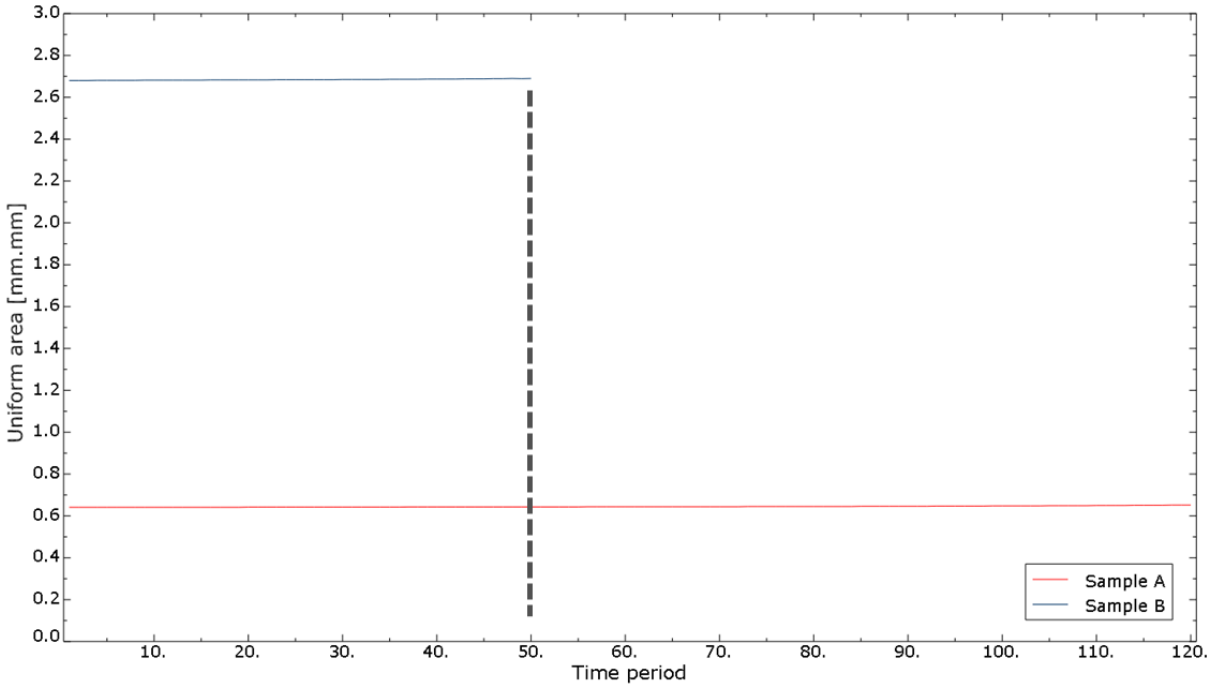

Figure 3-28: Biaxial uniform area calculated from numerical simulation.

Although this method is simple, it is very effective, because the stress sensitivity is much less evident than strains for any variation in the material parameters range, and consequently the

reaction forces acting in the uniform area will not suffer major changes between initial guess and corrected curve. To reach this conclusion the author conducted tests in four different rubber compounds varying the quantities of a soft carbon-black in order to obtain significantly different material parameters as shown in Table 3-2. The formulations were named as follows: D00 (pure natural rubber), DS10, DS30, DS60 (10%, 30% and 60% of a soft carbon black type).

From material parameters, a FE simulation was carried out only for Sample A, because it has a very low biaxiality degree and supported very high deformations in the experiment. Figures 3-29 to 3-31 show respectively the reaction force, nominal stress and nominal strain responses over the analysis time.

Table 3-2: Arruda-Boyce coefficients according to carbon-black quantities in NR compounds

Error type	Coefficients [MPa]	D00	DS10	DS30	DS60
Abaqus®: Relative Error	μ	0.419	0.509	1.110	2.029
	λ_L	3.628	3.405	3.091	3.056
	D	4.551E-03	3.721E-03	1.685E-03	9.202E-04

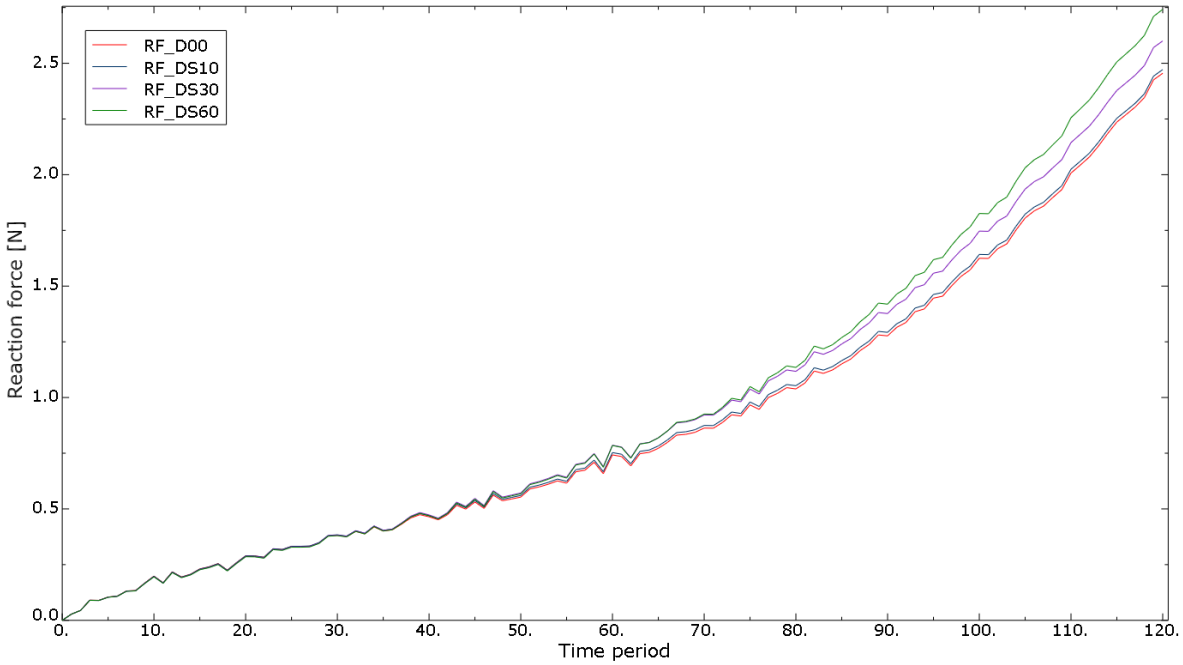

Figure 3-29: Reaction forces around the uniform area obtained from numerical simulation for different NR compounds.

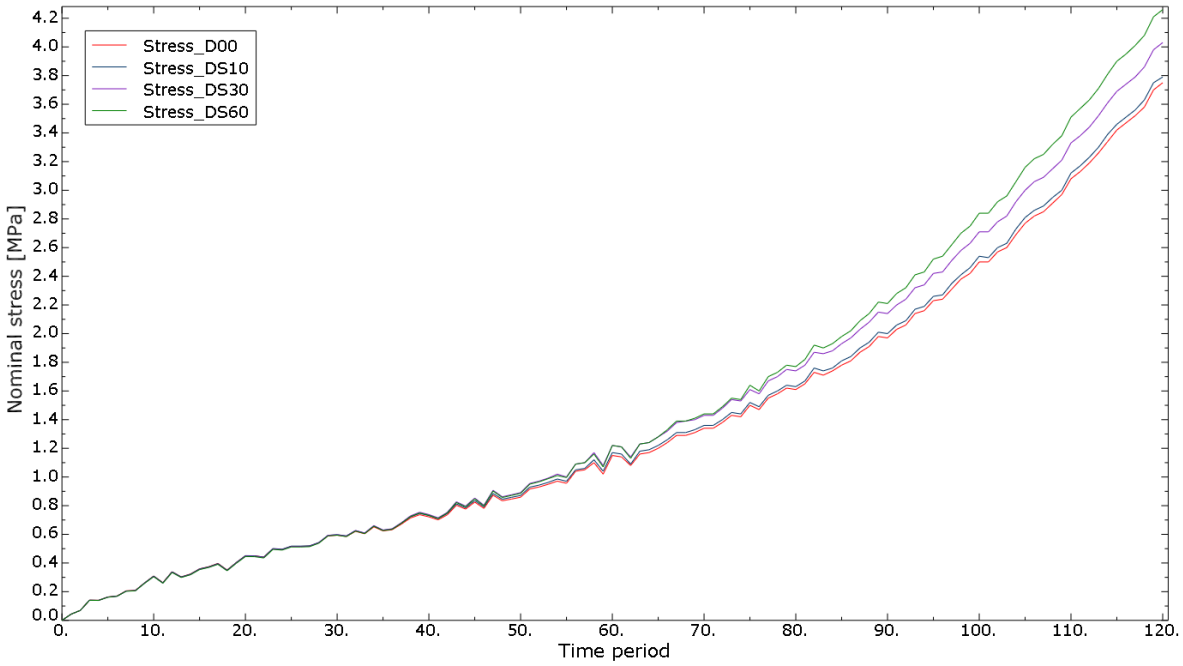

Figure 3-30: Biaxial nominal stresses obtained from numerical simulation for different NR compounds.

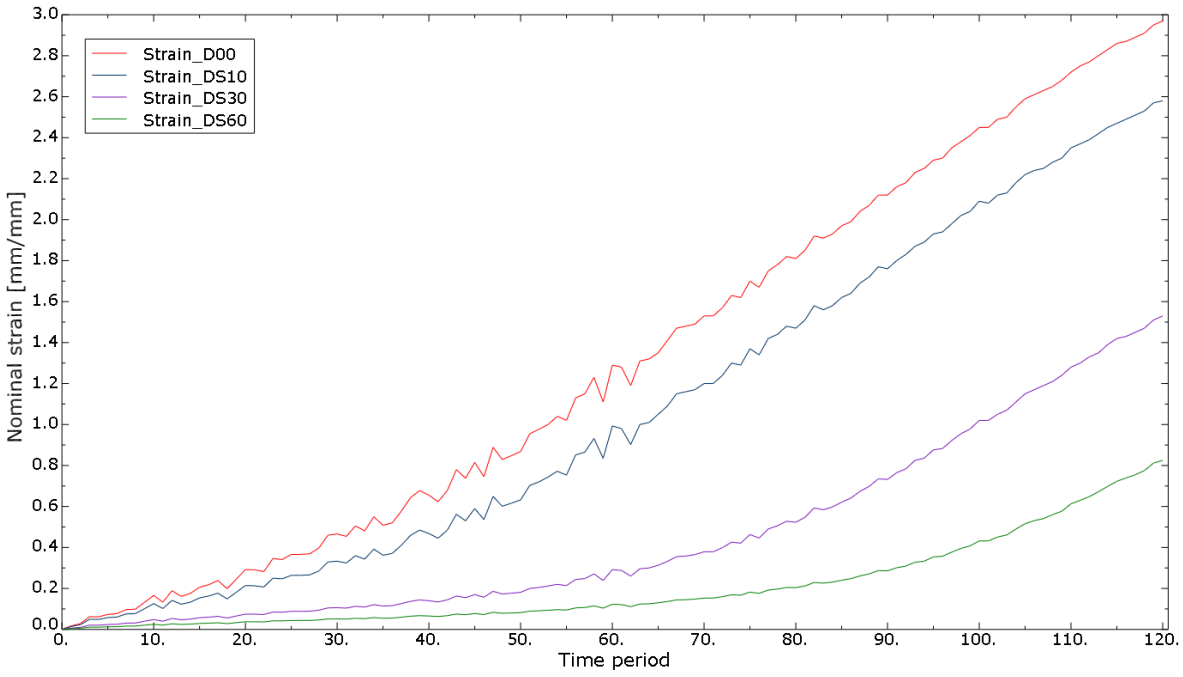

Figure 3-31: Biaxial nominal strains obtained from numerical simulation for different NR compounds.

It is clear to note that, when the constitutive coefficients variation is relatively small, the nominal stresses are very similar and only one iteration of the proposed procedure is enough to correct the experimental stress-strain curve obtained from the initial treatment. In case of higher variations, more iterations should be performed. However, this condition must be hard to happen, and both samples (A and B) converged in only one iteration as will be shown in section 4.3.2.1.

To ensure the potential of the proposed methodology the implemented optimization algorithm used for prototype data fitting was run coupled with FEA aiming to match the stretching force and biaxial strain measured from DIC. Although the work conducted by Barroso *et al*. (2012) seeks to match force in terms of prescribed displacement, the author understands that gripping system may influence on final results and added nodal strain response inside optimization code. Finally, a classical bulge test was also carried out to validate the nominal stress-strain response between both theories, while they should match. All the results concerning this validation process will be presented in section 4.3.2.2.

To represent the rubber bulge test and validate material constitutive parameters when dome is stretched, a symmetry model was built through a mesh composed of 4-node doubly curved thin shell with reduced integration and hourglass control (S4R). In this case, plane stress modeling could not be used since pressure forces are not acting in the element plane. Despite this fact, a very refined mesh was performed in the dome in order to overcome mesh dependency problems. The specimen modeling and boundary conditions for this experiment is represented in Figure 3-32. The highlighted gray area corresponds to the rubber constrained between both flanges.

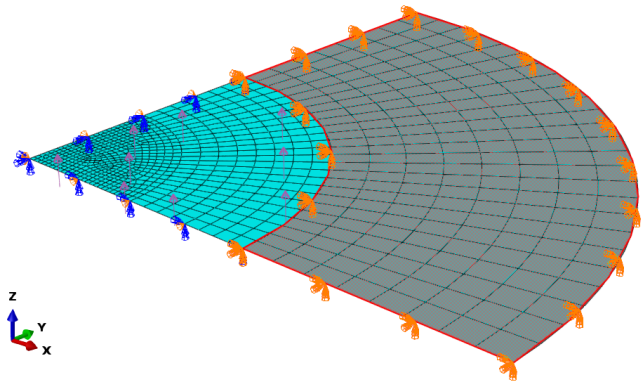

Figure 3-32: Bulge test specimen finite element modeling.

3.3.3 Simple compression FEA modeling

A numerical simulation of the compression test was performed by using a two-dimensional axisymmetric FE model due to its rotational symmetry. Axisymmetric elements convert a 3D problem into a 2D problem, making it a smaller model with faster execution and easier post-processing. For more detail about the axisymmetric formulation used in the analysis see section 3.2.8 of the Abaqus® Theory Guide from Simulia (2016).

To represent the rubber material, 8-node biquadratic axisymmetric quadrilateral elements with hybrid formulation and linear pressure (CAX8H) were used in the mesh, and metal plates were modeled by using 4-node bilinear axisymmetric quadrilateral elements (CAX4). The hybrid formulation is suitable for strictly incompressible solids, such as rubber, being represented by the letter “H” at the end of element name.

The contact between elastomer and metal parts was enforced by a surface-to-surface contact algorithm, where the friction coefficient was varied from 0 (frictionless) to 1 (rough). The finite-sliding formulation was adopted to allow relative motion of the surfaces. For a brief description about nonlinear contact and finite-sliding formulation see sections 5.1.2 and 5.2.3 of the Abaqus® Theory Guide from Simulia (2016). In order to avoid penetration, rubber was set as slave surface (softer) in a densely meshed body, while metal plates were the masters in a coarser mesh. The capabilities of this implementation with its boundary conditions is shown in Figure 3-33.

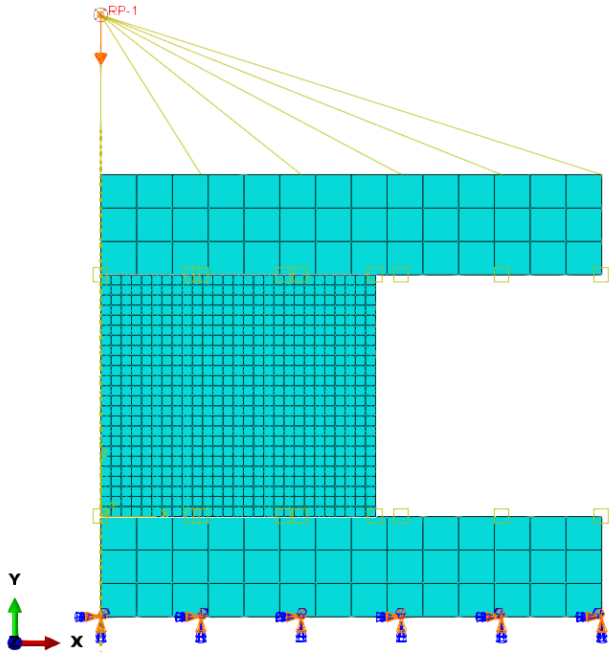

Figure 3-33: Simple compression test finite element modeling

3.3.4 Axial stiffness FEA modeling

For the case of axial stiffness simulation, the conical rubber spring under investigation has been treated as an axisymmetric model due to its rotational symmetry and load applied around its circumference. The implementation assumed that the elements are located exclusively in x, y plane, where the x-axis relates to the radial direction, and the 2D model will be rotated about the y-axis always considering the $x = 0$ position. Thereby, in post-processing, σ_x will be the radial stress, σ_y will be the axial stress, and σ_z will be the tangential stress.

In this analysis, different from compression test, the rubber pads were modeled by 4-node bilinear axisymmetric quadrilateral elements with hybrid formulation and constant pressure (CAX4H), while metal parts just by using 3-node linear axisymmetric triangle elements (CAX3). This simplified mesh was adopted aiming to avoid convergence problems. Considering that, the metal parts were manufactured by a carbon steel SAE 1045, the main material properties were designed as follows: modulus of elasticity $E = 200\ GPa$; density $\rho = 7.85.10^{-3}\ kg/m^3$ and Poisson's ratio $\nu = 0.3$.

Since the rubber is vulcanized and molded into the metal surfaces, parts cannot slide relative to each other. Then, a surface-based tie constraint was used to make the translational and rotational motion as well as all other active degrees of freedom equal for metal-rubber surface pairs. In this approach, a node on the slave face is tied to the master elements only if this node is really "in contact". Therefore, the tie constraint should be defined at the interface of the two zones to stitch the two meshes together. The final model with its boundary conditions is shown in Figure 3-34, where the 2D axisymmetric mesh is discretized into 2978 elements.

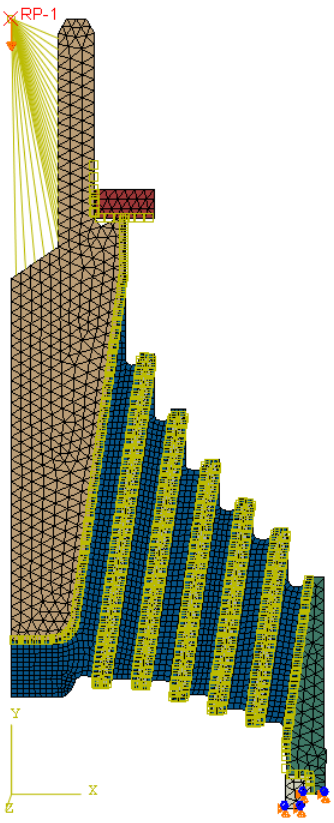

Figure 3-34: Conical rubber spring FE model for axial stiffness (axisymmetric section).

3.3.5 Radial stiffness FEA modeling

For the case of radial stiffness simulation, the conical rubber spring has been treated as a solid 3D model. Here, it was not possible to use the axisymmetric approach because the load is not applied in the axial direction. A brief review about the solid 3D formulation used in the analysis can be found in the sections 3.2.2 and 3.2.4 of the Abaqus® Theory Guide from Simulia (2016).

As with all simulations already presented in this project, FEA was performed using the commercial software Abaqus®. The rubber pads were modeled by a mesh composed of 8-node linear hex element with hybrid formulation and constant pressure (C3D8RH), the reduced integration and hourglass control was also inputted to reduce the volumetric constraints, avoiding the overly stiff behavior due to volumetric locking. The metal parts were modeled by using 10-node tetrahedrons with an improved surface stress formulation (C3D10I) considering the same material applied in the axial stiffness.

The implementation must be performed in two analysis steps. The first step relates to the vertical preloading in order to put the component in a pre-stressed condition. Afterwards, in the second step the radial force should be applied through an imposed displacement of 6mm. The 3D model was discretized into 213814 solid elements, being the implementation with its boundary conditions shown in Figure 3-35 for each step. The surface-based tie constraint approach was based on the same calculation method as in axial stiffness.

During the first step, the operation conditions experience large deformations. For this reason, the implemented mesh ends up deforming significantly from its original configuration and the replacement of a better quality mesh is required. When elements become so severely distorted during a geometrically nonlinear analysis, they no longer provide a good discretization of the problem. To overcome this situation, a mesh solution mapping was implemented in the model at the end of the first step, ensuring a high quality mesh since from the beginning of second step ought to a remeshing procedure in the deformed shape.

Through this technique, the solution from the old deformed mesh is imported to the new mesh and the analysis can continue taking into account the stress state obtained from previous step.

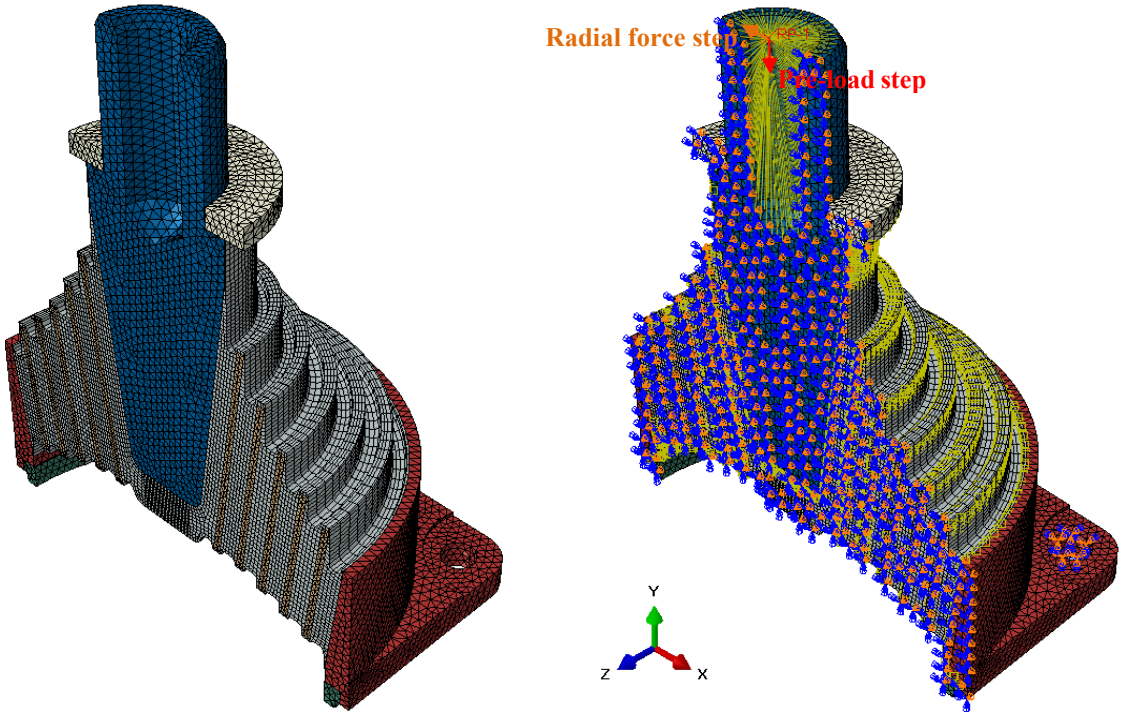

(a) (b)

Figure 3-35: Conical rubber spring FE model for radial stiffness. (a) mesh; (b) entire model with its boundary conditions.

3.4 Analytical solution for radial stiffness

The radial stiffness is a key design parameter for conical rubber spring and is determined by the relation between perpendicular force applied in the main axle and its displacement over the loading. As rubber pads are bonded between several layers of rigid steel plates, the compression behavior becomes more evident. In terms of function, the stiffness (also called as spring rate) is defined according to equation (3-22).

$$K = {}^{F}/_{d} \tag{3-22}$$

where F is the applied force and d is the displacement.

The deformation caused by compressing a rubber pad between two parallel rigid plates generates very complex deformation states which is dependent on a shape factor "S", that is,

the ratio of one loaded area to force-free area (HOLOWNIA, 1971). Thus, the stiffness K is defined in terms of geometry (area "A" and thickness "t") and compression modulus E_c.

$$S = \frac{loaded\ area}{force - free\ area} = \frac{A_L}{A_B} \tag{3-23}$$

$$K = {}^{A.E_c}/_{t} \tag{3-24}$$

where force-free area was named as A_B, because it corresponds to the total surface area that is free to bulge.

The main challenge here is to define the correct E_c because it is strongly affected by the shape factor of a component. Although many different analytical solutions have been developed for some design examples, they are limited to fairly simple geometries. The first analysis of the compression stiffness was performed by Rocard (1937) through an energy approach, and further developments were made by Gent and Lindley (1959) and Gent and Meinecke (1970). Later, Kelly and Konstantinidis (2011) formulated a version of these analyses which was applicable to bearings with shape factors greater than about five.

Therefore, in order to account for more complex geometry effects and/or for nonlinear elastomer properties, the basic equations should be modified. From this assumption, three basic geometric shapes were adopted to formulate the analytical solution for the conical rubber spring: Planar sandwich forms, Laminate bearings and Tube form bearings, as presented in Figure 3-36.

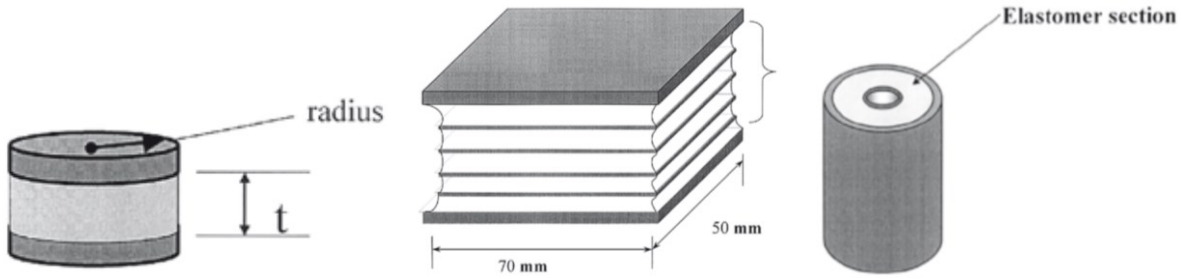

(a) (b) (c)

Figure 3-36: Basic geometric shapes for calculating compression modulus and shape factors. (a) Planar sandwich forms; (b) Laminate bearings; (c) Tube form bearings.
Source: Adapted from Gent (2012)

The effective compression modulus for a flat sandwich block is a function of both material properties and component geometry and can be given by the following equation (GENT, 2012):

$$E_c = E_0.(1 + \phi.S^2) \tag{3-25}$$

where, E_0 is the initial Young's modulus and ϕ corresponds to an elastomer compression coefficient determined empirically. This coefficient was added in the equation just to correct the experimental deviation from theoretical equations.

For isotropic polymeric materials, there are simple relationships between elastic constants such as shear modulus G, Young's modulus E_0, bulk modulus B, and Poisson's ratio ν. Thus, from the data fitting procedure applied in FEA, the shear modulus can be obtained according to the constitutive model which best match experimental curves. As long as two of these constants should be known, an estimate of the Poisson's ratio is applied and all other parameters can be predicted. Under these circumstances, the relationship between G and ν returns E_0 and B, as follows:

$$E_0 = 2G.(1 + \upsilon) \tag{3-26}$$

$$B = \frac{2G.(1 + \upsilon)}{3.(1 - 2\upsilon)} \tag{3-27}$$

In the case of laminate bearings, the compression stiffness is also calculated from E_c, but, as each elastomeric layer is considered to be identical, this relationship is now written in terms of the total number of layers N.

$$K = {}^{A.E_c}/_{t.N} \tag{3-28}$$

where E_c and t are related to each individual layer.

As for tube form bearings, the radial stiffness becomes higher because rubber is used in compression and tension, providing also greater stability. The effective loaded area depends on the load direction and/or deflection of interest. Although axial and torsional loadings result in an easy calculation of the loaded area, radial deflections correspond to much more complex relations. For this reason, they are estimated approximately based on a projected area as follows (GENT, 2012):

$$A_L = (d_0 - d_i).L \tag{3-29}$$

where, d_0 is the outer diameter and d_i the inner diameter of the tube mounting.

To further complicate the calculation, some kind of pre-compression is generally induced in order to enhance performance and fatigue life.

In conventional tube form bearings, this pre-compression can be applied by enlarging the inner diameter or reducing the outer diameter. Another option is to apply a very high pressure, able to cause residual pre-compression during the molding stage. From Figure 3-37 it is possible to observe the effect of pre-compression on elastomer behavior. Pre-compressed tubes effectively make the “tension side” work in compression, whereas in pre-compression free tubes one side of the elastomer works in tension and the other works in compression (GENT, 2012).

Also, according to Gent (2012), radial stiffness can be nearly twice as high in pre-compressed elastomers. However, this assumption can only be valid until the deflection reaches a point where the initial pre-compression is relieved (Figure 3-38).

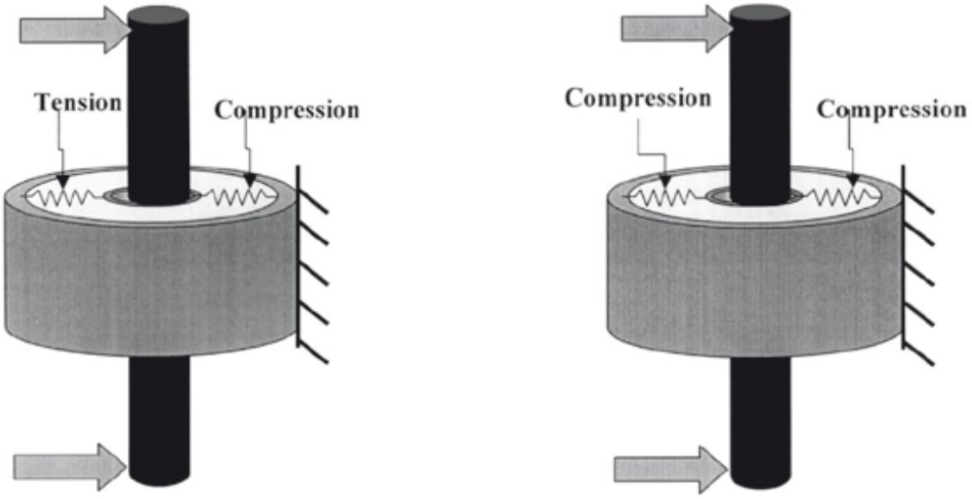

Figure 3-37: Tube form bearing stress distribution for: (a) Unpre-compressed elastomers; (b) Pre-compressed elastomers.

Source: Adapted from Gent (2012)

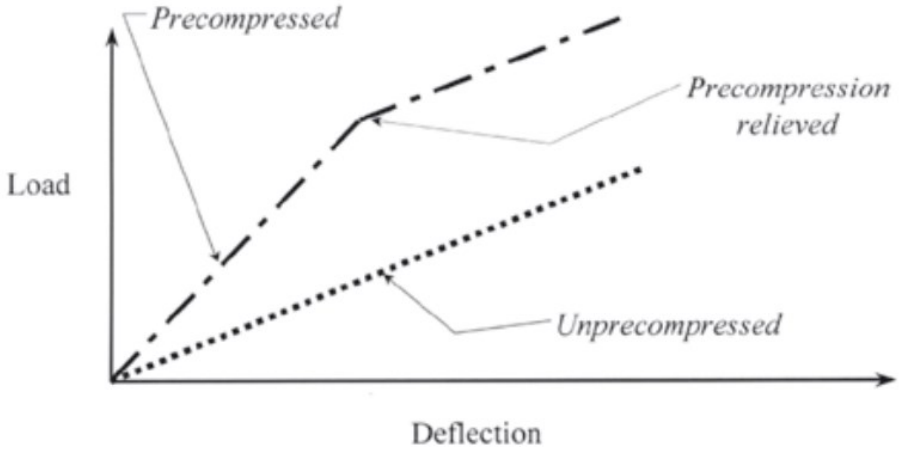

Figure 3-38: Load-deflection curve comparison for pre-compressed and unpre-compressed rubbers on tube form mountings.

Source: Adapted from Gent (2012)

This behavior was also verified in the pre-compressed conical rubber spring, due to an apparent increase in the laminate loaded areas, where consequently, there was some compensation to the numerator of the equation (3-24). For this reason, although the manufacturer company only requires the radial stiffness in a pre-compressed condition, it was also computed without pre-compression, where the comparison results will be shown in section 4.6.

Since the conical rubber spring geometry is very complex, the surface area for calculating the shape factor was extracted for each laminate bearing directly from Siemens NX®, a Computer-aided design (CAD) software. Then, the radial stiffness was calculated for each different layer, taking into account the three main conditions stated above, and was associated in series as they are connected end-to-end. From this assumption the equivalent radial stiffness K_{eq} could be obtained through the following equation:

$$\frac{1}{K_{eq}} = \sum_{i=1}^{N} \frac{1}{K_i} \tag{3-30}$$

where i is related to each different layer over the spring.

4

RESULTS

4.1 Experimental tests for rubber characterization

As already mentioned in the current Dissertation, rubber-like materials can only be characterized if at least uniaxial and equal biaxial stretching tests are performed to fit the model and extract material parameters. Based on this assumption, experimental results concerning these deformation modes were obtained according to the methodology already described in section 3.1.

4.1.1 Uniaxial stretching

Since rubber mixture is not always homogeneous and can vary even in a given batch, three dogbone shape samples were manufactured and tested experimentally according to the both strain measurement approaches already discussed in section 3.1.2. The importance to compare the results obtained from machine extensometer and DIC technique, is to validate the uniaxial response obtained under high strain levels, in which due to stochastic pattern damage of DIC method, is only possible to be captured by extensometer clip gauges.

From Figure 4-1, it is worth noting that the variation between three samples became more evident after strain levels reached values higher than 350%. On the other hand, Figure 4-2 was not able to show greater variations because the maximum strain values computed from DIC methodology were lower than 400%. The region evaluated by the DIC technique can be demonstrated through the surface component which is highlighted in blue and has seven-point measurements as shown in Figure 4-3.

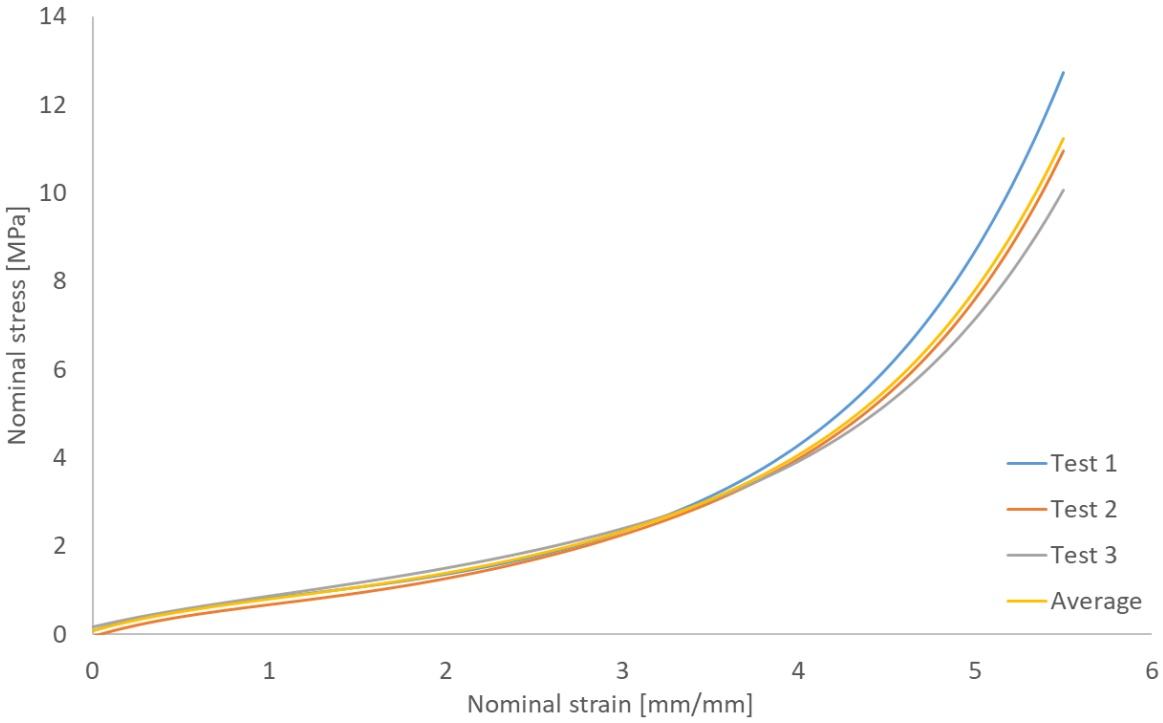

Figure 4-1: Stress-strain curves for tensile test samples measured according to clip gauges coupled to the Instron machine.

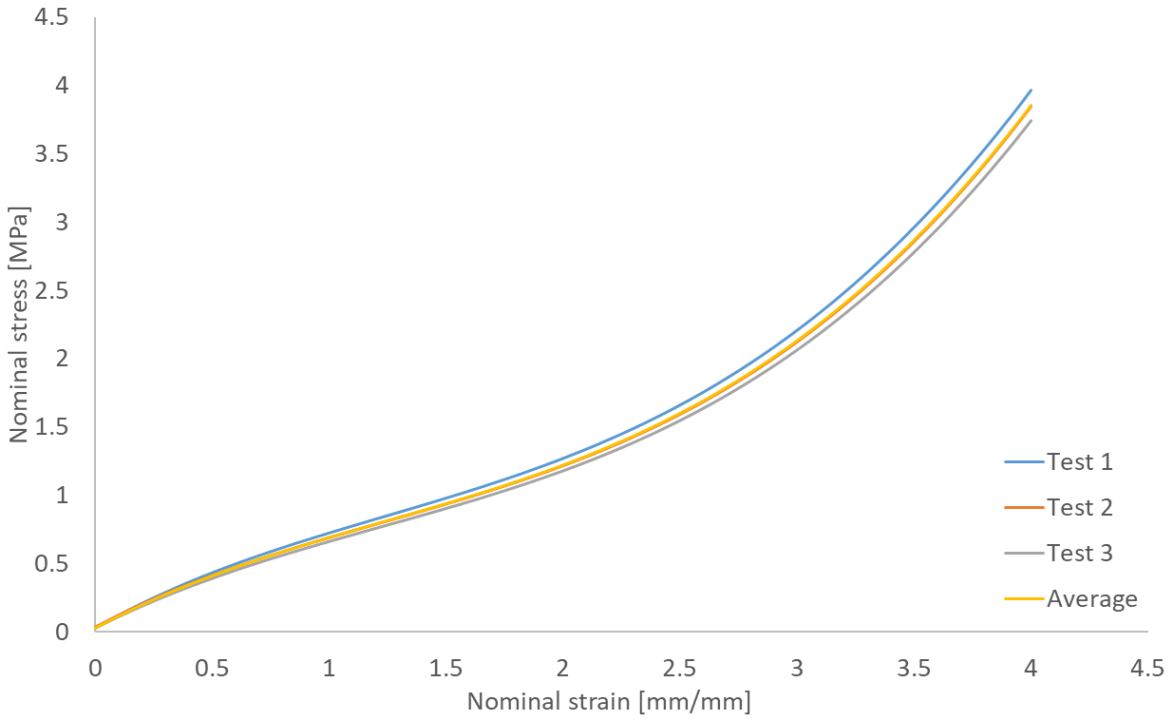

Figure 4-2: Stress-strain curves for tensile test samples measured according to DIC technique.

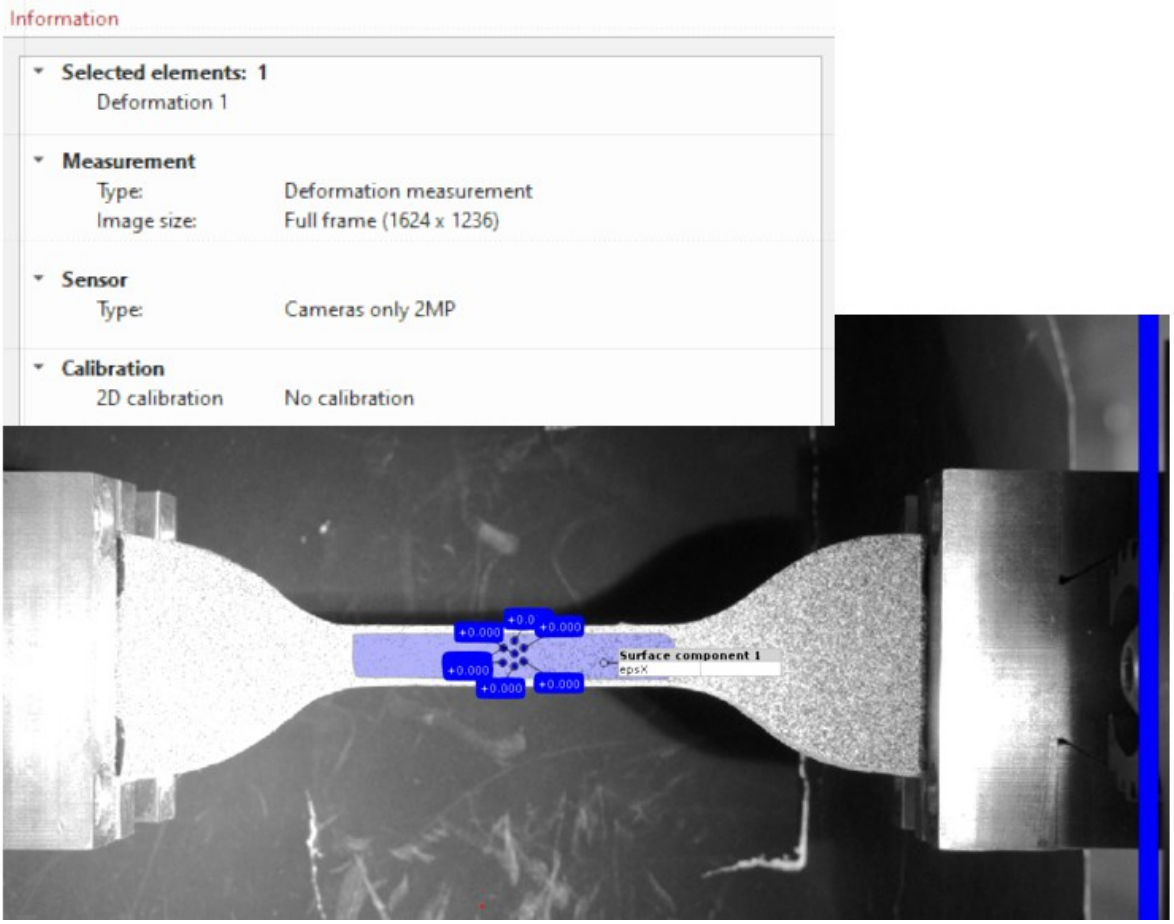

Figure 4-3: Surface component obtained for uniaxial strains measurements.

Although DIC method has presented to be very effective over the last years and has been used in many fields, it is not able to capture accurate measurements after its stochastic contrast black and white pattern starts to damage itself ought to high deformations (Figure 4-4). For this reason, only a maximum value could be reached according to the pattern creation. In the case of the present Dissertation, the total measured strain was up to 400% as depicted in Figure 4-5. Nevertheless, the measurement points presented almost no significant deviation between them, which shows the characterization of the uniaxial plane stress state around the neck area of the sample.

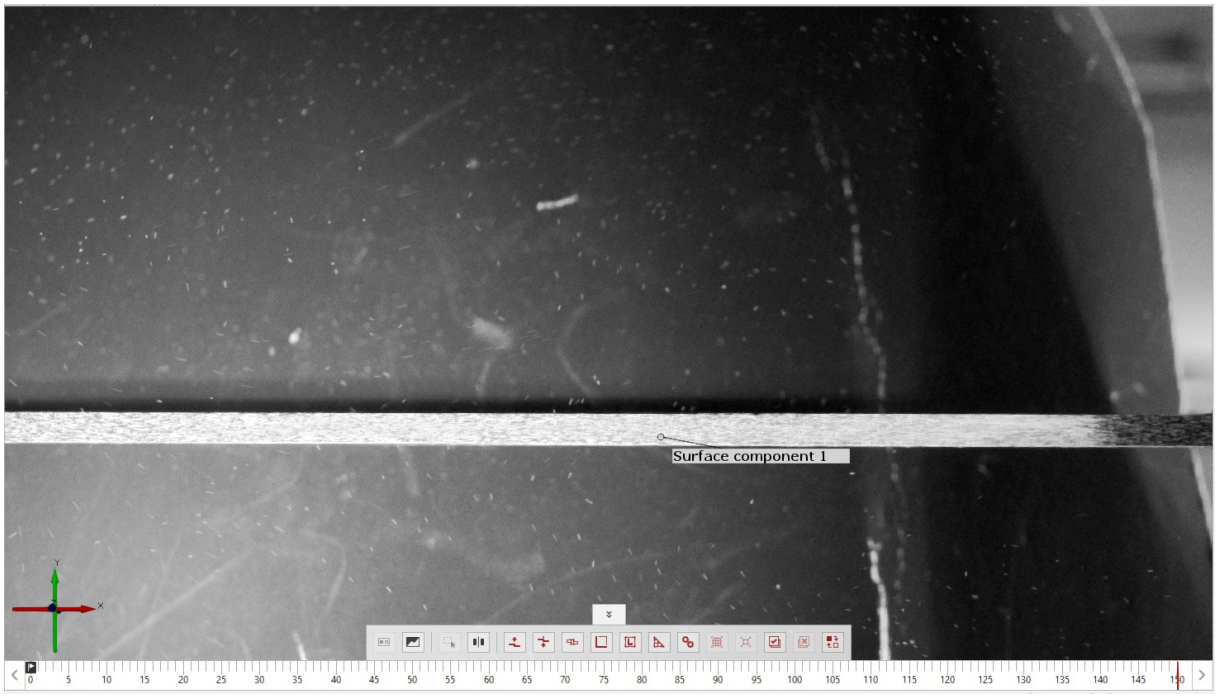

Figure 4-4: Damaged stochastic pattern during 400% of deformation.

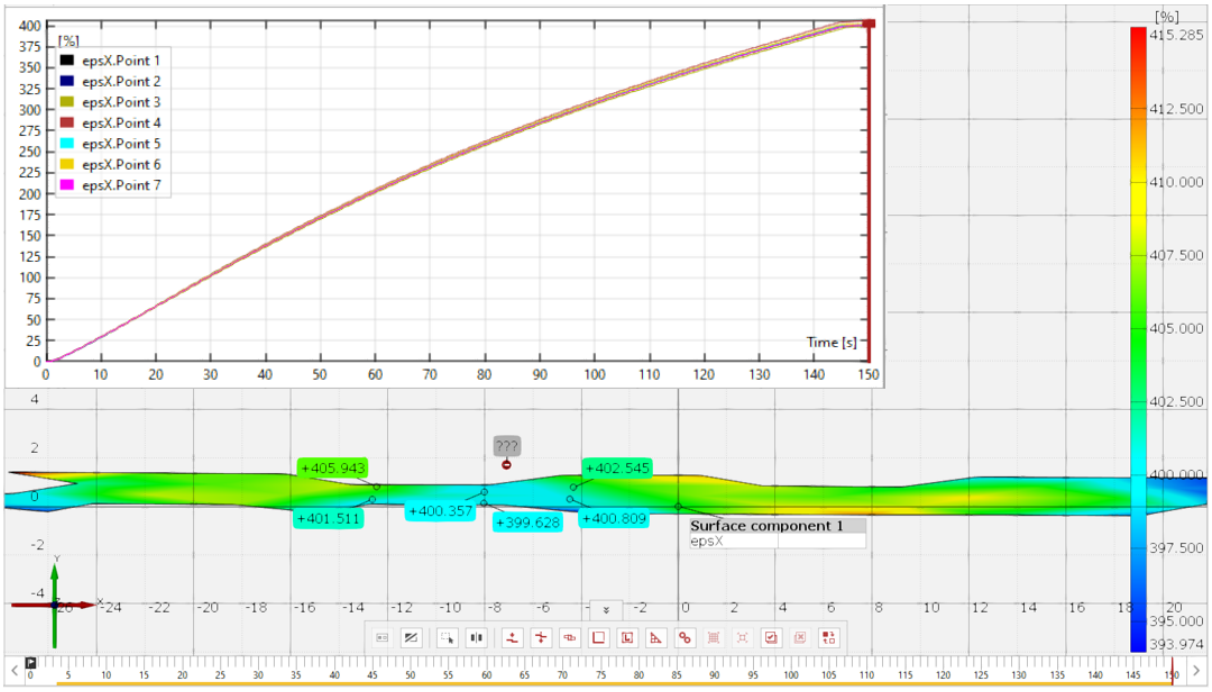

Figure 4-5: Seven-point strain measurements plotted over time.

Finally, the experimental stress-strain curve obtained through DIC could be compared to extensometers results extracted from Instron machine (Figure 4-6). It is worthwhile to note that both curves presented a very similar behavior. Thus, the use of clip gauges in uniaxial experiments can be a useful alternative when higher strain levels should be captured.

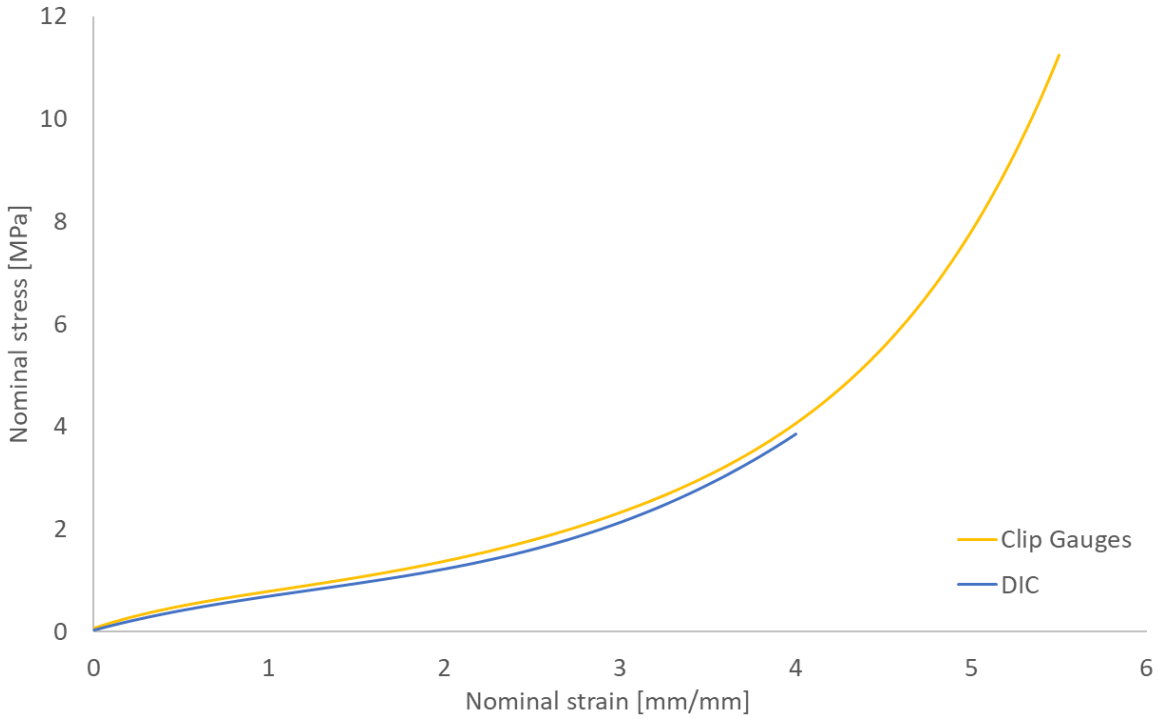

Figure 4-6: Average stress-strain curve of the tensile test. Comparison between DIC method and machine clip gauges.

4.1.2 Equal biaxial stretching

4.1.2.1 Cruciform extension

Based on the methodology already described in section 3.1.3.1, equal biaxial experiments were initially carried out in a cruciform way taking into account two different shapes for the samples (Sample A and Sample B). During the tests, acquisition was taken under displacement steps, where a picture of the central area was being captured after 2mm of clamps opening. In addition, extension force to open each side was also being computed synchronized with the correct picture position in both axes (x and y) as shows Figure 4-7 for Sample A and Figure 4-8 for Sample B.

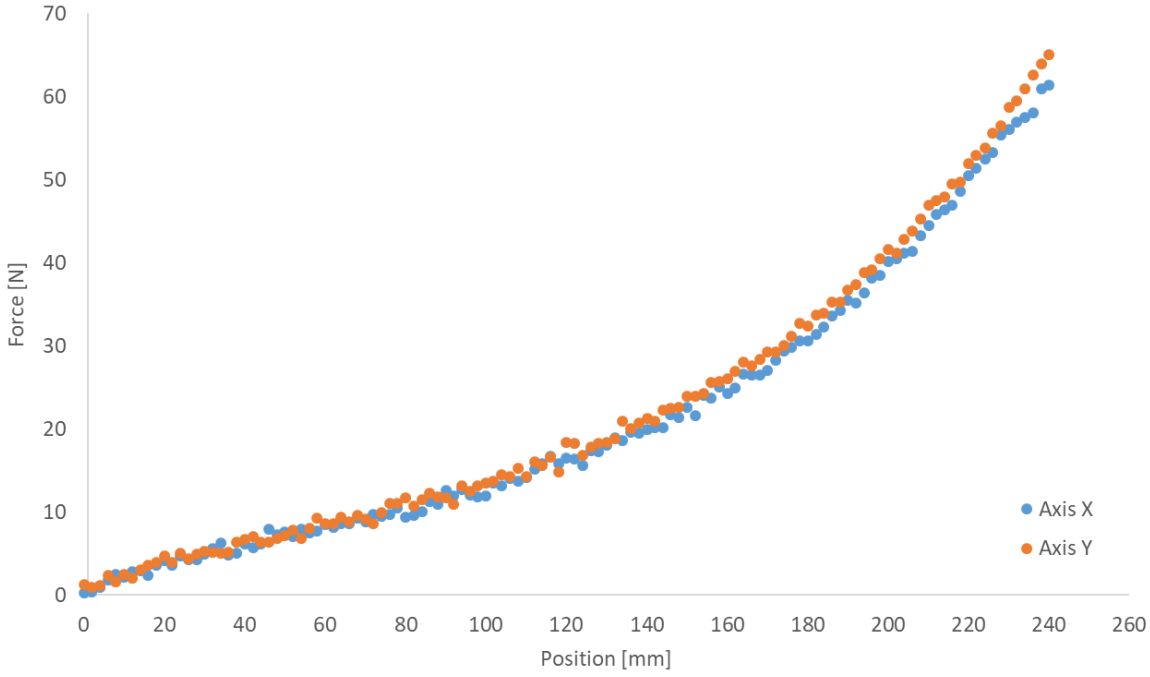

Figure 4-7: Cruciform biaxial stretching captured for sample A.

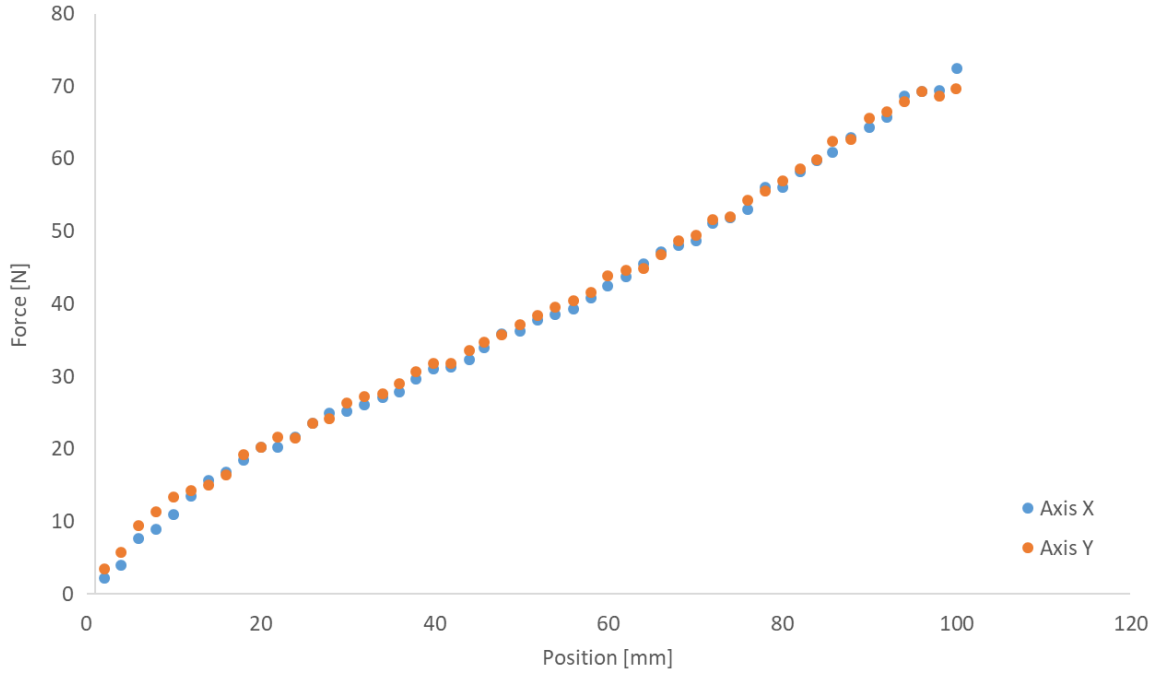

Figure 4-8: Cruciform biaxial stretching captured for sample B.

For the strain measurements two different points related to “x” and “y” axis, were evaluated around the center position. One point was located in the center before loading while the another point passed to be in the center after loading (Figures 4-9 and 4-10 for sample A and B

respectively). The strain response in the both axes over time step can be seen as in Figures 4-11 and 4-12 respectively for A and B samples.

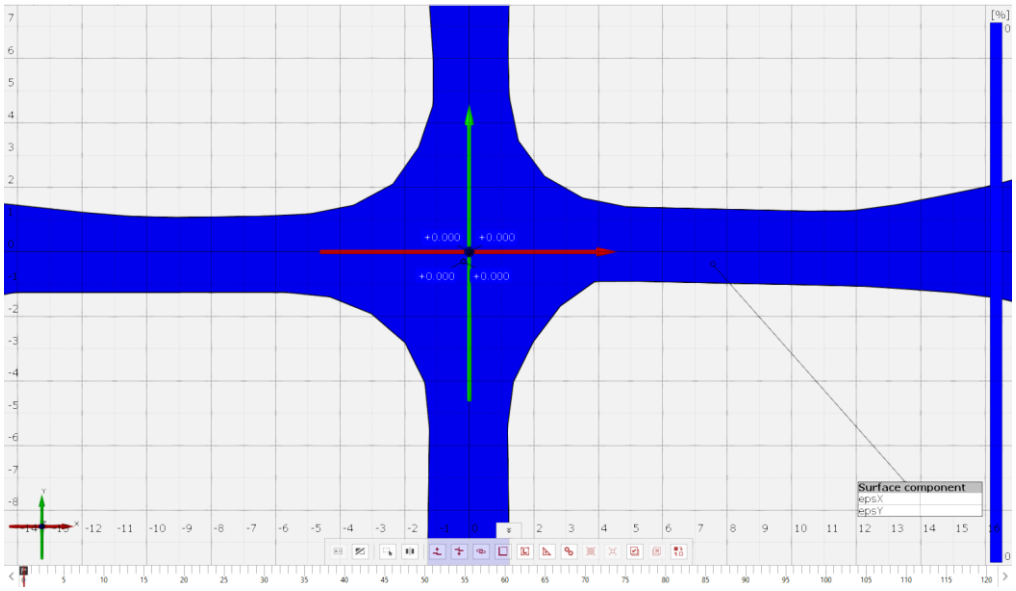

Figure 4-9: Central points for biaxial strain measurements in sample A.

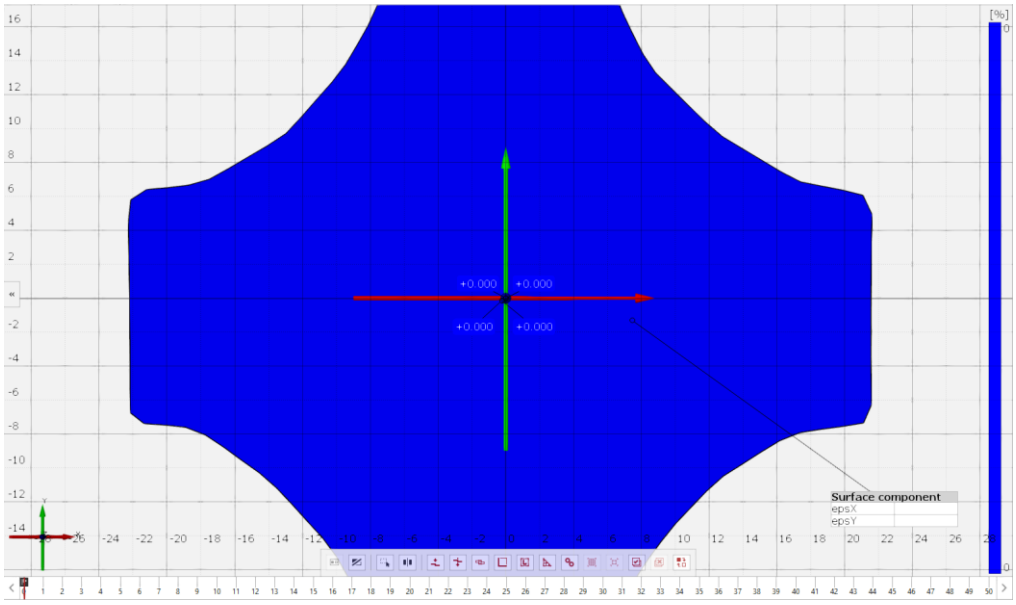

Figure 4-10: Central points for biaxial strain measurements in sample B.

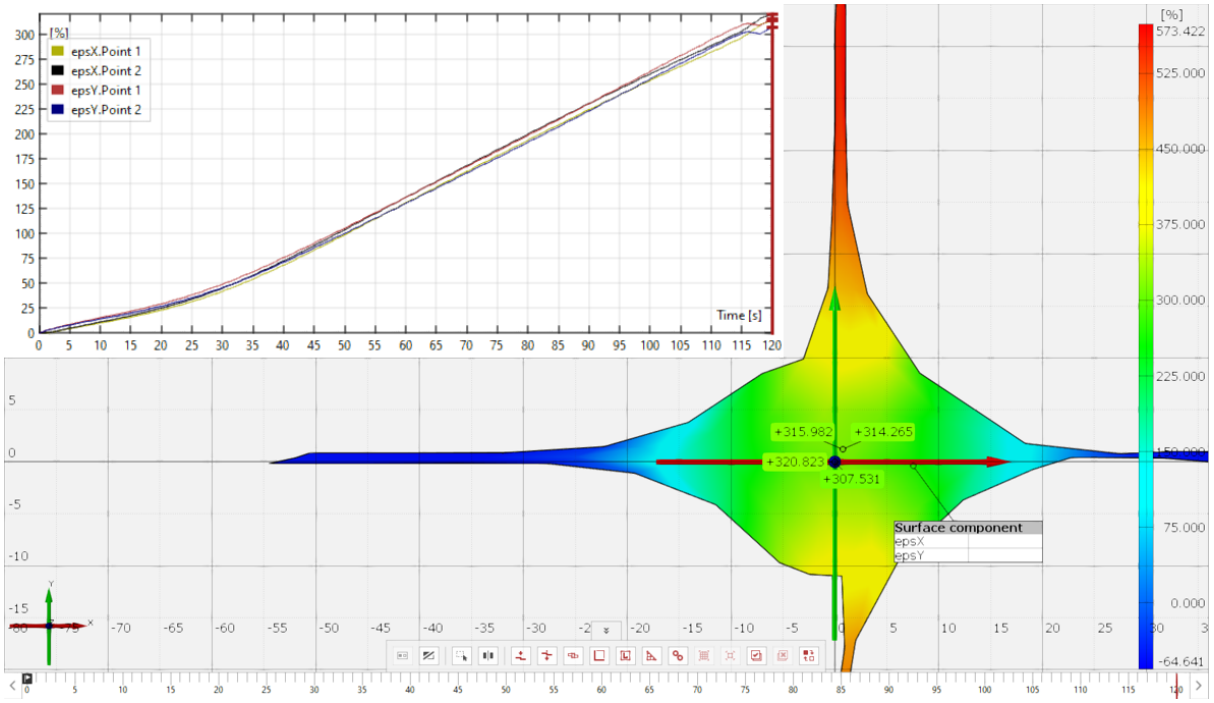

Figure 4-11: Equal biaxial strain response over time step for sample A.

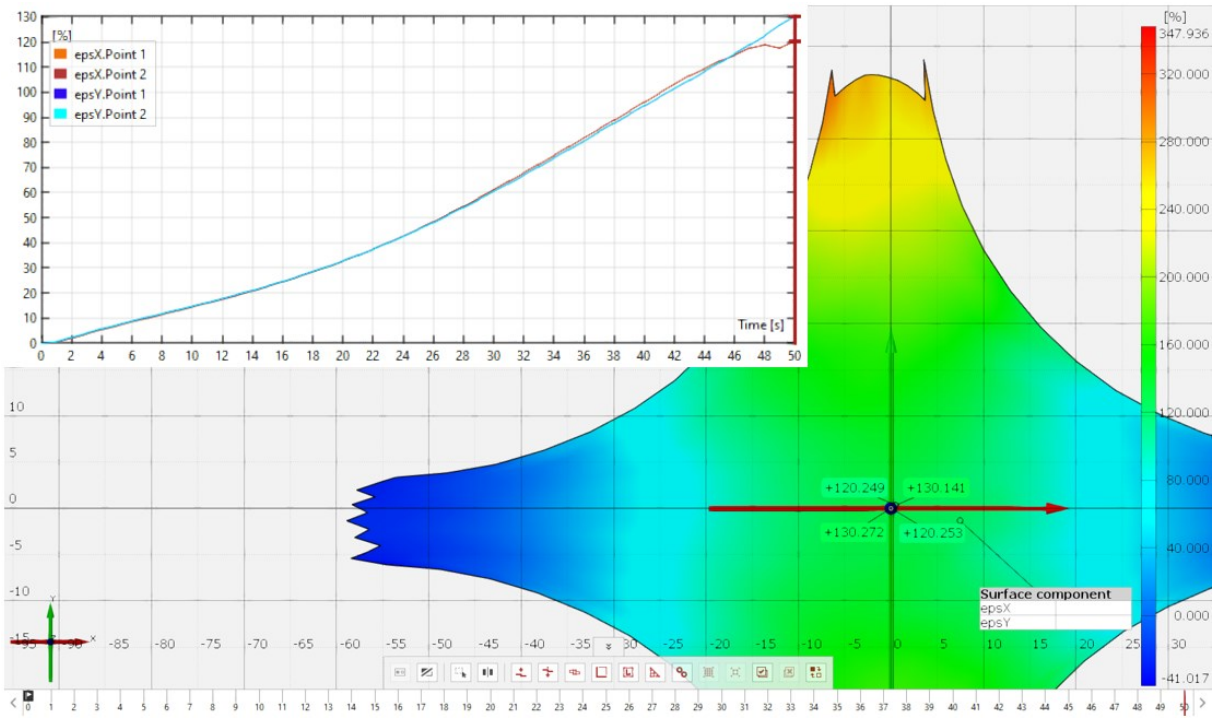

Figure 4-12: Equal biaxial strain response over time step for sample B.

As long as the uniform area around the central zone is unknown, an initial guess should be defined based on Figure 3-27 already described in Methods section (Chapter 3). According to delimited width dimensions and thickness, the initial area could be calculated for both samples as follows:

$$A_0^{sampleA} = 5.2 \,.\, 2.22 = 11.54\, mm^2 \tag{4-1}$$

$$A_0^{sampleB} = 23.6 \,.\, 2.22 = 52.39\, mm^2 \tag{4-2}$$

where A_0 is related to the initial guess area for nominal stress calculation over the experiment.

Providing that extension forces were exactly synchronized with strain measurements from DIC method, the initial nominal stress-strain curve could be constructed for both samples as depicted in Figure 4-13.

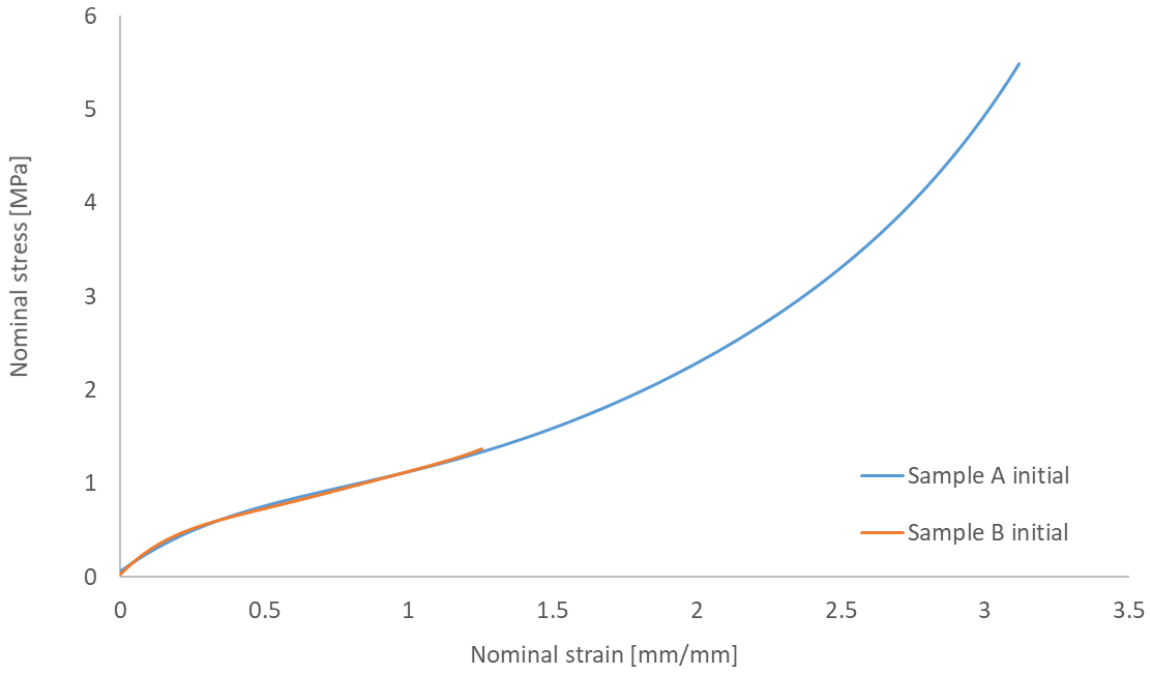

Figure 4-13: Initial stress-strain curve of the equal biaxial extension test in a cruciform device.

The corrected curve can only be obtained after an initial FEA and, for this reason it will be demonstrated in the section 4.3.2.1.

4.1.2.2 Bulge inflation

In order to validate the proposed methodology for the cruciform extension experimental data, a conventional bulge test was performed. First of all, to reach the equal biaxial nominal stress-strain curve some geometric variations were taken into account according to a sample of points distributed inside a radius of 6mm.

As already explained in section 3.1.3.2, the principal Cauchy stresses can be obtained from thin-walled spherical pressure vessel theory, where it is dependent on sheet curvature radius (R). From this assumption, two different initial values of rubber sheet width (a) were set as a reference to compare and validate final results, since the curvature radius should remain the same regardless its reference point around the dome. The sheet changes were extracted according to pressure increase as plotted in Figure 4-14, for an average points around $a = 3mm$ and $a = 6mm$.

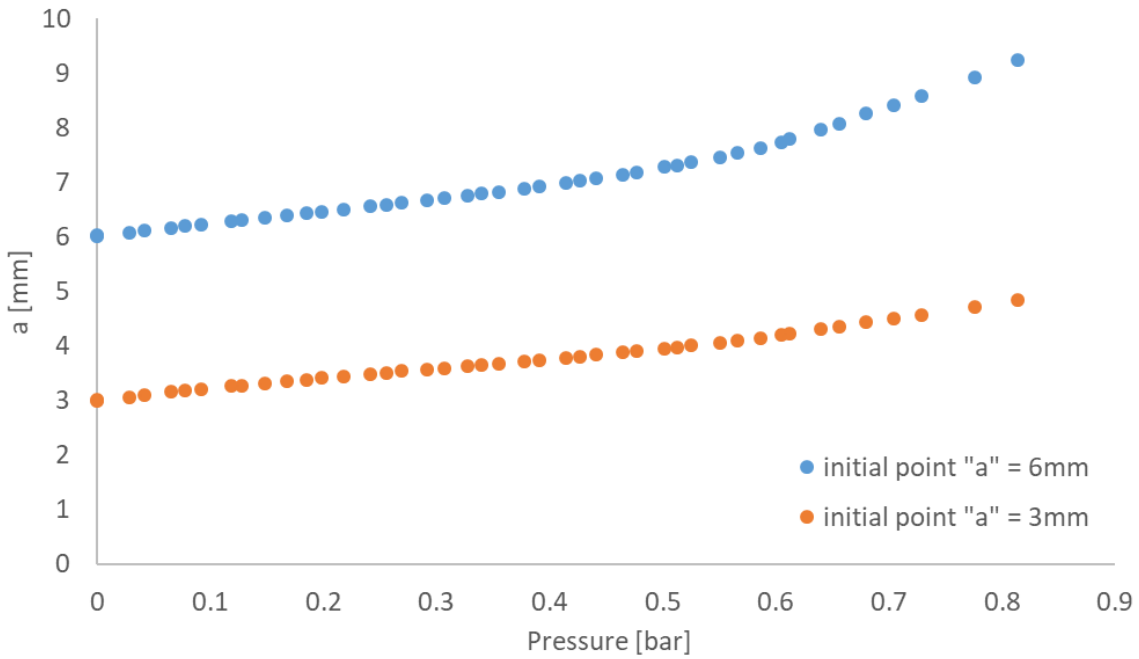

Figure 4-14: Bulge test sheet width over pressure increase.

From sheet points, it is possible to define the deflection height (δ) according to equation (4-3), where the evolution of Z_{max} and Z_{point} is presented according to Figure 4-15.

$$\delta = Z_{max} - Z_{point} \tag{4-3}$$

where Z_{max} is the deflection apex around the dome and Z_{point} is the reference deflection related to the point a of the rubber sheet.

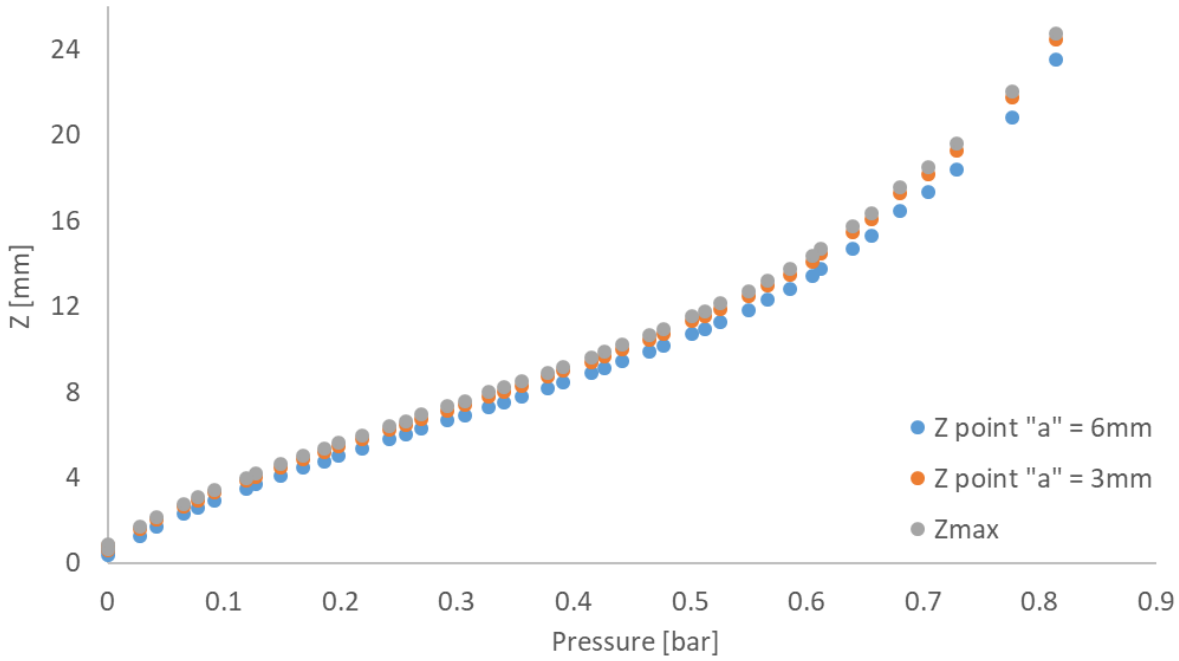

Figure 4-15: Bulge test reference deflections over pressure increase.

Finally, based on the relationship between δ and a, the curvature radius could be obtained synchronized with pressure (Figure 4-16) from equation (3-3) derived in section 3.1.3.2.

The measurements of strain state were directly extracted from dome according to calibrated 3D cameras which capture synchronized images with pressure. Based on DIC method, the principal strain values were obtained from VIC-3D software, where the last step able to give accurate results due to pattern damage is depicted in Figures 4-17 and 4-18 for ε_1 and ε_2 respectively. It is very important to note that the component surface around the dome is in a perfect shape for both images.

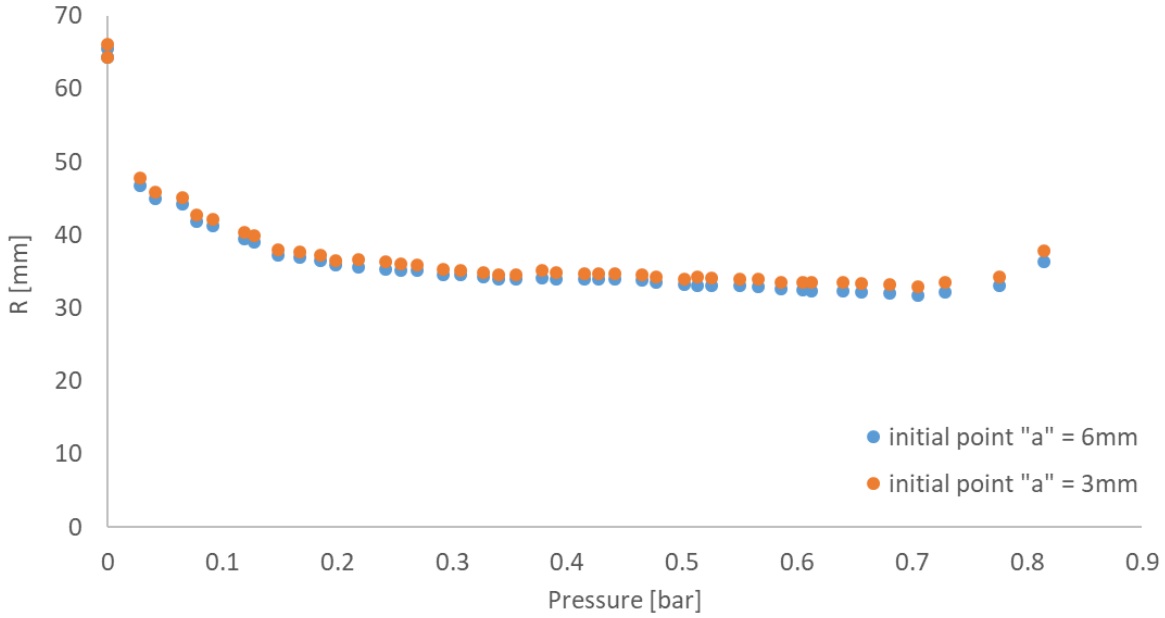

Figure 4-16: Bulge test curvature radius over pressure increase.

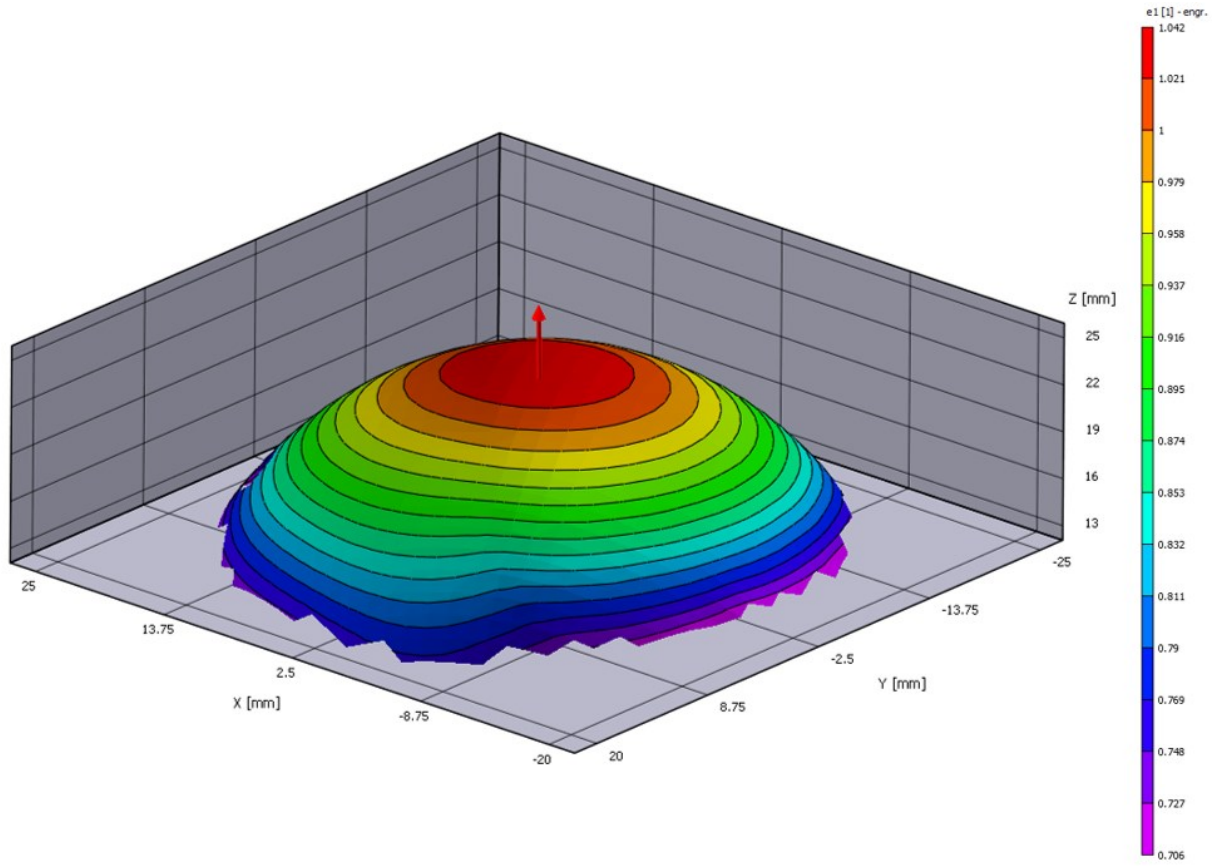

Figure 4-17: Bulge test nominal principal strain ε_1 in the last step.

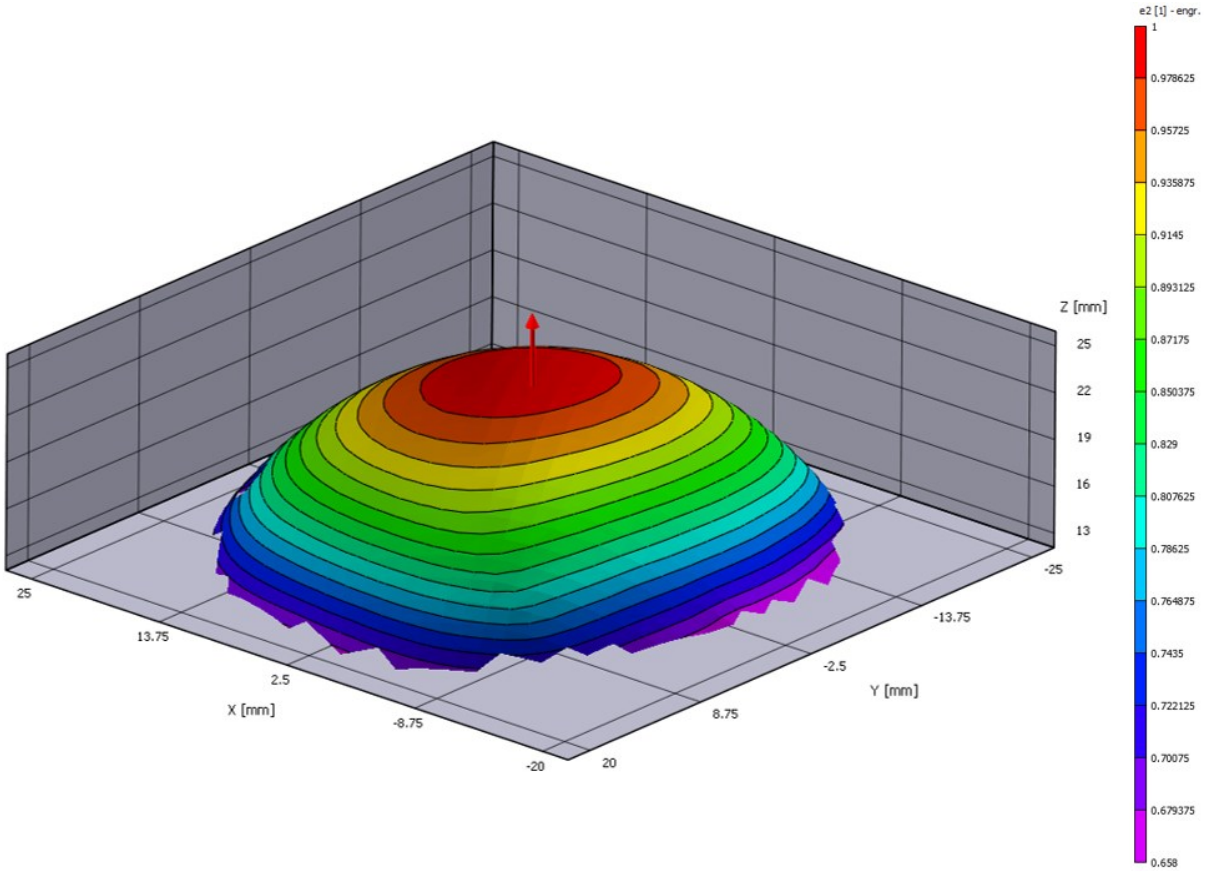

Figure 4-18: Bulge test nominal principal strain ε_2 in the last step.

Since nominal strains were defined by DIC technique, it was possible to calculate the stretch along thickness direction (λ_3) as presented in Figure 4-19. Because of the specimen geometry, Cauchy stresses could be assumed according to equation (3-2) derived in section 3.1.3.2, and then nominal stress can finally be obtained as follows:

$$\lambda_3 = \frac{1}{(1+\varepsilon_L)^2} \tag{4-4}$$

$$\varepsilon_L = ln(1+\varepsilon_N) \tag{4-5}$$

$$\sigma_N = \frac{\sigma_L}{1+\varepsilon_N} \tag{4-6}$$

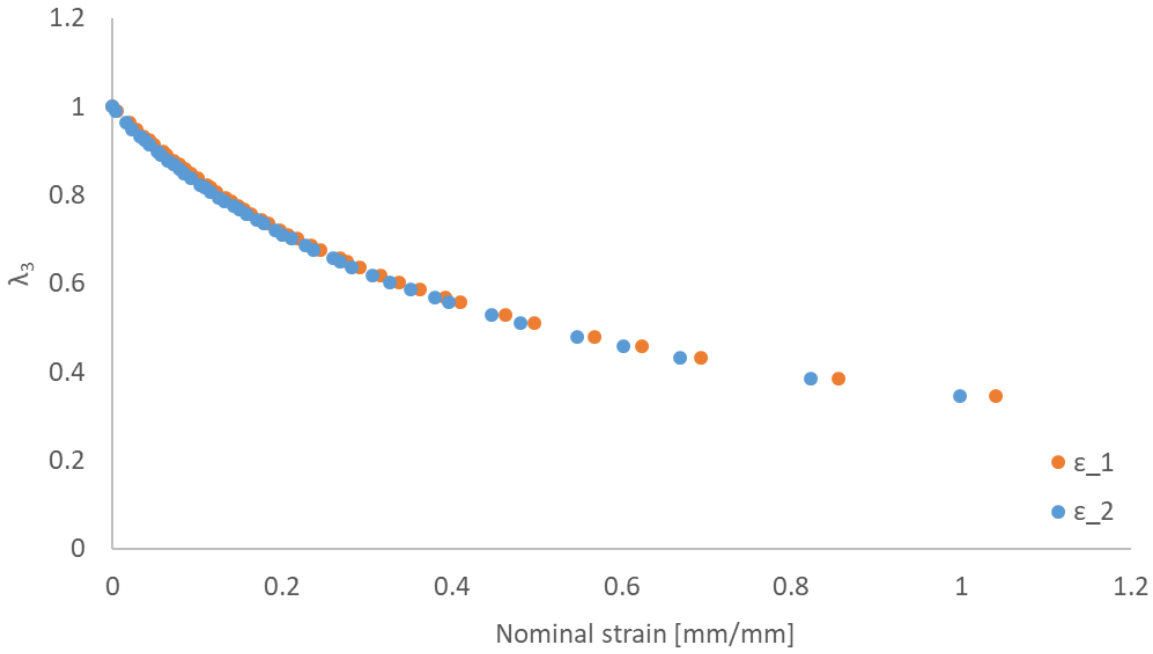

Figure 4-19: Bulge test thickness stretch over nominal strains

Lastly, the nominal stress-strain curve from bulge test experimental data could be raised according to Figure 4-20, and it will be compared to corrected curves from cruciform stretching in section 4.3.2.1.

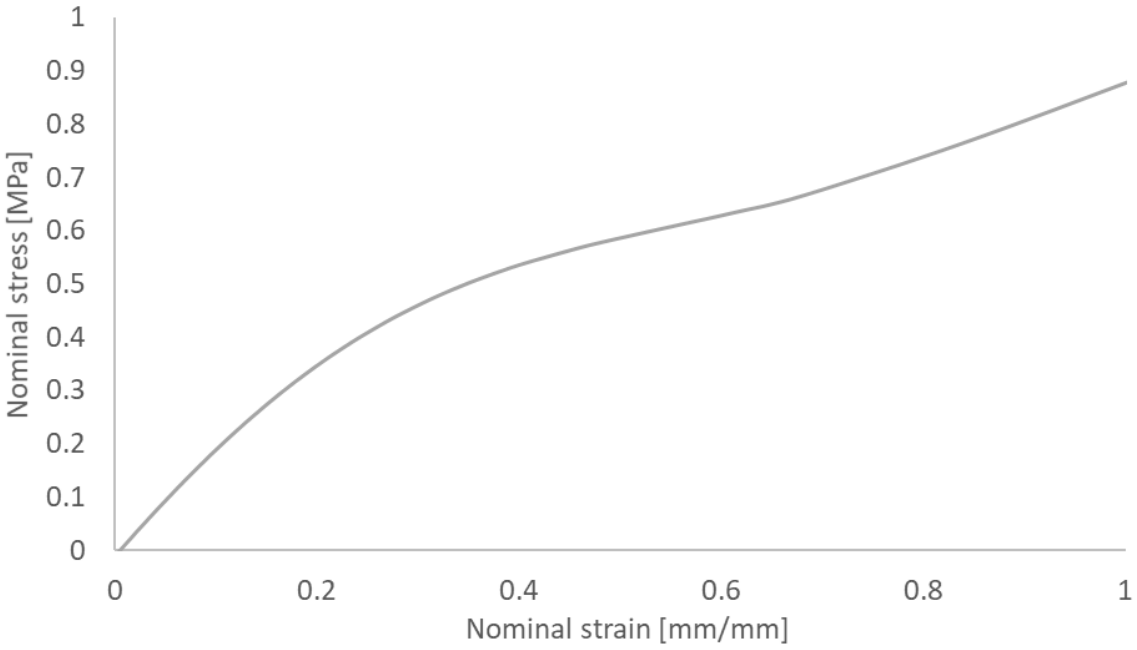

Figure 4-20: Bulge test equal biaxial stress-strain curve

4.1.3 Simple compression

This is a very simple experiment where normal stresses are applied to the specimen surface. The compression behavior would be required for formulating rubber-like material models but data from this test do not represent pure states of strain due to friction between machine plates and rubber surface. As a comparison and validation of this assumption for the material studied, some experimental tests were performed on oily and rough surfaces according to the explanation provided in section 3.1.4.

As already expected, the compression stiffness for rough surface is much higher than the oily one, where the entire curve can be evaluated based on Figure 4-21.

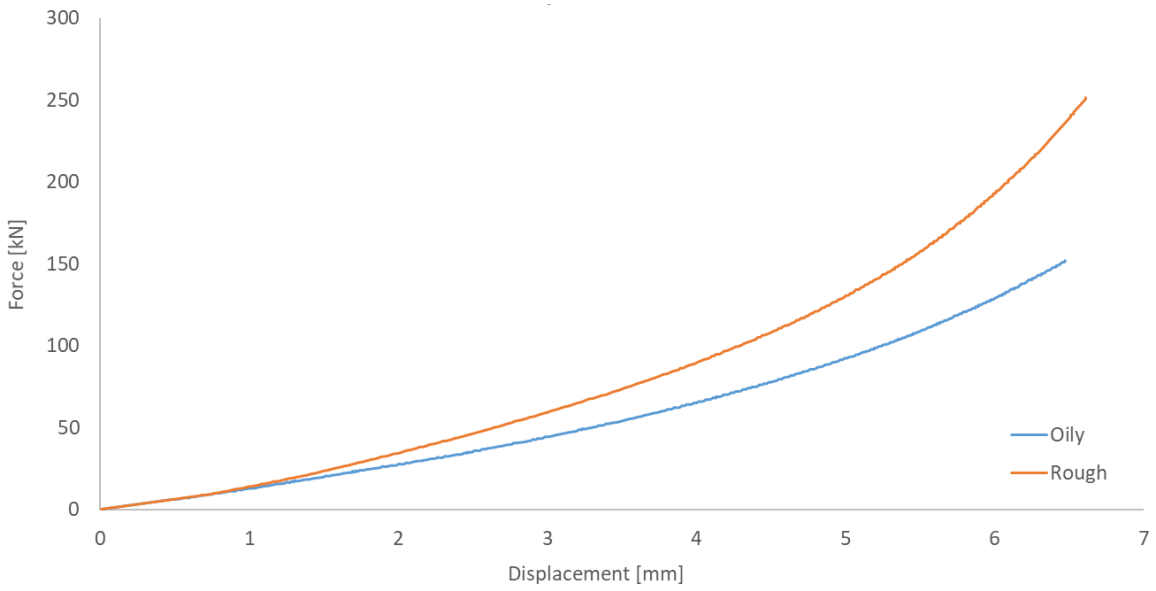

Figure 4-21: Rubber compression stiffness in oily and rough surfaces

Since elastomers behave very differently in compression than in tension, a combination of the whole curve was carried out, taking into account the positive part from tensile test already presented in section 4.1.1 combined with stress-strain curves obtained from compression tests, according to Figure 4-22. The difference between responses of oily and rough conditions occurs due to friction effects that cannot be measured.

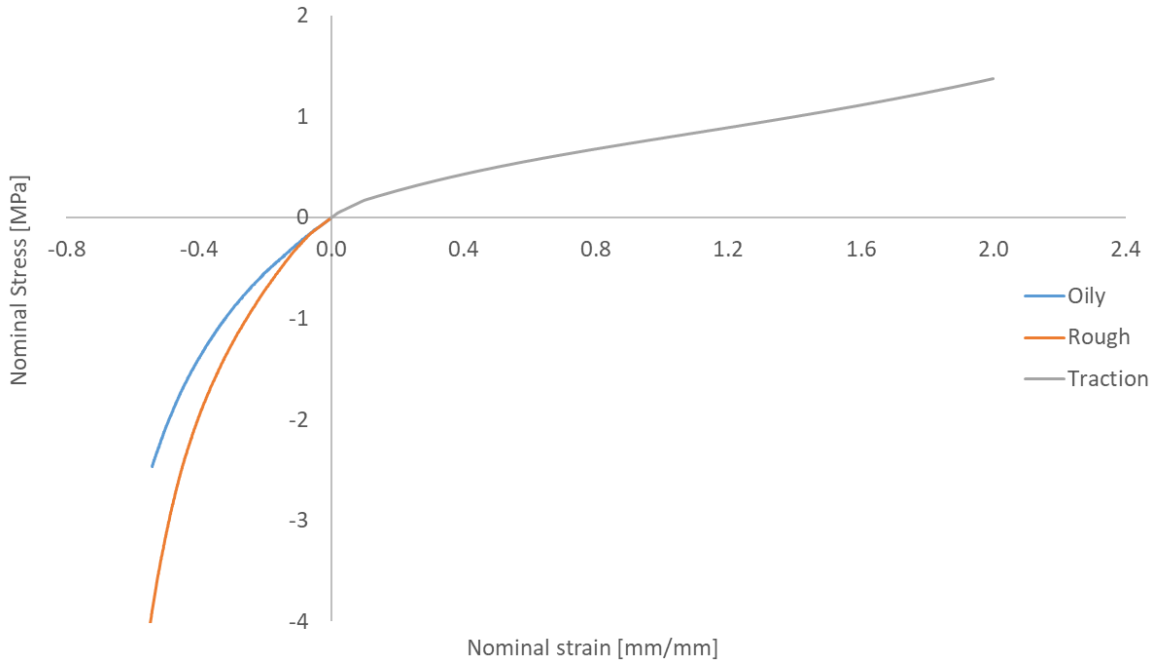

Figure 4-22: Stress-strain curves for uniaxial traction and compression tests.

As far as compression behavior is concerned, it is possible to state that it is equivalent to equibiaxial response because the free surfaces come together when an elastomer is radially strained in all directions of a single plane. Thus, biaxial strains and stresses can be rewritten in terms of compression responses as follows:

$$\varepsilon_b = \sqrt{\frac{1}{\varepsilon_c + 1}} - 1 \tag{4-7}$$

$$\sigma_b = \frac{\sigma_c}{(1 + \varepsilon_b)^3} \tag{4-8}$$

where the subscripts b and c is related to biaxial and compression responses respectively.

Analyzing the biaxial curve obtained from bulge test together with the compression converted curves in Figure 4-23, it is possible to understand that the effects of friction significantly affect the measured stiffness even in an oily surface. This is a problem because friction values for elastomers are related to a function of normal force and cannot be well characterized.

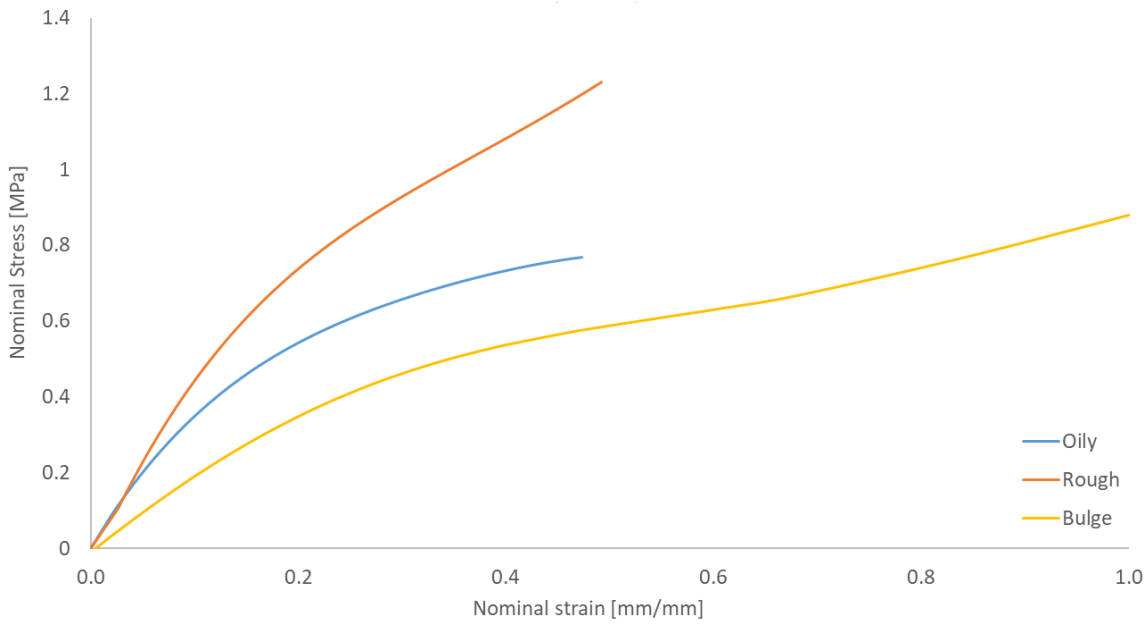

Figure 4-23: Comparative of biaxial responses through compression tests

4.2 Data fitting procedure for hyperelastic models

In order to obtain the material constants for a model, data fitting procedures should be performed according to experimental test data. Due to easiness of execution and processing data only uniaxial extension set is usually used, what leads to inaccurate results. To initially analyze the shortcoming of this usual approach a detailed examination was conducted in the main classical constitutive models. In this situation, data fitting routines were run into the commercial software Abaqus® for uniaxial and biaxial data obtained from cruciform extension and bulge test.

For the tensile test (uniaxial extension) only three out of seven models showed to be stable for all strain ranges, including: Neo-Hooke, Yeoh and Arruda-Boyce. The uniaxial data and theoretical fitted curves are shown in Figure 4-24 and the other deformation modes obtained through this adjustment can be seen in Figure 4-25 for planar shear and Figure 4-26 for biaxial extension.

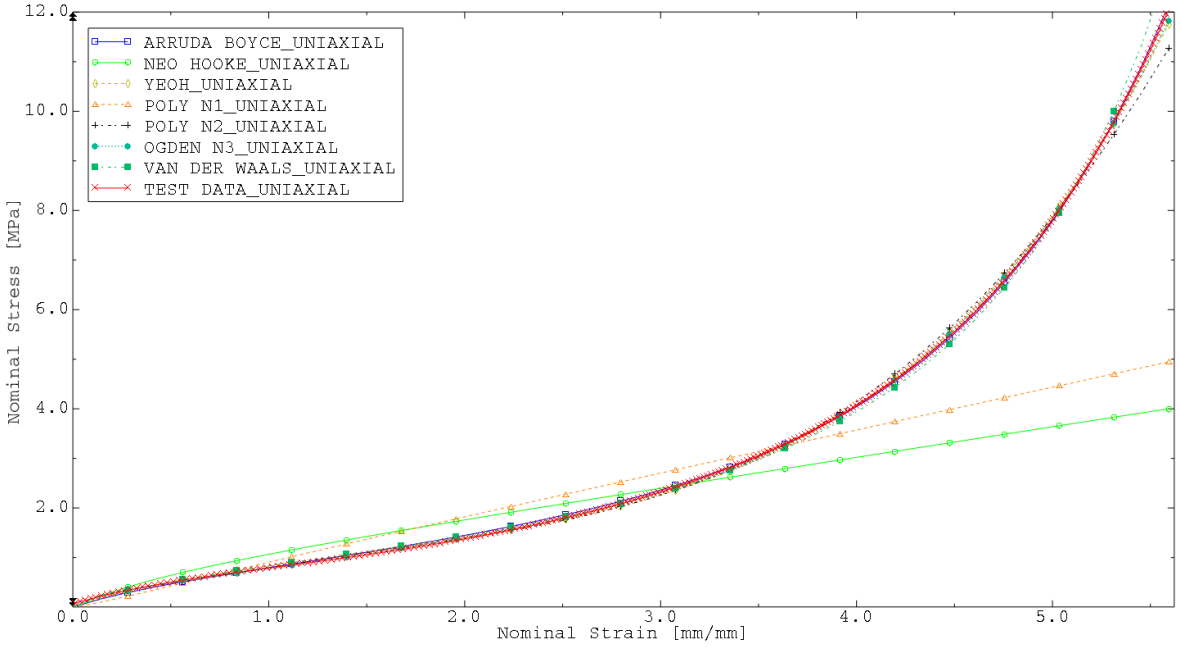

Figure 4-24: Nominal stress-strain curves adjusted using uniaxial data.

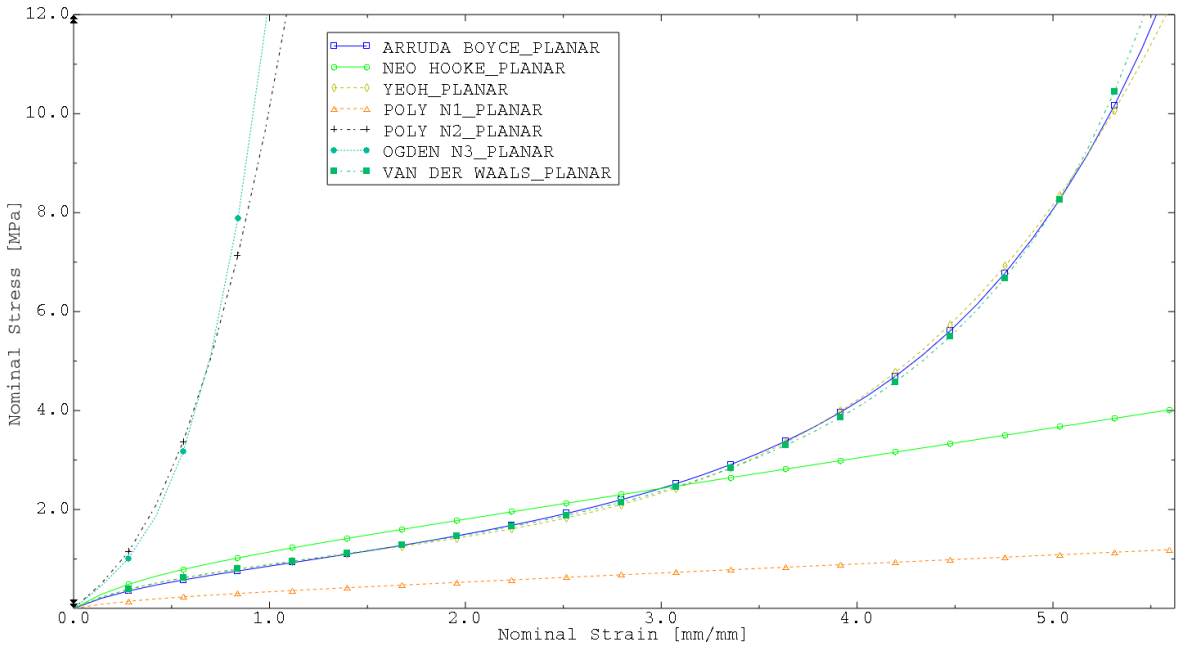

Figure 4-25: Planar shear nominal stress-strain curves obtained from uniaxial data fitting constants

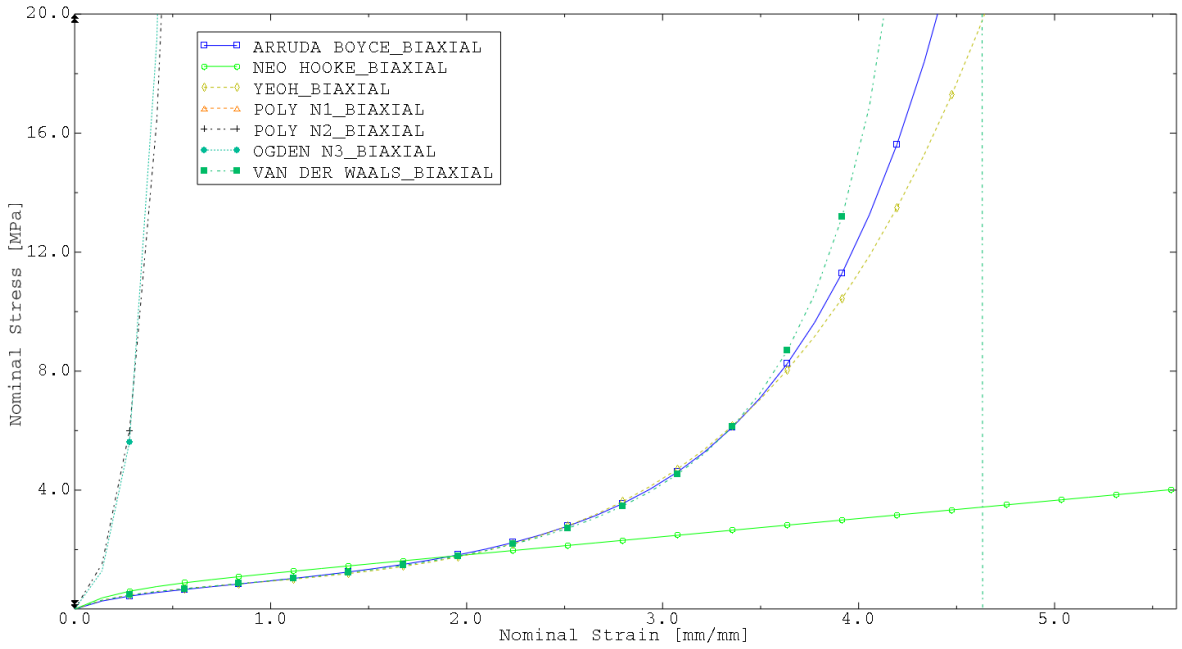

Figure 4-26: Biaxial nominal stress-strain curves obtained from uniaxial data fitting constants

The material coefficients predicted by the use of only uniaxial data for each constitutive model can also be analyzed by Table 4-1. Then, from the presented curves in Figure 4-24, it is possible to note that the uniaxial data could present a suitable adjustment only by higher order phenomenological constitutive models and micromechanics. The lower order models, such as Mooney-Rivlin (Poly N1) and Neo-Hooke tried to fit the data linearly and for this reason the relative error curves presented in Figure 4-27 had only two minimum points over the strain. Furthermore, these models also presented the highest accumulated relative errors according to Figure 4-28.

Table 4-1: Material models coefficients based on uniaxial extension data fitting

Arruda-Boyce		Yeoh		Mooney-Rivlin		Polynomial N=2		Ogden N=3		van der Waals	
μ	0.417199	C_{10}	0.241022	C_{10}	0.427634	C_{10}	-1.05616	μ_1	-0.20836	μ	0.497754
μ_0	0.438546	C_{20}	-1.40E-03	C_{01}	-3.38E-01	C_{20}	3.44E-02	μ_2	5.22E-03	λ_m	8.111323
λ_L	3.560303	C_{30}	1.54E-04	μ_0	1.80E-01	C_{01}	1.522366	μ_3	1.064307	α	0.265486
		μ_0	4.82E-01		-	C_{11}	-1.92E-01	α_1	3.875555	β	0
Neo-Hooke			-		-	C_{02}	6.52E-01	α_2	5.857766		-
C_{10}	0.304525		-		-	μ_0	9.32E-01	α_3	-6.28211		-
μ_0	6.09E-01		-		-		-	μ_0	0.861162		-

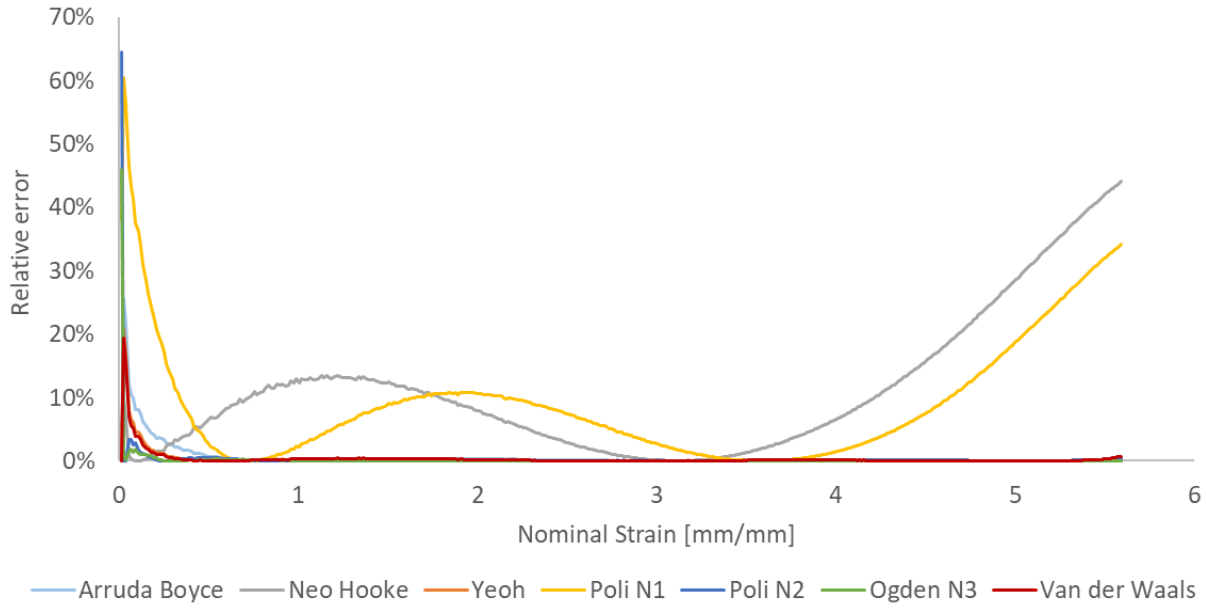

Figure 4-27: Relative errors over strain range for uniaxial data fitting

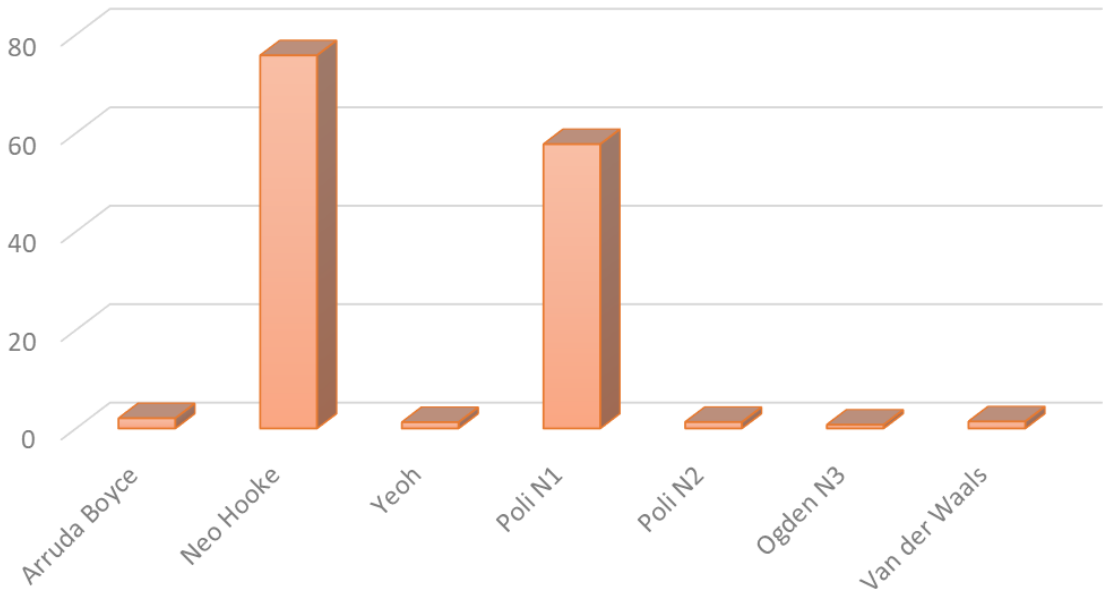

Figure 4-28: Accumulated relative error according to each constitutive model for uniaxial data fitting

Now, the same procedure has been executed for the equal biaxial experiments herein conducted. In the cruciform extension, both samples, A and B, were evaluated and the data fitting results were compared. For sample A four out of seven models showed to be stable for all strain ranges, including: Neo-Hooke, Mooney-Rivlin, Yeoh and Arruda-Boyce, whereas for sample B only three models presented stability, such as: Neo-Hooke, Yeoh and Arruda-Boyce. From Figures 4-29 to 4-34 it is possible to compare the theoretical fitted curves obtained through biaxial test data in sample A and B respectively.

It is worth noting that, because of each sample endured different values of maximum strains, some models like, Neo-Hooke and Mooney-Rivlin could return acceptable representations only for moderate levels of strain (up to approximately 130%) due to their lower order constitutive formulations. Thus, when deformations start to get higher these more simplified models start to lose their accuracy.

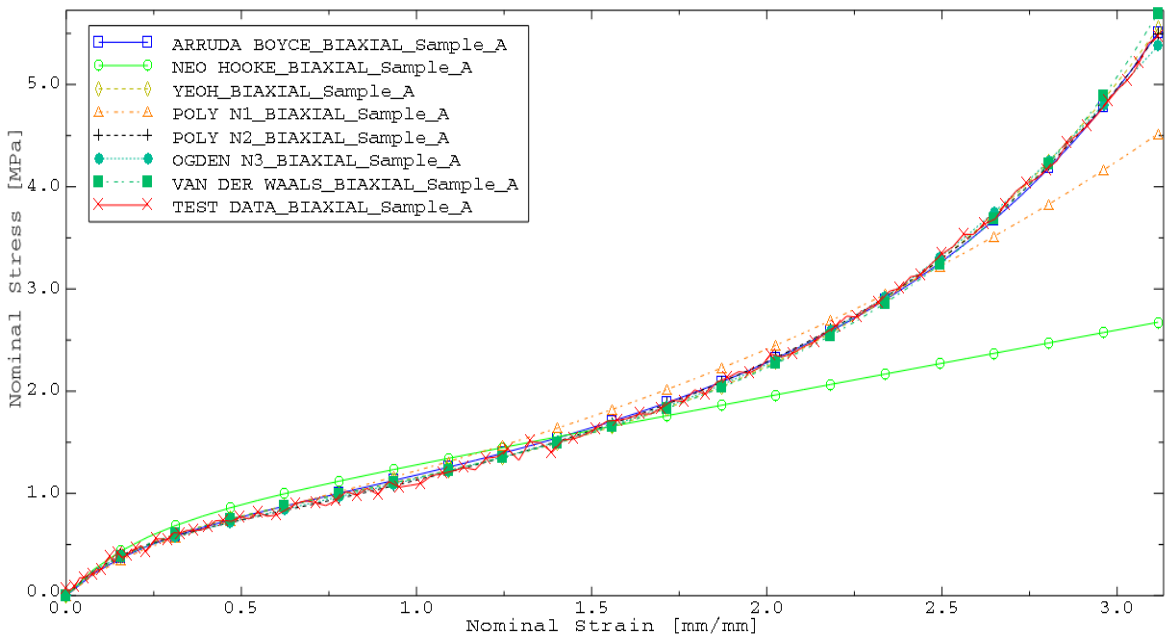

Figure 4-29: Nominal stress-strain curves adjusted using sample A biaxial data.

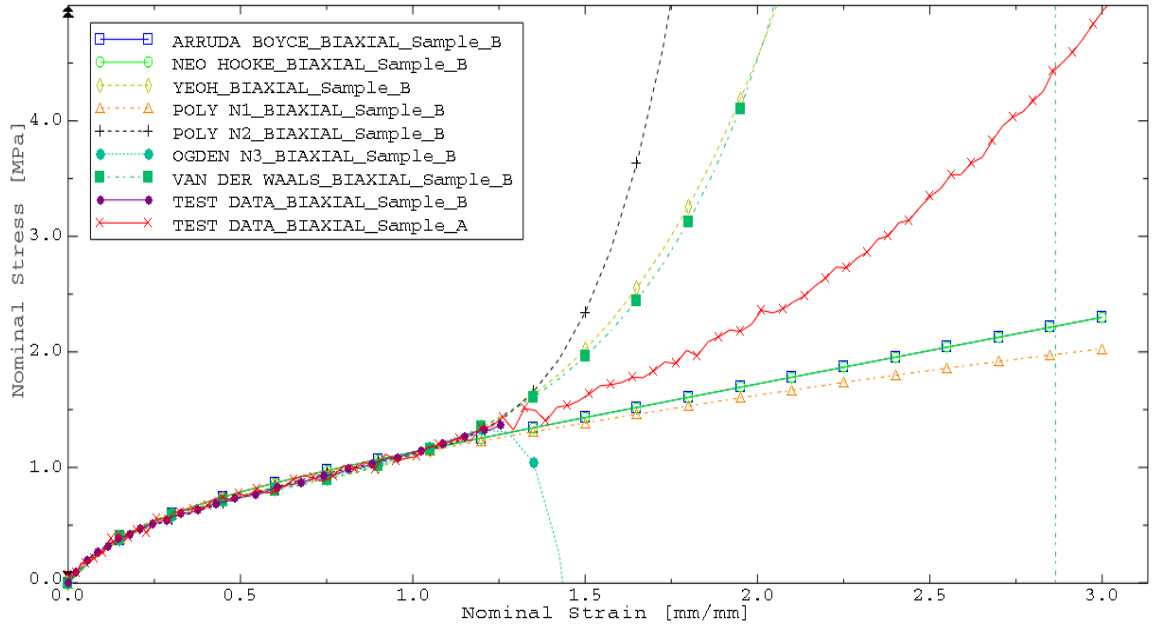

Figure 4-30: Nominal stress-strain curves adjusted using sample B biaxial data.

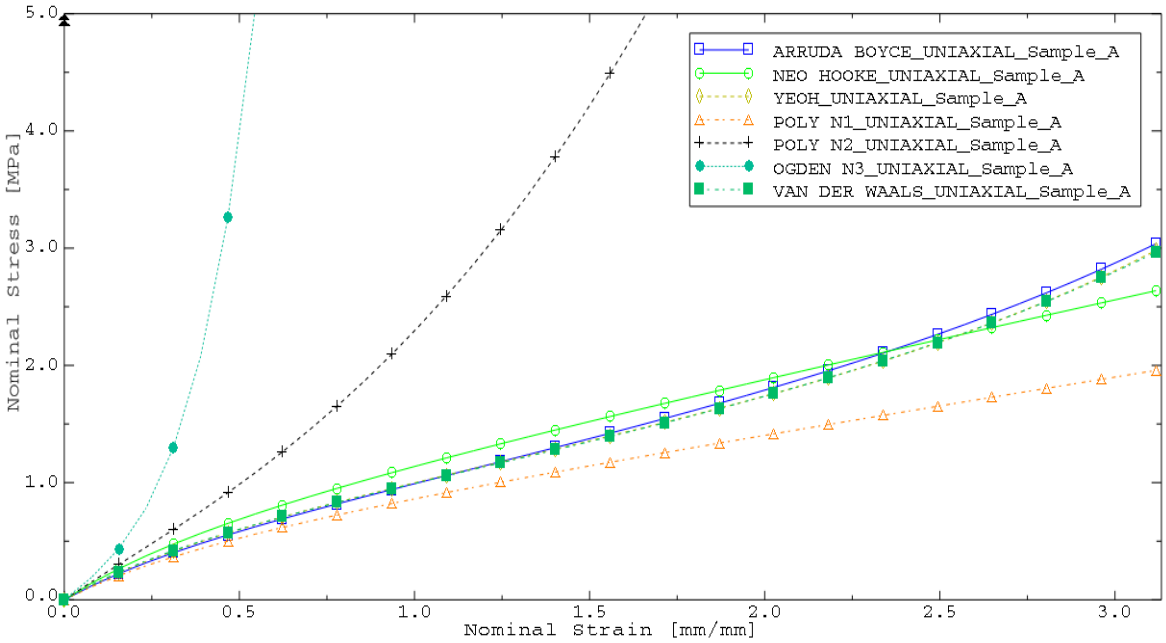

Figure 4-31: Uniaxial nominal stress-strain curves obtained from sample A biaxial data fitting constants.

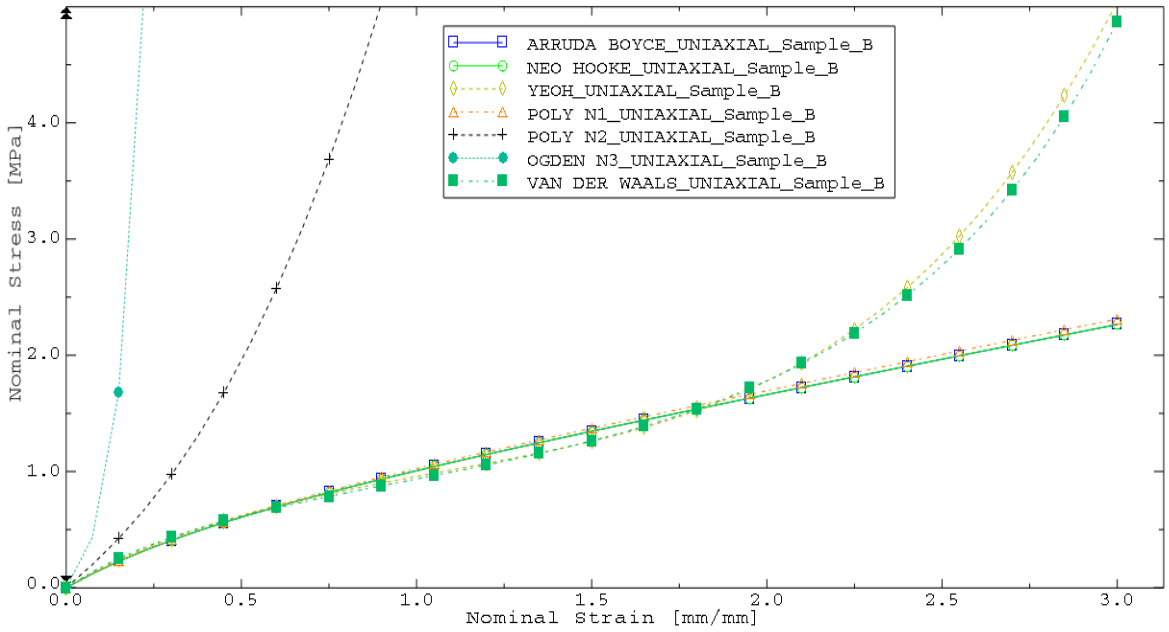

Figure 4-32: Uniaxial nominal stress-strain curves obtained from sample B biaxial data fitting constants.

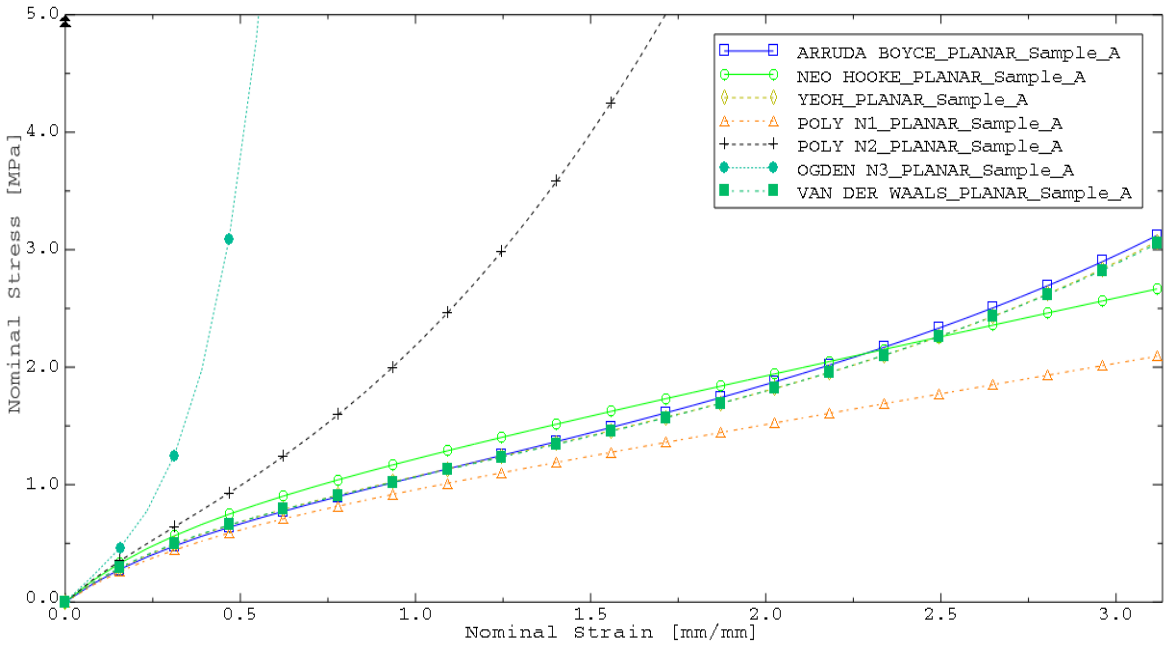

Figure 4-33: Planar shear nominal stress-strain curves obtained from sample A biaxial data fitting constants.

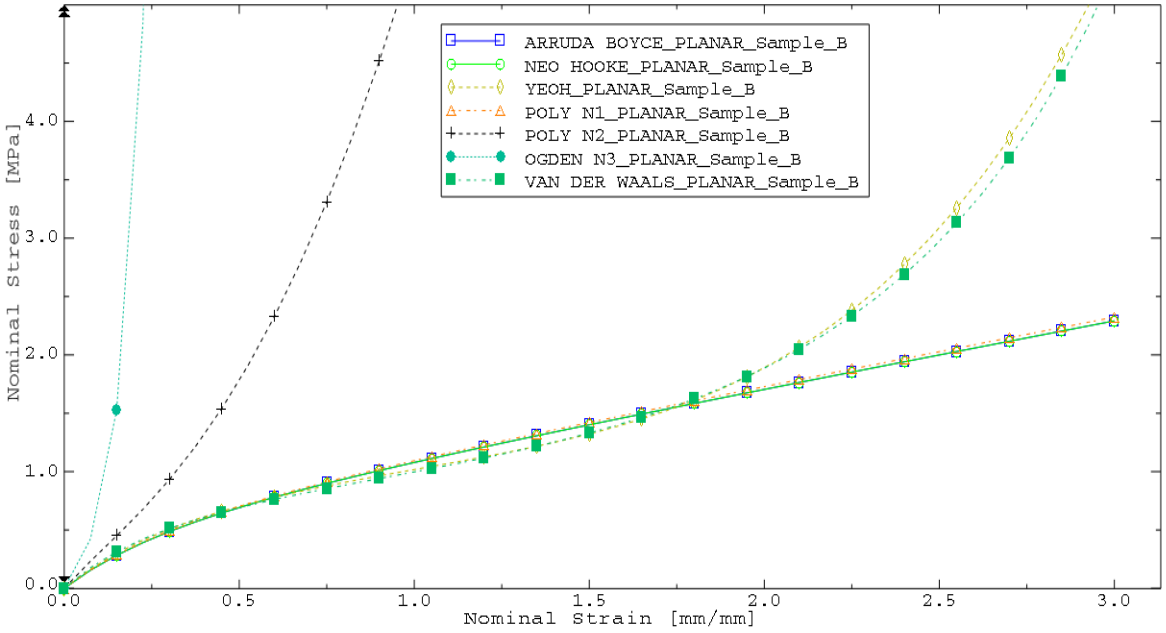

Figure 4-34: Planar shear nominal stress-strain curves obtained from sample B biaxial data fitting constants.

According to Tables 4-2 and 4-3 the material coefficients predicted by the use of biaxial data for each constitutive model can be respectively compared for sample A and sample B.

Table 4-2: Material models coefficients based on sample A biaxial extension data fitting.

Arruda-Boyce		Yeoh		Mooney-Rivlin		Polynomial N=2		Ogden N=3		van der Waals	
μ	0.521822	C_{10}	0.283708	C_{10}	0.236648	C_{10}	0.536051	μ_1	0.531414	μ	0.587275
μ_0	0.546889	C_{20}	-1.07E-04	C_{01}	1.84E-02	C_{20}	5.50E-02	μ_2	0.439485	λ_m	8.11645
λ_L	3.665995	C_{30}	1.39E-04	μ_0	5.10E-01	C_{01}	-0.20065	μ_3	-0.21963	α	0.251463
		μ_0	5.67E-01		-	C_{11}	-2.10E-04	α_1	2.302632	β	0
Neo-Hooke			-		-	C_{02}	3.13E-05	α_2	10.10689		-
C_{10}	0.324915		-		-	μ_0	6.71E-01	α_3	-5.0536		-
μ_0	6.50E-01		-		-		-	μ_0	0.751264		-

Table 4-3: Material models coefficients based on sample B biaxial extension data fitting.

Arruda-Boyce		Yeoh		Mooney-Rivlin		Polynomial N=2		Ogden N=3		van der Waals	
μ	0.575092	C_{10}	0.306922	C_{10}	0.294124	C_{10}	1.098274	μ_1	0.456039	μ	0.676959
μ_0	0.575092	C_{20}	-1.20E-02	C_{01}	-2.55E-03	C_{20}	2.65E-01	μ_2	1.415853	λ_m	5.528815
λ_L	1678.449	C_{30}	1.20E-03	μ_0	5.83E-01	C_{01}	-0.67743	μ_3	-0.70791	α	0.57904
		μ_0	6.14E-01		-	C_{11}	-4.06E-02	α_1	-7.18E-02	β	0
Neo-Hooke			-		-	C_{02}	5.40E-03	α_2	18.51233		-
C_{10}	0.287546		-		-	μ_0	8.42E-01	α_3	-9.25618		-
μ_0	5.75E-01		-		-		-	μ_0	1.163983		-

Although the material curves are similar until their respective strain ranges, some coefficients were quite different depending on the constitutive mode. This happens because the adjustment can only map the experimental curve until its final maximum strain. After this value, the theoretical fitted curves can suffer severe changes when compared with an experimental curve with higher strain values. This effect can be analyzed in Figure 4-30, where theoretical curves from sample B turned out completely different from sample A after its final strain range.

Finally, the relative error over the strain and its accumulated sum were computed for both samples as presented in Figures 4-35 and 4-36 for sample A, and Figures 4-37 and 4-38 for sample B. The Neo-Hooke model presented the worst adjustment, accounting for an accumulated error much larger than other models for sample A (Figure 4-36). On the other hand, for sample B, the accumulated error ended up being equivalent among all the models analyzed (Figure 4-38) ought to the lower strains which were reached by the sample during biaxial stretching.

It is important to point out that, sample B just presented lower values of accumulated relative error compared to sample A because it reached only a 125% of nominal strain, whereas sample A reached approximately 311%. If the same lower strain range had been considered for sample A, it would have presented an accumulated sum of about 1 for the worst fitted constitutive model, that is, almost like sample B values.

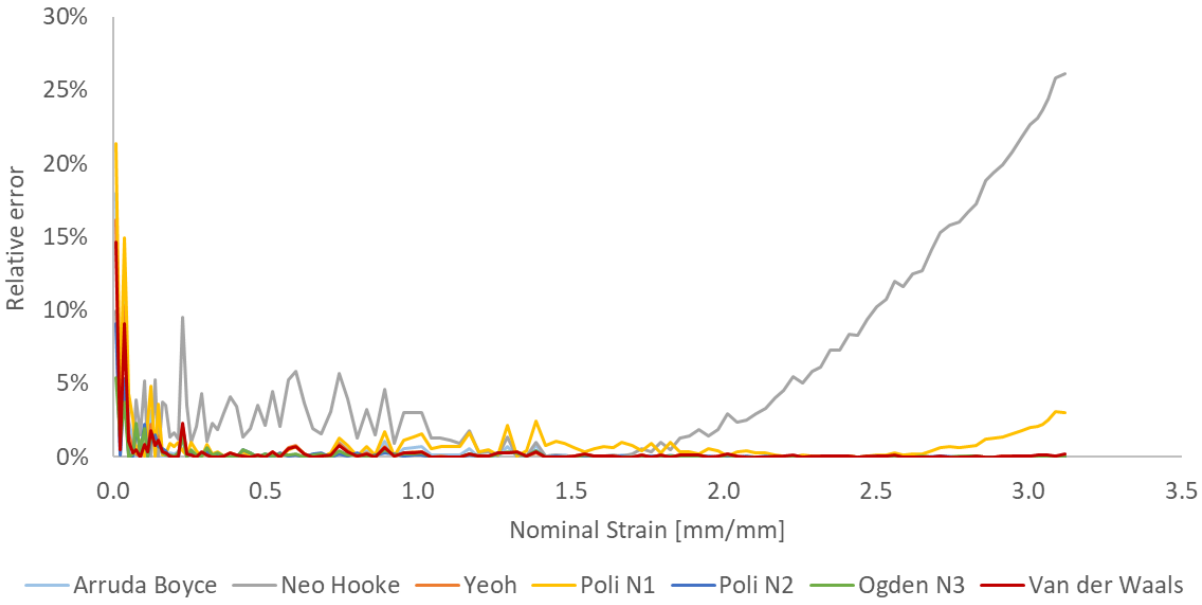

Figure 4-35: Relative errors over strain range for sample A biaxial data fitting.

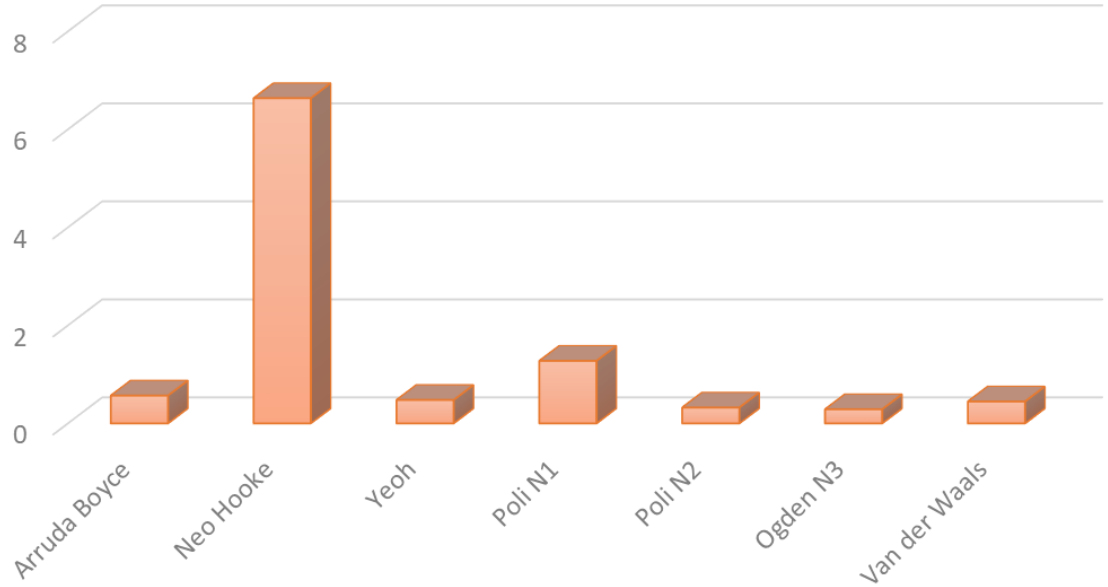

Figure 4-36: Accumulated relative error according to each constitutive model for sample A biaxial data fitting.

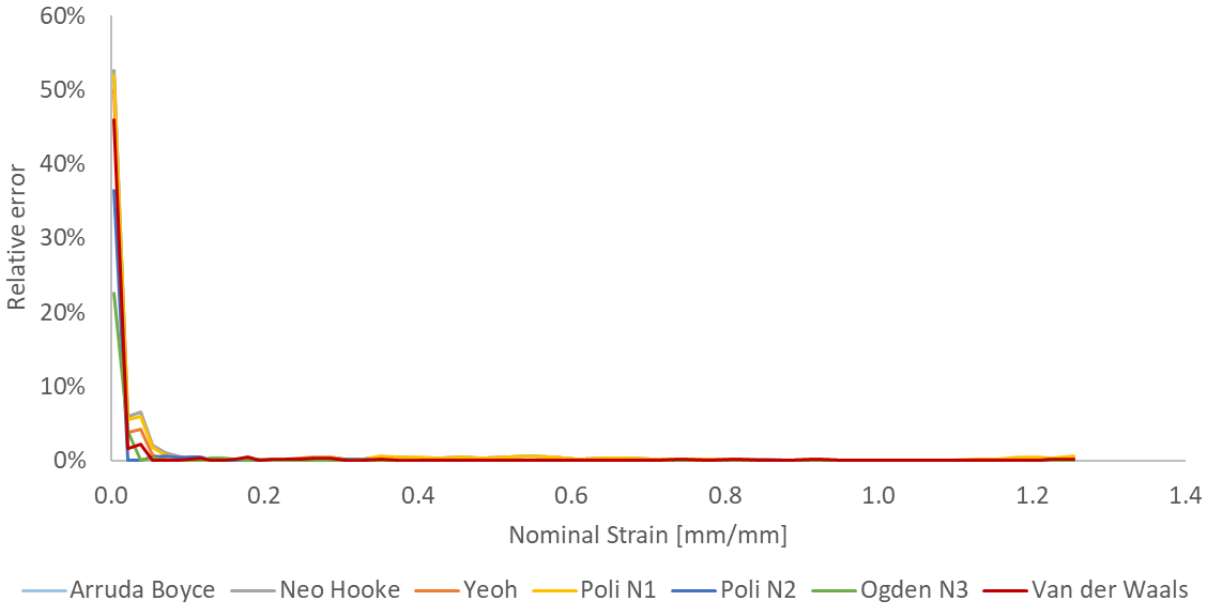

Figure 4-37: Relative errors over strain range for sample B biaxial data fitting.

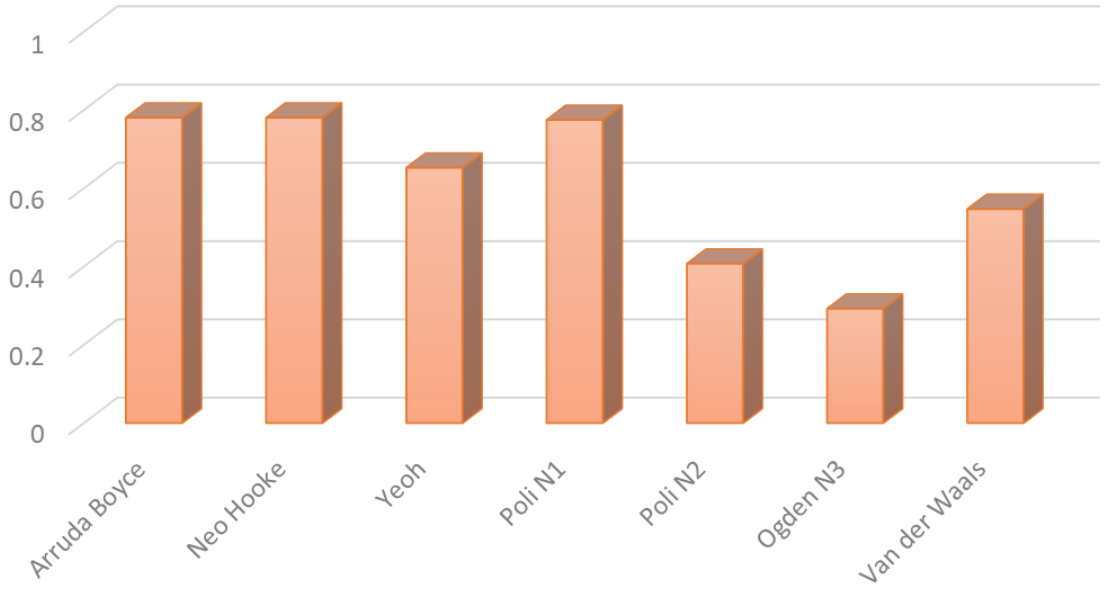

Figure 4-38: Accumulated relative error according to each constitutive model for sample B biaxial data fitting.

As far as equal biaxial behavior is concerned, data fitting routines for bulge test were also carried out. This evaluation becomes important, since corrected curves obtained from FEA in cruciform extension should be compared to bulge test data in order to validate the proposed

methodology for biaxial data treatment. Therefore, the theoretical fitted curves obtained through bulging a circular specimen can be analyzed in Figures 4-39 to 4-41.

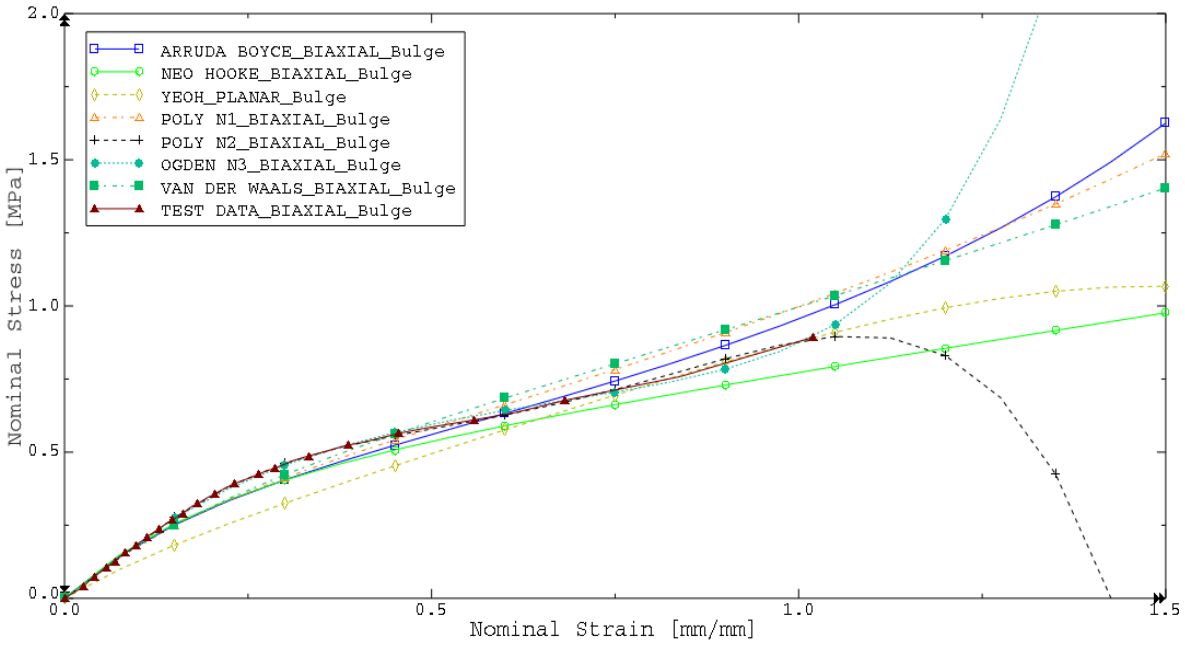

Figure 4-39: Nominal stress-strain curves adjusted using bulge test biaxial data.

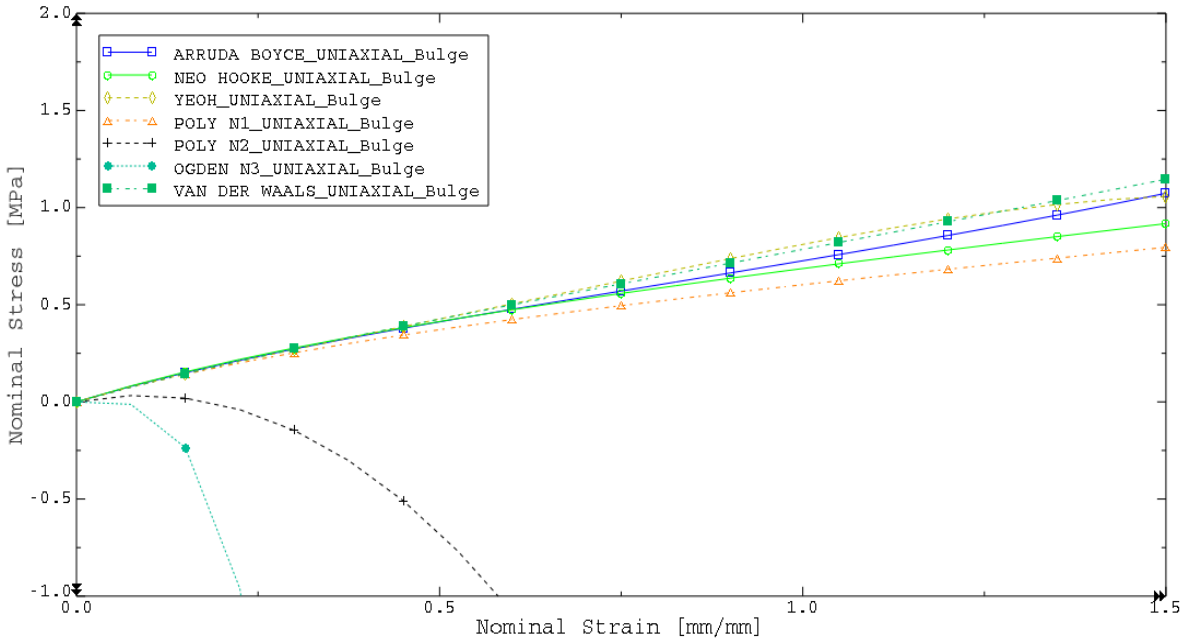

Figure 4-40: Uniaxial nominal stress-strain curves obtained from bulge test biaxial data fitting constants.

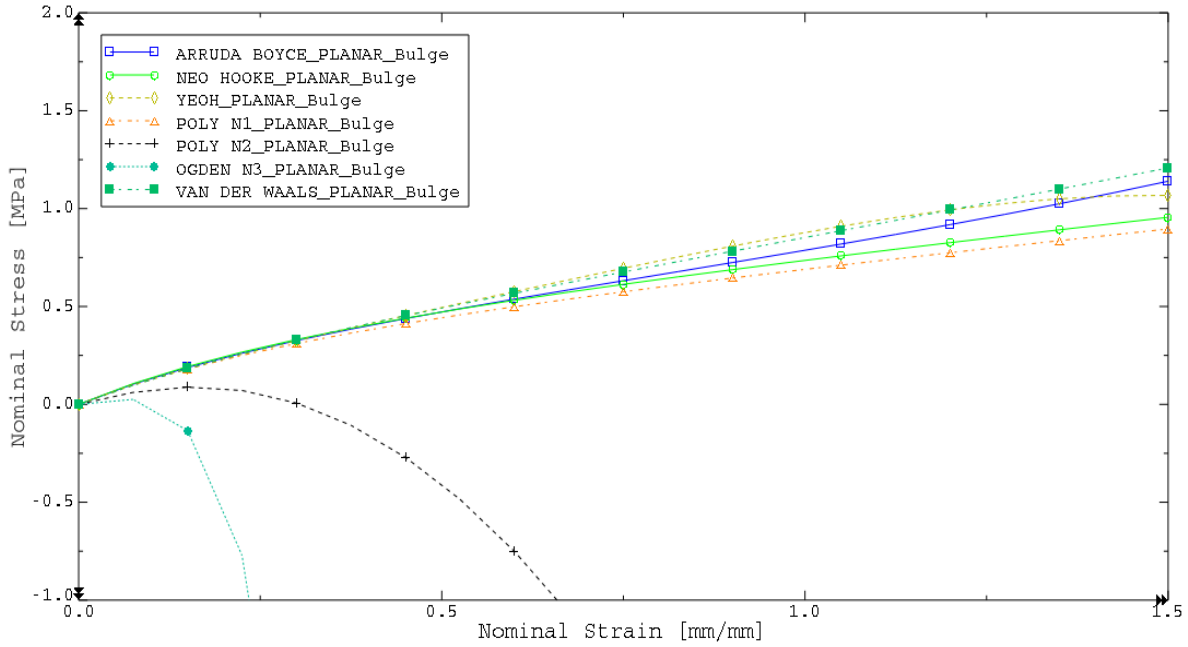

Figure 4-41: Planar shear nominal stress-strain curves obtained from bulge test biaxial data fitting constants.

Then, the material coefficients predicted by the use of only biaxial data obtained from bulge test for each constitutive model can also be analyzed by Table 4-4.

Table 4-4: Material models coefficients based on bulge test biaxial data fitting.

Arruda-Boyce		Yeoh		Mooney-Rivlin		Polynomial N=2		Ogden N=3		van der Waals	
μ	3.44E-01	C_{10}	1.82E-01	C_{10}	1.61E-01	C_{10}	-0.4234	μ_1	0.42062	μ	3.51E-01
μ_0	3.82E-01	C_{20}	1.92E-02	C_{01}	2.32E-02	C_{20}	-2.63E-01	μ_2	-4.49E-01	λ_m	491.3677
λ_L	2.537302	C_{30}	-2.27E-03	μ_0	3.68E-01	C_{01}	0.545549	μ_3	0.224288	α	-2.74E-01
		μ_0	3.64E-01		-	C_{11}	6.14E-02	α_1	9.51E-01	β	0
Neo-Hooke			-		-	C_{02}	-8.80E-03	α_2	16.61512		-
C_{10}	1.96E-01		-		-	μ_0	2.44E-01	α_3	-8.30754		-
μ_0	3.92E-01		-		-		-	μ_0	1.96E-01		-

Because this experiment could not reach high levels of strain (maximum of 102%), the relative error curves plotted in Figure 4-42 presented very similar values. Likewise, this same assumption can also be stated when Figure 4-43 is evaluated for accumulated error.

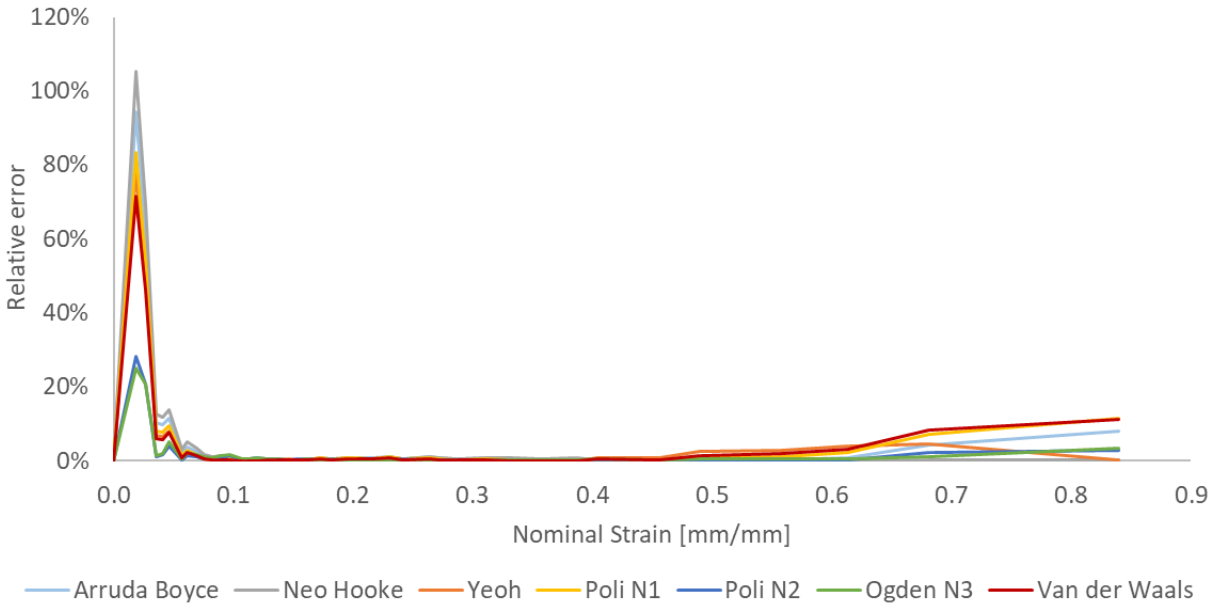

Figure 4-42: Relative errors over strain range for bulge test biaxial data fitting.

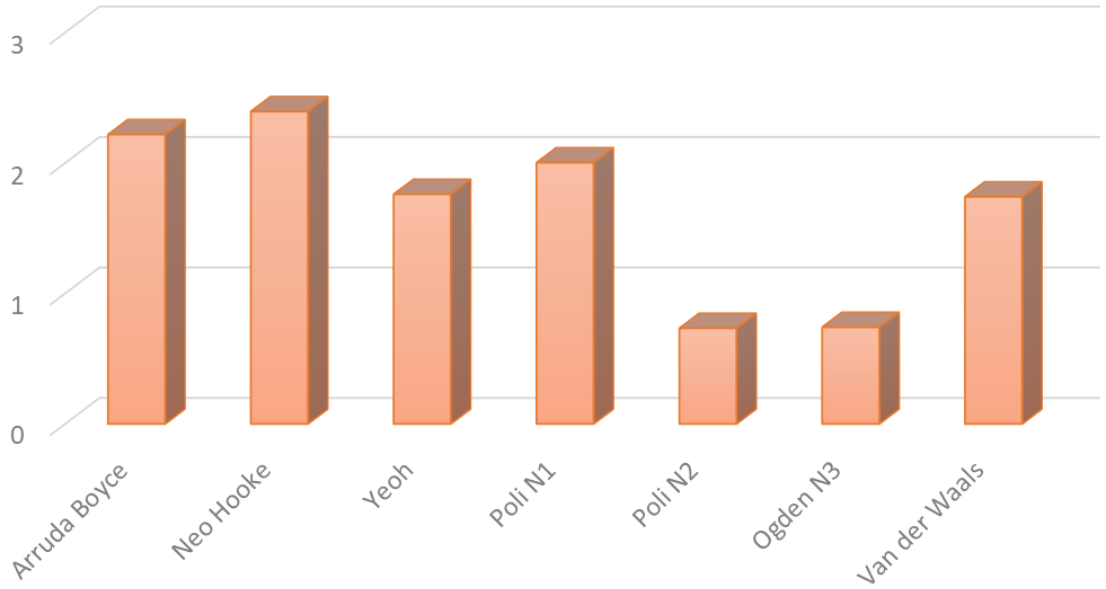

Figure 4-43: Accumulated relative error according to each constitutive model for bulge test biaxial data fitting.

Similarly to other experiments, there were only three out of seven models which showed to be stable for all strain ranges, and they are: Neo Hooke, Mooney-Rivlin and Arruda-Boyce. It is worthwhile to point out that Arruda-Boyce was the only model that presented stability for all experiments herein conducted, whereas Ogden N3, Polynomial N2 and van der Waals could

not be stable for none of the experiments although they presented good solutions regarding data fittings.

4.3 Validation of tests on specimens thorough Finite Element simulation

In order to evaluate the efficiency of the constitutive parameters obtained for the stable models with best data fitting, FE simulations were conducted on uniaxial and biaxial experimental tests according to the geometric shape and boundary conditions. Thus, Arruda-Boyce and Yeoh models were analyzed for uniaxial and cruciform extension, whereas for bulge test only Arruda-Boyce model was tested due to lack of stability in the Yeoh model. In addition, the simple compression experiment was also modeled through FEA and compared to the biaxial data, taking into account the oily and rough compression surfaces.

4.3.1 Uniaxial stretching

In this experiment a dogbone shape was modeled according to the methodology already described in section 3.3.2. The pure mode of uniaxial deformation could be obtained through a force amplitude that was applied to the upper stretching clamp while the lower one got fixed. True strain-stress responses were computed through an average of the values in the central region of the specimen, in such a way that, the maximum principal stresses could be analyzed according to Figure 4-44.

Hence, for a better comparison between experimental and simulated curves, both the forces and the stresses were plotted over the strains as shown in Figures 4-45 and 4-46 respectively. This approach was considered because clamps greatly influence the tensile load and consequently impact the correct strain calculation.

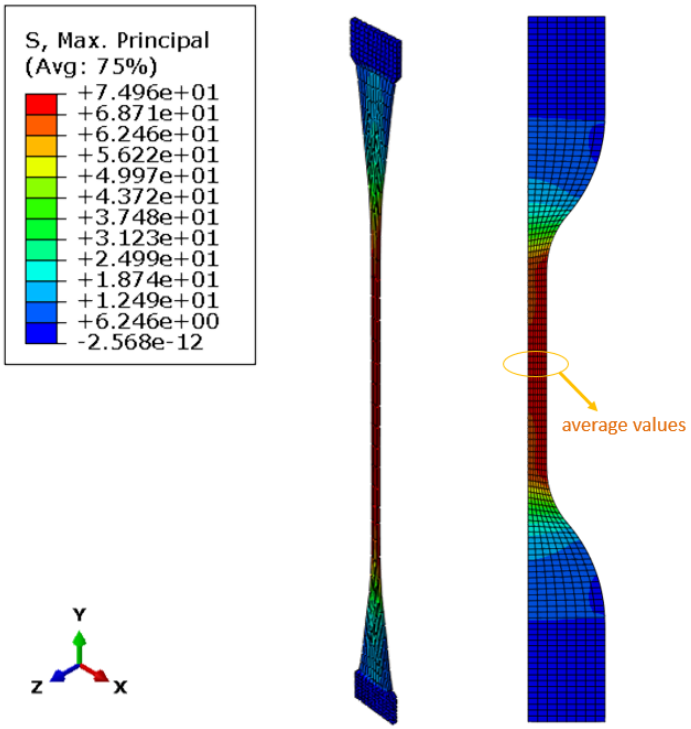

Figure 4-44: Uniaxial true stress distribution in a dogbone shape

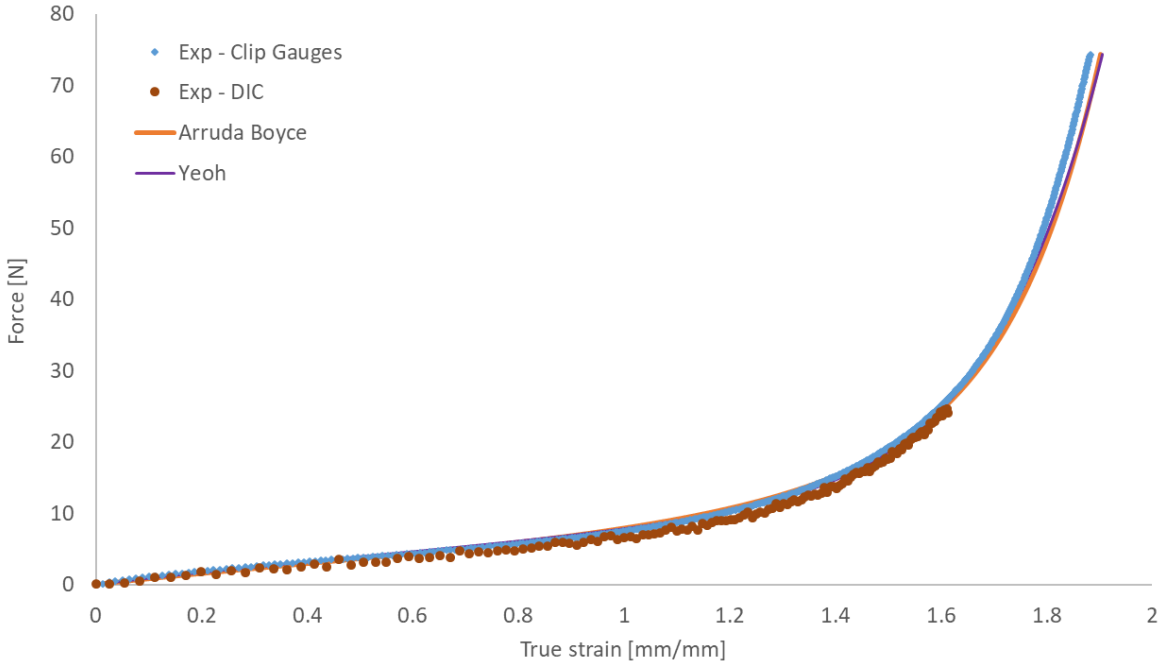

Figure 4-45: Uniaxial forces plotted over simulated true strains.

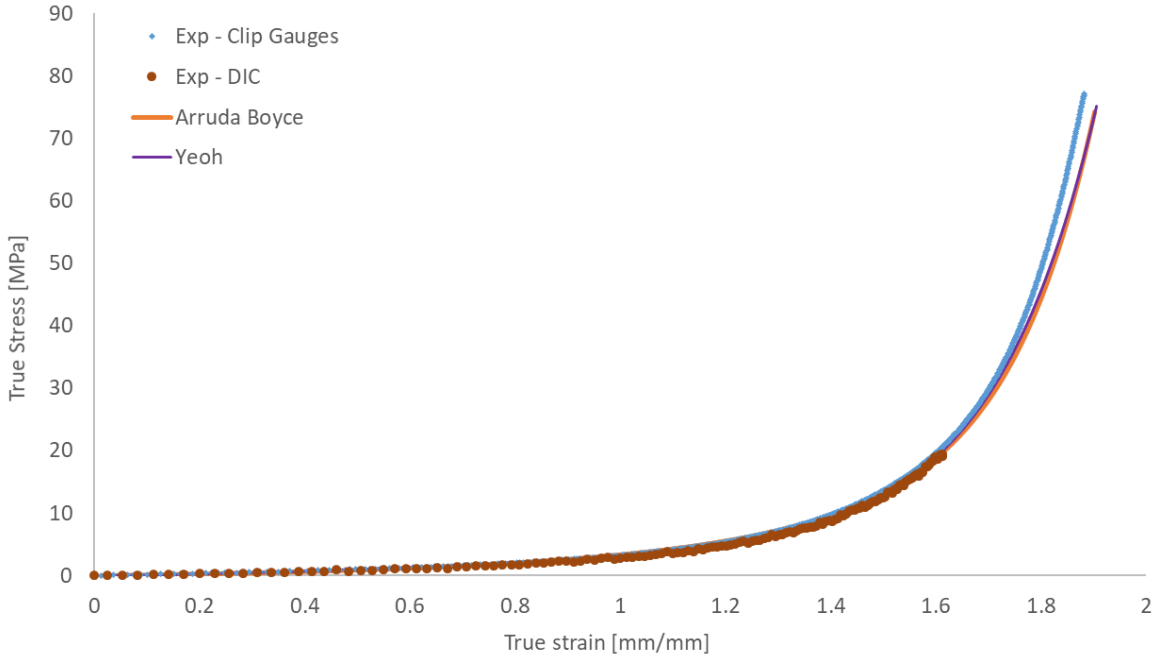

Figure 4-46: Simulated and experimental uniaxial true stress-strain curves.

Considering that relative errors should be accounted in order to infer the constitutive models performance (DESTRADE *et al.*, 2017; OGDEN *et al.*, 2004), both Arruda-Boyce and Yeoh models presented very similar maximum error values regarding its stress-strain slope. The comparison between error curves over analysis time period is depicted in Figure 4-47.

Although the maximum errors presented very close values, 25% and 21% for Arruda-Boyce and Yeoh respectively, the time to run the analysis was much higher for the Yeoh model, that is, 1 hour and 25 minutes against half the time for Arruda-Boyce (which was 45 minutes). Under these circumstances, Arruda-Boyce model turned out a more efficient option.

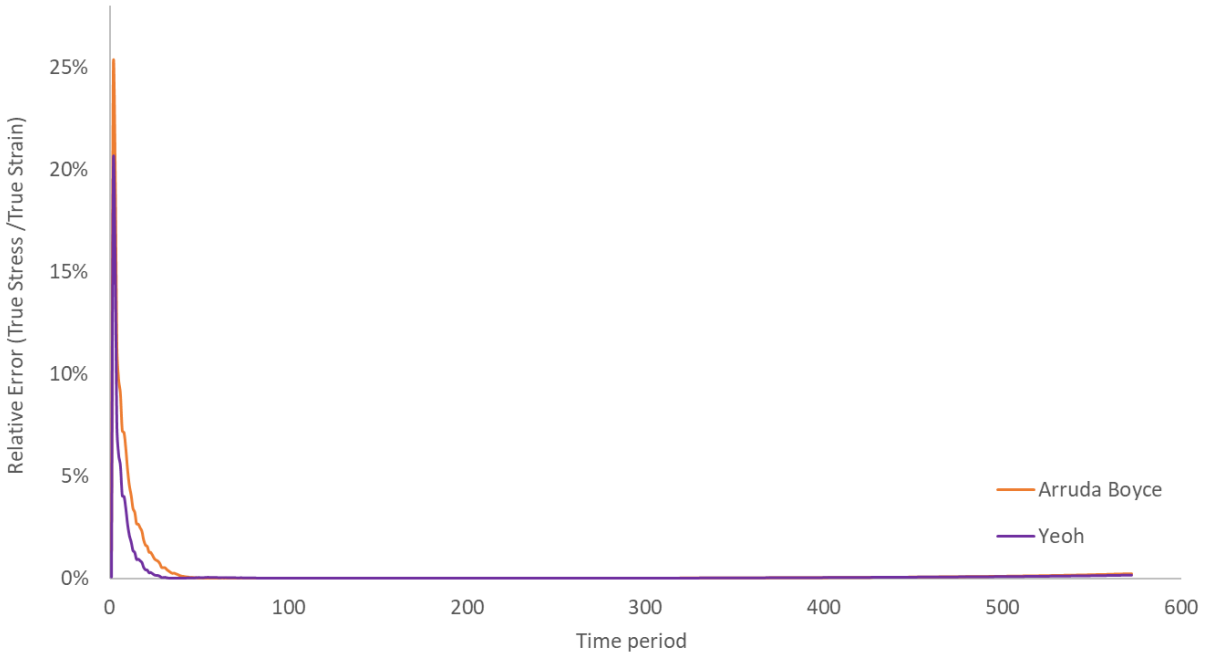

Figure 4-47: Relative error curves over analysis time period for uniaxial extension.

4.3.2 Equal biaxial stretching

4.3.2.1 Cruciform extension

In the case of equal biaxial deformation mode obtained by cruciform extension, the stretches in the sample center are indeed larger than that at the entire outer region for the same level of loading. This effect can be well analyzed for samples A and B respectively in Figures 4-48 and 4-49, where initial theoretical curves were obtained from non-corrected material parameters that were defined according to stress-strain relations of the outer region. Moreover, though these simulated stress-strain curves matched with the experimental ones, they were not able to follow the entire strain range (Figures 4-50 and 4-51). This happens because the initial FE constitutive modeling was not built according to the nominal stress-strain curves that should be extracted from the uniform region observed in central area of the specimen. Just like uniaxial tests, forces were plotted over the strains due to stress concentrations produced between clamps (FUJIKAWA *et al.*, 2014) .

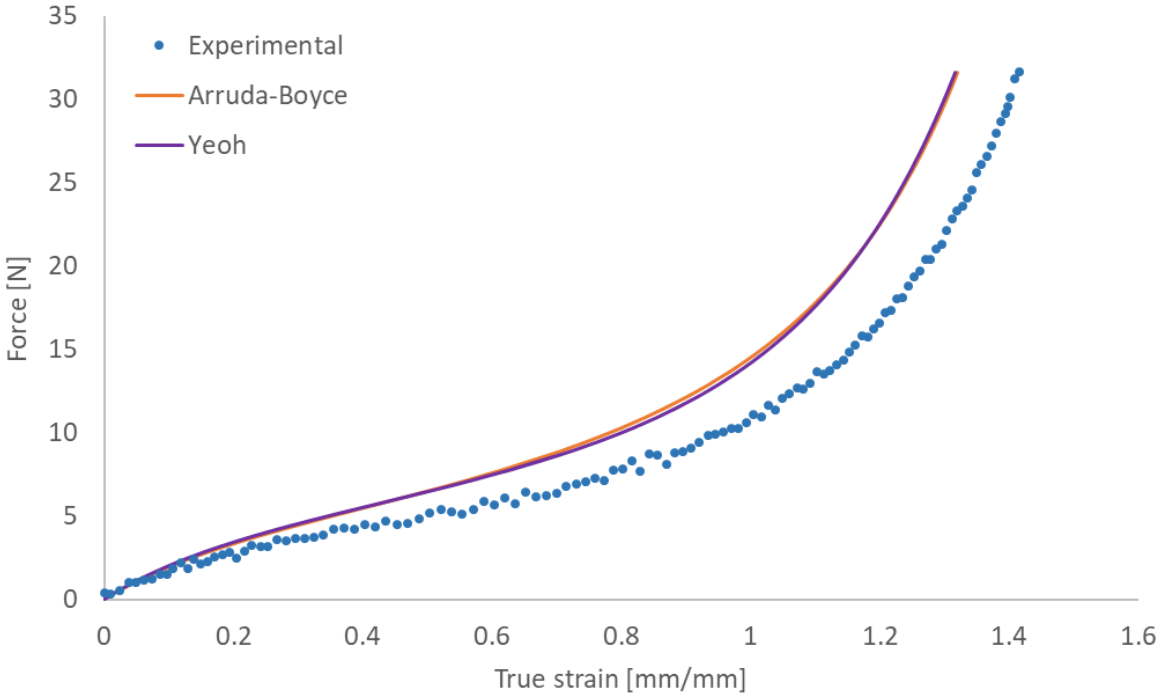

Figure 4-48: Initial sample A curves for cruciform extension forces plotted over simulated true strains.

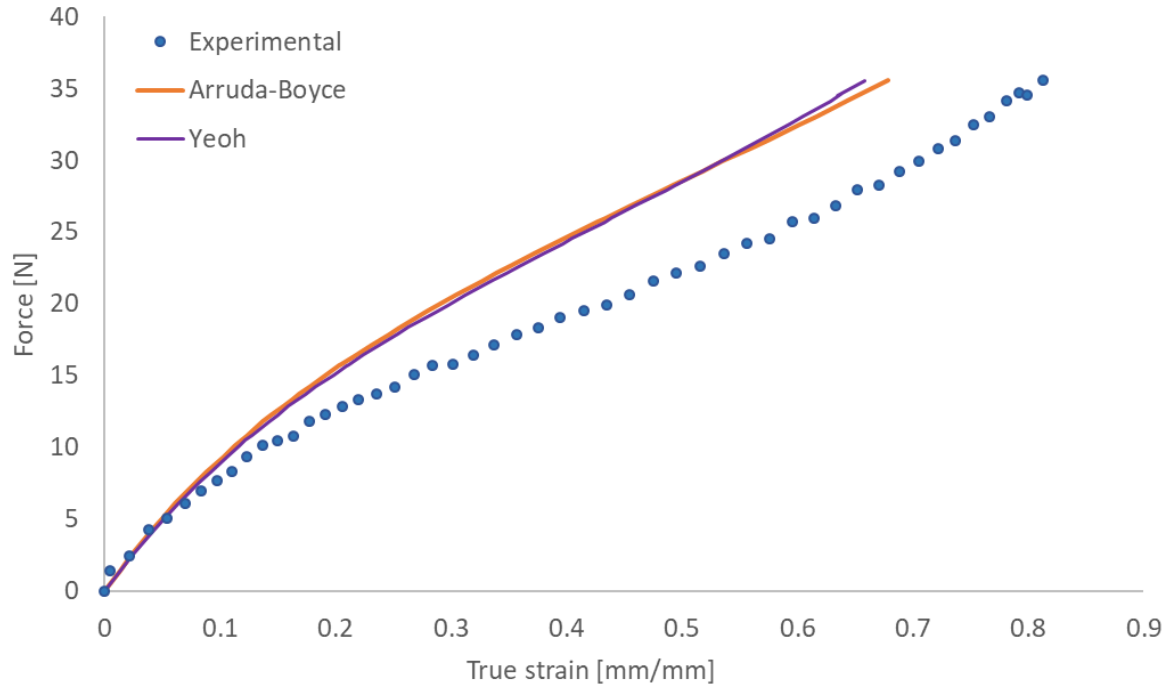

Figure 4-49: Initial sample B curves for cruciform extension forces plotted over simulated true strains.

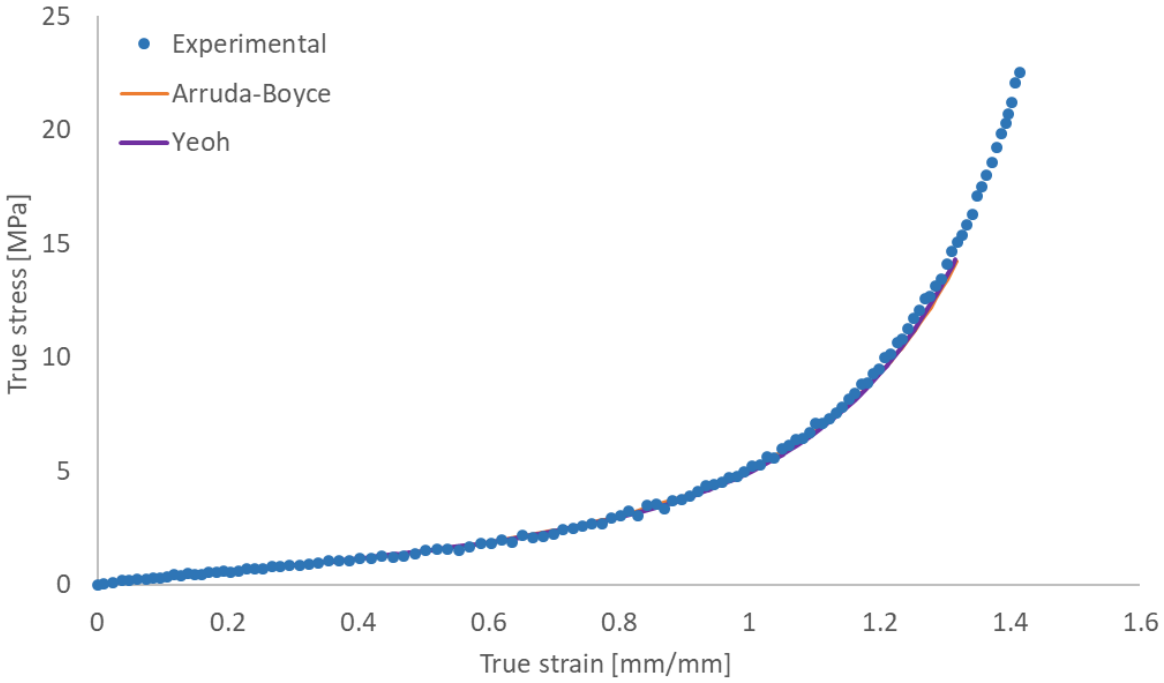

Figure 4-50: Simulated and experimental cruciform extension true stress-strain curves obtained from sample A initial material parameters.

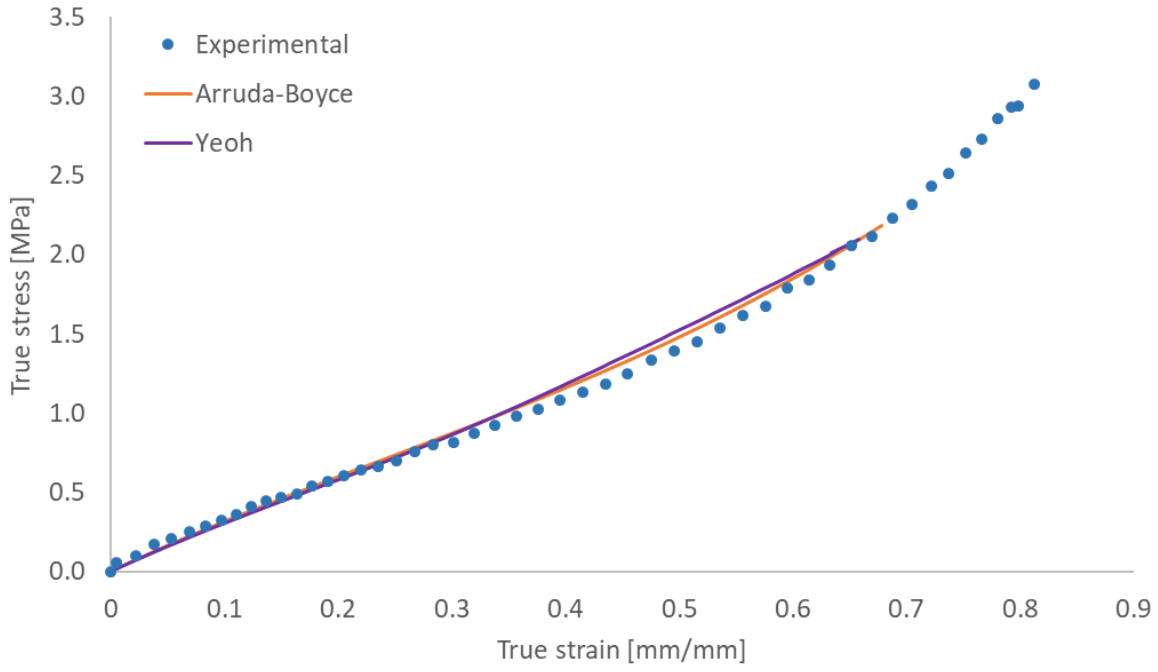

Figure 4-51: Simulated and experimental cruciform extension true stress-strain curves obtained from sample B initial material parameters.

Thus, aiming to obtain the corrected stresses synchronized with the strains measured through DIC, the uniform area size was evaluated according to the stress distributions of sample A and B (Figures 4-52 and 4-53 respectively) simulated through initial guess material parameters.

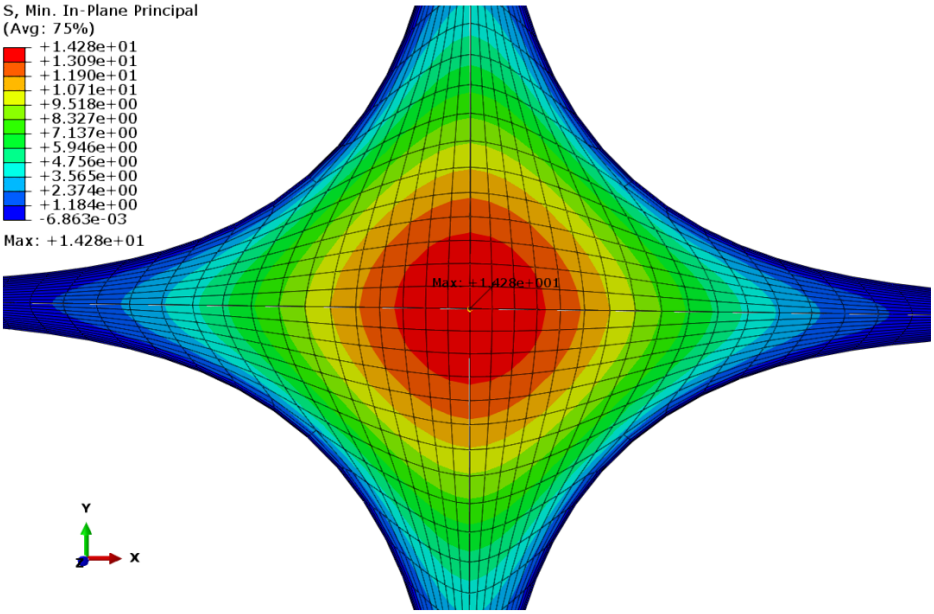

Figure 4-52: Sample A equal biaxial true stresses based on initial guess material parameters.

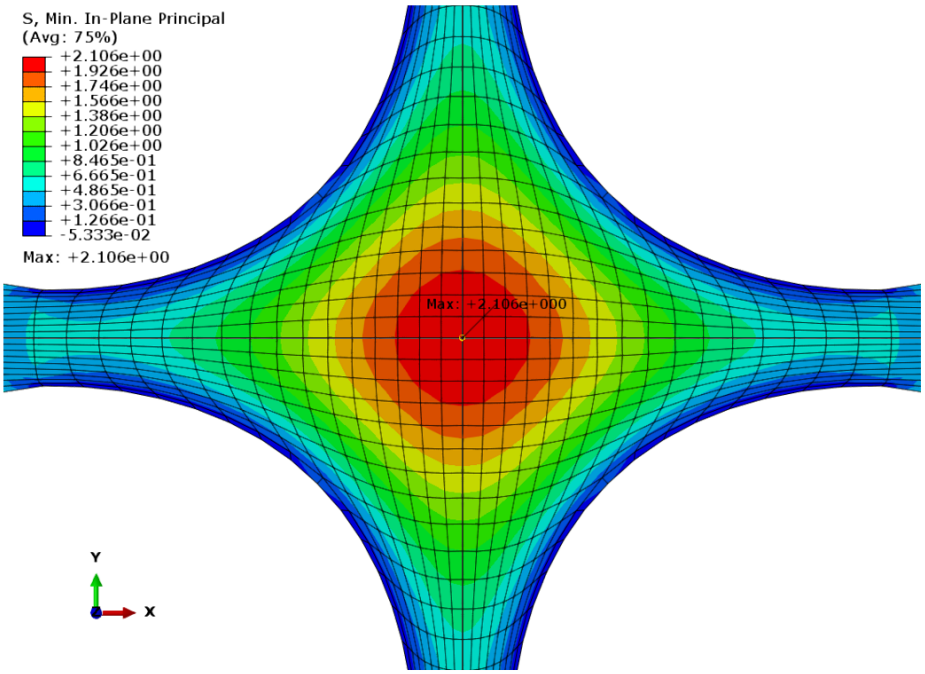

Figure 4-53: Sample B equal biaxial true stresses based on initial guess material parameters.

Taking into account the stress distributions presented in Figures 4-52 and 4-53, reaction forces were extracted directly from Abaqus® environment for both axis “x” and “y” according to the mesh dimensions around the symmetry point. Therefore, this relation between stretching forces around the uniform area defined at the center can be seen in Figures 4-54 and 4-55 for sample A, and Figures 4-56 and 4-57 for sample B. Although these figures show only the last simulation step, the procedure was applied for all force amplitudes that were synchronized with the measured strains over the analysis.

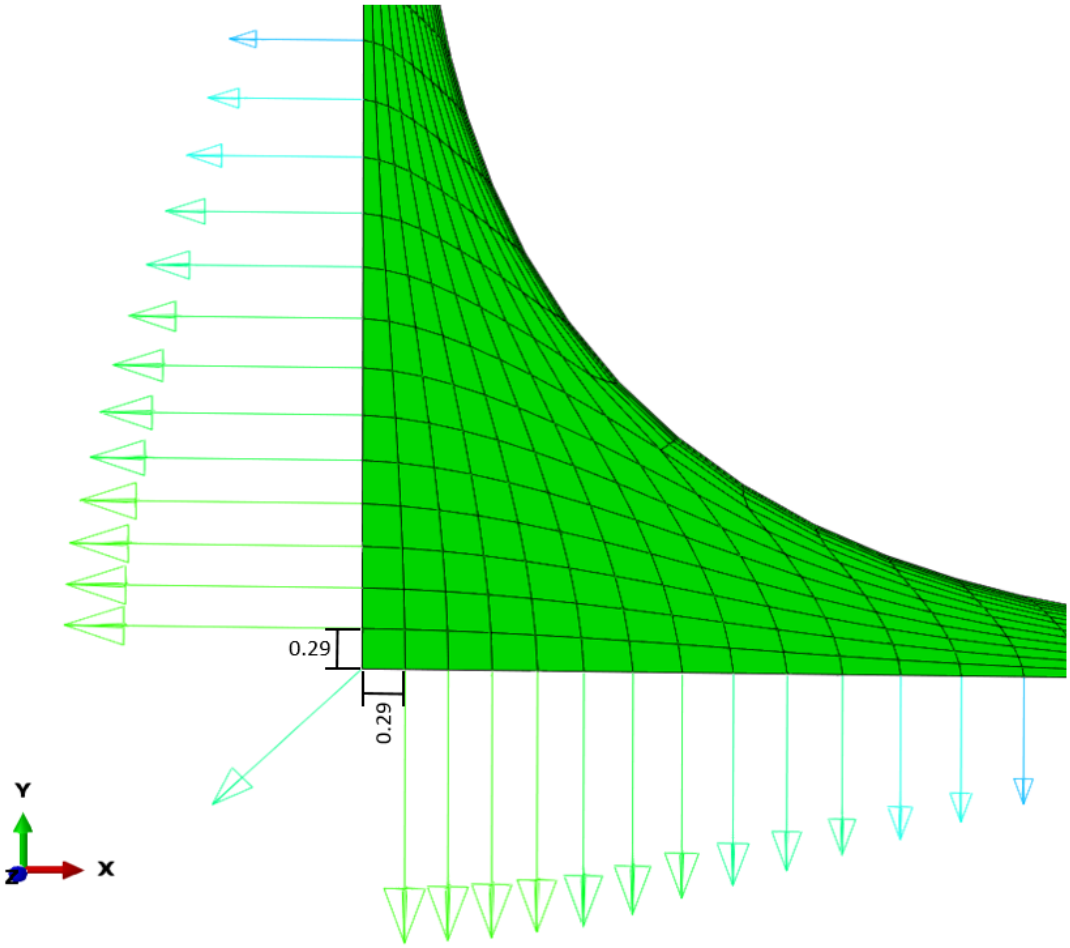

Figure 4-54: Sample A mesh dimensions around the central point for uniform area

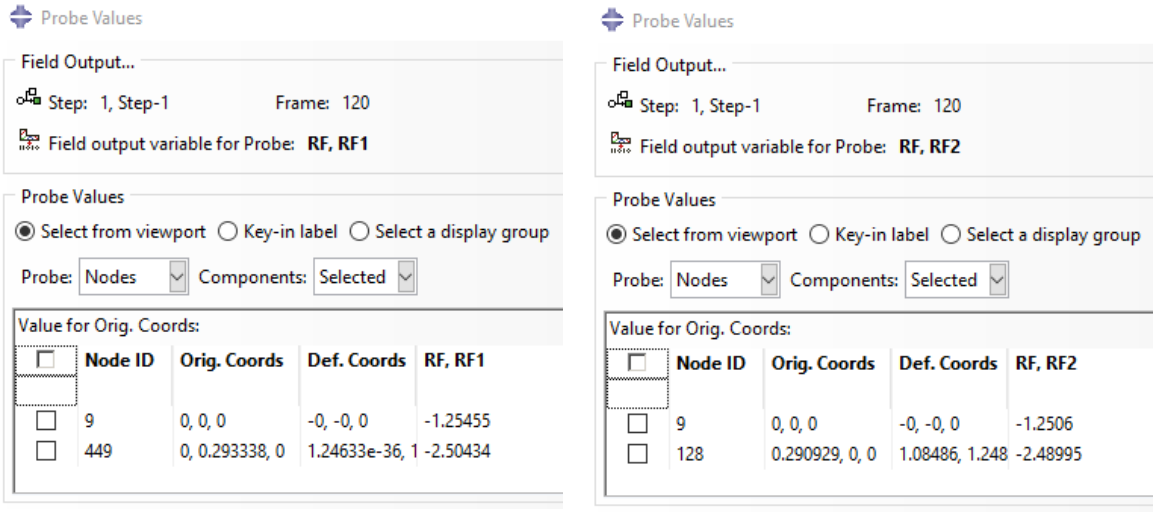

(a) (b)

Figure 4-55: Sample A reaction forces extracted from Abaqus®. (a) axis “x”; (b) axis “y”.

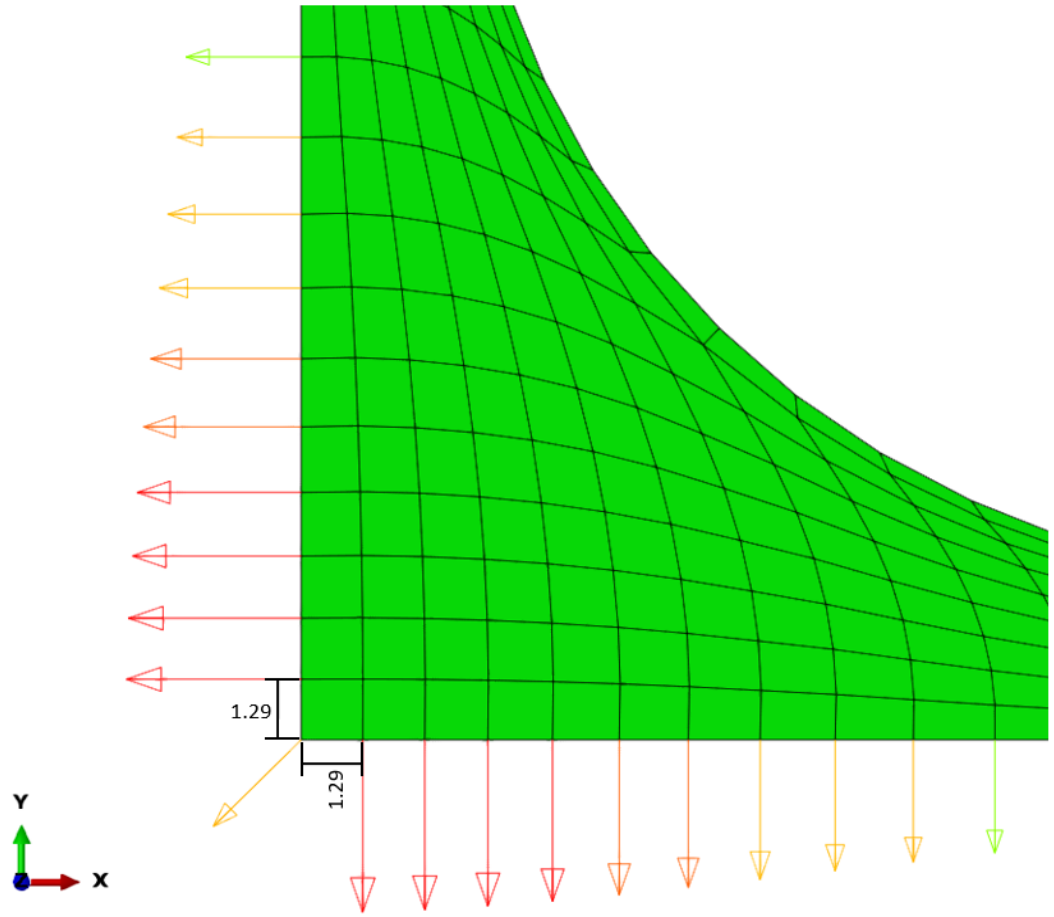

Figure 4-56: Sample B mesh dimensions around the central point for uniform area

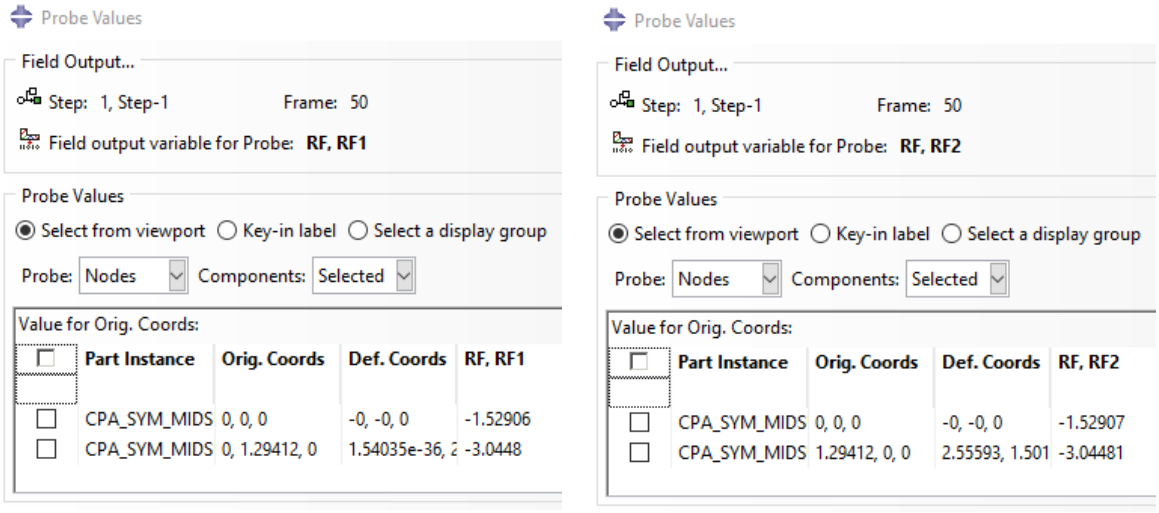

(a) (b)

Figure 4-57: Sample B reaction forces extracted from Abaqus®. (a) axis “x”; (b) axis “y”.

Finally, the corrected nominal stresses could be calculated over the analysis for each axis through the conventional relation between forces and area. Just as a validation, the average of theoretical stresses calculated from uniform region were compared to the nominal stresses obtained directly from FEA of the specimen.

Then, according to the Figures 4-58 and 4-59 for samples A and B respectively it is possible to note that both curves should match, being the difference between them almost negligible. This means that the proposed procedure is able to return accurate results in the treatment of equal biaxial experimental data even when the sample is subjected to high levels of deformation.

As a result, the corrected nominal stress-strain curves obtained from cruciform extension are plotted in Figure 4-60, where both curves are compared to bulge test experimental data. Finally, it is worth noting that, all biaxial curves show almost the same behavior when evaluated according to the maximum strains of each experiment, empowering even more the methodology applied when the problem must deal with high levels of deformation.

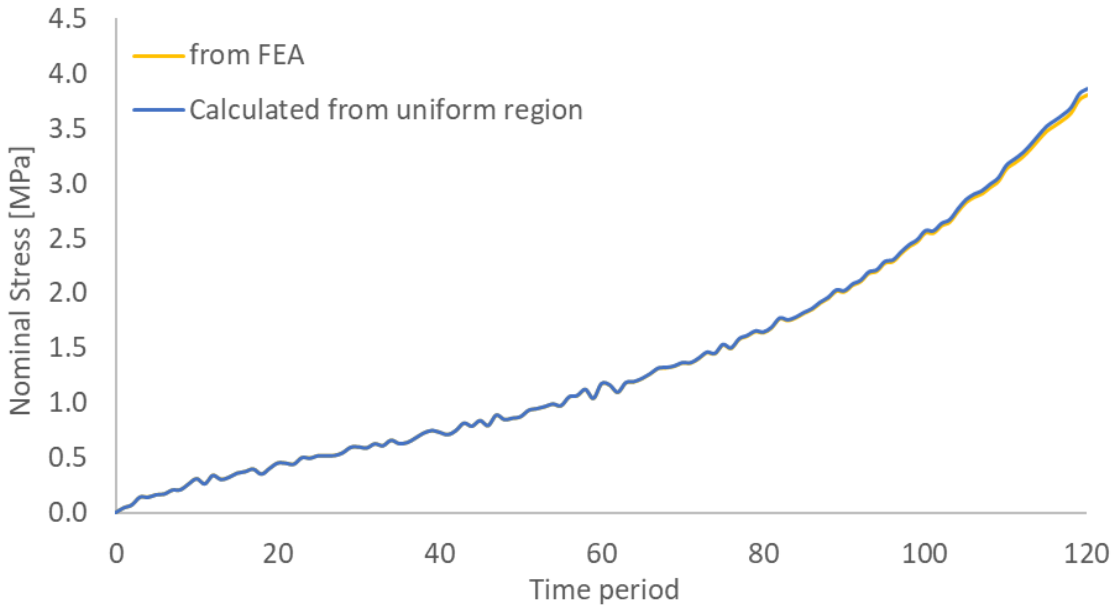

Figure 4-58: Nominal stress validation for sample A.

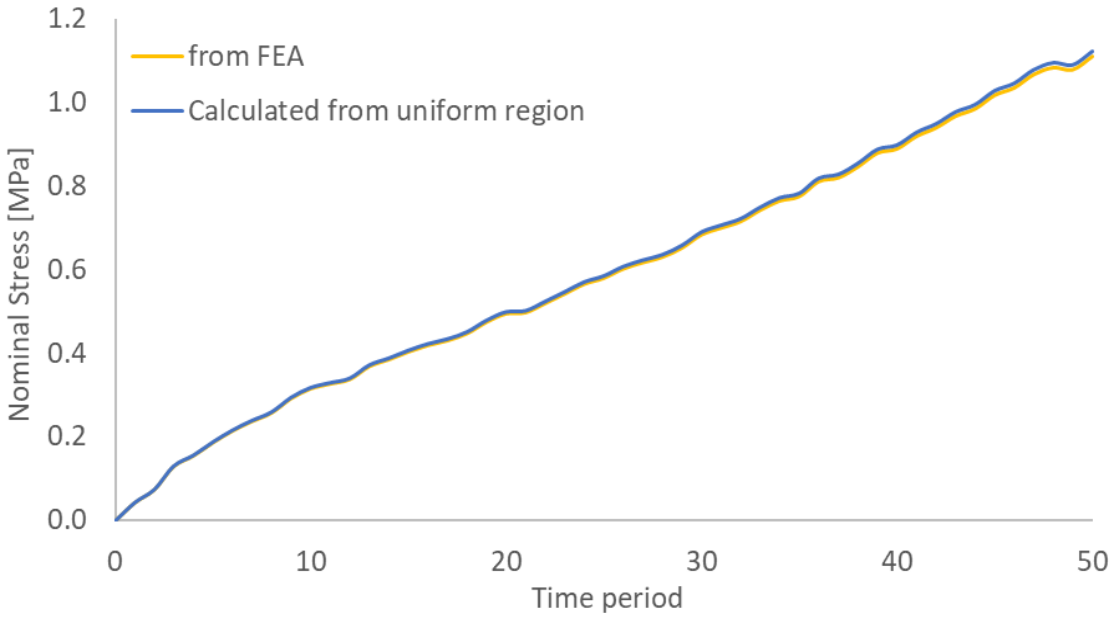

Figure 4-59: Nominal stress validation for sample B.

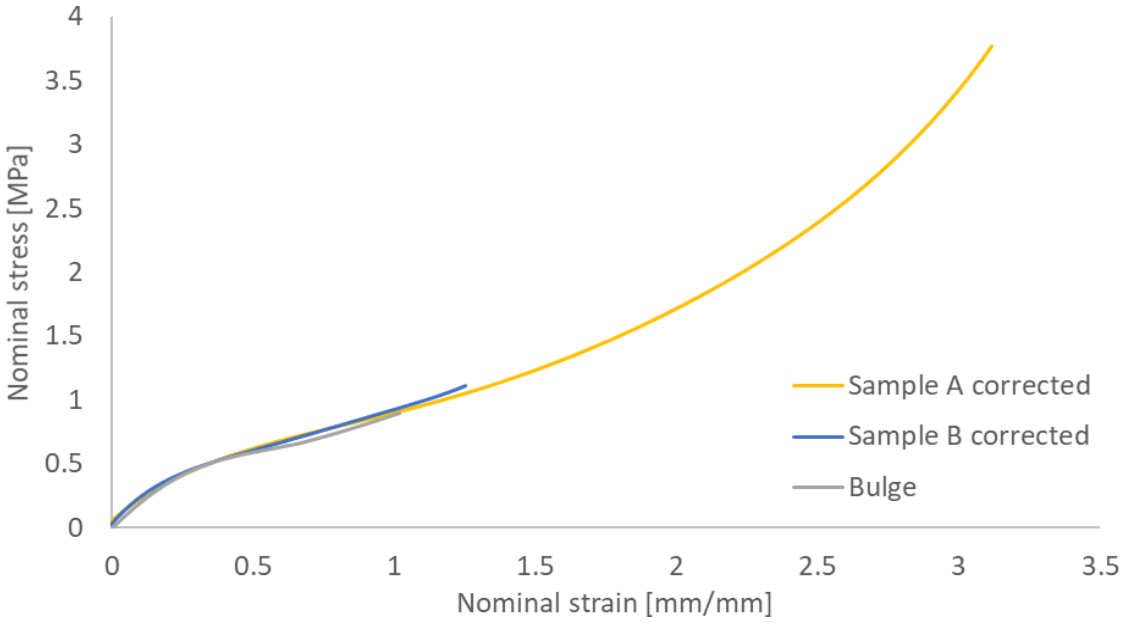

Figure 4-60: Comparison of final stress-strain curves for biaxial test samples.

After corrected nominal stress-strain curves were obtained, a new data fitting procedure should be performed. Like initial guess experimental curves four out of seven models showed to be stable for sample A, including: Neo-Hooke, Mooney-Rivlin, Yeoh and Arruda-Boyce. From Figure 4-61 final theoretical fitted curves are compared to the biaxial test data.

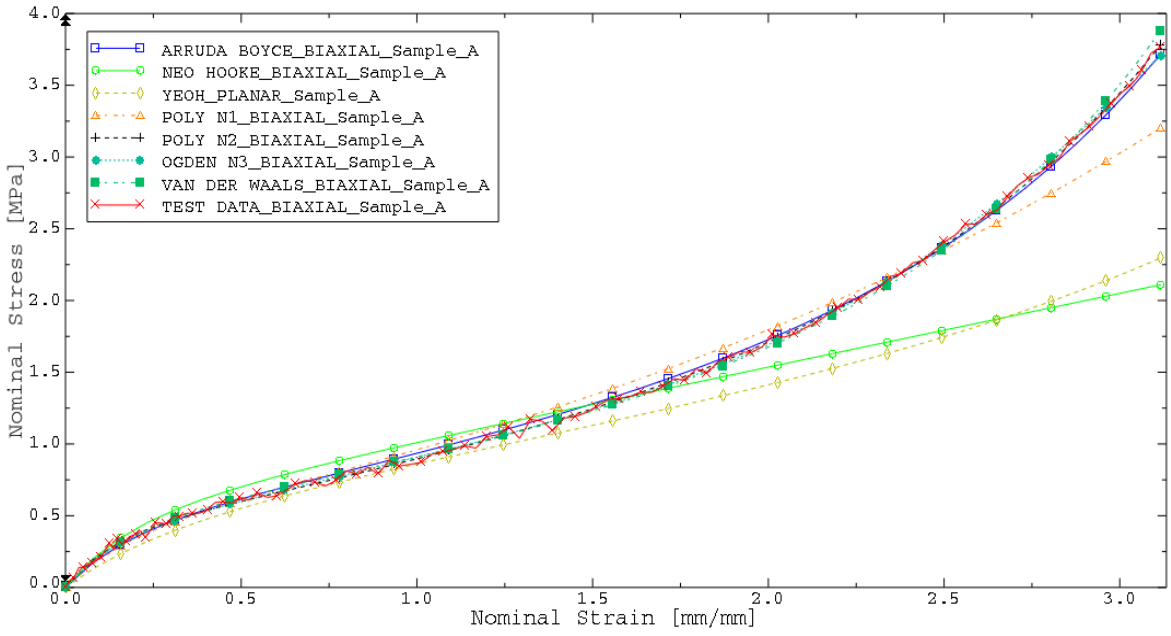

Figure 4-61: Sample A corrected stress-strain curves adjusted through cruciform extension.

Hence, from Table 4-5 the accurate material coefficients predicted by the use of only biaxial corrected data in a cruciform extension were finally discovered for each constitutive model.

Table 4-5: Material models coefficients based on corrected sample A cruciform extension data fitting.

Arruda-Boyce		Yeoh		Mooney-Rivlin		Polynomial N=2		Ogden N=3		van der Waals	
μ	0.422461	C_{10}	0.229610	C_{10}	0.198746	C_{10}	0.412404	μ_1	0.432091	μ	0.477965
μ_0	0.439851	C_{20}	-3.41E-04	C_{01}	1.12E-02	C_{20}	3.92E-02	μ_2	0.331748	λ_m	8.575475
λ_L	3.940081	C_{30}	8.96E-04	μ_0	4.20E-01	C_{01}	-0.14489	μ_3	-0.16582	α	0.250584
		μ_0	4.59E-01		-	C_{11}	-1.24E-04	α_1	2.223626	β	0
Neo-Hooke			-		-	C_{02}	1.87E-05	α_2	10.2905		-
C_{10}	0.256293		-		-	μ_0	5.35E-01	α_3	-5.14536		-
μ_0	5.13E-01		-		-		-	μ_0	0.598021		-

The relative error computation over the strain is presented in Figure 4-62 followed by its accumulated sum in Figure 4-63. Just like all other models, Neo-Hooke presented the worst adjustment for both specific relative errors and its accumulated value.

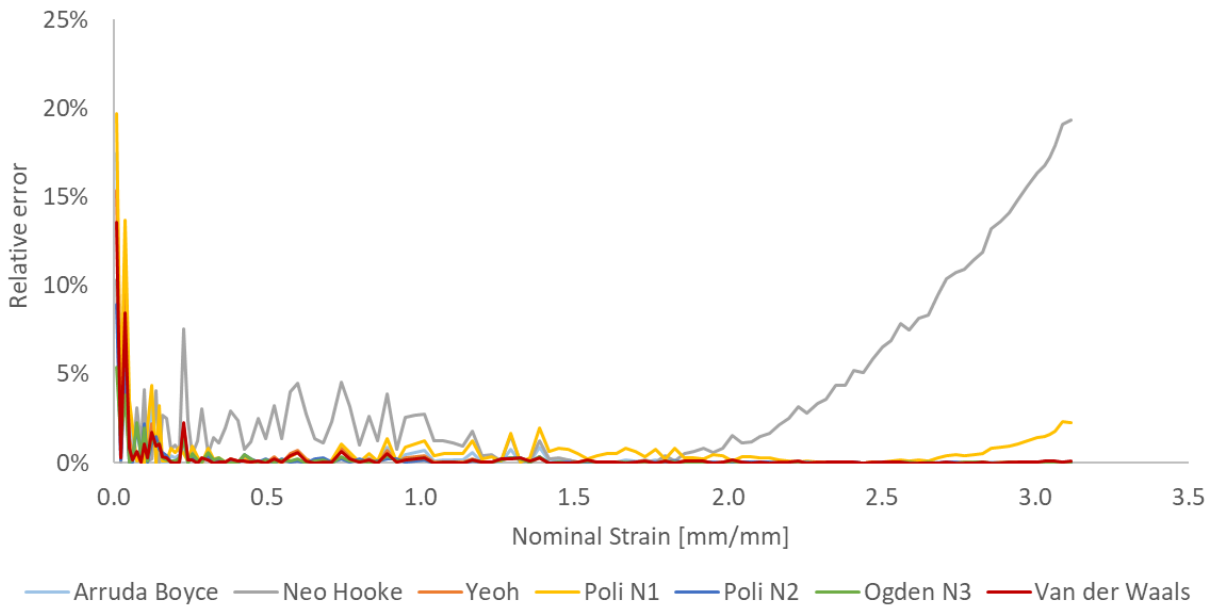

Figure 4-62: Relative errors over strain range for sample A corrected biaxial data fitting.

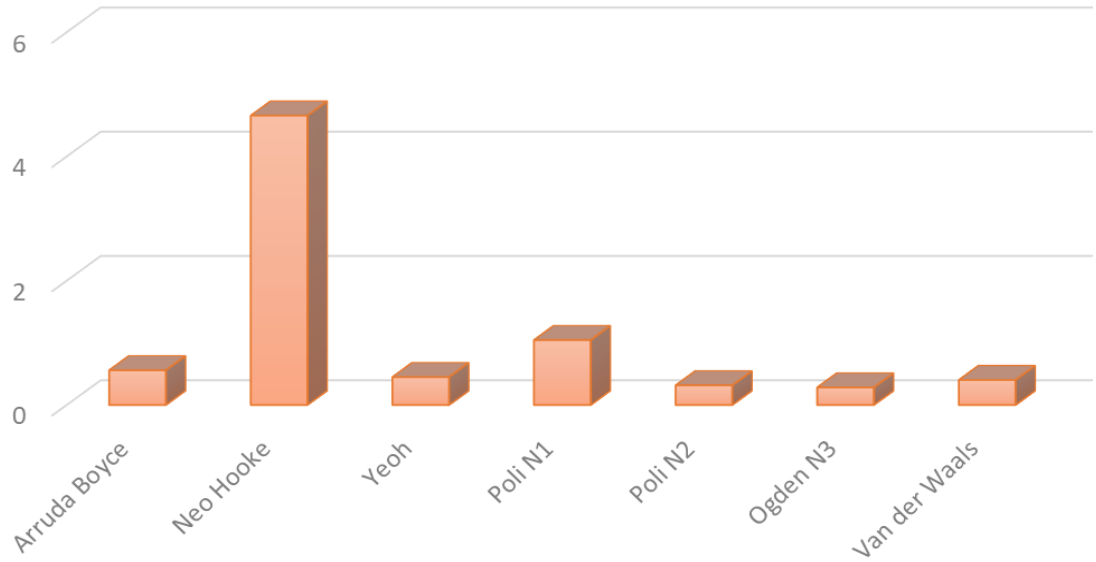

Figure 4-63: Accumulated relative error according to each constitutive model for sample A corrected biaxial data fitting.

Exactly the same procedure has been performed for sample B, but in this case, only three out of seven models showed to be stable for all strain ranges, which they are: Neo-Hooke, Arruda-Boyce and Yeoh. Then, the final theoretical fitted curves corrected from initial guess test data can be evaluated according to Figure 4-64.

Like sample A, the accurate material coefficients were predicted for sample B, taking into account the use of only biaxial corrected data in a cruciform extension, as shows Table 4-6 for each constitutive model.

Table 4-6: Material models coefficients based on corrected sample B cruciform extension data fitting.

Arruda-Boyce		Yeoh		Mooney-Rivlin		Polynomial N=2		Ogden N=3		van der Waals	
μ	0.470856	C_{10}	0.249304	C_{10}	0.240247	C_{10}	0.849494	μ_1	0.375486	μ	0.545372
μ_0	0.470857	C_{20}	-8.64E-03	C_{01}	-1.87E-03	C_{20}	2.04E-01	μ_2	1.170852	λ_m	5.667507
λ_L	1634.511	C_{30}	8.67E-04	μ_0	4.77E-01	C_{01}	-0.51477	μ_3	-0.58542	α	0.547287
		μ_0	4.99E-01		-	C_{11}	-3.22E-02	α_1	-0.10576	β	0
Neo-Hooke			-		-	C_{02}	4.28E-03	α_2	20.34048		-
C_{10}	0.235428		-		-	μ_0	6.69E-01	α_3	-10.1702		-
μ_0	4.71E-01		-		-		-	μ_0	0.960916		-

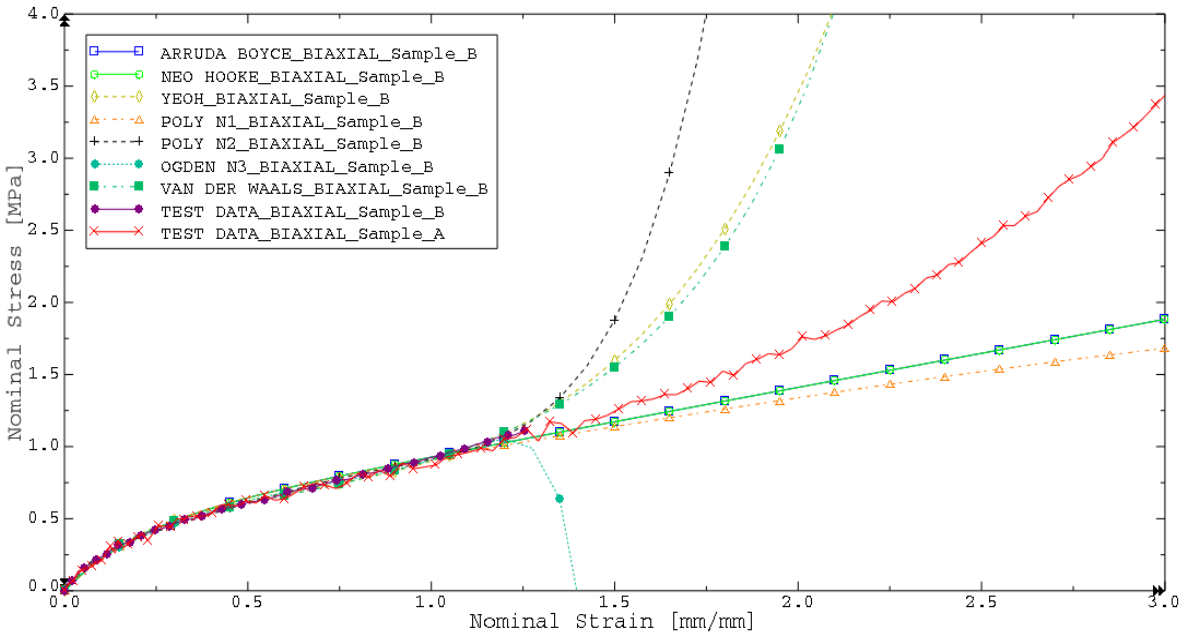

Figure 4-64: Sample B corrected stress-strain curves adjusted through cruciform extension

Finally, the relative error computation is presented over the strain for sample B in Figure 4-65 and its accumulated sum in Figure 4-66. As this sample experiences much lower levels of strain the relative errors did not present major differences between constitutive models.

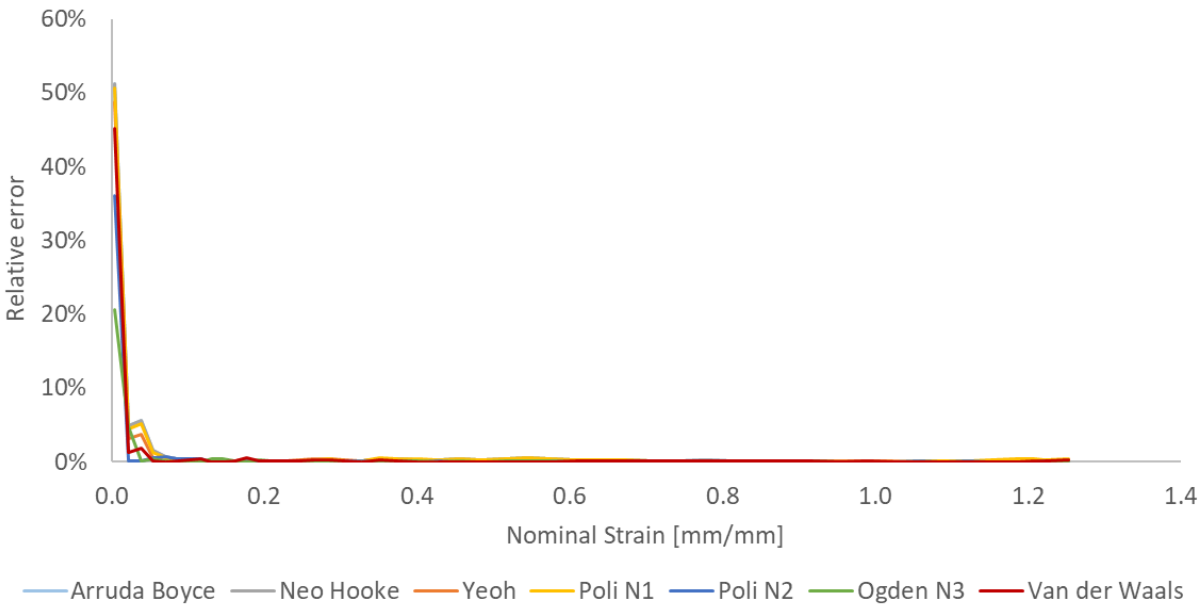

Figure 4-65: Relative errors over strain range for sample B corrected biaxial data fitting.

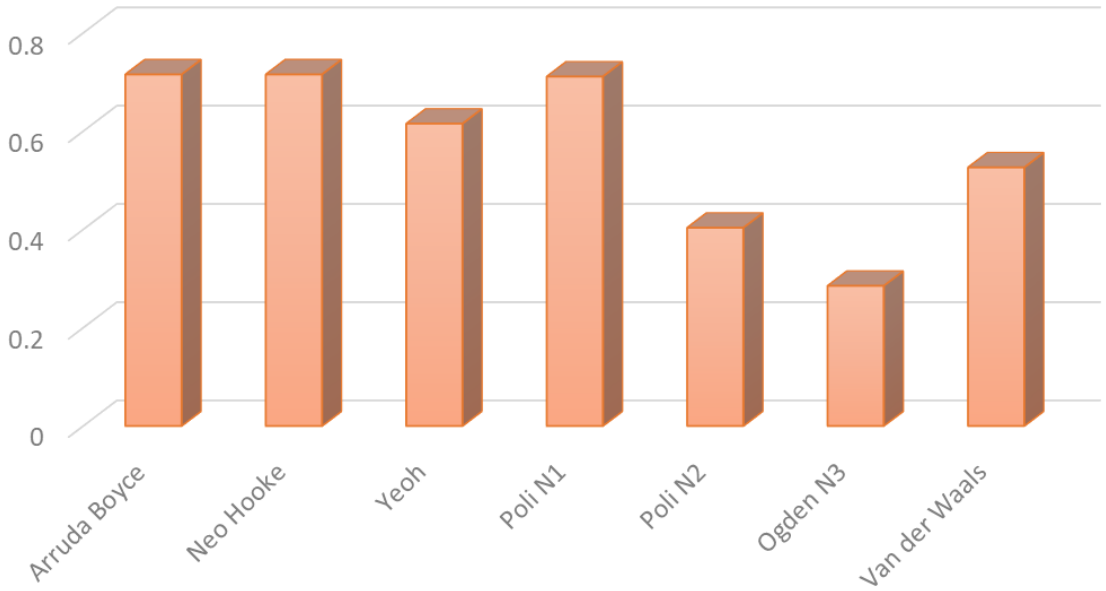

Figure 4-66: Accumulated relative error according to each constitutive model for sample B corrected biaxial data fitting.

After constitutive parameters were obtained from an accurate data fitting according to the uniform biaxial extension area, a new FEA was carried out in order to check the efficiency and validate the proposed methodology.

The strain and stress true responses were computed in the central region of the specimen, where the maximum principal stresses of sample A could be analyzed according to Figure 4-67. Then, experimental and simulated curves were compared according to both the forces and the stresses which were plotted over the strains respectively in Figures 4-68 and 4-69.

Based on the same consideration applied in uniaxial tensile test the force amplitude was analyzed over the strains because of the high influence of the clamps in the uniform strain calculation around the center.

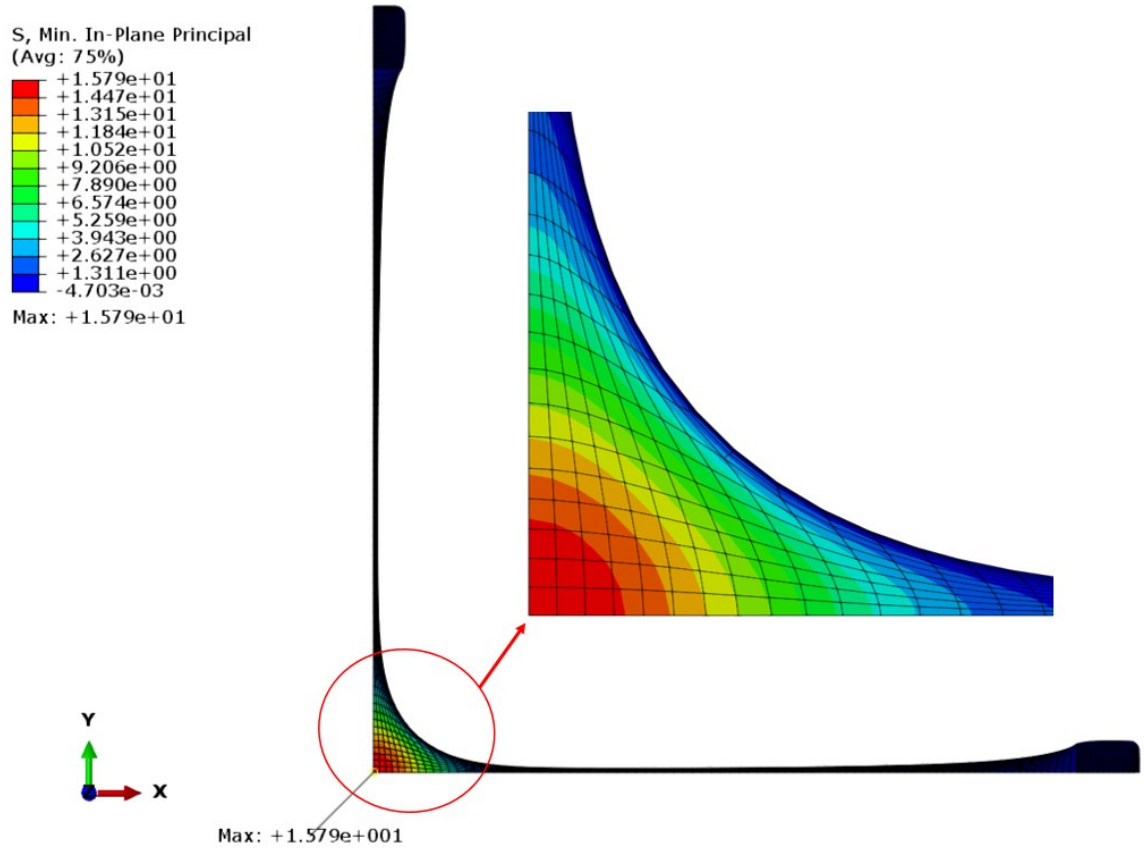

Figure 4-67: Sample A equal biaxial true stress distribution in a cruciform shape.

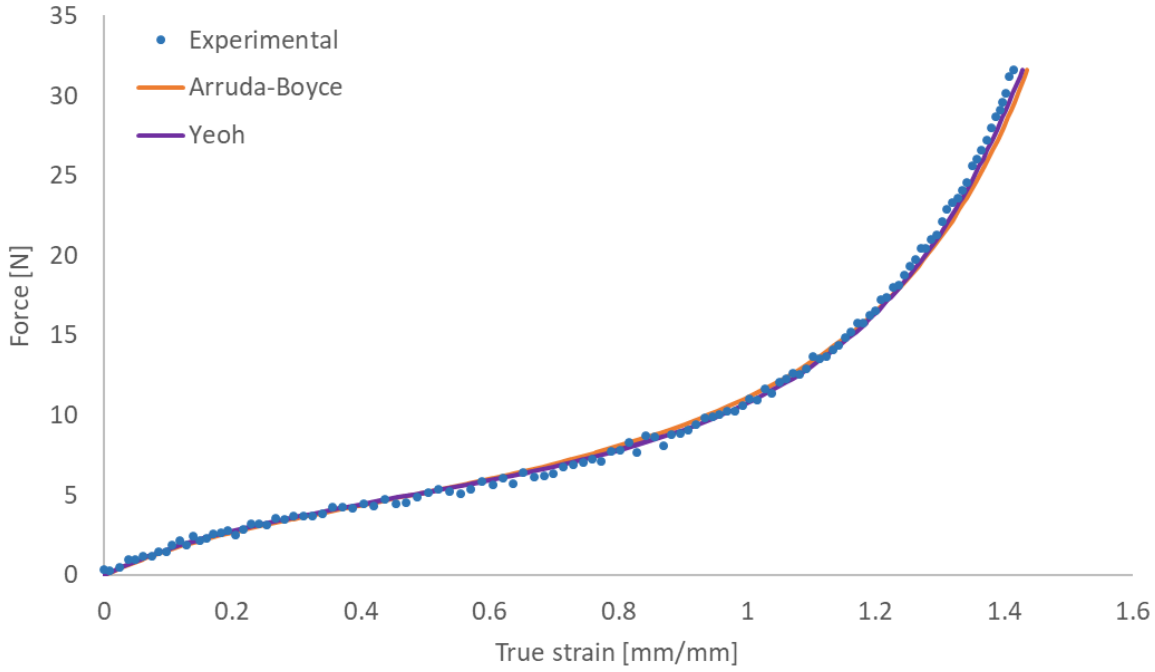

Figure 4-68: Sample A cruciform extension forces plotted over uniform true strains.

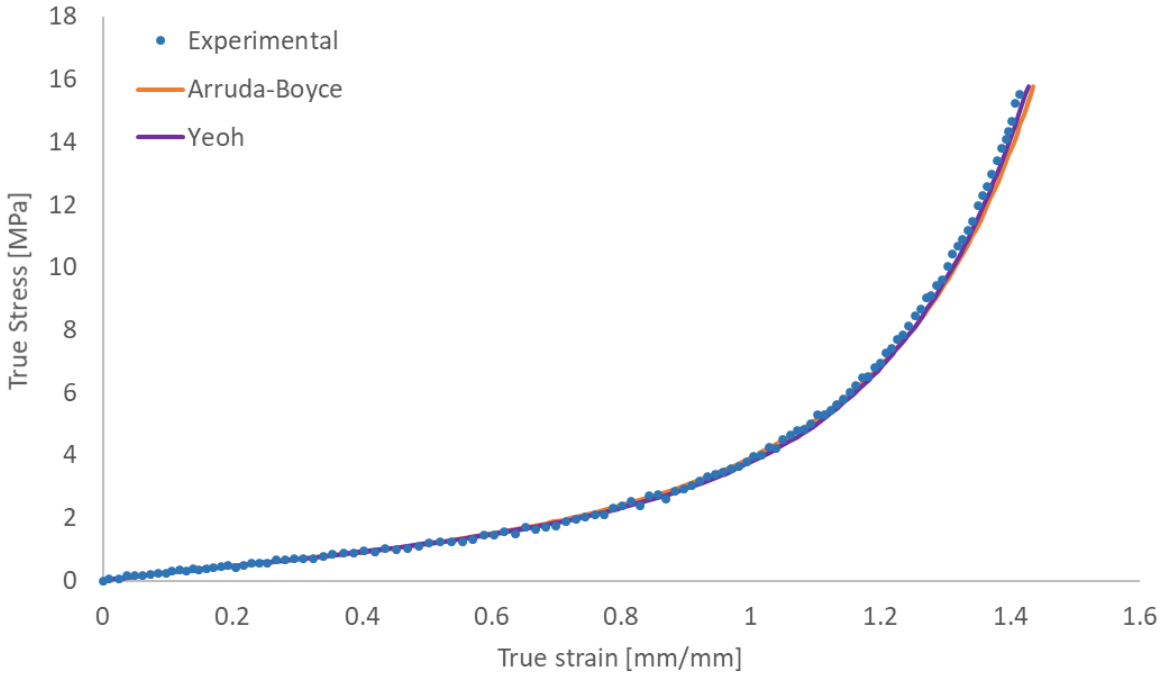

Figure 4-69: Simulated and experimental sample A equal biaxial true stress-strain curves.

The performance of Arruda-Boyce and Yeoh models were almost the same, being the relative errors projected according to final stress-strain slope in Figure 4-70.

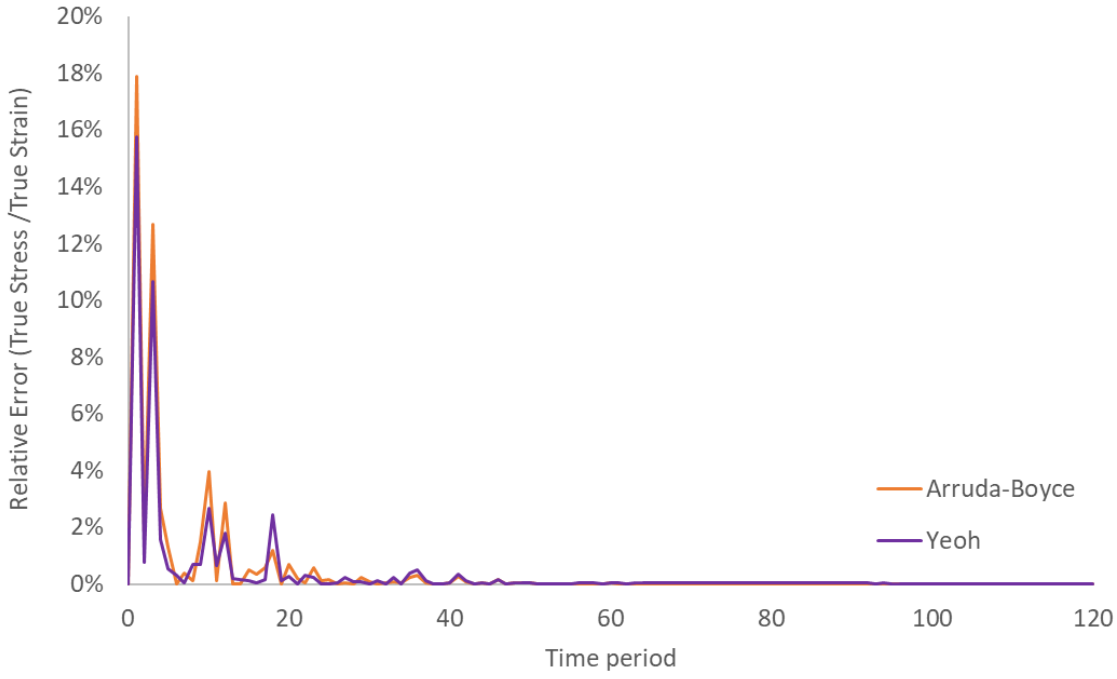

Figure 4-70: Relative error curves over analysis time period for sample A biaxial extension.

To better visualize the error difference between models a response interval was zoomed in, considering the time period after step 20, as shows Figure 4-71.

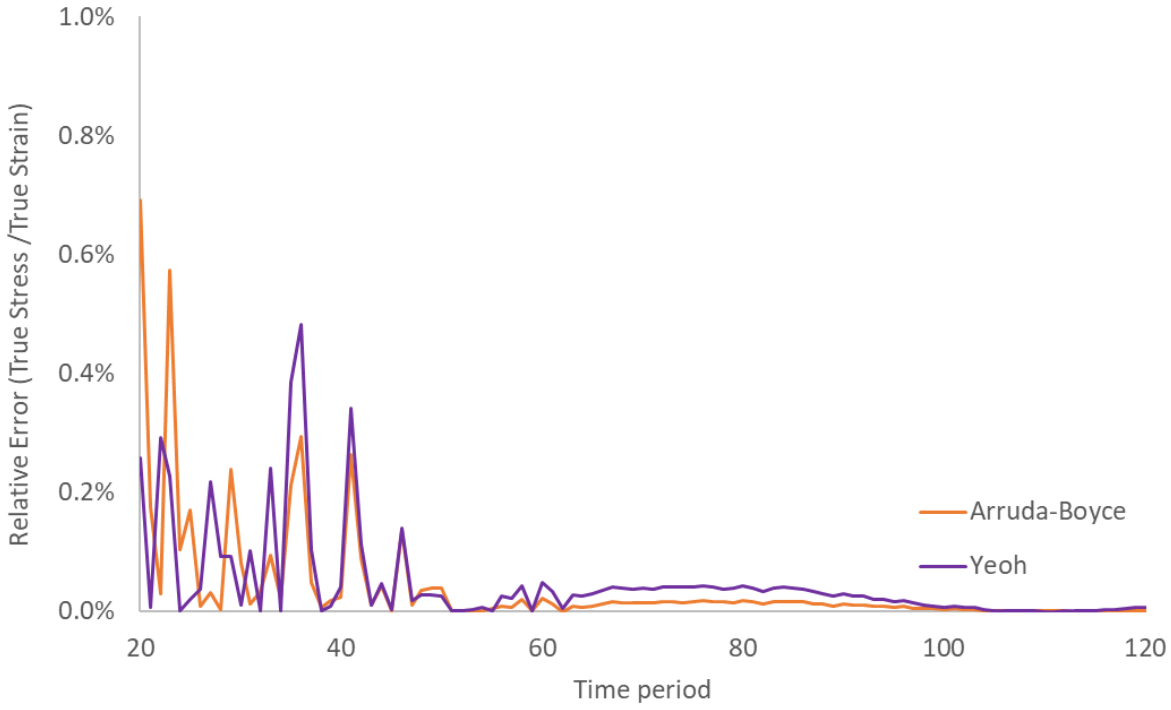

Figure 4-71: Zoom in of relative error curves over analysis time period for sample A biaxial extension.

The principal stress distributions of sample B is depicted in Figure 4-72, while the experimental and simulated curves compared according to the forces and the stresses amplitudes are respectively plotted in Figures 4-73 and 4-74.

Taking the same procedure of sample A, the relative errors projected according to final stress-strain slope is presented in Figure 4-75, and the respective details selected according to a time interval after step 10 is depicted in Figure 4-76. The same way as sample A, the performance of both models evaluated were practically the same.

It is possible to note that, opposite than initial guess force-strain curves of Figures 4-48 and 4-49 for samples A and B respectively, the corrected curves obtained through uniform region matched very well experimental data with simulated models.

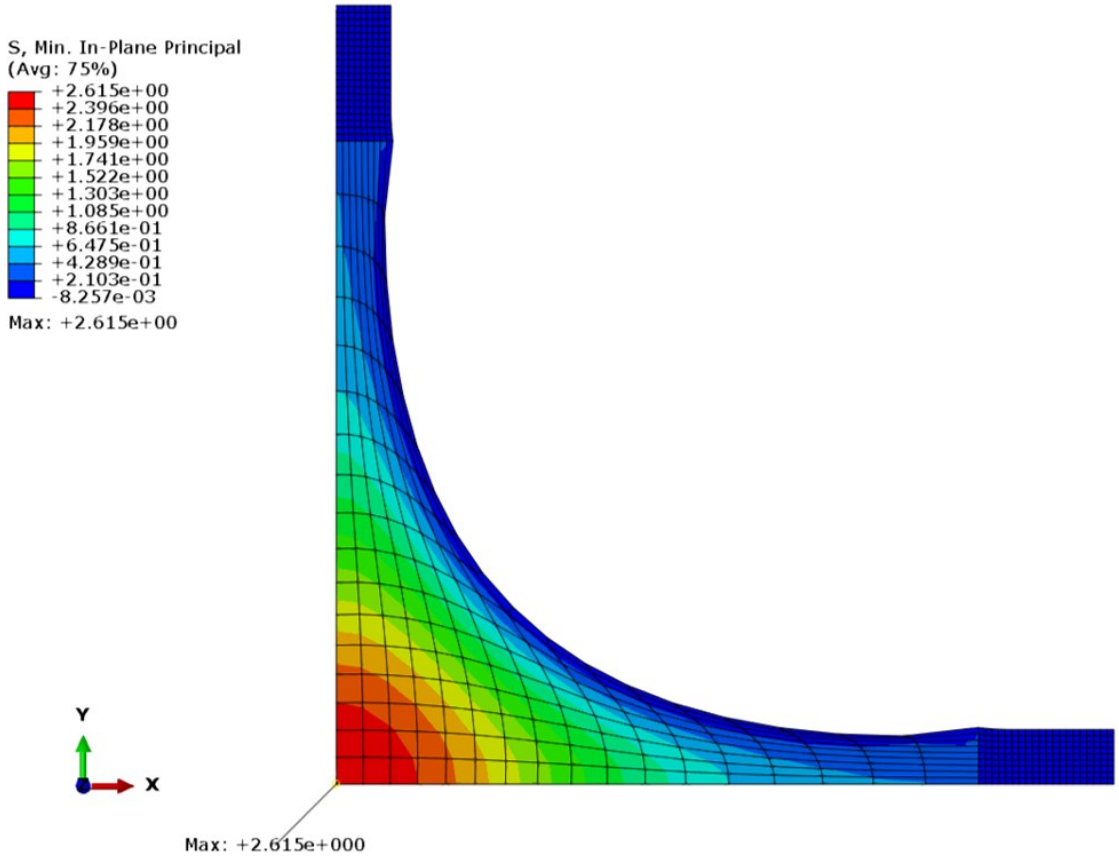

Figure 4-72: Sample B equal biaxial true stress distribution in a cruciform shape.

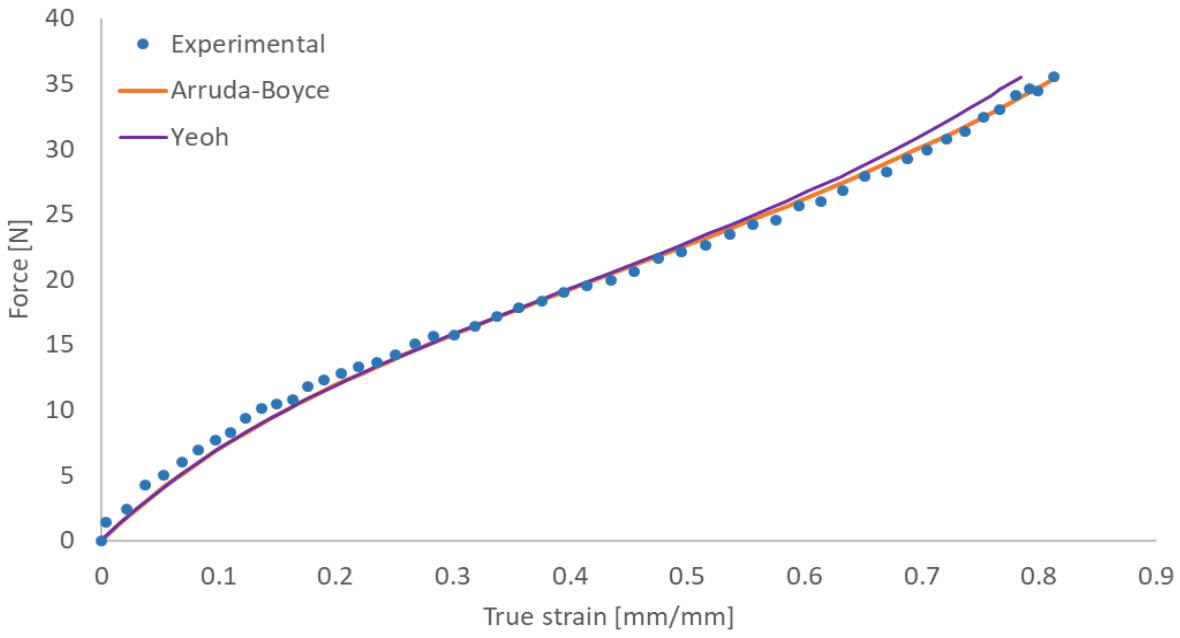

Figure 4-73: Sample B cruciform extension forces plotted over uniform true strains.

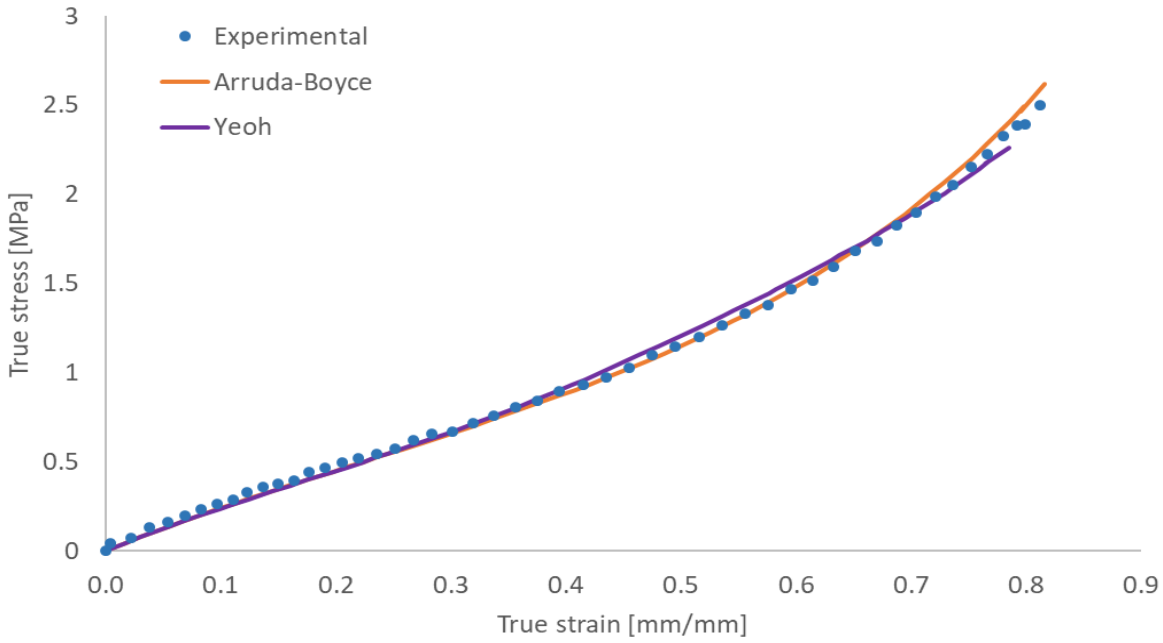

Figure 4-74: Simulated and experimental sample B equal biaxial true stress-strain curves.

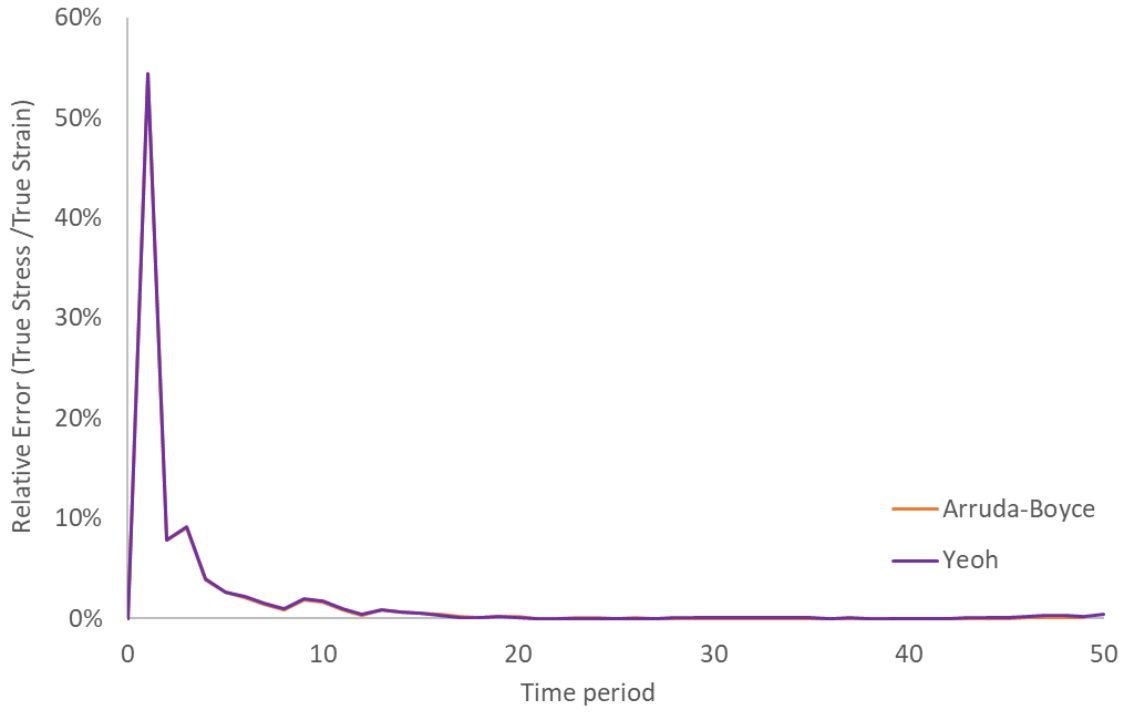

Figure 4-75: Relative error curves over analysis time period for sample B biaxial extension.

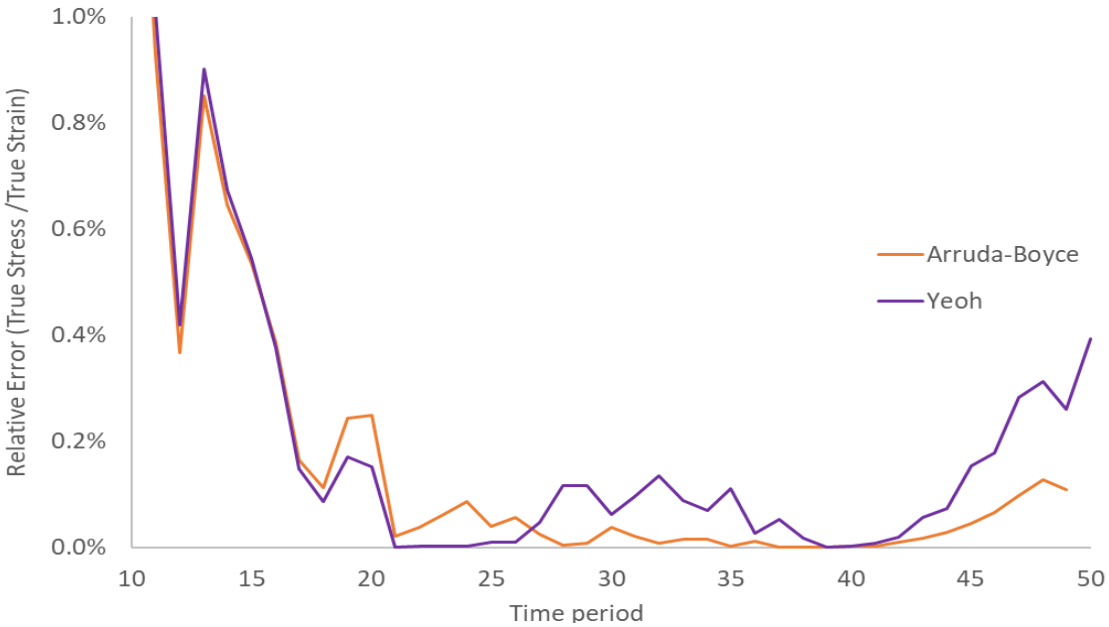

Figure 4-76: Zoom in of relative error curves over analysis time period for sample B biaxial extension.

4.3.2.2 Bulge inflation

The simulation of bulge test was conducted based on a quarter of symmetry considering the application of pressure amplitudes experienced in the tests. In order to evaluate the shape of bulge profile the total deflection response was extracted and is depicted in Figure 4-77 followed by stress distribution in Figure 4-78.

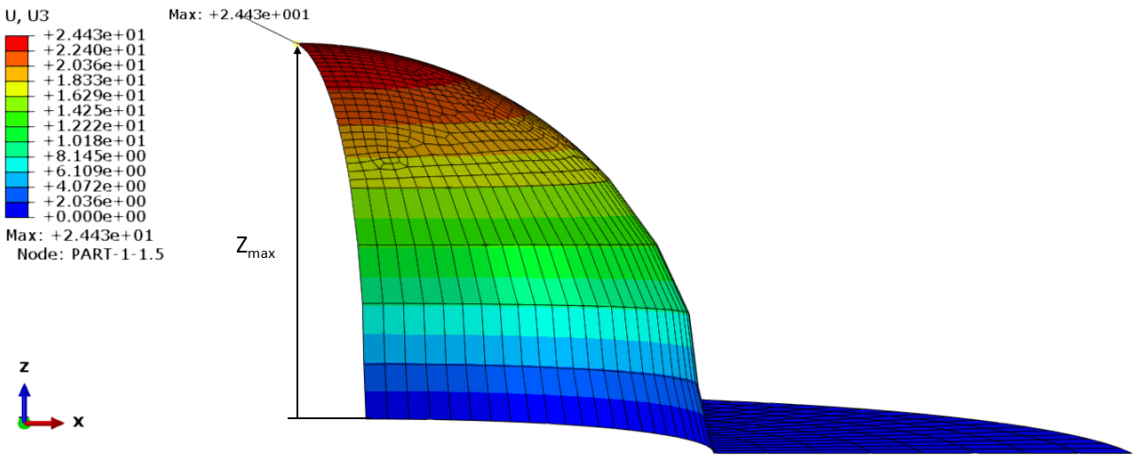

Figure 4-77: Bulge inflation final deflection.

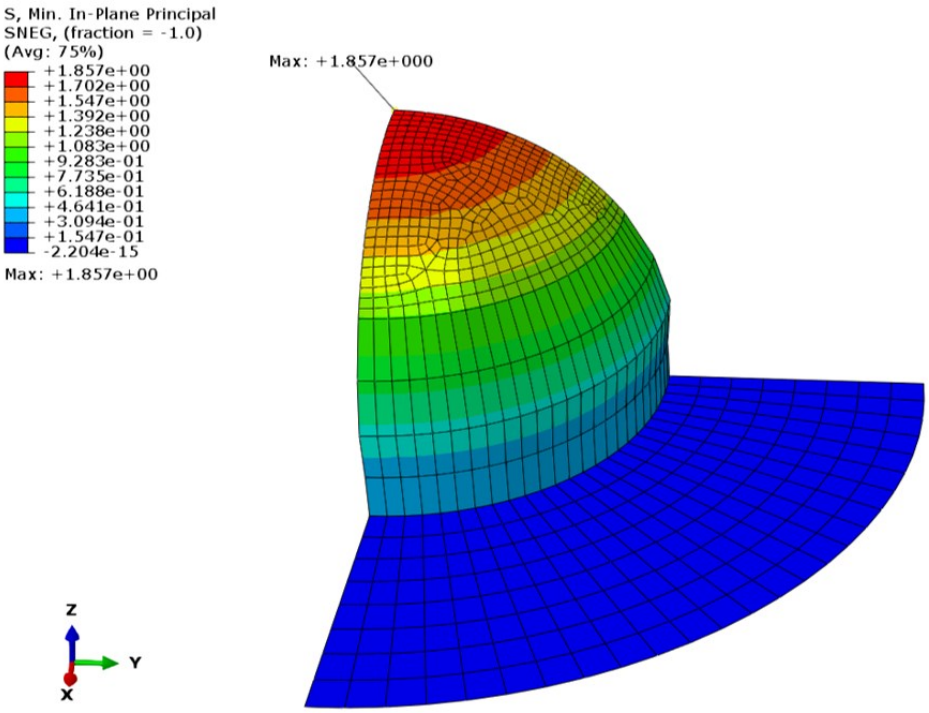

Figure 4-78: Bulge inflation equal biaxial true stress distribution around dome center.

Since Arruda-Boyce was a stable model with a reasonable relative error, FE simulation was performed according to this hyperelastic material law. Then, as a comparison pressure was plotted over maximum deflection in Figure 4-79 and over true strains in Figure 4-80 against experimental data.

Based on equation (3-2), the experimental calculated stress was also compared to simulated response, taking into account the strains measured through DIC. Thus, the true stress-strain curves can be evaluated in Figure 4-81.

From presented results it is possible to state that the Arruda-Boyce hyperelastic model could predict with high accuracy the experimental tests response. This happens because this eight chain model is always stretched in the principal direction and in response to any deformation the chains in the reference frame can undergo stretches describable by the principal values of stretch. In addition, this model extends equally under biaxial extension as well as uniaxial extension (ARRUDA and BOYCE, 1993).

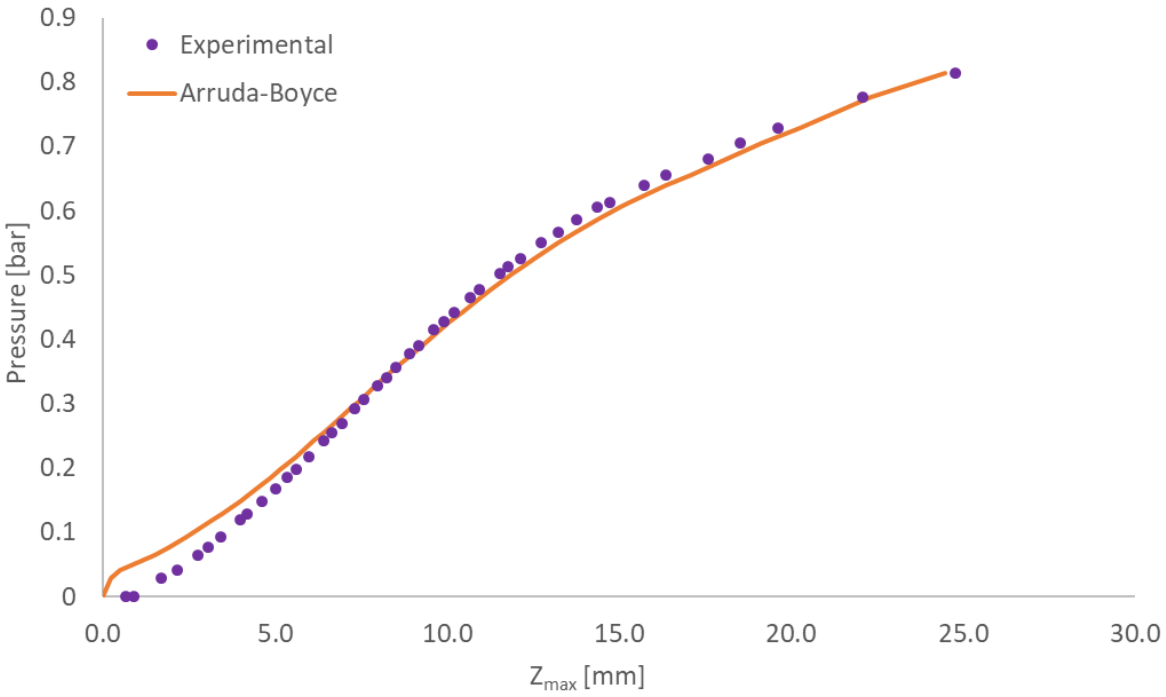

Figure 4-79: Bulge inflation pressure plotted over maximum deflections in the dome.

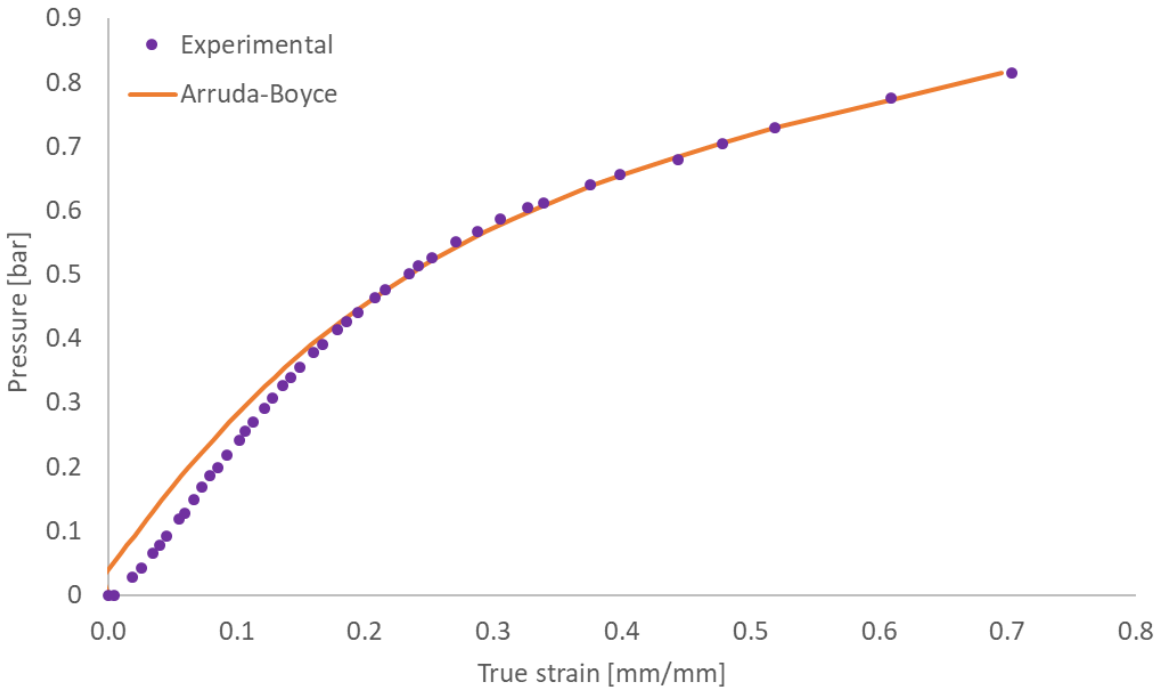

Figure 4-80: Bulge inflation pressure plotted over true strains in the dome.

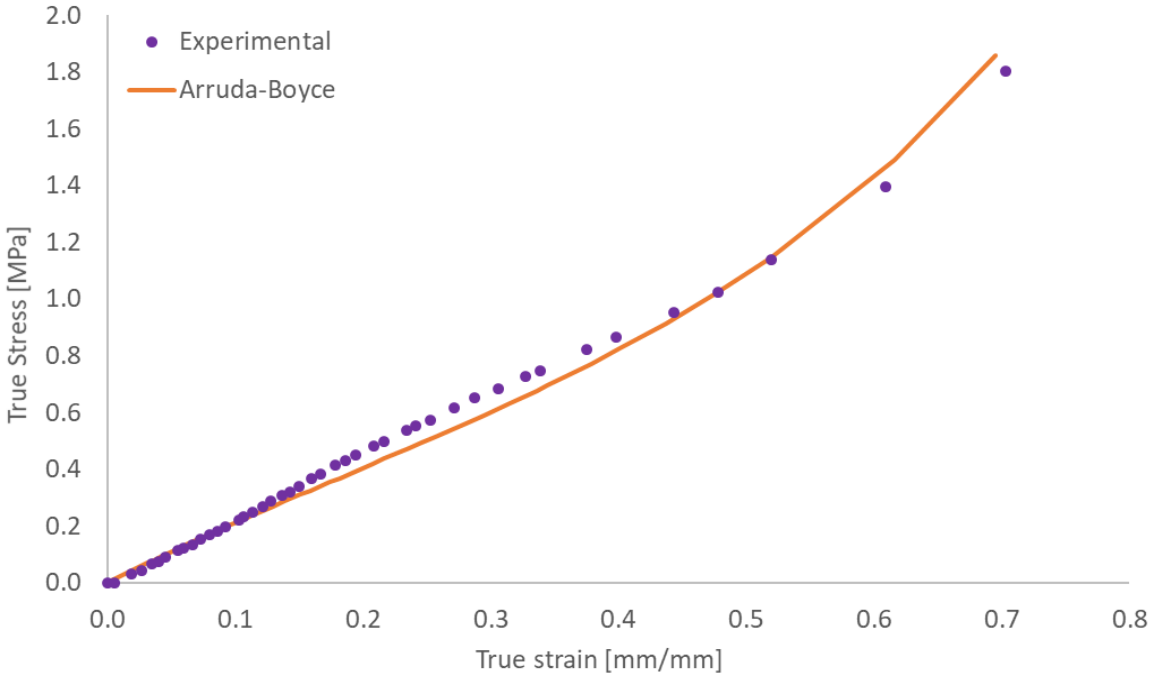

Figure 4-81: Simulated and experimental bulge test true stress-strain curves.

The relative error curve regarding stress-strain slop is presented in Figure 4-82 with a maximum value a bit higher than 20%.

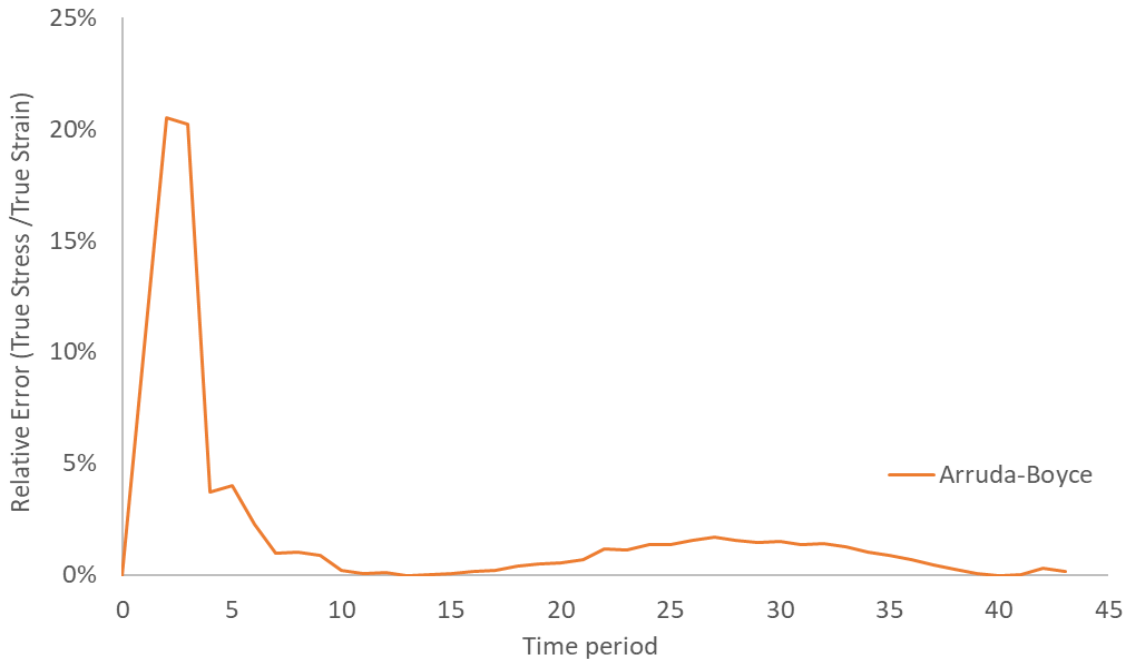

Figure 4-82: Relative error curves over analysis time period for bulge inflation.

4.3.3 Simple compression

The simple compression experiment was carried out aiming to compare its efficiency related to biaxial response. This test is known as not being uniform and can vary considerably due to the presence of irregularities and asperities on the specimen surfaces. For this reason, experiments were conducted in an oily and rough surface in order to be compared to FEA, where a thorough analysis took into account four different cases of simulation models, being two of them analyzed with biaxial stretch material response in the constitutive modeling under contact conditions of frictionless and no slippage between rubber and machine plates. Next, the other cases considered simple compression experiment data (oily and rough) in the constitutive modeling, but as the friction effects were already accounted in the material response only frictionless contact condition was analyzed.

From Figure 4-83, it is possible to analyze the difference between stiffness curves obtained through biaxial extension material data fitting. This happens because the experimental curves account for an intermediate level of unknown friction between contact conditions simulated.

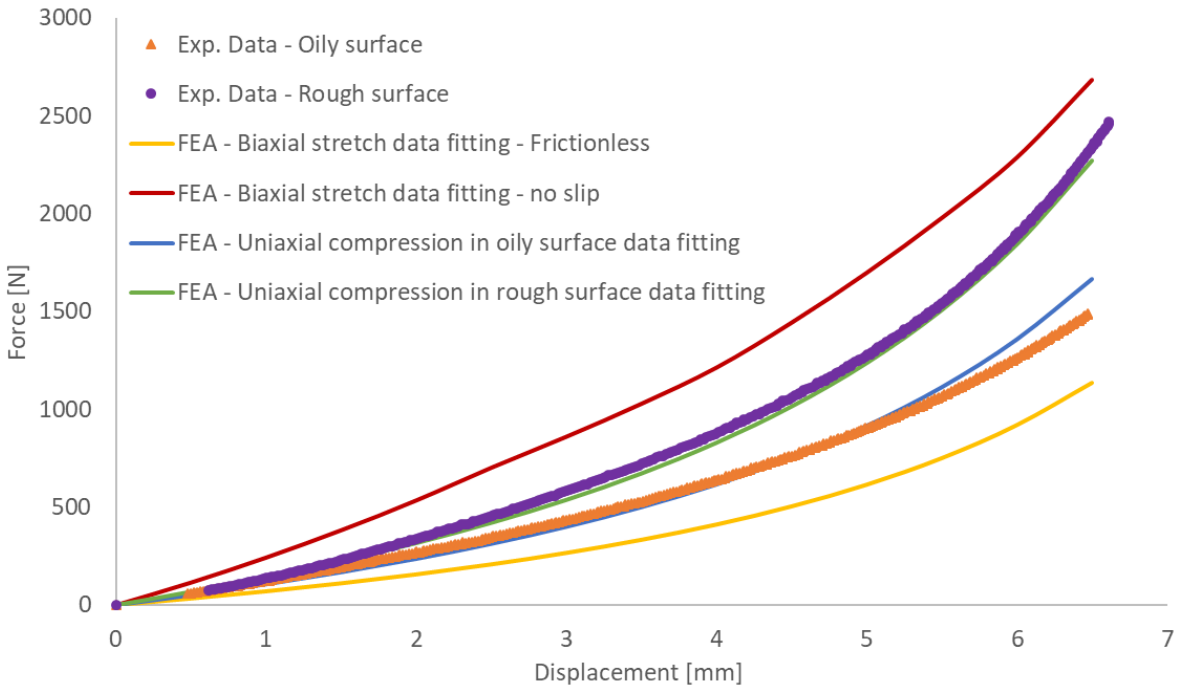

Figure 4-83: Simple compression stiffness curves according to material and contact condition.

Although simulated curves obtained through simple compression data fitting matched experimental curves, the deformation behavior and stress distribution did not agree with the physical phenomenon. This effect can be understood in Figures 4-84 to 4-87, which represent the four different cases simulated (biaxial data fitting and frictionless - case 1, biaxial data fitting and no slip - case 2, simple compression in oily surface data fitting - case 3, and simple compression in rough surface data fitting - case 4, respectively). It is worth paying attention that, for simple compression presented in Figures 4-86 and 4-87, they could not bulge around the specimen sides. This is incorrect, since this effect really exists due to friction between surfaces, and if the correct friction could be known, its effects could not be accounted by the constitutive material model in data fitting procedure.

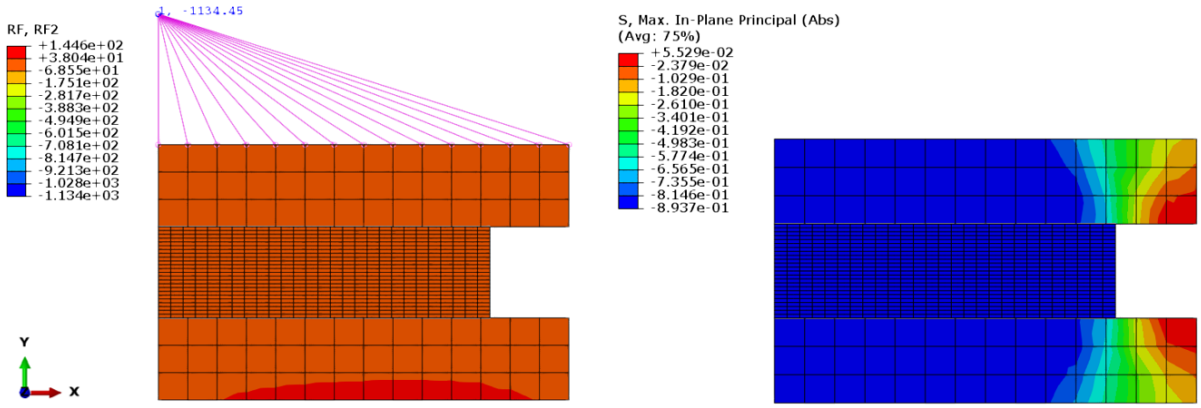

Figure 4-84: Simple compression mechanical behavior simulated under case 1.

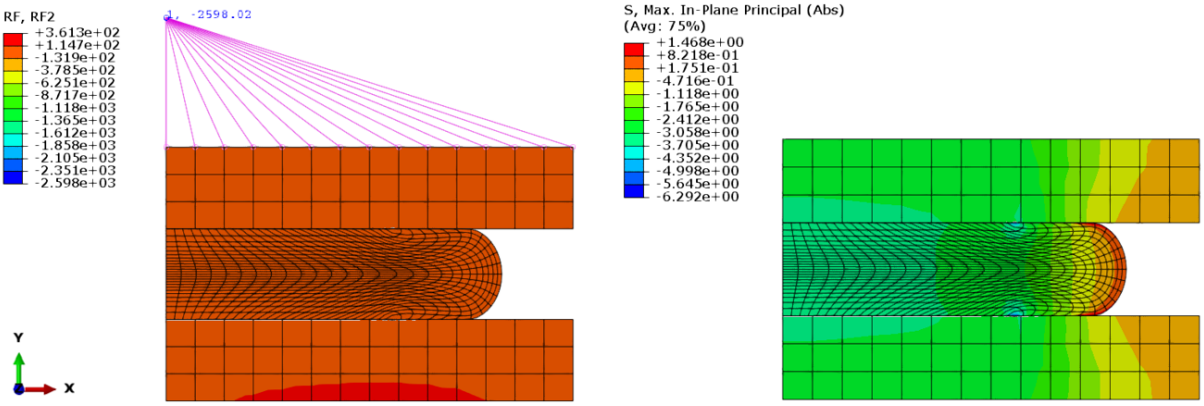

Figure 4-85: Simple compression mechanical behavior simulated under case 2.

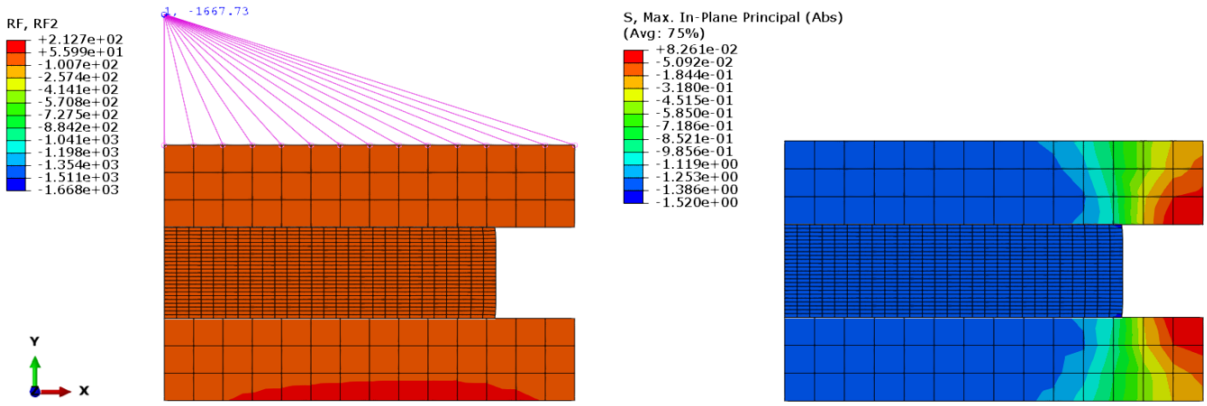

Figure 4-86: Simple compression mechanical behavior simulated under case 3.

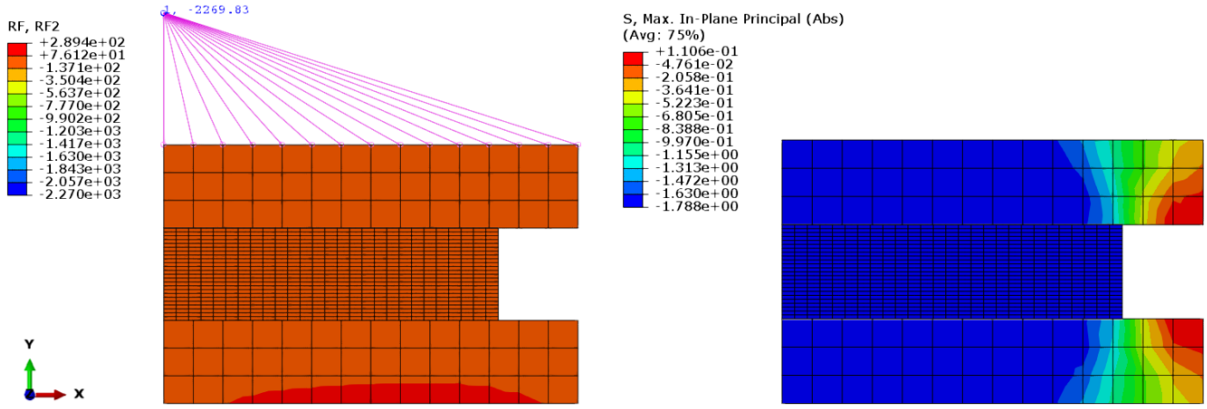

Figure 4-87: Simple compression mechanical behavior simulated under case 4.

Finally, taking into account the relation between equal biaxial and simple compression stress-strain response presented in equations (4-7) and (4-8), it is possible to compare the biaxial response obtained by simple compression under frictionless condition simulated in case 1 with cruciform extension and bulge inflation results. Final curves can be evaluated in Figure 4-88, where this comparison is only presented for sample B in order to show a detailed view between curves, and in Figure 4-89 where all biaxial responses obtained in the present Dissertation were plotted.

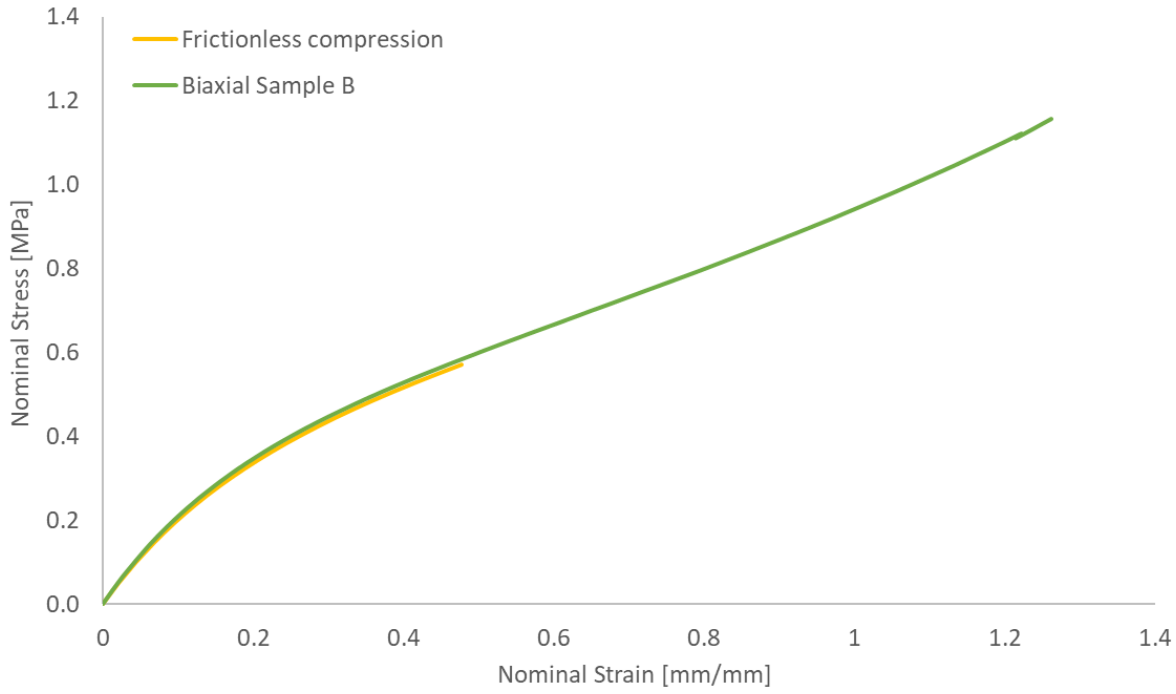

Figure 4-88: Case 1 simple compression and sample B cruciform extension biaxial response.

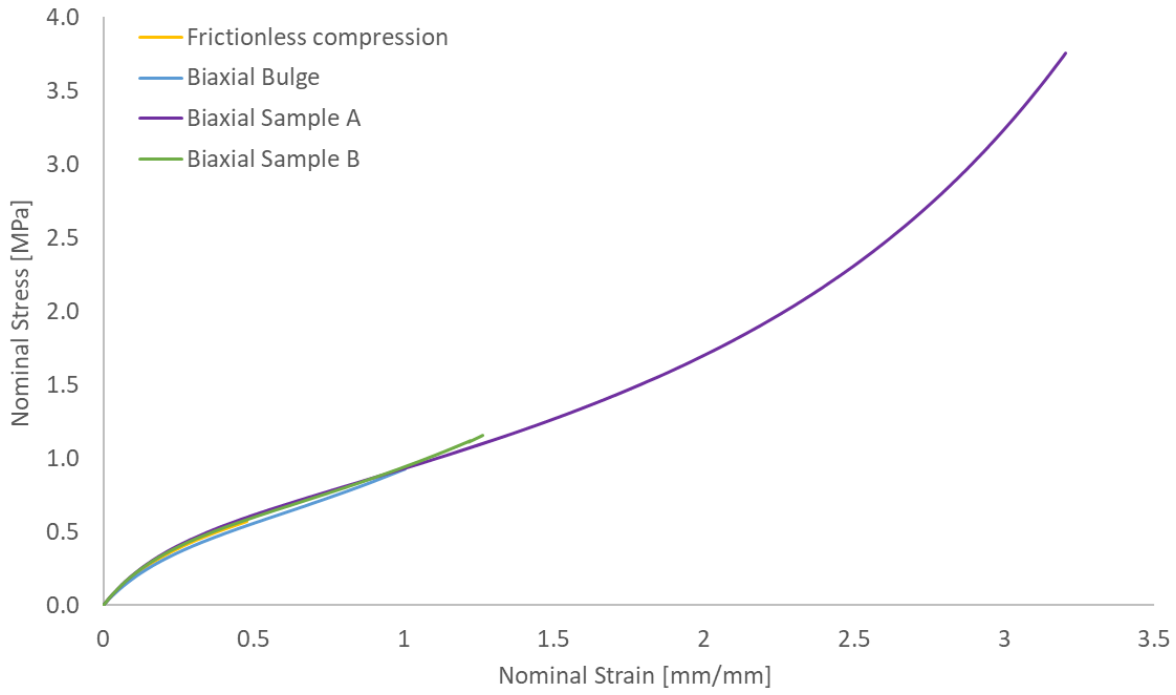

Figure 4-89: Case 1 simple compression compared with all biaxial responses.

4.4 Conical rubber spring experimental tests

Since one of the aims in the present Dissertation is to predict the mechanical behavior of a conical rubber spring by means of FEA, experimental tests were conducted in prototypes taking into account the axial and the radial loading conditions. In both situations, the curve was extracted after 3rd cycle when rubber properties became stable due to Mullins effect.

4.4.1 Axial loading

In the case of axial loading, the cyclically force-displacement responses in the spring were recorded up to a maximum force of approximately 40kN, as shown in Figure 4-90, at a high peak of displacement. Then, from cyclic curves the final stable axial stiffness is depicted in Figure 4-91, considering the last stable curve obtained in the 3rd cycle.

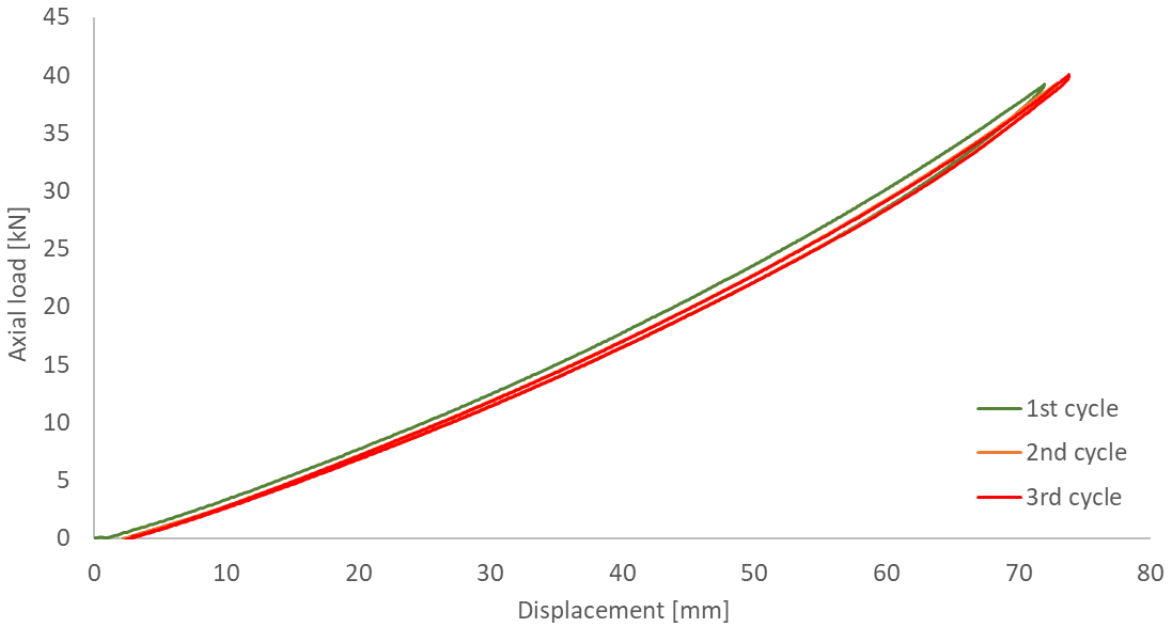

Figure 4-90: Conical rubber spring axial stiffness under cyclic loading

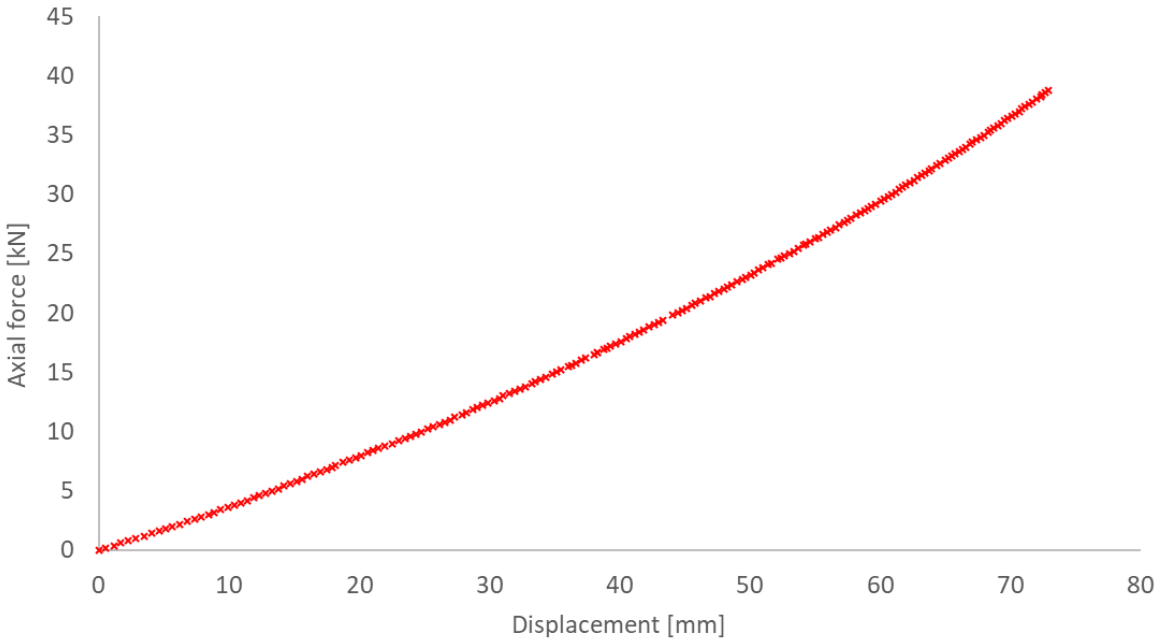

Figure 4-91: Conical rubber spring final stable axial stiffness curve

Based on NF EN 13913 (2004), axial stiffness should be calculated linearly according to the range described in section 3.2.2. The component must present a static vertical stiffness of 650 N/mm ± 15 %, which implies that the experimental response shown in Table 4-7 is in accordance with the target.

Table 4-7: Axial stiffness calculation between $AW0_{max}$ and $AW2_{max}$.

$AW0_{max}$ / $AW2_{max}$		
Load (kN)	Displacement (mm)	Stiffness (N/mm)
23.0	49.67	657
35.1	68.10	

4.4.2 Radial loading

In the case of radial loading, although the technical standard NF EN 13913 (2004) requests this test under a vertical preload of approximately 20kN, tests free of this pre-compression were also carried out in order to take its effects into account. The cyclically force-displacement responses were recorded up to a maximum displacement of 6mm, as shown in Figure 4-92 for the pre-compressed spring in radial stiffness and Figure 4-93 for the pre-compression free case.

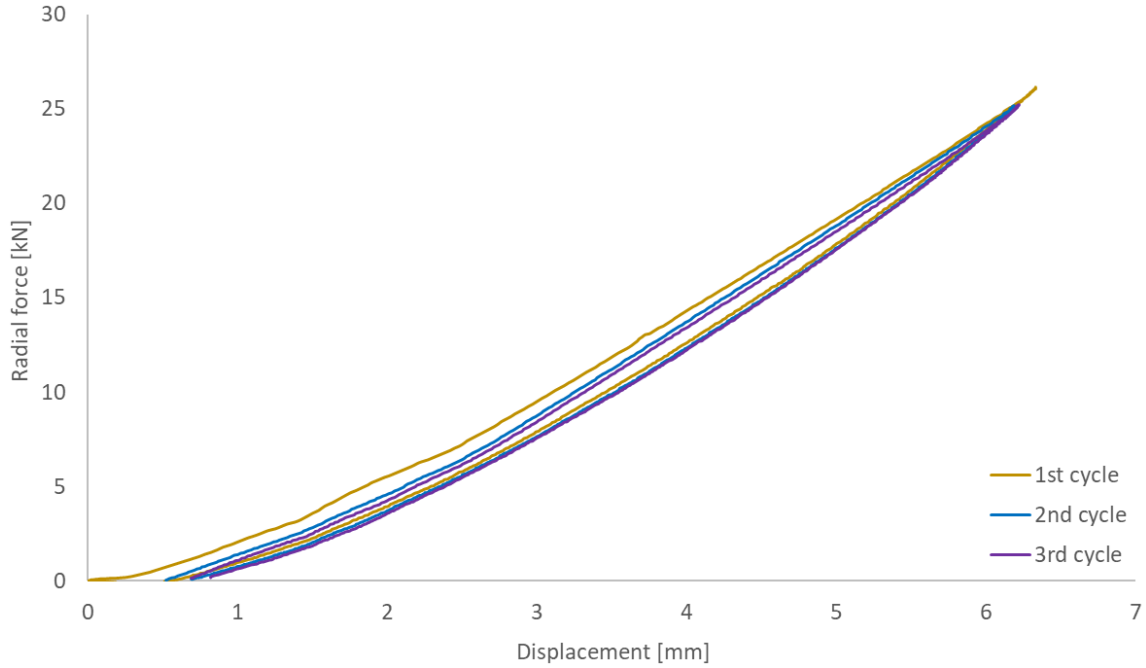

Figure 4-92: Pre-compressed conical rubber spring radial stiffness under cyclic loading.

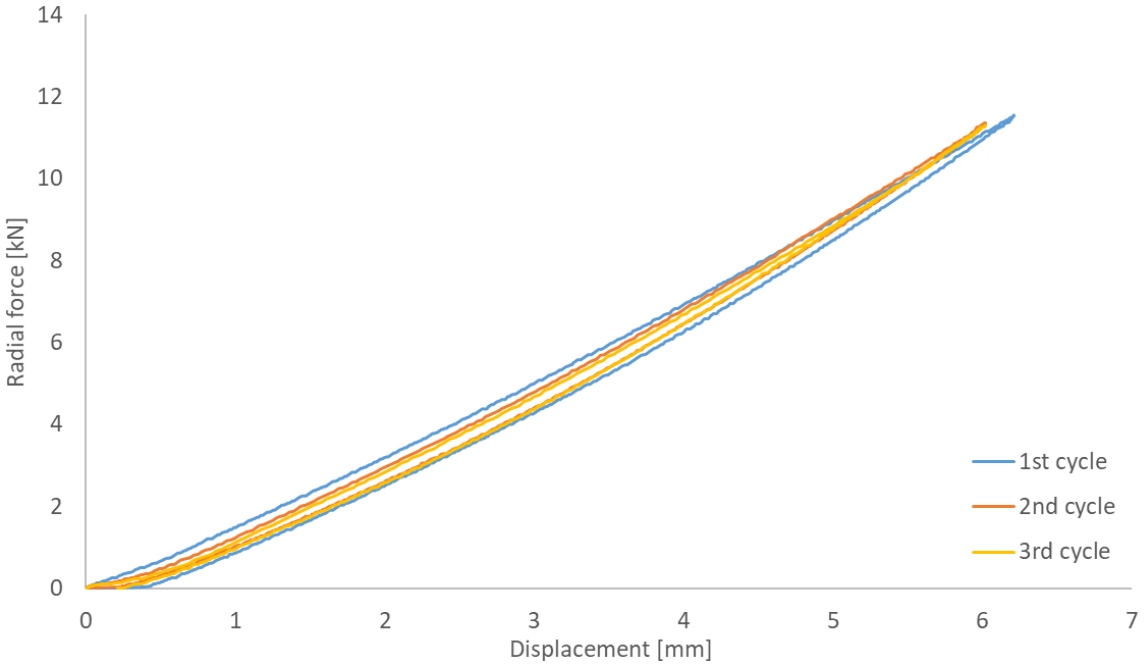

Figure 4-93: Pre-compression free conical rubber spring radial stiffness under cyclic loading.

From cyclic curves the final stable radial stiffness for both cases of vertical preload is plotted in Figure 4-94, considering the last stable curve obtained in the 3rd cycle. It is important to pay attention that, as the displacement gets higher the pre-compressed condition starts to show a

stiffness curve which is almost two times greater when compared with the pre-compression free case.

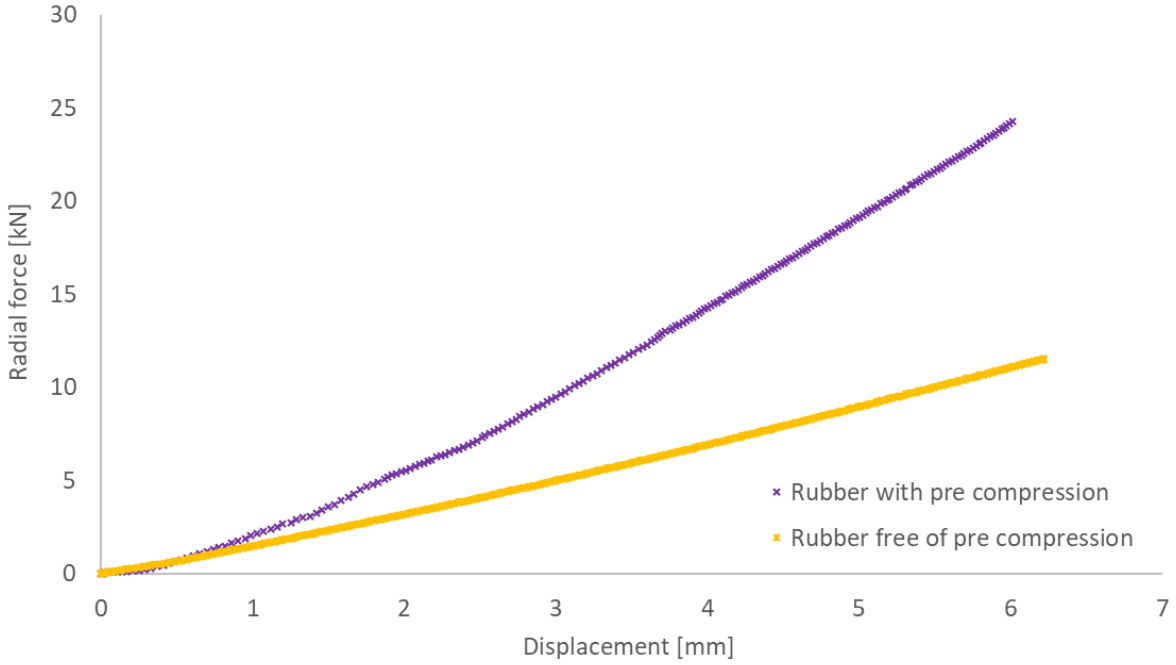

Figure 4-94: Conical rubber spring final stable radial stiffness curves

According to NF EN 13913 (2004) the component must present a static radial stiffness of 5600 N/mm ± 15 % under the vertical preload condition. Thus, from Table 4-8 it is possible to verify that the response is in accordance with the target.

Table 4-8: Radial stiffness calculation from pick to pick.

Pick to Pick		
Displacement (mm)	Load (kN)	Stiffness (N/mm)
6.00	26.05	4986
0.82	0.225	

4.5 Conical rubber spring Finite Element simulation

Since the aim of the present Dissertation is to understand rubber mechanical behavior under multiaxial deformation modes, experimental tests in a conical rubber spring were carried out in

the axial and radial directions and compared to FEA results, considering the hyperelastic constitutive laws obtained through uniaxial and biaxial experimental data. In addition, a pattern search optimization algorithm was implemented in the Abaqus® environment in order to find out the material parameters that best fit the prototype multiaxial deformation modes with the smallest possible error (as methodology described in section 3.3).

Based on an extensive research conducted by Lalo *et al.* (2019) on the performance of the classical constitutive models in the literature for the component in question, Arruda-Boyce model was chosen as the one which best correlated the prototype load-deflection experimental curve. From this assumption, comparative analyses were carried out in the material parameters here obtained.

4.5.1 Axial loading

When the spring was subjected to the axial loading large deflections were observed during the experimental tests. For this reason, taking into account the multiaxial deformations transferred to the rubber, three cases of data fitting were analyzed.

The first case, which was named as case 1, fitted the material model considering uniaxial tensile test and cruciform biaxial extension in sample A, being the theoretical curves compared to the experimental data in Figure 4-95 for the uniaxial deformation mode and in Figure 4-96 for the biaxial mode. Next, the second case (case 2) considered the uniaxial tensile test together with cruciform biaxial extension in sample B, where theoretical curves can be compared to the experimental data in Figure 4-97 for uniaxial direction and Figure 4-98 for the biaxial one. Finally, considering that in many situations the material curve is only fitted according to the uniaxial test data due to its test simplicity, a third case (case 3) was analyzed taking into account only its effect, being shown in Figure 4-99.

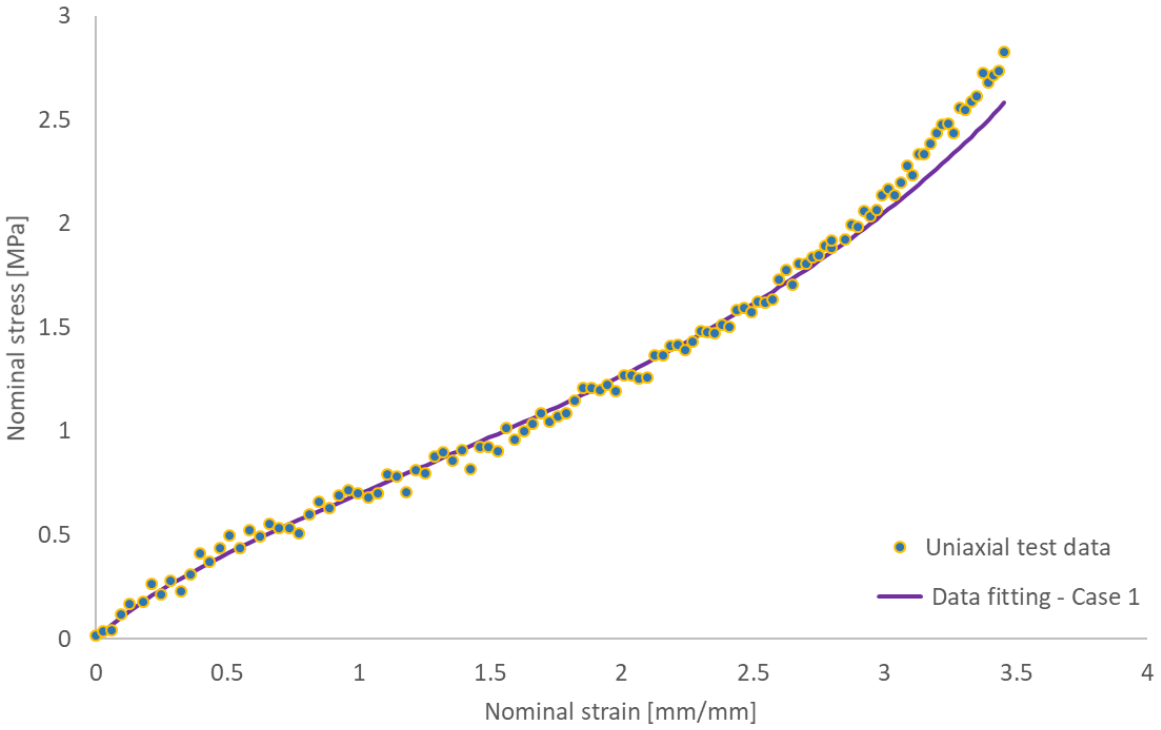

Figure 4-95: Uniaxial stress-strain curve prediction according to data fitting of case 1.

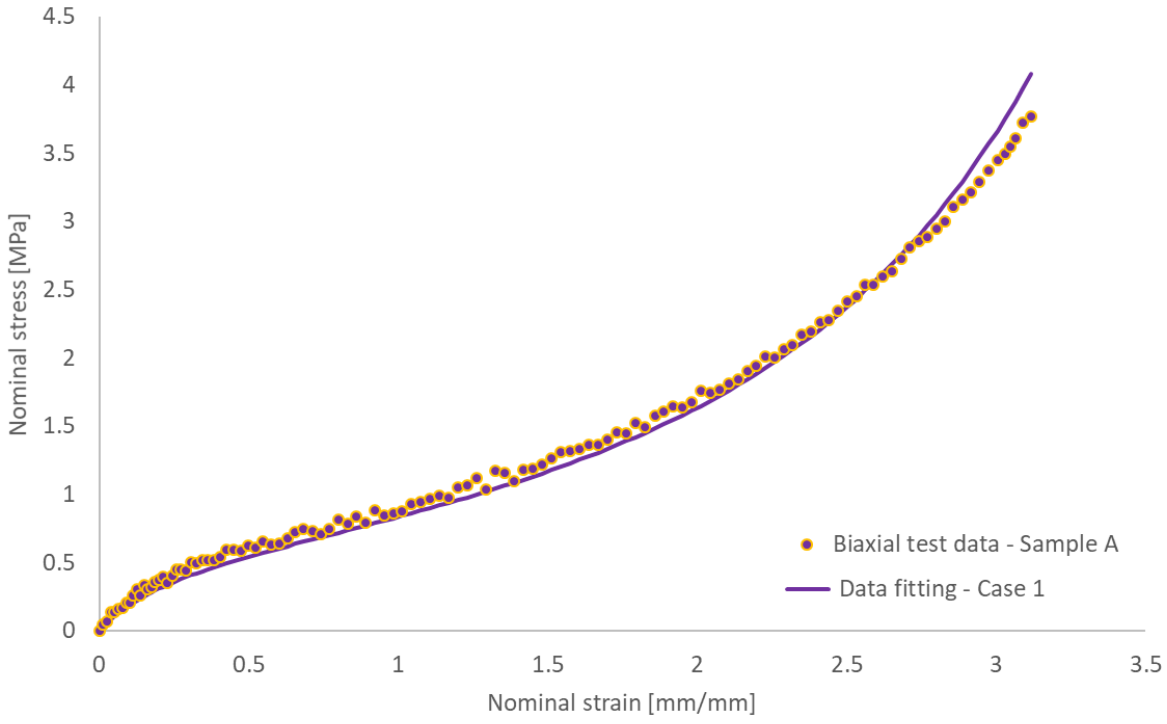

Figure 4-96: Biaxial stress-strain curve prediction according to data fitting of case 1.

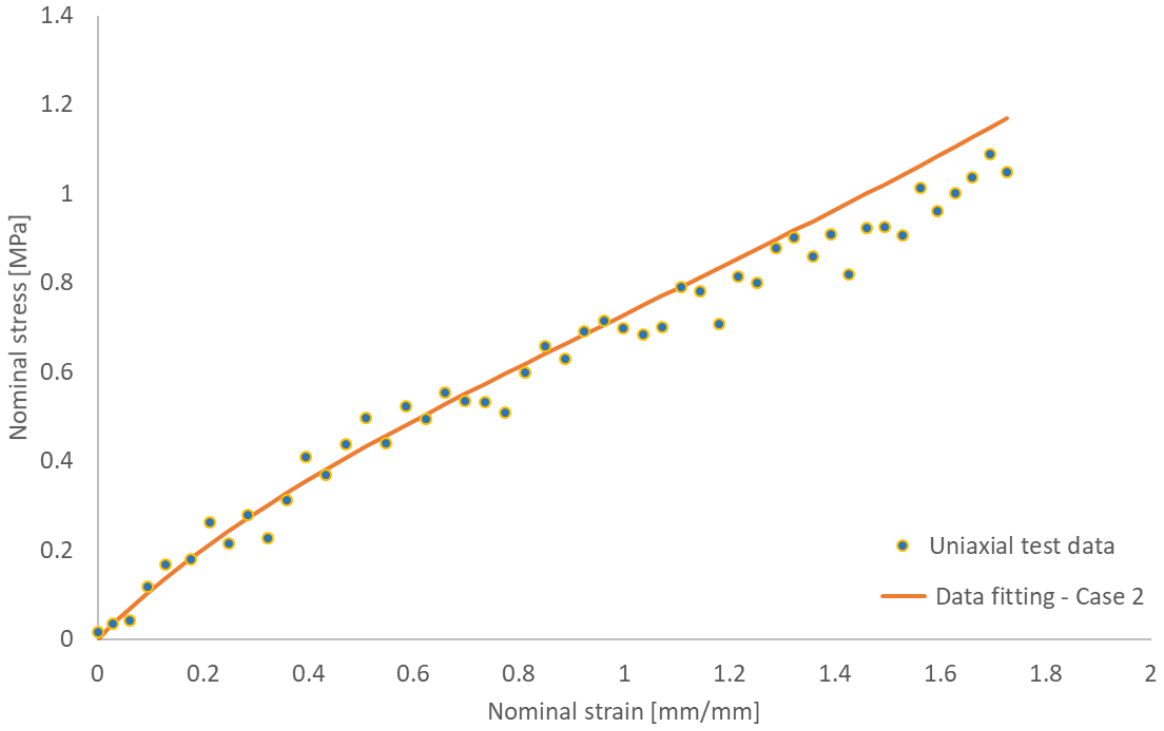

Figure 4-97: Uniaxial stress-strain curve prediction according to data fitting of case 2.

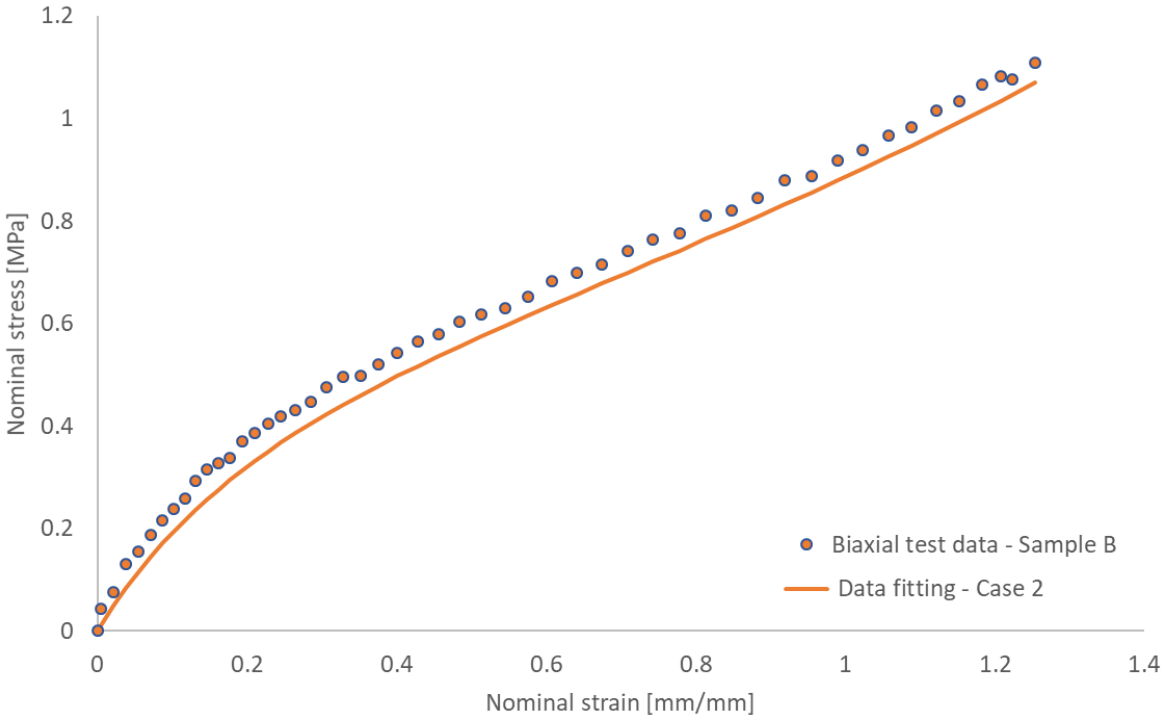

Figure 4-98: Biaxial stress-strain curve prediction according to data fitting of case 2.

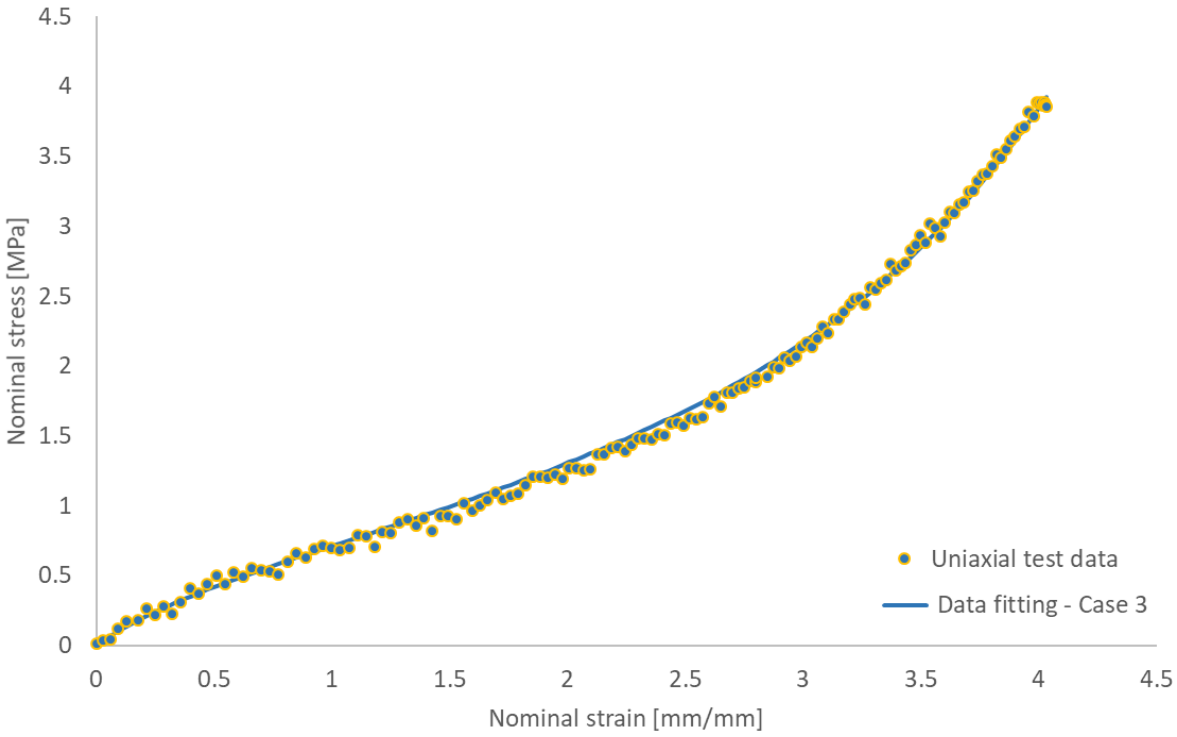

Figure 4-99: Uniaxial stress-strain curve prediction according to data fitting of case 3.

Since the curve fitting method was implemented aiming to minimize the relative and absolute errors, it is important to mention that the number of points and strain levels should be equivalent in uniaxial and biaxial extension experiments. This assumption has to be considered in order to minimize the tendency for a better fit in one test compared to another, since the errors are counted as the sum of each point of the experiment.

Although rubber material could be considered as almost incompressible due to its quantity and type of carbon-black, FE computational simulation was first run based on optimized material parameters obtained through prototype experimental data. The optimization process was conducted together with Arruda-Boyce model where material parameters were assigned as design variables in the pattern search algorithm, which returned a Poisson's ratio equal to $\nu = 0.4985$. Thus, Table 4-9 shows the comparison between materials analyzed taking into account the constitutive coefficients obtained in cases 1,2 and 3, with the volumetric behavior calculated from the optimum FEA.

Table 4-9: Material constants comparison between cases 1, 2, 3 and optimum FEA.

Arruda-Boyce model	μ	λ_L	D
Optimum FEA	0.345	2.98	0.01622
Case 1	0.367	3.60	0.01559
Case 2	0.375	3.26	0.01508
Case 3	0.395	3.44	0.01441

According to Figure 4-100, it is possible to compare the undeformed (a) and deformed (b) shapes. The maximum magnitude displacement value occurs around the metal axle, more exactly at the point where the concentrated load was applied. Although the rubber section undergoes large strains, it still keeps a reasonable shape, without excessive distortion.

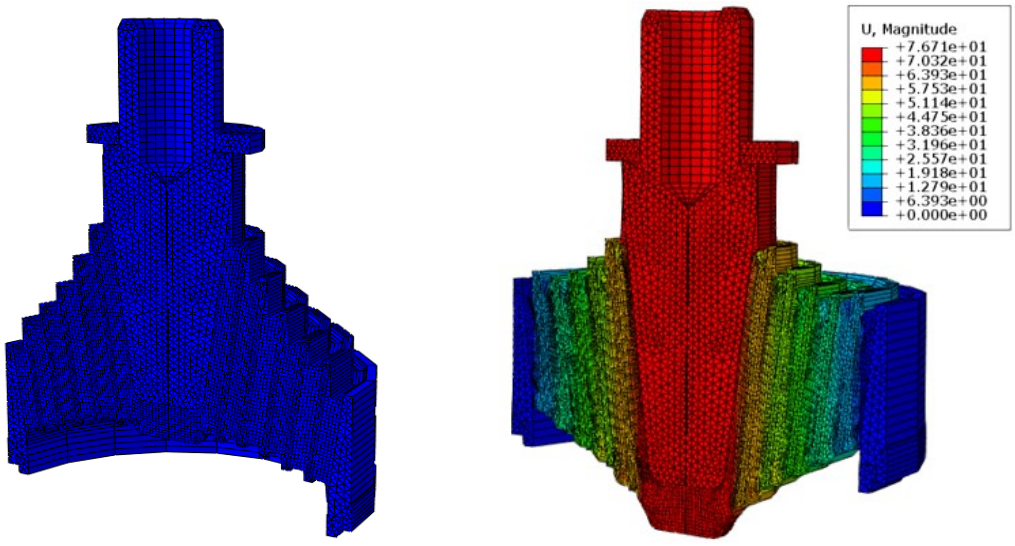

(a) (b)

Figure 4-100: Conical rubber spring deflection [mm] under axial load: (a) undeformed shape and (b) deformed shape.

For a better visualization of the deformed geometry in the vertical direction, Figures 4-101 and 4-102 show respectively the final shape in front view for axial displacements and von Mises equivalent stresses distributions to ensure that there is no plasticity phenomenon in the steel parts.

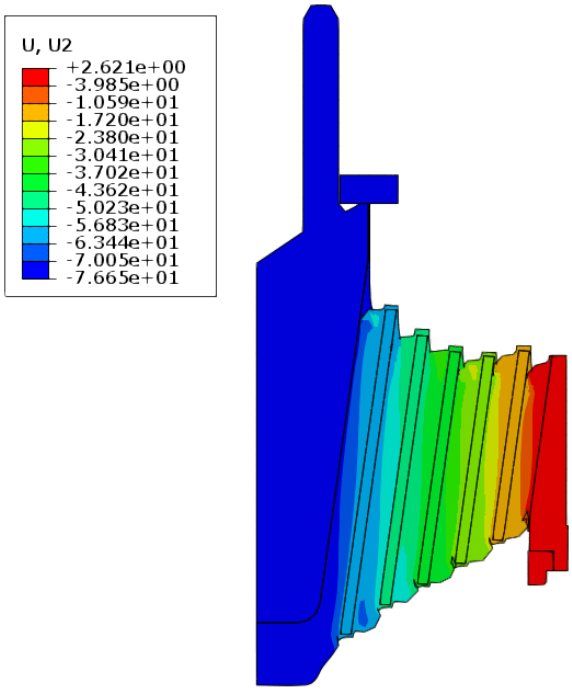

Figure 4-101: Conical rubber spring vertical displacements distribution [mm].

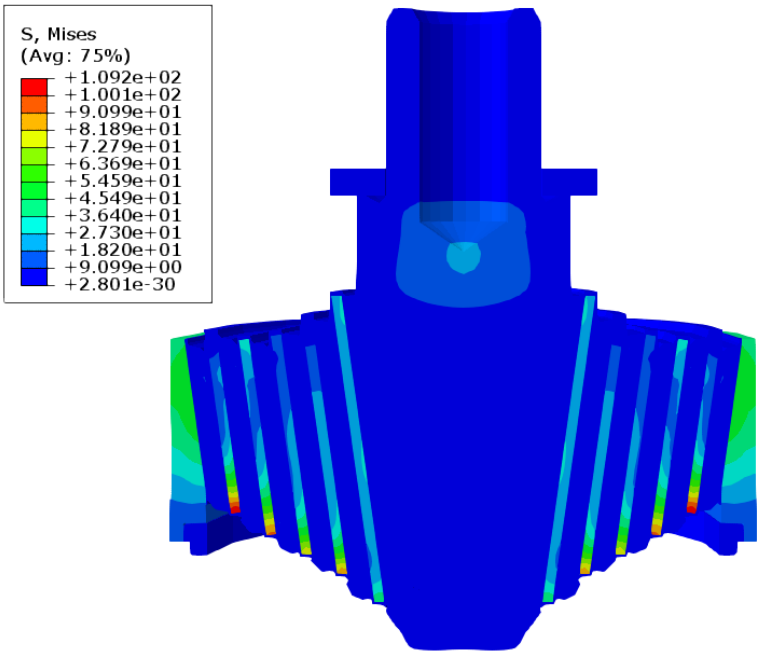

Figure 4-102: Conical rubber spring von Mises equivalent stresses distribution [MPa] under axial loading.

From load-deflection curves in Figure 4-103, it is possible to note that case 3 presented the worst accuracy among other cases of data fitting, whereas case 1 presented the best correlation when compared to the optimized models and experimental data. This really makes sense, as case 1 considered both deformation modes uniaxial and biaxial for higher levels of strain.

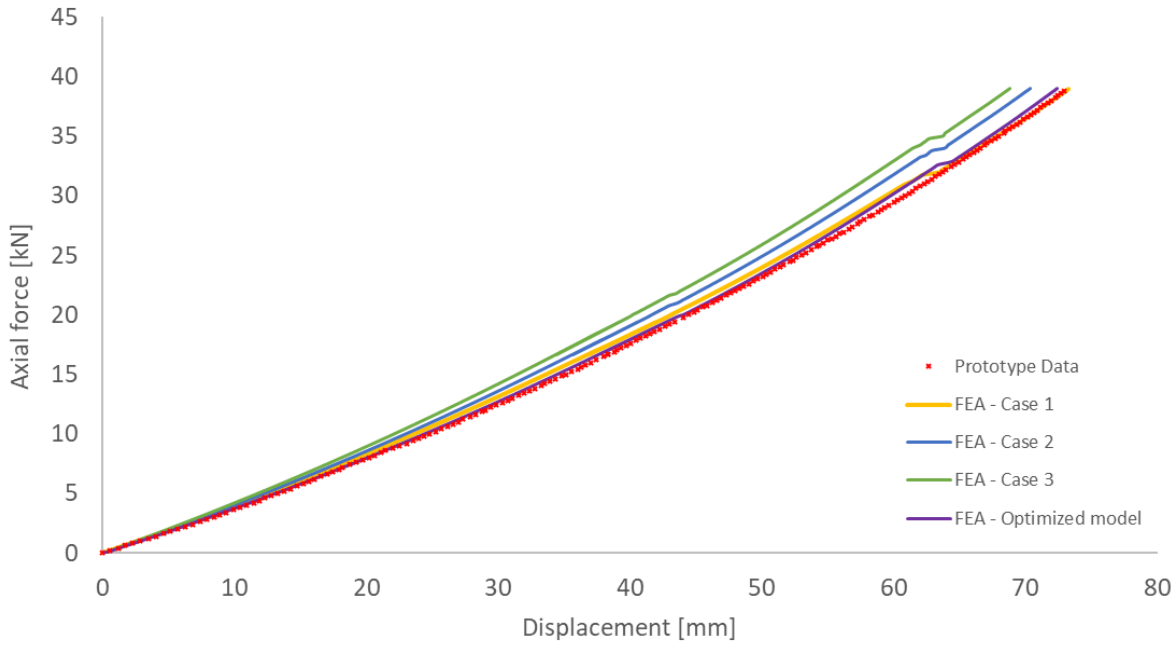

Figure 4-103: Conical rubber spring prototype experimental data compared to Arruda-Boyce model under axial deflection.

The optimization algorithm efficiency in relation to data fitting from case 1 can be proved when relative and absolute errors are evaluated over the analysis as shown respectively in Figures 4-104 and 4-105. Although the optimized model allows a more accurate adjustment, the prototype test data will always be necessary for the material characterization, aiming as an objective function minimizing the error between the curves computed by the area difference. This is a huge problem when a new component is under development process and there is no experiments. For this reason, the solution of case 1 can be considered as a great option when predicting an elastomeric component behavior with a reasonable accuracy.

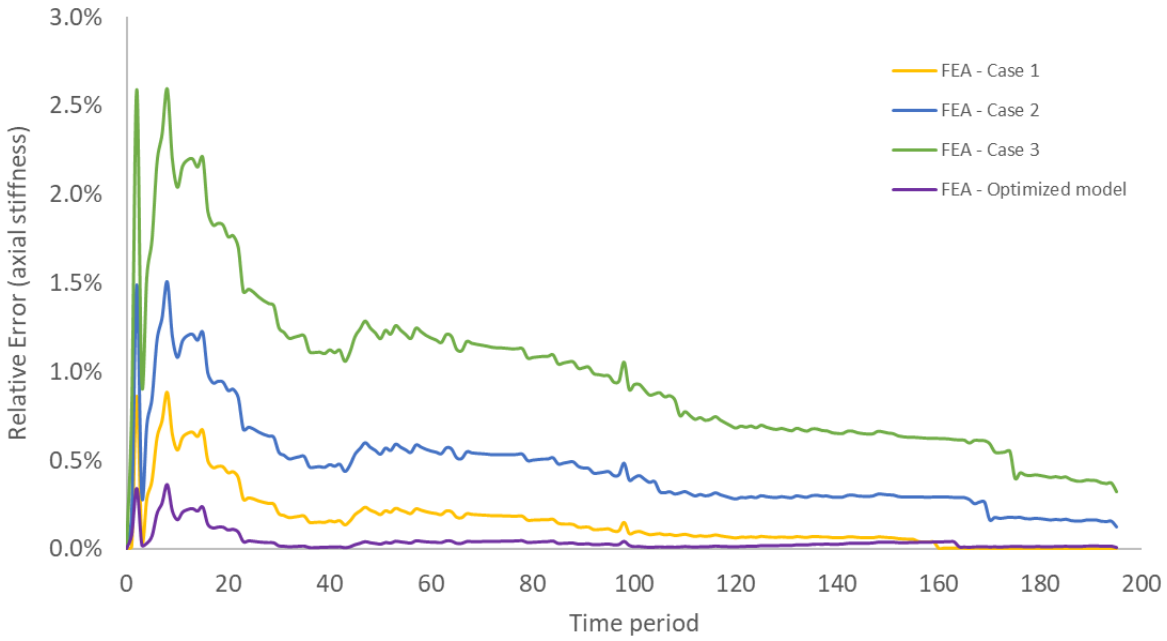

Figure 4-104: Arruda-Boyce model relative errors over analysis for axial stiffness.

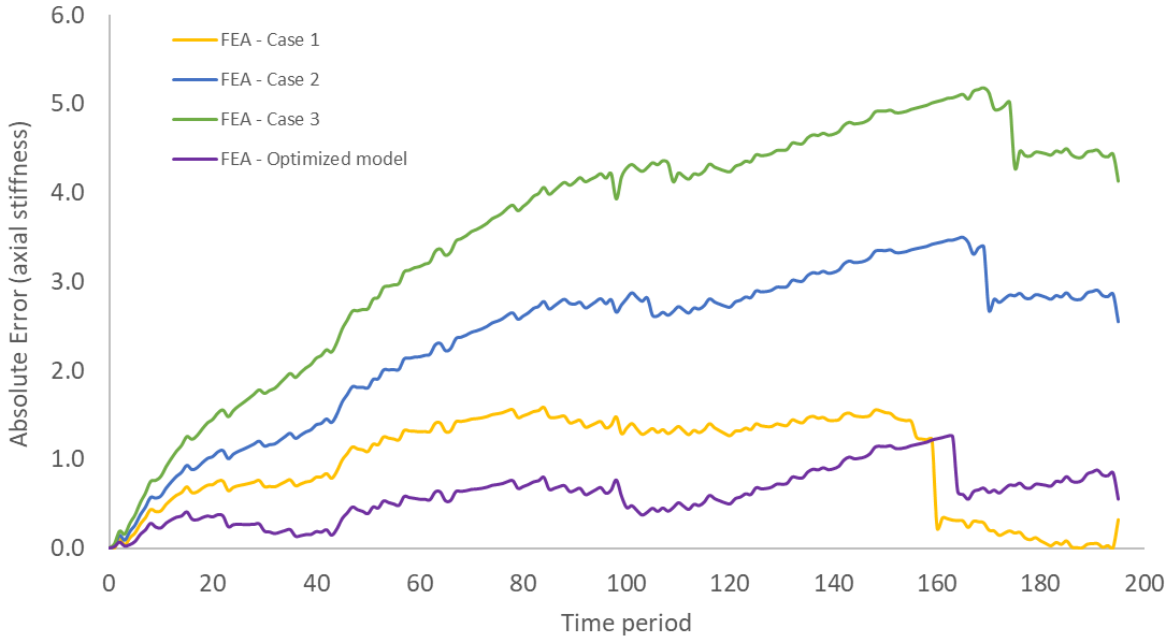

Figure 4-105: Arruda-Boyce model absolute errors [N/mm] over analysis for axial stiffness.

4.5.2 Radial loading

Considering the annular geometry of the conical rubber spring, another important loading direction was considered in order to evaluate a different type of multiaxial deformation mode. In this case the spring was subjected to a radial deflection taking into account two different situations of pre-loading. Initially, a pure displacement of 6mm was radially imposed in the component without any effect of pre-compression loading. After that, an axial compressive pre-load of 20kN was applied before the imposed radial deflection.

From the pattern search optimization algorithm, accurate fitted hyperelastic material coefficients were obtained according to the experimental radial stiffness under the pre-compression free condition. In this case, it is important to mention that, although Arruda-Boyce model performed very well under axial loading, it could not find any parameters to fit the radial stiffness curve accurately. This shortcoming occurred because of some limitations of the model regarding the order of the data fitting, in which is based on μ and λ_l to control the initial and final slopes of the entire theoretical curves. For this reason, considering the number of parameters available in the Yeoh material model and its performance in relation to strain ranges stability, it was adopted and could be able to match the component simulation with experimental curve.

As a result, the Yeoh material parameters for this case of loading are shown according to Table 4-10, while the final deformed shape can be seen in Figure 4-106 followed by von Mises equivalent stresses distributions in Figure 4-107. From the material coefficients obtained, it is possible to infer a change in the volumetric behavior, since the Poisson's ratio has now a value of $\upsilon = 0.4933$.

Table 4-10: Yeoh material constants for the pre-compressed free radial stiffness.

Yeoh model	C_{10}	C_{20}	C_{30}	D
Optimum FEA	0.526	6.578	1.800	0.25546

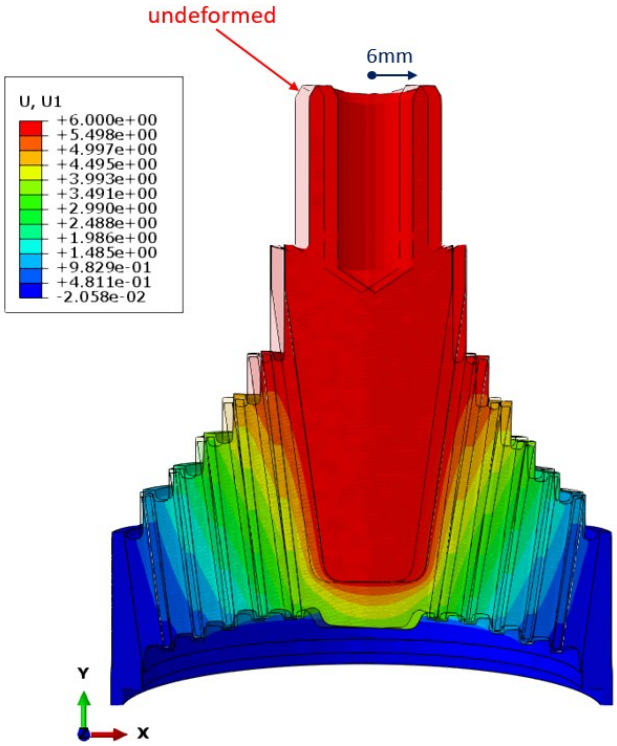

Figure 4-106: Conical rubber spring radial deflection [mm] in the pre-compression free condition.

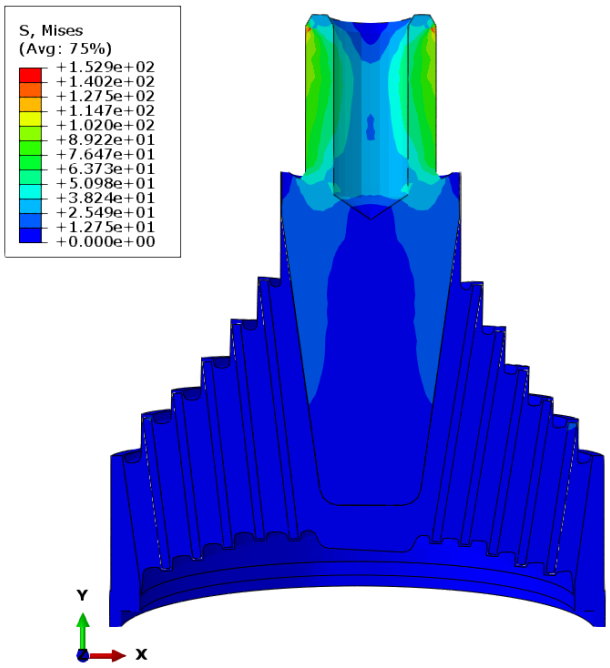

Figure 4-107: Conical rubber spring von Mises equivalent stresses distribution [MPa] under radial loading in the pre-compression free condition.

Considering the material model and its parameters obtained by the implemented optimization algorithm for axial deflection (see section 4.5.1) and analyzing the results in Figure 4-108, it is possible to note a great difference in the radial stiffness curve when compared to the experimental data. This is because the material model used in the previous loading mode is no longer capable of reproducing the results with the same accuracy for the current multiaxial deformation mode, being the reason why Yeoh model started to be implemented for radial loading simulation. In this situation, the inner conical sleeves are displaced towards the fixed outer sleeve, causing a bulge effect outwards at the free ends due to bulk incompressibility of the rubber. This behavior caused both deviatoric and volumetric changes in the material due to friction effects.

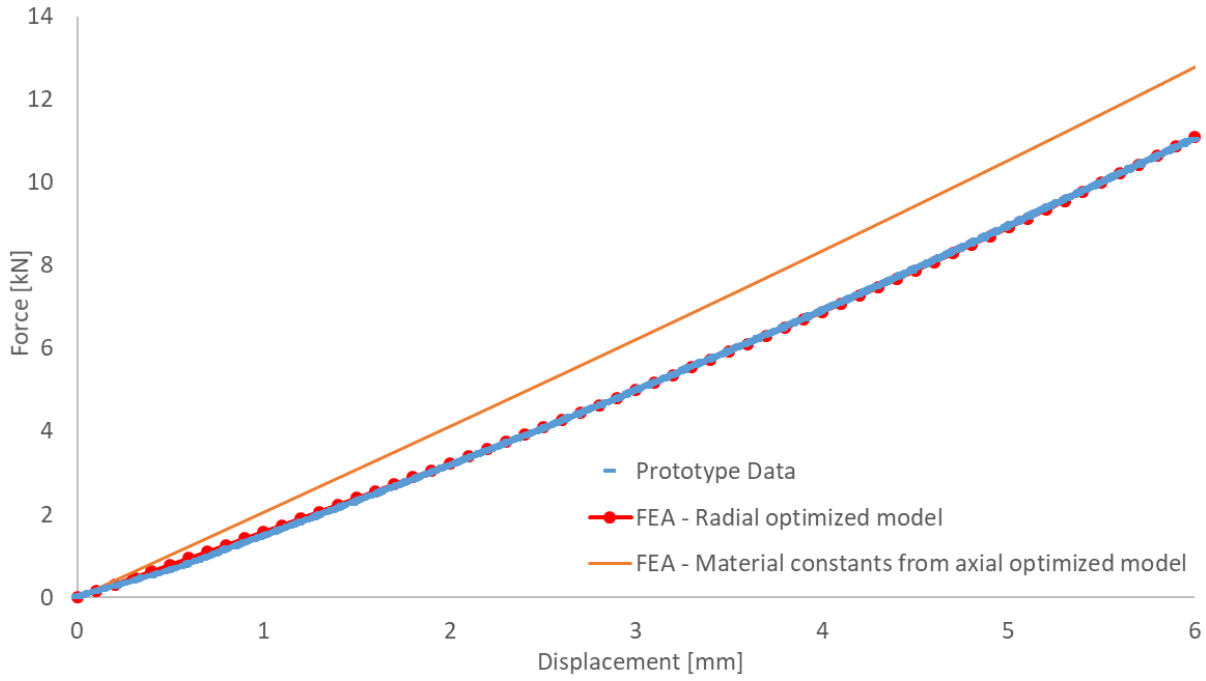

Figure 4-108: Conical rubber spring prototype experimental data compared to FEA under pre-compression free radial loading.

As far as the pre-compressed condition is concerned, the same optimization procedure for material fitting was carried out, but because the mesh deformed significantly from its original configuration after axial preload, a solution mapping technique was applied. As explained in section 3.3.5 the FE simulation for this loading condition was performed in two analysis steps.

Considering the good accuracy provided by Arruda-Boyce model during the vertical deflection, the first step was able to provide reliable results without much effort. The final axial displacements concerning this first step with a detailed view of the distorted mesh is shown in Figure 4-109. Then, based on the deformed shape obtained, a remesh procedure was conducted taking care to not generate significant discontinuities in relation to the old mesh. The regenerated and better quality mesh can be analyzed in Figure 4-110.

It is really worth mentioning that very high discontinuities between old and new meshes means that the mesh can be too coarse or that the remeshing procedure should have been done at an earlier stage before too much distortion occurred.

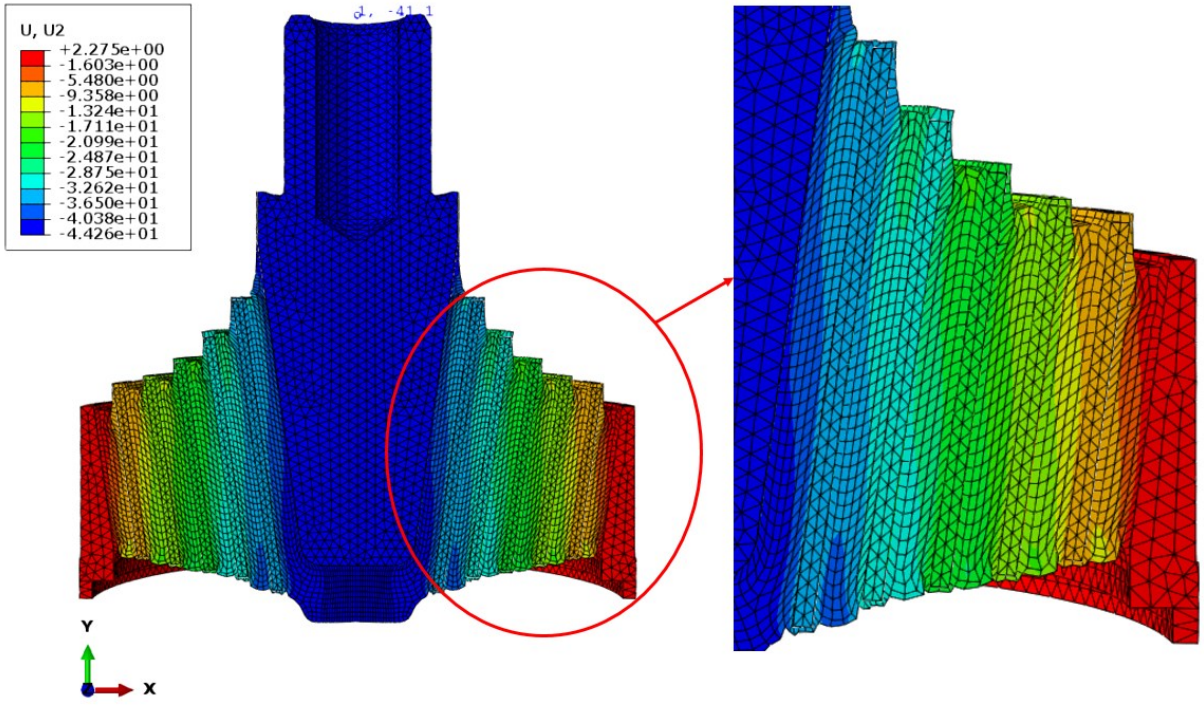

Figure 4-109: Deformed conical rubber spring [mm] and distorted mesh after vertical preload.

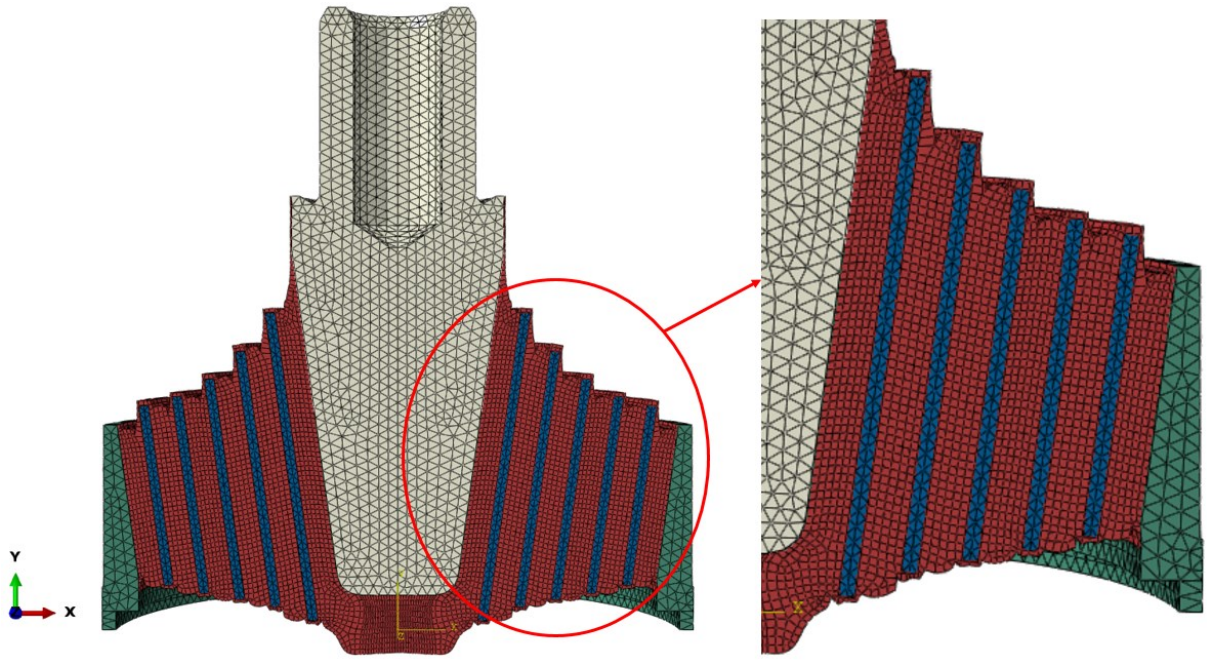

Figure 4-110: Conical rubber spring regenerated mesh after vertical preload.

Based on step 1 results, the same radial deflection of 6mm was analyzed in the second step, where only Yeoh model could have a reasonable performance in terms of material coefficients during optimization process. This means that, it is possible to infer that rubber can lead to different properties depending on the multiaxial deformation mode that it was subjected.

Furthermore, bulk compressibility has an important effect on the radial stiffness due to bulge effect occurred under compression, which is accentuated by the vertical preload. Consequently, Poisson's ratio is able to modify the mechanical behavior predicted by the FEA of rubber components and give rise to the accuracy of the simulation result.

From this point, the final deformed shape is presented by Figure 4-111 and the von Mises equivalent stresses distributions can be seen in Figure 4-112. It is important to mention that, the maximum yield strength of the metal parts is 530MPa and for this reason they worked only in the linear elastic regime.

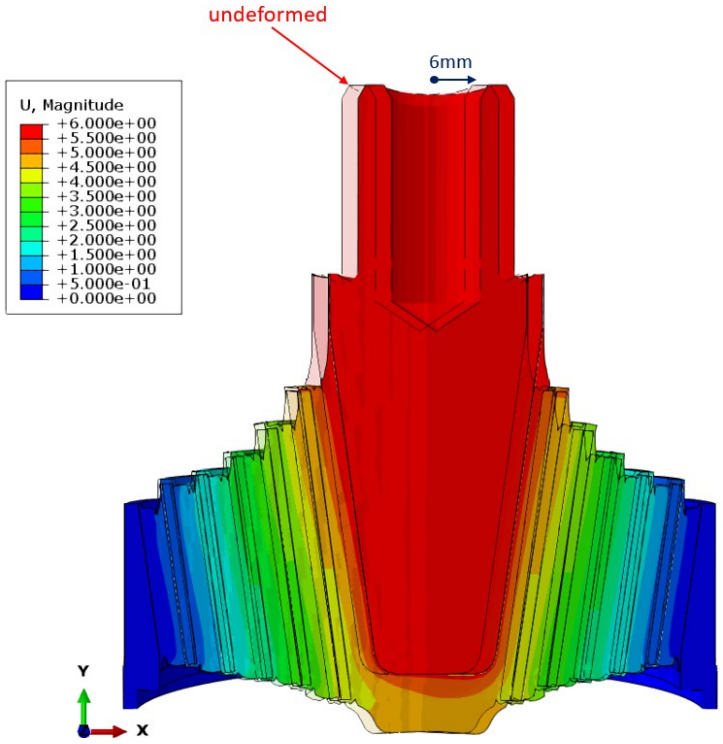

Figure 4-111: Conical rubber spring radial deflection [mm] considering the vertical pre-compression loading condition.

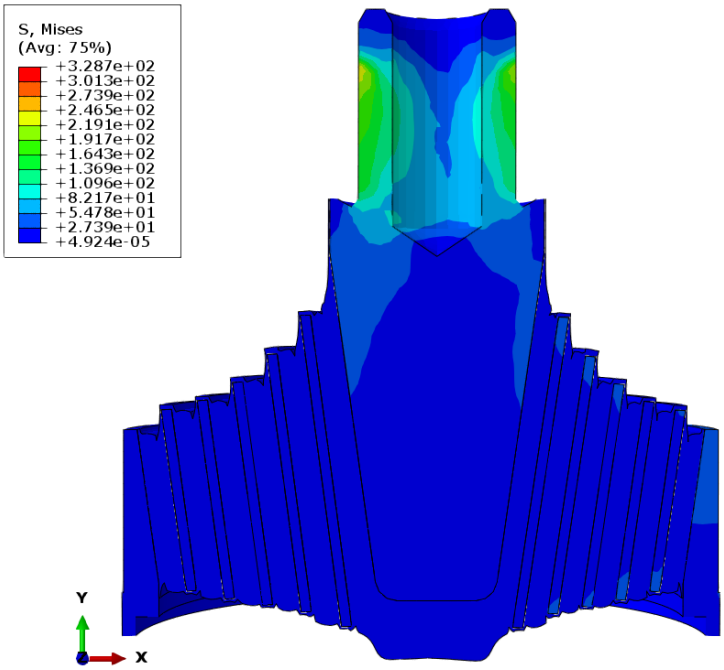

Figure 4-112: Conical rubber spring von Mises equivalent stresses distribution [MPa] under vertical pre-compression and radial deflection.

Finally, the simulated radial stiffness curves compared to the experimental data under a vertical preload are plotted according to Figure 4-113. It is possible to observe that, there was an increase in the difference between curves of the model simulated with material parameters obtained by optimization process in axial loading and prototype test. On the other hand, if only the pre-compression effect is analyzed during radial deflection, the correlation between FEA with material parameters free of pre-compression (Table 4-10) and optimized material model taking into account the axial pre-compression effect (Table 4-11) becomes acceptable up to displacements of 2mm. This means that, the pre-compression effect due to vertical preload influences the rubber behavior only under higher levels of deformation.

Table 4-11: Yeoh material constants for the radial stiffness under pre-compression.

Yeoh model	C_{10}	C_{20}	C_{30}	D
Optimum FEA	0.0557	19.178	22.500	0.25546

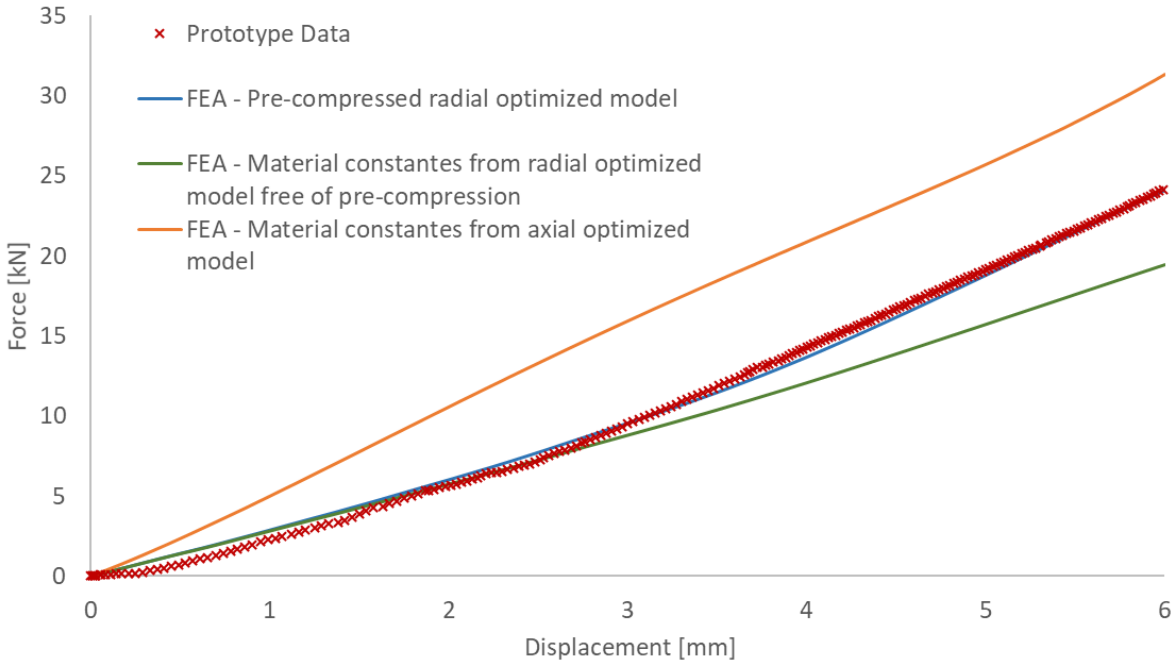

Figure 4-113: Conical rubber spring prototype experimental data compared to FEA under pre-compression and radial deflection.

4.6 Conical rubber spring analytical solution

Considering that the performance of a product is influenced by elastomer compression modulus and its geometry details, an analytical solution for radial stiffness was proposed according to the methodology described in section 3.4.

Since the conical rubber spring under study has a complex design, the main geometric properties required to fulfill equation (3-24) were extracted direct from Siemens NX® CAD software. Based on a combination of laminate and tube form bearings for planar sandwich shapes, the loaded conical area for each layer was adopted according to Figure 4-114, whereas the respective rubber thickness returned a constant value of approximately 10mm for all layers involved by the spring, as presented in Figure 4-115. Table 4-12 represents the exact loaded area values extracted for each layer.

Table 4-12: Loaded area according to each layer of the conical rubber spring.

Layer number	Loaded Area (A_L) [mm^2]
N1	10358.01
N2	13722.63
N3	15115.86
N4	16321.23
N5	17474.32
N6	18673.68

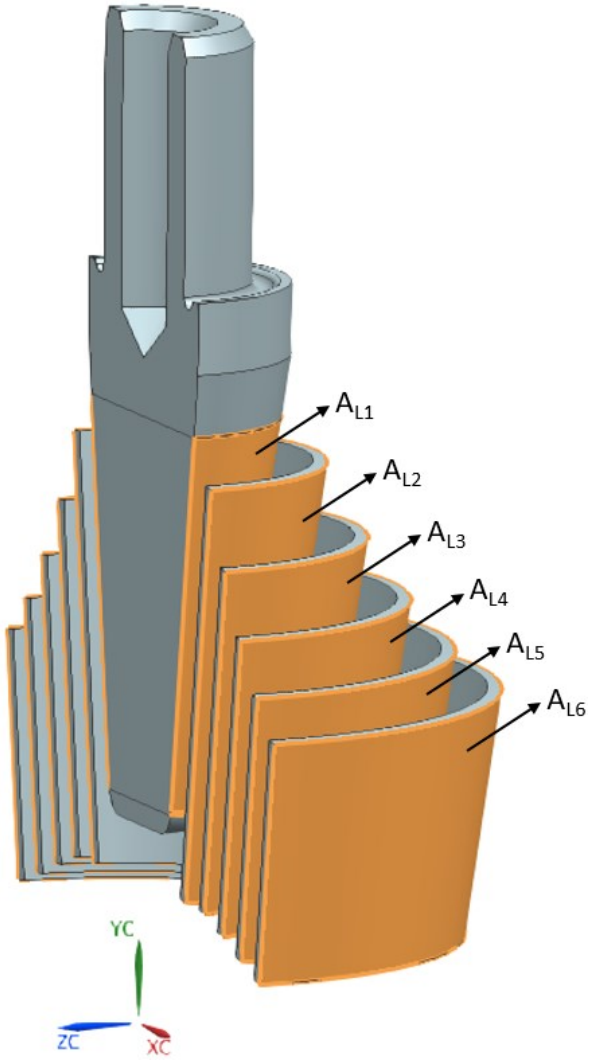

Figure 4-114: Representation of the loaded area for each rubber layer.

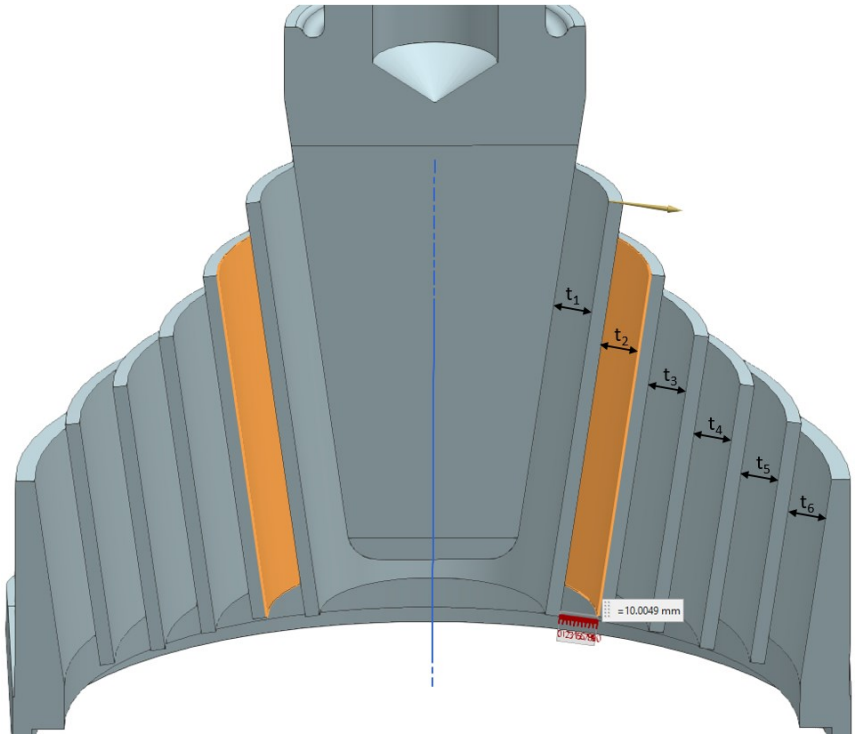

Figure 4-115: Representation of the rubber thickness for each conical layer.

Taking into account the complexity of calculating E_c, at least an uniaxial tensile test should be performed in order to estimate the shear modulus from material parameters obtained through a given hyperelastic constitutive model.

Based on data fitting already conducted for uniaxial extension and its respective parameters defined in Table 4-1, it is possible to define the initial Young's modulus E_0 - equation (4-9) - through the simple relation described in equation (3-26). Since the Arruda-Boyce model presented stability for all strain levels and returned a reasonable fitted curve, an initial shear modulus of $\mu_0 = G = 0.4385$ was adopted. In addition, considering the compressibility degree of Table 2-2, a value of $\upsilon = 0.4995$ was also defined.

$$E_0 = 2.0.4385.(1 + 0.4995) = 1.3152 \text{ MPa} \tag{4-9}$$

The coefficient ϕ is an empirically determined material property, which was included here to correct the experimental deviation from theoretical equations. It is dependent on the E_0 according to the relation curve represented by Figure 4-116.

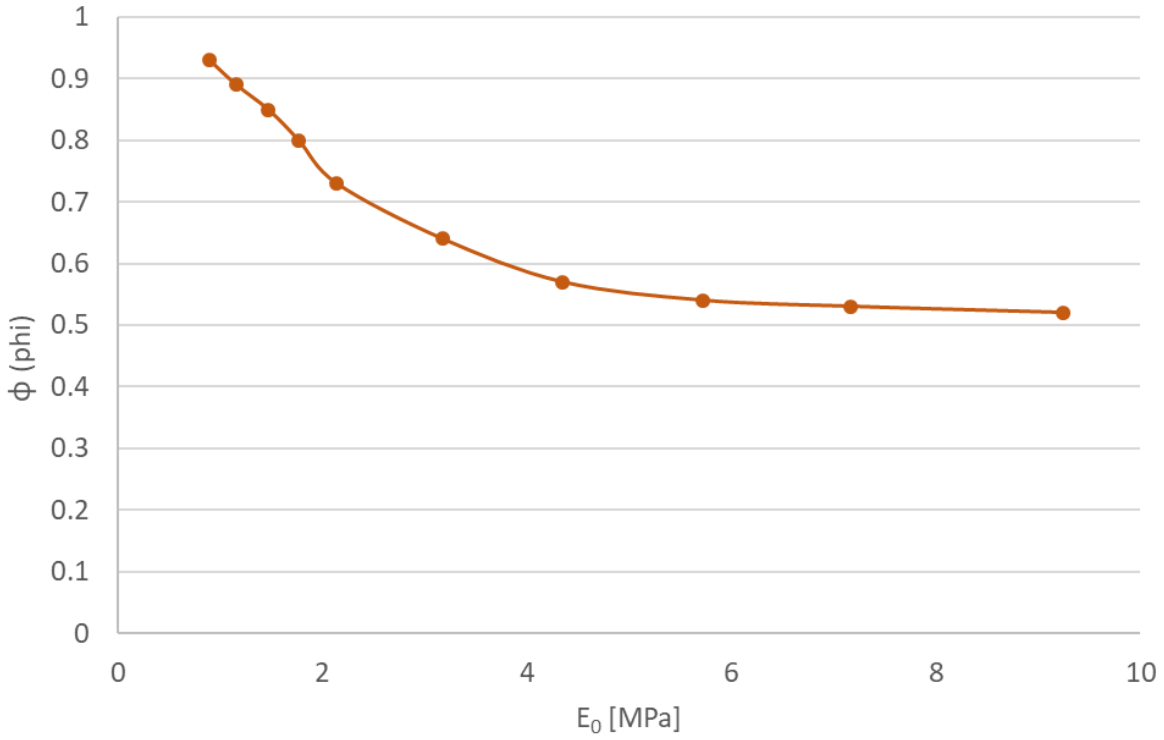

Figure 4-116: Relation between initial Young's modulus and coefficient ϕ.

Interpolating data points from the relation curve of Figure 4-116, the coefficient ϕ is defined as a third order function as follows:

$$\phi = -0.0016.{E_0}^3 + 0.034.{E_0}^2 - 0.2477.E_0 + 1.133 \quad (4\text{-}10)$$

The compression modulus (E_c) is really affected by the shape of a geometric design. For this reason, the shape factor (S) should be determined according to the relation between loaded area and force-free area derived in equation (3-23).

The force-free area (A_B), which is associated with the area that is free to bulge, was defined for each layer considering the same procedure performed for the determination of A_L, but in this case it was calculated from external and internal diameters on the middle surface (D_e and D_i respectively).

Therefore, the compression modulus and associate radial stiffness for each layer can be analyzed according to Table 4-13.

Table 4-13: Radial stiffness according to shape factors and material parameters of each layer.

Layer number	D_e [mm]	D_i [mm]	Force-Free Area (A_B) [mm^2]	S	E_c [MPa]	K [N]
N1	75.3228	60.0278	3251.8546	3.1853	12.82	13275.31
N2	100.2399	82.8372	5004.6003	2.7420	9.84	13511.73
N3	125.1855	107.7662	6374.0645	2.3715	7.69	11634.17
N4	150.4734	132.7118	7900.8499	2.0658	6.16	10049.27
N5	176.1190	157.9995	9509.6955	1.8375	5.14	8991.29
N6	201.0000	183.6450	10485.8728	1.7808	4.91	9113.14

Finally, the radial stiffness for the overall structure is obtained according to equation (3-30) based on an association of springs in series. Thus, considering the values obtained the analytical solution is:

$$\frac{1}{K_{eq}} = \frac{1}{13275.31} + \frac{1}{13511.73} + \frac{1}{11634.17} + \frac{1}{10049.27} + \frac{1}{8991.29} + \frac{1}{9113.14} \tag{4-11}$$

$$K_{eq} = 1799.37 \text{ N} \tag{4-12}$$

The radial stiffness obtained from experimental data (K_{exp}) under the condition free of pre-compression is:

$$K_{exp} = {}^{11100}/_{6} = 1850 \text{ N} \tag{4-13}$$

Just as a comparison the relative error between these values is lower than 15%, and for this reason is in accordance with the technical standard variation required for conical rubber spring (NF EN 13913, 2004).

$$Er = \left(1 - \frac{T_i^{th}}{T_i^{test}}\right).100 = \left(1 - \frac{1799.37}{1850}\right).100 = 2.74\% \tag{4-14}$$

5

FINAL CONSIDERATIONS

5.1 Conclusions

Since the present Dissertation aimed to investigate the rubber behavior under different modes of large multiaxial deformation, a complex geometry, known as conical rubber spring, that includes several conical-laminated elastomeric bearings was subjected to different cases of real working load found in the railway industry.

Considering that, the equal biaxial extension plays an important role to mechanically characterize the deformation behavior, experimental tests were conducted on samples with different cruciform shapes in order to achieve high strain levels for data fitting taking into account the effect of the geometric variables of the specimen on the uniformity of stress around the central region. Several research can be found in the literature focusing on the geometric design of the specimens to improve the sample biaxiality degree and to increase the uniformity of stress-strain area. However, according to the experiments conducted by the Author, the higher is the biaxiality degree the lower is the maximum strain supported by the sample and consequently the lower will be the equal biaxial strains.

From this assumption, a novel methodology based on reverse response through the strain field measured by DIC and FEA was developed to account the uniform stress-strain relation regardless area size. The finite element simulations introduced in this work dealt with nearly incompressible hyperelastic material under quasi-static condition. The development of the proposed approach was based on studies from other rubber compound formulations, where the variation of the carbon-black amounts presented low sensitivity of the reaction forces and consequently of the stress response over the simulation. The effectiveness of the solution was validated through the bulge test method and showed high level of accuracy. Besides the

proposed method being efficient, its application is very simple and low computational consuming.

The reduced phenomenological models with a higher number of terms, such as Yeoh, and the Arruda-Boyce micromechanical model allowed better curve fittings for the problem under study. However, although several techniques concerning uniaxial and biaxial data fitting were applied to describe a unique rubber constitutive modeling, the formulated equations for theoretical stress became inapplicable for the radial load-deflection relations due to the compressive force arising from the bonded condition at the loaded surfaces. When the rubber is compressed by metal parts, deformation occurs by a simple homogeneous compression followed by shearing deformation due to friction effects. Since the compressive strain is associated with the lateral profile, it is strongly dependent on the shape factor and the compression modulus. Thus, when the complete absence of slippage was considered between surfaces, the stress-strain relations became not uniform throughout the rubber pad and the material started to harden sharply as it was compressed. For this reason, it is important to emphasize that the most suitable hyperelastic constitutive model depends on the loading direction, geometry and rubber compound formulation. There is no universal hyperelastic model suitable for all possible deformation cases.

From this point, a pattern search optimization method was implemented to characterize the rubber behavior when performing in the overall component and to predict the load-deflection relations for each loading direction. Therefore, when the output of the simulation is compared to the experimentally obtained load-deflection curves, it can be observed the huge influence of the constitutive constants under different multiaxial loading cases. That is the reason why very complex rubber component geometries show a great challenge for numerical simulations. Even with experimental test data for the main pure deformation modes, it is not always possible to obtain the component response with a high accuracy degree.

Finally, the analytical solution proposed for the conical rubber spring under radial deflection presented reasonable results when compared to the experimental data. However, the effects of vertical pre-compression were not taken into account for this solution.

5.2 Future Works

From the present Dissertation, the following suggestions for future work are proposed:

Considering the importance and challenges regarding the compression behavior in rubbers, a study about the shape variations during compressive loading for different compound formulations is proposed. Based on a half symmetry circular block sample, the DIC technique is proposed to capture large compressive strains for thick and thin blocks with other shape variations.

Another important issue is related to the Mullins effect and viscoelastic behavior during cyclic multiaxial deformations. There are several research related to this topic, but none of them comprised this phenomenon in real working load conditions for complex geometry components. The Mullins effect is still misunderstood and it is not clear which mechanical quantity rules this phenomenon. In addition, different rubber compound formulations can be evaluated since higher carbon-black amounts increase this effect.

In regard to biaxial behavior it is important to develop solutions for bulge test under large strains. In this case, a study concerning stochastic patterns, tracking, lights and lens distortion should be taken into account. Afterwards, it is important that the material characterization is applied to other multiaxial deformation modes evolving tension-torsion effects.

Since the complexity of rubber behavior is higher as the variation in the number of data involved during a product development process increases, the study of some tools evolving artificial intelligence becomes necessary in order to allow the creation of more sophisticated solutions. In this situation, machine intelligence can learn and acquire information, rationally and conclusively, performing very well this advanced task. Based on artificial neural networks the output data (experimental tests results) can be obtained according to a determined input (compound formulation) as the network has been trained.

Finally, with the adventure of 3d printed thermoplastic elastomers, the development of components with complex geometries becomes more accessible. From this point, experiments concerning the influence of 3d printing parameters should also be evaluated together with FEA

in order to evaluate the anisotropy induced by printing. Depending on the application and manufacturing process a new constitutive approach can be developed based on strain energy potentials and artificial neural networks. When the mechanical behavior and material strength is a concern, optimization tools for frame lattice can also be powerful in the infill pattern definition.

To summarize, there are many other applications to be discovered and discussed with relation to rubber, ranging from effects of aging, hostile environments, temperature variation, manufacturing process and so on. Thus, real world applications, not only brand new but also tough challenging, are still wide open for future research concerning rubber-like materials behavior.

References

ADEEL, Y. J.; MUHAMMAD, A. I.; ZEESHAN, A. Characterization of Hyperelastic (Rubber) Material Using Uniaxial and Biaxial Tension Tests. **Advanced Materials Research**, v. 570, p. 1–7, 2012.

ADKINS, J. E.; GENT, A. N. Load-deflexion relations of rubber bush mountings. **British Journal of Applied Physics**, v. 5, n. 10, p. 354–358, 1954.

AKHRASS, D. AL *et al.* Integrating a logarithmic-strain based hyperelastic formulation into a three-field mixed finite element formulation to deal with incompressibility in finite-strain elastoplasticity. **Finite Elements in Analysis and Design**, v. 86, p. 61–70, 2014.

ALI, A.; HOSSEINI, M.; SAHARI, B. B. A Review of Constitutive Models for Rubber-Like Materials. **American Journal of Engineering and Applied Sciences**, v. 3, n. 1, p. 232–239, 2010.

ALLURI, R. *et al.* 3D printed hyperelastic "bone" scaffolds and regional gene therapy: A novel approach to bone healing. . **Journal of Biomedical Materials Research Part A**, v. 106, n. 4, p. 1104–1110, 2018.

ALTIDIS, P.; ADAMS, V. **Analyzing Hyperelastic Materials with Some Practical Considerations.** Midwest ANSYS Users Group. **Anais**. 2005. Available at: <http://www.ewp.rpi.edu/hartford/~ernesto/F2010/EP2/Materials4Students/Hill/ANSYSUsersGroupHyperelasticMaterials.pdf>

AMIN, A. F. M. S.; ALAM, M. S.; OKUI, Y. An improved hyperelasticity relation in modeling viscoelasticity response of natural and high damping rubbers in compression : experiments , parameter identification and numerical verification. **Mechanics of Materials**, v. 34, n. 2, p. 75–95, 2002.

ANSYS INC. **ANSYS Mechanical User's Guide**. [s.l: s.n.]. v. 15317

ARENZ, R. J.; LANDEL, R. F.; TSUGE, K. Miniature Load-cell instrumentation for Finite-deformation Biaxial Testing of Elastomers. **Experimental Mechanics**, v. 15, n. 3, p. 114–120, 1975.

ARRUDA, E. M.; BOYCE, M. C. A three-dimensional constitutive model for the large stretch behavior of rubber elastic materials. **Journal of the Mechanics and Physics of Solids**, v. 41, n. 2, p. 389–412, 1993.

ASTM D1171-18. **Standard Test Method for Rubber Property—Surface Ozone Cracking Outdoors or Chamber (Triangular Specimens)**. West Conshohocken: ASTM International, 2018.

ASTM D2084-19. **Standard Test Method for Rubber Property—Vulcanization Using Oscillating Disk Cure Meter**. West Conshohocken: ASTM International, 2019.

ASTM D2240-15. **Standard Test Method for Rubber Property—Durometer Hardness**. West Conshohocken: ASTM International, 2015.

ASTM D2632-15. **Standard Test Method for Rubber Property—Resilience by Vertical Rebound**. West Conshohocken: ASTM International, 2015.

ASTM D395-18. **Standard Test Method for Rubber Property—Compression Set**. West Conshohocken: ASTM International, 2018.

ASTM D412-16. **Standard Test Methods for Vulcanized Rubber and Thermoplastic Elastomers—Tension**. West Conshohocken: ASTM International, 2016.

ASTM D429-14. **Standard Test Method for Rubber Property—Adhesion to Rigid Substrates**. West Conshohocken: ASTM International, 2014.

ASTM D573-04. **Standard Test Method for Rubber Property—Deterioration in an Air Oven**. West Conshohocken: ASTM International, 2015.

ASTM D575-91. **Standard Test Methods for Rubber Properties in Compression**. West Conshohocken: ASTM International, 2018.

ASTM D624-12. **Standard Test Method for Rubber Property—Tear Resistance**. West Conshohocken: ASTM International, 2012.

AVANZINI, A.; BATTINI, D. Integrated Experimental and Numerical Comparison of Different Approaches for Planar Biaxial Testing of a Hyperelastic Material. **Advances in Materials Science and Engineering**, v. 2016, n. May, p. 1–12, 2016.

BAASER, H.; NOLL, R. Simulation von Elastomerbauteilen - Materialmodelle und Versuche

zur Parameterbestimmung. **DVM-Tag Elastomere**, v. 2, p. 110, 2009.

BARROSO, A. *et al.* **Biaxial testing of composites in uniaxial machines: manufacturing of a device, analysis of the specimen geometry and preliminary experimental results.** 15TH EUROPEAN CONFERENCE ON COMPOSITE MATERIALS. **Anais**.Venice, Italy: 2012

BATRA, R. C.; MUELLER, I.; STREHLOW, P. Treloar's biaxial tests and Kearsley's bifurcation in rubber sheets. **Mathematics and mechanics of solids**, v. 10, n. 6, p. 705–713, 2005.

BEDA, T. Modeling Hyperelastic Behavior of Rubber : A Novel Invariant-Based and a Review of Constitutive Models. **Journal of Polymer Science: Part B**, v. 45, p. 1713–1732, 2007.

BEDA, T. An approach for hyperelastic model-building and parameters estimation a review of constitutive models. **European Polymer Journal**, v. 50, n. 1, p. 97–108, 2014.

BERGSTRÖM, J. S.; BOYCE, M. C. Mechanical behavior of particle filled elastomers. **Rubber chemistry and technology**, v. 72, n. 4, p. 633–656, 1999.

BHATNAGAR, N. *et al.* Development of a biaxial tensile test fixture for reinforced thermoplastic composites. **Polymer Testing**, v. 26, p. 154–161, 2007.

BLANCHARD, A. F.; PARKINSON, D. Breakage of carbon-rubber networks by applied stress. **Industrial & Engineering Chemistry**, v. 44, n. 4, p. 799–812, 1952.

BODAGHI, M. *et al.* Materials & Design Large deformations of soft metamaterials fabricated by 3D printing. **Materials & Design**, v. 131, n. May, p. 81–91, 2017.

BORST, R. DE *et al.* **Non-linear finite element analysis of solids and structures**. 2nd. ed. [s.l.] John Wiley & Sons, 2012.

BORTOLI, D. D.; WRUBLESKI, E.; MARCZAK, R. J. Hyperfit – Curve Fitting Software For Incompressible Hyperelastic Material Models. **21st Brazilian Congress of Mechanical Engineering**, n. April 2016, 2011.

ÇAKMAK, U. D.; KALLAÍ, I.; MAJOR, Z. Temperature dependent bulge test for elastomers. **Mechanics Research Communications**, v. 60, p. 27–32, 2014.

CAM, J. LE; TOUSSAINT, E. Volume Variation in Stretched Natural Rubber : Competition between Cavitation and Stress-Induced Crystallization. **Macromolecules**, v. 41, p. 7579–7583,

2008.

CAM, J. LE; TOUSSAINT, E. Mechanics of Materials Cyclic volume changes in rubber. **Mechanics of Materials**, v. 41, n. 7, p. 898–901, 2009.

CAO, J. *et al.* Large elastic deformations of soft solids up to failure: new hyperelastic models with error estimation. **Acta Mechanica**, v. 228, n. 3, p. 1165–1175, 2017.

CARROLL, M. M. A strain energy function for vulcanized rubbers. **Journal of Elasticity**, v. 103, n. 2, p. 173–187, 2011.

CHEN, H. L. *et al.* Experimental study of temperature distribution in rubber material during microwave heating and vulcanization process. **Heat and Mass Transfer/Waerme- und Stoffuebertragung**, v. 53, n. 3, p. 1051–1060, 2017.

CHEN, Z. *et al.* Macroindentation of a soft polymer: Identification of hyperelasticity and validation by uni/biaxial tensile tests. **Mechanics of Materials**, v. 64, p. 111–127, 2013.

CHEVALIER, L. *et al.* Digital image correlation used to analyze the multiaxial behavior of rubber-like materials. **European Journal of Mechanics, A/Solids**, v. 20, n. 2, p. 169–187, 2001.

CHEVALIER, L.; MARCO, Y. Tools for Multiaxial Validation of Behavior Laws Chosen for Modeling Hyper-elasticity of Rubber-like Materials. **Polymer Engineering & Science**, v. 42, n. 2, p. 280–298, 2002.

CLOUGH, J. M. *et al.* Covalent Bond Scission in the Mullins Effect of a Filled Elastomer : Real-Time Visualization with Mechanoluminescence. **Advanced Funct. Mater.**, v. 26, n. 48, p. 9063–9074, 2016.

CORRELATED SOLUTIONS, I. **Digital Image Correlation: Overview of Principles and Software**. Columbia: University of South Carolina, 2009.

COVENEY, V. A.; JOHNSON, D. E.; TURNER, D. M. A triboelastic model for the cyclic mechanical behavior of filled vulcanizates. **Rubber Chemistry and Technology**, v. 68, n. 4, p. 660–670, 1995.

CRISFIELD, M. A. . **Nonlinear Finite Element Analysis of Solids and Structures - Volume 2: Advanced Topics**. London, UK: John Wiley & Sons, 2000.

CROCKER, L.; DUNCAN, B. Measurement Methods for Obtaining Volumetric Coefficients for Hyperelastic Modelling of Flexible Adhesives. **National Physical Laboratory**, n. 3, 2001.

DARGAZANY, R.; ITSKOV, M. Constitutive modeling of the Mullins effect and cyclic stress softening in filled elastomers. **Physical Review E**, v. 88, n. 1, p. 1–13, 2013.

DAY, J.; MILLER, K. Equibiaxial Stretching of Elastomeric Sheets: An Analytical Verification of Experimental Technique. **Testing and Analysis**, 2000.

DESTRADE, M.; MURPHY, J. G.; SACCOMANDI, G. Simple shear is not so simple. **International Journal of Non-Linear Mechanics**, v. 47, n. 2, p. 210–214, 2012.

DESTRADE, M.; OGDEN, R. W. On the third- and fourth-order constants of incompressible isotropic elasticity. **J. Acoust. Soc. Am.**, v. 128, n. 6, p. 3334–3343, 2010.

DESTRADE, M.; SACCOMANDI, G.; SGURA, I. Methodical fitting for mathematical models of rubber-like materials. **Proceedings of the Royal Society A: Mathematical, Physical and Engineering Sciences**, v. 473, n. 2198, 2017.

DIANI, J.; FAYOLLE, B.; GILORMINI, P. A review on the Mullins effect. **European Polymer Journal**, v. 45, n. 3, p. 601–612, 2009.

DICK, J. S. **How to Improve Rubber Compounds**. Munich: Hanser Publications, 2014.

DOGHRI, I. **Mechanics of Deformable Solids: Linear, Nonlinear, Analytical and Computational Aspects**. [s.l.] Springer-Verlag Berlin Heidelberg, 2000.

DORFMANN, A. Stress softening of elastomers in hydrostatic tension. **Acta Mechanica**, v. 165, n. 3, p. 117–137, 2003.

DORFMANN, A.; OGDEN, R. W. A constitutive model for the Mullins effect with permanent set in particle-reinforced rubber. **International Journal of Solids and Structures**, v. 41, n. 7, p. 1855–1878, 2004.

DROZDOV, A. D. Constitutive equations in finite elasticity of rubbers. **International Journal of Solids and Structures**, v. 44, n. 1, p. 272–297, 2007.

DROZDOV, A. D.; DORFMANN, A. Stress – strain relations in finite viscoelastoplasticity of rigid-rod networks : applications to the Mullins effect. **Continuum Mech. Thermodyn.**, v. 13, n. 3, p. 183–205, 2001.

EIJDEN, R. VAN. Numerical-experimental analysis of an improved bulge test for thin films. **Eindhoven University of Technology**, 2008.

EYERER, P.; HIRTH, T.; ELSNER, P. **Polymer Engineering: Technologien und Praxis**. [s.l.] Springer, 2008.

FEICHTER, C.; MAJOR, Z.; LANG, R. W. Method for Measuring Biaxial Deformation on Rubber and Polypropylene Specimens. **Experimental Analysis of Nano and Engineering Materials and Structures**, p. 273–274, 2007.

FLETCHER, W. P.; GENT, A. N. Nonlinearity in the dynamic properties of vulcanized rubber compounds. **Rubber Chemistry and Technology**, v. 27, n. 1, p. 209–222, 1953.

FLINT, C. F.; NAUNTON, W. J. S. Physical testing of Latex films. **Transacions of the Institutuin of the Rubber Industry**, v. 12, n. 5, p. 367–406, 1937.

FLORY, P. J.; REHNER, J. Statistical mechanics of cross-linked polymer networks. **The Journal of Chemical Physics**, v. 326, n. 1567, p. 565–584, 1943.

FREAKLY, P. K. .; PAYNE, A. R. **Theory and practice of engineering with rubber**. New York: Applied Science Publishers, 1978.

FUJIKAWA, M. *et al.* Determining Stress–Strain in Rubber with In-Plane Biaxial Tensile Tester. **Experimental Mechanics**, v. 54, n. 9, p. 1639–1649, 2014.

FUJIKAWA, M.; KAMIMURA, T.; MAKABE, C. Simple Calculation Technique of Nominal Stress/Strain in Biaxial Tensile Testing of Rubber Materials. v. 10, n. 1, p. 104–109, 2010.

FUNG, Y. **Biomechanics: Mechanical Properties of Living Tissues**. 2nd. ed. New York: Springer-Verlag, 1993.

FUNG, Y. **A First Course in Continuum Mechanics for Physical and Biological Engineers and Scientists**. 3rd. ed. Englewood Cliffs, New Jersey: Prentice-Hall, 1994.

GEHRMANN, O. *et al.* Estimation of the Compression Modulus of a Technical Rubber via Cyclic Volumetric Compression Tests. **Technische Mechanik**, v. 37, n. 1, p. 28–36, 2017.

GENOVESE, K.; LAMBERTI, L.; PAPPALETTERE, C. Mechanical characterization of hyperelastic materials with fringe projection and optimization techniques. **Optics and Lasers in Engineering**, v. 44, n. 5, p. 423–442, 2006.

GENT, A. **Engineering with Rubber: How to Design Rubber Components**. [s.l: s.n.].

GENT, A. N. A new constitutive relation for rubber. **Rubber Chemistry and Technology**, v. 69, n. 1, p. 59–61, 1996.

GENT, A. N.; LINDLEY, P. B. The Compression of Bonded Rubber Blocks. **Proceedings of the Institution of Mechanical Engineers**, v. 173, n. 1, p. 111–122, 1959.

GENT, A. N.; MEINECKE, E. A. Compression, bending, and shear of bonded rubber blocks. **POLYMER ENGINEERING AND SCIENCE**, v. 10, n. 1, 1970.

GIL-NEGRETE, N.; VIÑOLAS, J.; KARI, L. A simplified methodology to predict the dynamic stiffness of carbon-black filled rubber isolators using a finite element code. **Journal of Sound and Vibration**, v. 296, n. 4–5, p. 757–776, 2006.

GÖBEL, E. F. **Rubber springs design**. New York: John Wiley, 1978.

GRACIA, L. A. *et al.* Finite element simulation of the hysteretic behaviour of an industrial rubber. Application to design of rubber components. **Finite Elements in Analysis and Design**, v. 46, n. 4, p. 357–368, 2010.

GRECO, M.; COSTA, L. J. R. DA. Discussion on “the logarithmic strain measure applied to the nonlinear positional formulation for space truss analysis” [Finite Element in Analysis and Design 45 (2009) 632-639] and “nonlinear positional formulation for space truss analysis” [Finite Eleme. **Finite Elements in Analysis and Design**, v. 52, p. 93–95, 2012.

GREGORY, M. J. Dynamic properties of rubber in automotive engineering. **Elastomerics**, v. 117, n. 11, p. 19–24, 1985.

HANHI, K.; POIKELISPÄÄ, M.; TIRILÄ, H.-M. **Elastomeric Materials**. [s.l: s.n.].

HANSON, D. E. *et al.* Stress softening experiments in silica-filled polydimethylsiloxane provide insight into a mechanism for the Mullins effect. **Polymer**, v. 46, p. 10989–10995, 2005.

HARIHARAPUTHIRAN, H.; SARAVANAN, U. A new set of biaxial and uniaxial experiments on vulcanized rubber and attempts at modeling it using classical hyperelastic models. **Mechanics of Materials**, v. 92, p. 211–222, 2016.

HART-SMITH, L. J.; CRISP, J. D. C. Large elastic deformations of thin rubber membranes. **International Journal of Engineering Science**, v. 5, n. 1, p. 1–24, 1967.

HILL, J. M. Radical deflections of rubber bush mountings of finite lengths. **International Journal of Engineering Science**, v. 13, n. 4, p. 407–422, 1975a.

HILL, J. M. The Effect of Precompreesion on the Load-Deflection Relations of Long Rubber Bush Mountings. **Journal of Applied Polymer Science**, v. 19, p. 747–755, 1975b.

HILL, J. M. Radial deflections of thin precompressed cylindrical rubber bush mountings. **International Journal of Solids and Structures**, v. 13, 1977.

HOLOWNIA, B. P. Compression of bonded rubber blocks. **Journal of Strain Analysis**, v. 6, n. 2, p. 121–123, 1971.

HOLOWNIA, B. P. Effect of Poisson's Ratio on bonded rubber blocks. **Journal of Strain Analysis**, v. 7, n. 3, p. 236–242, 1972.

HOLOWNIA, B. P. Effect of carbon black on poisson's ratio of elastomers. **Rubber Chemistry and Technology**, v. 48, n. 2, p. 246–253, 1975.

HOLZAPFEL, G. A. **Nonlinear Solid Mechanics: A Continuum Approach for Engineering**. Austria: John Willey & Sons, 2000.

HOOKE, R.; JEEVES, T. A. "Direct Search" Solution of Numerical and Statistical Problems. **Journal of the ACM**, v. 8, n. 2, p. 212–229, 1961.

HORGAN, C. O. The remarkable Gent constitutive model for hyperelastic materials. **International Journal of Non-Linear Mechanics**, v. 68, p. 9–16, 2015.

HORTON, J. M.; GOVER, M. J. C.; TUPHOLME, G. E. Stiffness of Rubber Bush Mountings Subjected to Radial Loading. **Rubber Chemistry and Technology**, v. 73, n. 4, p. 619–633, 2000a.

HORTON, J. M.; GOVER, M. J. C.; TUPHOLME, G. E. Stiffness of Rubber Bush Mountings Subjected to Tilting Deflection. **Rubber Chemistry and Technology**, v. 73, n. 4, p. 619–633, 2000b.

HORTON, J. M.; TUPHOLME, G. E. Stiffness of spherical bonded rubber bush mountings. **International Journal of Solids and Structures**, v. 42, n. 11–12, p. 3289–3297, 2005.

HORTON, J. M.; TUPHOLME, G. E. Approximate radial stiffness of rubber bush mountings. **Materials and Design**, v. 27, n. 3, p. 226–229, 2006.

HOUWINK, R. Slipping of molecules during the deformation of reinforced rubber. **Rubber Chemistry and Technology**, v. 29, n. 3, p. 888–893, 1956.

ILSENG, A.; SKALLERUD, B. H.; CLAUSEN, A. H. **Volumetric compression of HNBR and FKM elastomers**Constitutive Models for Rubber IX-Proceedings of the 9th European Conference on Constitutive Models for Rubbers. **Anais**...2015

ISO 7619-I. **Determination of Indentation Hardness-Durometer method**. [s.l.] International Organization for Standardization, 2010.

ISO 7619-II. **Determination of Indentation Hardness IRHD Pocket Hardness.** International Organization for Standardization, 2010.

JAKEL, R. Analysis of Hyperelastic Materials with MECHANICA - Theory and Application Examples. n. April, 2010.

JAKUS, A. E. *et al.* Hyperelastic " bone ": A highly versatile , growth factor – free , osteoregenerative , scalable , and surgically friendly biomaterial. **Science Translational Medicine**, v. 8, n. 358, p. 1–16, 2016.

JAMES, H. M.; GUTH, E. Theory of the elastic properties of rubber. **The Journal of Chemical Physics**, v. 11, n. 10, p. 455–481, 1943.

JAMMALAMADAKA, U.; TAPPA, K. Recent Advances in Biomaterials for 3D Printing and Tissue Engineering. **Journal of Functional Biomaterials Review**, v. 9, n. 1, p. 22–36, 2018.

JERRAMS, S.; MURPHY, N.; HANLEY, J. The significance of equi-biaxial bubble inflation in determining elastomeric fatigue properties. **Advanced Elastomers - Technology, Properties and ApplicationsI**, n. 1975, 2012.

JOHLITZ, M.; DIEBELS, S. Characterisation of a polymer using biaxial tension tests. Part I: Hyperelasticity. **Archive of Applied Mechanics**, v. 81, n. 10, p. 1333–1349, 2011.

JOHNSON, M. A.; BEATTY, M. F. The Mullins effect in equibiaxial extension and its influence on the inflation of a balloon. **International Journal of Engineering Science**, v. 33, n. 2, p. 223–245, 1995.

JONES, D. F.; TRELOAR, L. R. G. The properties of rubber in pure homogeneous strain. **Journal of Physics D: Applied Physics**, v. 8, n. 11, p. 1285–1304, 1975.

KADLOWEC, J.; WINEMAN, A.; HULBERT, G. Elastomer bushing response: experiments and finite element modeling. **Acta Mechanica**, v. 163, n. 1–2, p. 25–38, 2003.

KALISKE, M.; ROTHERT, H. Constitutive approach to rate- independent properties of filled elastomers. **International Journal of Solids and Structures**, v. 35, n. 17, p. 2057–2071, 1998.

KAYA, N.; ERKEK, M. Y.; GUVEN, C. Hyperelastic modelling and shape optimisation of vehicle rubber bushings. **International Journal of Vehicle Design**, v. 71, n. 1–4, p. 212–225, 2016.

KEERTHIWANSA, R. *et al.* Elastomer testing: The risk of using only uniaxial data for fitting the Mooney-Rivlin hyperelastic-material model. **Materiali in Tehnologije**, v. 52, n. 1, p. 3–8, 2018.

KELLY, J. M.; KONSTANTINIDIS, D. A. **Mechanics of Rubber Bearings for Seismic and Vibration Isolation**. 222. ed. Chichester, UK: Wiley, 2011.

KILIAN, H.-G. Equation of state of real networks. **Polymer**, v. 22, n. 2, p. 209–217, 1981.

KILIAN, H. G.; ENDERLE, H. F.; UNSELD, K. The use of the van der Waals model to elucidate universal aspects of structure-property relationships in simply extended dry and swollen rubbers. **Colloid & Polymer Science**, v. 264, n. 10, p. 866–876, 1986.

KRAUS, G. Mechanical losses in carbon-black-filled rubbers. **Journal of Applied Polymer Science**, v. 39, p. 75–92, 1984.

KRAUS, G.; CHILDERS, C. W.; ROLLMANN, K. W. Stress Softening in Carbon Black-Reinforced Vulcanizates . Strain Rate and Temperature Effects. **Journal of Applied Polymer Science**, v. 10, n. 2, p. 229–244, 1966.

KROUSKOP, T. A. *et al.* Elastic Moduli of Breast and Prostate Tissues Under Compression. **ULTRASONIC IMAGING**, v. 20, p. 260–274, 1998.

LALO, D. F.; GRECO, M.; MERONIUC, M. Numerical Modeling and Experimental Characterization of Elastomeric Pads Bonded in a Conical Spring under Multiaxial Loads and Pre-Compression. **Mathematical Problems in Engineering**, v. 2019, p. 1–14, 2019.

LALO, D.; GRECO, M. **Rubber bushing hyperelastic behavior based on shore hardness and uniaxial extension.** Proceedings of the 24th ABCM International Congress of Mechanical

Engineering. **Anais**.2017. Available at: <http://abcm.org.br/anais-de-eventos/COB17/5280>

LAMBERT-DIANI, J.; REY, C. New phenomenological behavior laws for rubbers and thermoplastic elastomers. **European Journal of Mechanics - A/Solids**, v. 18, p. 1027–1043, 1999.

LĂZĂRESCU, L. *et al.* Investigation of bulge radius variation and its effect on the flow stress in the hydraulic bulge test. **Proceedings of the 14th International Conference on Metal Forming**, p. 395– 398., 2012.

LEE, H. S. *et al.* Prediction of the dynamic equivalent stiffness for a rubber bushing using the finite element method and empirical modeling. **International Journal of Mechanics and Materials in Design**, v. 15, n. 1, p. 1–15, 2017.

LI, J.; MAYAU, D.; LAGARRIGUE, V. A constitutive model dealing with damage due to cavity growth and the Mullins effect in rubber-like materials under triaxial loading. **Journal of the Mechanics and Physics of Solids**, v. 56, n. 3, p. 953–973, 2008.

LION, A. Phenomenological modelling of strain-induced structural changes in filler-reinforced elastomers. **KGK-Kautschuk Gummi Kunststoffe**, v. 58, n. 4, p. 157–162, 2005.

LION, A.; KARDELKY, C.; HAUPT, P. On the Frequency and Amplitude Dependence of the Payne Effect: Theory and Experiments. **Rubber Chemistry and Technology**, v. 76, n. 2, p. 533–547, 2003.

LIU, L.; LI, Y. Predicting the mixed-mode I/II spatial damage propagation along 3D-printed soft interfacial layer via a hyperelastic softening model. **Journal of the Mechanics and Physics of Solids**, v. 116, p. 17–32, 2018.

LOVE, A. **A Treatise on the Mathematical Theory of Elasticity**. [s.l.] Cambridge university press, 1982. v. I

LU, T.; WANG, J. A Constitutive Model for Soft Materials Incorporating Viscoelasticity and Mullins Effect. **Journal of Applied Mechanics**, v. 84, n. 2, p. 1–9, 2017.

LUO, R. K. *et al.* Stress evaluation of conical rubber spring system. **Transactions on Modelling and Simulation**, v. 30, p. 271–279, 2001.

LUO, Y.; LIU, Y.; YIN, H. P. Numerical investigation of nonlinear properties of a rubber

absorber in rail fastening systems. **International Journal of Mechanical Sciences**, v. 69, p. 107–113, 2013.

MAL, A. K.; SINGH, S. J. **Deformation of Elastic Solids**. [s.l.] Prentice Hall, 1991.

MANSOURI, M. R. *et al.* 3D-printed multimaterial composites tailored for compliancy and strain recovery. **Composite Structures**, v. 184, p. 11–17, 2018.

MANSOURI, M. R.; DARIJANI, H.; BAGHANI, M. On the Correlation of FEM and Experiments for Hyperelastic Elastomers. **Experimental Mechanics**, v. 57, n. 2, p. 195–206, 2016.

MARCKMANN, G.; VERRON, E. Comparison of Hyperelastic Models for Rubber-Like Materials. **Rubber Chemistry and Technology**, v. 79, n. 5, p. 835–858, 2006.

MARS, W. V.; FATEMI, A. Observations of the Constitutive Response and Characterization of Filled Natural Rubber Under Monotonic and Cyclic Multiaxial Stress States. **Journal of Engineering Materials and Technology**, v. 126, n. 1, p. 19, 2004.

MEDELLÍN, L. F. P.; LA PEÑA, J. Á. D. DE. Design of a biaxial test module for uniaxial testing machine. **Materials Today: Proceedings**, v. 4, n. 8, p. 7911–7920, 2017.

MEUNIER, L. *et al.* Mechanical experimental characterisation and numerical modelling of an unfilled silicone rubber. **Polymer Testing**, v. 27, n. 6, p. 765–777, 2008.

MILLER, K. Testing Elastomers for Hyperelastic Material Models in Finite Element Analysis. **Testing and Analysis**, Testing and Analysis Testing. p. 7, 2004a.

MILLER, K. What material tests are typically performed to calibrate a hyperelastic material model? **Testing and Analysis**, Testing and Analysis. p. 2, 2004b.

MOONEY, M. A theory of large elastic deformation. **Journal of Applied Physics**, v. 11, n. 9, p. 582–592, 1940.

MOONEY, M. Stress—Strain Curves of Rubbers in Simple Shear. **Journal of Applied Physics**, v. 35, n. 1, p. 23–26, 1964.

MOREIRA, D. C.; NUNES, L. C. S. Comparison of simple and pure shear for an incompressible isotropic hyperelastic material under large deformation. **Polymer Testing**, v. 32, n. 2, p. 240–248, 2013.

MOREIRA, P. Desenvolvimento de Algoritmo de Correlação Digital de Imagem para Avaliação de Grandes Deformações. 2015.

MORMAN, K. N.; PAN, T. Y. Application of finite-element analysis in the design of automotive elastomeric components. **Rubber Chem. Tech.**, v. 61, p. 503–533, 1988.

MORTON, M. **Rubber technology**. [s.l: s.n.].

MOTT, P. H.; DORGAN, J. R.; ROLAND, C. M. The bulk modulus and Poisson's ratio of "incompressible" materials. **Journal of Sound and Vibration**, v. 312, n. 4–5, p. 572–575, 2008.

MSC. **Nonlinear finite element analysis of elastomers. Whitepaper** MSC Software Corporation, , 2010. Available at: <http://linkinghub.elsevier.com/retrieve/pii/0045794987900162>

MSC. **Marc Theory and User Information**. [s.l.] MSC Software Corporation, 2016.

MULLINS, L. Softening of Rubber by Deformation. **Rubber Chemistry and Technology**, v. 42, n. 1, p. 339–362, 1969.

NEEDLEMAN, A. Material rate dependence and mesh sensitivity in localization problems. **Computer Methods in Applied Mechanics and Engineering**, v. 67, n. 1, p. 69–85, 1988.

NÉMETH, I. *et al.* **On the modelling of amplitude and frequency-dependent properties in rubber like solids.** Constitutive models for rubber-proceedings IV. **Anais**. Balkema, 2005

NF EN 13913. **Railway Applications - Rubber Suspension Components - Elastomer-Based Mechanical Parts**. [s.l.] AFNOR - Association Francaise de Normalisation, 2004.

NGUYEN, C. T.; VU-KHANH, T.; LARA, J. Puncture characterization of rubber membranes. **Theoreticaland Applied Fracture Mechanics**, v. 42, n. 1, p. 25–33, 2004.

NUNES, L. C. S. Mechanical characterization of hyperelastic polydimethylsiloxane by simple shear test. **Materials Science & Engineering A**, v. 528, n. 3, p. 1799–1804, 2011.

OBATA, Y.; KAWAI, H. Mechanical Properties of Natural Rubber Vulcanizates. **Journal of Polymer Science: Part A**, v. 8, p. 903–919, 1970.

OGDEN, R. W. Large deformation isotropic elasticity. On the correlation of theory and

experiment for incompressible rubber-like solids. **Philosophical Transactions of the Royal Society of London – Series A**, v. 326, n. 1567, p. 565–584, 1972.

OGDEN, R. W. **Non linear elastic deformations**. N.Y.: [s.n.].

OGDEN, R. W.; ROXBURGH, D. G. A pseudo-elastic model for the Mullins effect in filled rubber. **Proc. R. Soc. Lond. A**, v. 455, p. 2861–2877, 1999.

OGDEN, R. W.; SACCOMANDI, G.; SGURA, I. Fitting hyperelastic models to experimental data. **Computational Mechanics**, v. 34, n. 6, p. 484–502, 2004.

OLSSON, A. K. **Finite Element procedures in modelling the dynamic properties of rubber**. [s.l.] Lund University, 2007.

PANCHERI, F. Q.; DORFMANN, L. Strain controlled biaxial stretch: An experimental characterization of natural rubber. **Rubber Chemistry and Technology**, v. 87, n. 1, p. 120–138, 2012.

PAYNE, A. R. The dynamic properties of carbon black-loaded natural rubber vulcanizates. Part I. **Journal of Applied Polymer Science**, v. 6, n. 19, p. 57–63, 1962.

PAYNE, A. R. The dynamic properties of carbon black-loaded natural rubber vulcanizates. Part II. **Journal of Applied Polymer Science**, v. 6, n. 21, p. 368–372, 1963.

PAYNE, A. R.; WHITTAKER, R. E. Low strain dynamic properties of filled rubbers. **Rubber Chemistry and Technology**, v. 44, n. 2, p. 440–478, 1971.

PENG, S. H.; SHIMBORI, T.; NADERI, A. **Measurement of Elastomer's Bulk Modulus by means of a Confined Compression Test**145th meeting of the Rubber Division. **Anais**...Chicago, Illinois: American Chemical Society, 1994

PETEK, N.K., KICHER, T. P. An empirical model for the design of rubber shear bushings. **Rubber Chemistry and Technology**, v. 60, p. 298–309, 1987.

PUCCI, E.; SACCOMANDI, G. A Note on the Gent Model for Rubber-Like Materials. **Rubber Chemistry and Technology**, v. 75, n. 5, p. 839–852, 2002.

RENAUD, C. *et al.* The Yeoh model applied to the modeling of large deformation contact/impact problems. **International Journal of Impact Engineering**, v. 36, n. 5, p. 659–666, 2009.

RENDEK, M.; LION, A. Amplitude dependence of filler-reinforced rubber: Experiments, constitutive modelling and FEM–Implementation. **International Journal of Solids and Structures**, v. 47, n. 21, p. 2918–2936, 2010.

REUGE, N. *et al.* Elastomer biaxial characterization using bubble inflation technique. I: Experimental investigations. **Polymer Engineering & Science**, v. 41, n. 3, p. 522–531, 2001.

RITTO, T. G.; NUNES, L. C. S. Bayesian model selection of hyperelastic models for simple and pure shear at large deformations. **Computers and Structures**, v. 156, p. 101–109, 2015.

RIVLIN, R. S. Large Elastic Deformations of Isotropic Materials. II. Some Uniqueness Theorems for Pure, Homogeneous Deformation. **Philosophical Transactions of the Royal Society A: Mathematical, Physical and Engineering Sciences**, v. 240, n. 822, p. 491–508, 1948a.

RIVLIN, R. S. Large Elastic Deformations of Isotropic Materials. IV. Further Developments of the General Theory. **Philosophical Transactions of the Royal Society A: Mathematical, Physical and Engineering Sciences**, v. 241, n. 835, p. 379–397, 1948b.

RIVLIN, R. S.; SAUNDERS, D. W. Large Elastic Deformations of Isotropic Materials. VII. Experiments on the Deformation of Rubber. **Philosophical Transactions of the Royal Society A: Mathematical, Physical and Engineering Sciences**, v. 243, n. 865, p. 251–288, 1951.

ROBINSON, M. *et al.* Mechanical characterisation of additively manufactured elastomeric structures for variable strain rate applications. **Additive Manufacturing**, v. 27, n. October 2018, p. 398–407, 2019.

ROCARD, Y. Note sur le calcul des propriétès élastiques des supports en caoutchouc adhérent. **Journal de Physique et le Radium**, v. 8, n. 5, p. 190–203, 1937.

SASSO, M. *et al.* Characterization of hyperelastic rubber-like materials by biaxial and uniaxial stretching tests based on optical methods. **Polymer Testing**, v. 27, n. 8, p. 995–1004, 2008.

SCHMIDT, L. R.; CARLEY, J. F. Biaxial stretching of heat-softened plastic sheets using an inflation technique. **International Journal of Engineering Science**, v. 13, n. 6, p. 563–578, 1975.

SEBESAN, I. *et al.* Rubber Suspension , a Solution of the future for Railway Vehicles. **Materiale Plastice**, v. 52, n. 1, p. 93–97, 2015.

SEIBERT, H.; SCHEFFER, T.; DIEBELS, S. Biaxial testing of elastomers - Experimental setup, measurement and experimental optimisation of specimen's shape. **Technische Mechanik**, v. 34, n. 2, p. 72–89, 2014.

SELVADURAI, A. P. S. Deflections of a rubber membrane. **Journal of the Mechanics and Physics of Solids**, v. 54, n. 6, p. 1093–1119, 2006.

SETH, B. R. **Generalized strain measure with applications to physical problems.** IUTAM Symposium on Second Order Effects in Elasticity, Plasticity and Fluid Mechanics. **Anais**.1961

SHAHZAD, M. *et al.* Mechanical Characterization and FE Modelling of a Hyperelastic Material. **Materials Research**, v. 18, n. 5, p. 918–924, 2015.

SHANKS, R. A.; KONG, I. **Advances in Elastomers I**. [s.l: s.n.]. v. 11

SIMULIA. **Abaqus analysis user's manual, Version 6.13**. [s.l.] Dassault Systems, 2016.

SOCIETY, R. M. **Rail Motor Bogies – The Official Website**. Disponível em: <http://www.railmotorsociety.org.au/rm_bogie_frame.htm>. Acesso em: 4 jul. 2017.

SUMMERSGILL, F. C.; KONTOE, S.; POTTS, D. M. A comparison of the mesh dependence of the nonlocal and local strain softening methods in a biaxial compression analysis A comparison of the mesh dependence of the nonlocal and local strain softening methods in a biaxial compression analysis. n. August, 2014.

SUMMERSGILL, F. C.; KONTOE, S.; POTTS, D. M. Critical Assessment of Nonlocal Strain-Softening Methods in Biaxial Compression. v. 17, n. 7, p. 1–14, 2017.

SUTTON, M. A.; ORTEU, J.-J.; SCHREIER, H. W. **Image Correlation for Shape, Motion and Deformation Measurements**. [s.l: s.n.]. v. 10

THIEL, C. *et al.* International Journal of Non-Linear Mechanics Shear , pure and simple. **International Journal of Non-Linear Mechanics**, v. 112, p. 57–72, 2019.

TIMOSHENKO, S. P. **Theory of Elasticity**. 3rd. ed. New York, NY: McGraw-Hill, 1970.

TOBAJAS, R.; IBARTZ, E.; GRACIA, L. **A comparative study of hyperelastic constitutive models to characterize the behavior of a polymer used in automotive engines**Proceedings of 2nd International Electronic Conference on Materials. **Anais**. 2016. Available at: <http://sciforum.net/conference/ecm-2/paper/3398>

TOMANEK, A. **A Compendium for Practical Use, Instruction and Reference. Silicones & Industry**. Munich, Vienna: Publishers, Hanser, 1993.

TØMMERNES, V. Implementation of the Arruda-Boyce Material Model for Polymers in Abaqus. n. June, 2014.

TRELOAR, L. R. G. The elasticity of a network of long-chain molecules I. **T. Faraday Soc.**, v. 39, p. 36–41, 1943a.

TRELOAR, L. R. G. The elasticity of a network of long-chain molecules II. **T. Faraday Soc.**, v. 39, p. 241–246, 1943b.

TRELOAR, L. R. G. Stress-strain data for vulcanised rubber under various types of deformation. **Trans. Faraday Soc. 39**, v. 39, 1943c.

TRELOAR, L. R. G. Strains in an inflated rubber sheet, and the mechanism of bursting. **Transacions of the Institutuin of the Rubber Industry**, v. 19, n. 6, p. 201–212, 1944.

TRELOAR, L. R. G. The elasticity of a network of long-chain molecules III. **T. Faraday Soc.**, v. 42, p. 83–94, 1946.

TRELOAR, L. R. G. **The Physics of Rubber Elasticity**. London: Oxford University Press, 1975.

ULMER, J. D. Strain dependence of dynamic mechanical properties of carbon black-filled rubber compounds. **Rubber Chemistry and Technology**, v. 69, n. 1, p. 15–47, 1996.

VALANIS, K. C.; LANDEL, R. F. The strain-energy function of a hyperelastic material in terms of the extension ratios. **Journal of Applied Physics**, v. 38, n. 7, p. 2997–3002, 1967.

VENKATESH, K.; MURTHY, P. L. S. Experimental validation and data acquisition for hyper elastic material models in finite element analysis. **International Journal of Mechanical and Industrial Engineering**, v. 2, n. 4, p. 72–76, 2012.

VERONDA, D. R. *et al.* Mechanical Characterization of Skin-Finite Deformations. **J. Biomechanics**, v. 3, p. 111–124, 1970.

WANG, M. C.; GUTH, E. Statistical theory of networks of non-gaussian flexible chains. **The Journal of Chemical Physics**, v. 20, n. 7, p. 1144–1157, 1952.

WHITE, J.; DE, S. K.; NASKAR, K. **Rubber Technologist's Handbook, Volume 2**. [s.l.] Smithers Rapra Technology Limited All, 2009. v. 2

XIAN, X. **Development of a Bulge Test Experimental Setup**. [s.l.] Politecnico di Milano, 2015.

YEOH, O. H. **Characterization of Elastic Properties of Carbon-Black-Filled Rubber Vulcanizates. Rubber Chemistry and Technology**, 1990. Available at: <http://rubberchemtechnol.org/doi/abs/10.5254/1.3538289>

YEOH, O. H. Some Forms of the Strain Energy Function for Rubber. **Rubber Chemistry and Technology**, v. 66, n. 5, p. 754–771, 1993.

YEOH, O. H. Phenomenological Theory of Rubber Elasticity. *In*: **Comprehensive Polymer Science and Supplements**. [s.l: s.n.]. .

ZHAO, X. *et al.* Novel Design of Cruciform Specimens for Planar Biaxial Testing of Soft Materials. **Experimental Mechanics**, v. 54, n. 3, p. 343–356, 2013.

ZHENG, Y. P. *et al.* BIOMECHANICAL ASSESSMENT OF PLANTAR FOOT TISSUE IN DIABETIC PATIENTS USING AN ULTRASOUND INDENTATION SYSTEM. **Ultrasound in Med. & Biol.**, v. 26, n. 3, p. 451–456, 2000.

ZIMMERMANN, J.; STOMMEL, M. The mechanical behaviour of rubber under hydrostatic compression and the effect on the results of finite element. **Arch Appl Mech**, v. 83, n. 2, p. 293–302, 2013a.

ZIMMERMANN, J.; STOMMEL, M. Influence of the mechanical stress and the filler content on the hydrostatic compression behaviour of natural rubber. **IOP Conference Series: Materials Science and Engineering**. **Anais**. IOP Publishing, 2013b

APPENDIX A

FINITE ELEMENT HYBRID FORMULATION

In the theory of hybrid formulation pressure (surface force) is treated as an uncoupled variable and therefore it must receive a suitable formulation through the weak form of the Finite Element Method (FEM). Since in almost incompressible problems the bulk modulus K is relatively high, its relation to the pressure is given through the Cauchy stress tensor:

$$\boldsymbol{\sigma} = K(J-1).\boldsymbol{I} = -p.\boldsymbol{I} \tag{1}$$

$$p = -K(J-1) \tag{2}$$

Linearizing the equation (2) in relation to the displacement field (PUCCI and SACCOMANDI, 2002), we have:

$$p = -K\left(\frac{\partial u}{\partial x} + \frac{\partial v}{\partial y} + \frac{\partial w}{\partial z}\right) \tag{3}$$

Therefore, it worth mentioning that pressure p has less variation in relation to displacements field and, for this reason, it must be treated as an uncoupled term, that is, it must be treated separately as an independent variable in the FEM formulation (AL AKHRASS *et al.*, 2014). If the problem is effectively incompressible, a relatively high value of the variable K is assigned, forcing it to an incompressibility condition solved by a penalty procedure, in which the pressure variables act as Lagrange multipliers to force the condition of incompressibility.

In view of the above, the hybrid formulation can be used by FEM, where different shape functions are adopted to describe the fields of pressure and displacement. In the case of pressure, a lower order variation must be attributed:

$$p = \Sigma N_{pi}.p_i\,; \qquad u = \Sigma N_i.u_i\,; \qquad v = \Sigma N_i.v_i\,; \qquad w = \Sigma N_i.w_i \tag{4}$$

where p_i refers to the nodal pressure variables constituting the vector $\boldsymbol{p}$, and u_i, v_i, w_i the nodal displacements that constitute the vector $\boldsymbol{d}$.

Thus, the equation (4) can be rewritten as:

$$p = \boldsymbol{N}_p{}^T.\boldsymbol{p}\,; \qquad \delta p = \boldsymbol{N}_p{}^T.\delta\boldsymbol{p}\,; \qquad d = \boldsymbol{N}^T.\boldsymbol{d} \tag{5}$$

All in all, the boundary value problem can be expressed in the weighted form, integrating the solid domain through a weight function. Therefore, through the Principle of Virtual Work

(PVW) one can obtain the equilibrium condition of the internal forces $\boldsymbol{q}_i$ and external $\boldsymbol{q}_e$ in the volume (CRISFIELD, 2000).

$$\delta \boldsymbol{q}_e = \delta \boldsymbol{q}_i = \int \boldsymbol{B}_{nl}^T \delta \boldsymbol{S} dV_o + \int \delta \boldsymbol{B}_{nl}^T \boldsymbol{S} dV_o \tag{6}$$

The forces and pressures variables coupling vector is called $\boldsymbol{a}$ and can be derived as:

$$\boldsymbol{a} = \int \boldsymbol{B}_{nl}^T \boldsymbol{g}_{t\boldsymbol{K}2} \delta p dV_o = \boldsymbol{P} \delta \boldsymbol{p} \tag{7}$$

where δp is the pressure variation in terms of nodal variables $\delta \boldsymbol{p}$ and $\boldsymbol{g} = \boldsymbol{q}_i - \boldsymbol{q}_e$. The subscript $\boldsymbol{K}2$ shows that the tensor refers to the 2nd Piola-Kirchoff stress tensor. Thus, the differentiation of the matrix $\boldsymbol{P}$ is given by:

$$\boldsymbol{P} = \frac{\partial \boldsymbol{q}_i}{\partial \boldsymbol{p}} = \frac{\partial \boldsymbol{g}}{\partial \boldsymbol{p}} = \int \boldsymbol{B}_{nl}^T \boldsymbol{g}_{t\boldsymbol{K}2} \boldsymbol{N}_p^T dV_o \tag{8}$$

In addition, the pressure-displacement relationship of equation (2) should still be considered. In this case, the Galerkin Method must be applied to obtain the weak form of equation (2) by multiplying it by δp and integrating it over the element.

$$\int \left((J-1) + \frac{p}{K} \right) \delta p dV_o = \delta \boldsymbol{p}^T \int \boldsymbol{N}_p \left((J-1) + \frac{p}{K} \right) dV_o = \delta \boldsymbol{p}^T \boldsymbol{f} = \boldsymbol{0} \tag{9}$$

This relationship should hold for any $\delta \boldsymbol{p}$, where $\boldsymbol{f}$ represents the lack of pressure compatibility:

$$\boldsymbol{f} = -\int \boldsymbol{N}_p \left((J-1) + \frac{p}{K} \right) dV_o = 0 \tag{10}$$

The equations above represent the governing relationships between the displacement and nodal pressure variables. For a purely incompressible problem, the term p/k from equation (10) would disappear and this equation could be used in the weak form of the incompressibility constraint.

It is worth mentioning that the governing equation (10) involves the pressure and not its derivative, so it is not necessary the pressure to be continuous between the elements. Hence,

they can be treated as internal variables of the system. As a way to reduce the number of additional unknowns, in general one of these conditions (force or displacement) is admitted in the strong form, while the second is the weak form obtained by weighting. Since the formulations was adopted to the almost incompressible materials the weak form has been attributed to the pressure.

APPENDIX B

MESH DEPENDENCY PROBLEMS ON SHELL ELEMENTS

Mesh dependency is a shortcoming associated with numerical solutions of localized problems under quasi-static loading conditions. This effect becomes very evident during the strain softening, especially in cases of biaxial deformation of narrow bands subjected to intense straining. This problem occurs because the equations governing incremental equilibrium lose ellipticity (NEEDLEMAN, 1988; SUMMERSGILL, *et al*., 2014; 2017).

In situations where the material is considered to be almost incompressible, the use of reduced integration in the Gaussian Quadrature method is advisable because the displacement-based FE formulations always over-estimate the stiffness matrix, becoming susceptible to volumetric locking. However, because the use of fewer integration points produce a less stiff element, care should be taken in order to avoid some instabilities ought to stiffness matrix tending to zero, which is known as hourglass mode.

In Abaqus® commercial software the use of reduced integration is mandatory for 4-node shell elements, being this, the only option available for this type of element. Therefore, this constraint can lead to a high mesh dependency problem when the biaxial deformation mode is simulated through shell elements. Although the cruciform extension can also be represented by plane stress elements, which are not influenced by volumetric locking, a mesh dependency study was conducted taking into account the responses of sample A due to its narrow bands, which consequently present a low biaxiality degree, and supported high levels of strain. This study is somehow important since some other applications can face this problem due to modeling conditions, e.g. bulge test under high strain levels.

In the proposed study four different mesh sizes were adopted in a quarter of symmetry model, and are depicted respectively in Figures B-1 to B-4 according to the following mesh sizes:

- Model 1: Mesh size = 1.0mm; total number of elements = 314; total number of nodes = 399;
- Model 2: Mesh size = 0.6mm; total number of elements = 945; total number of nodes = 811;
- Model 3: Mesh size = 0.3mm; total number of elements = 3573; total number of nodes = 3310;
- Model 4: Mesh size = 0.1mm; total number of elements = 29634; total number of nodes = 28846;

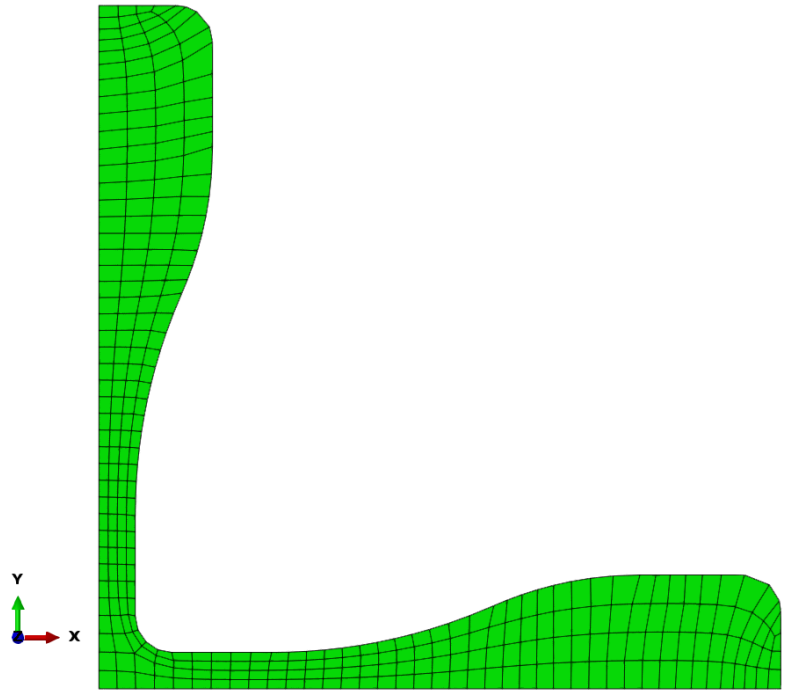

Figure B-1: Cruciform biaxial extension represented by a mesh size of 1.0mm.

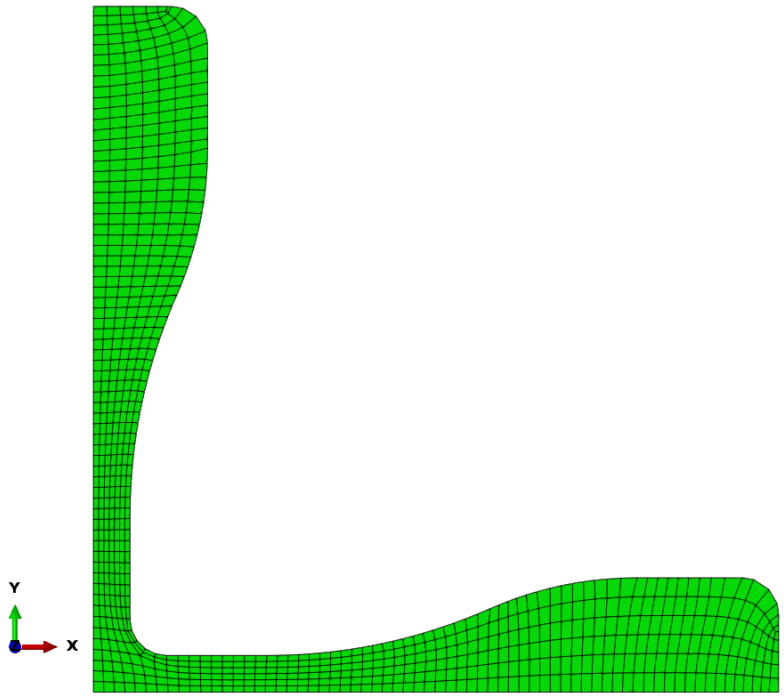

Figure B-2: Cruciform biaxial extension represented by a mesh size of 0.6mm.

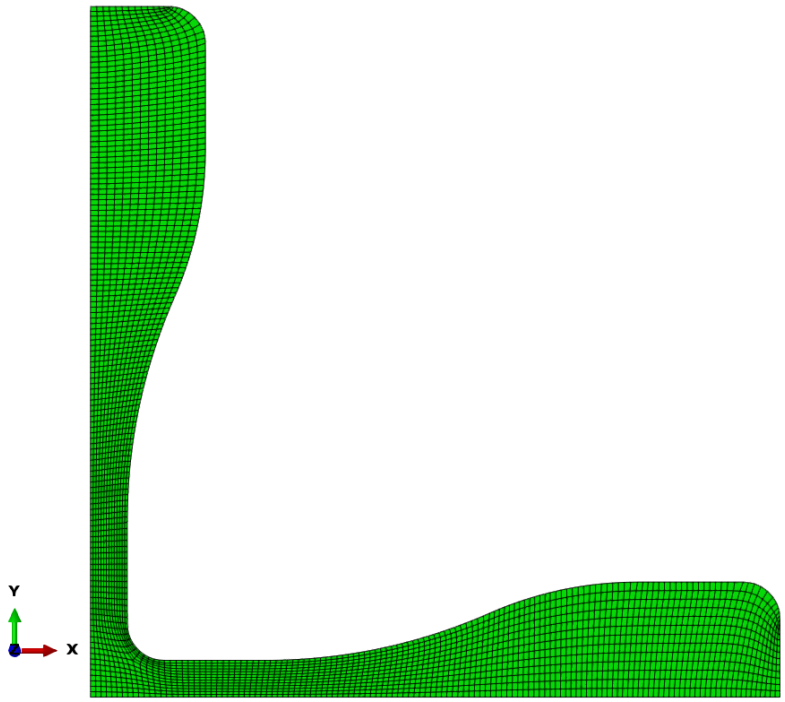

Figure B-3: Cruciform biaxial extension represented by a mesh size of 0.3mm.

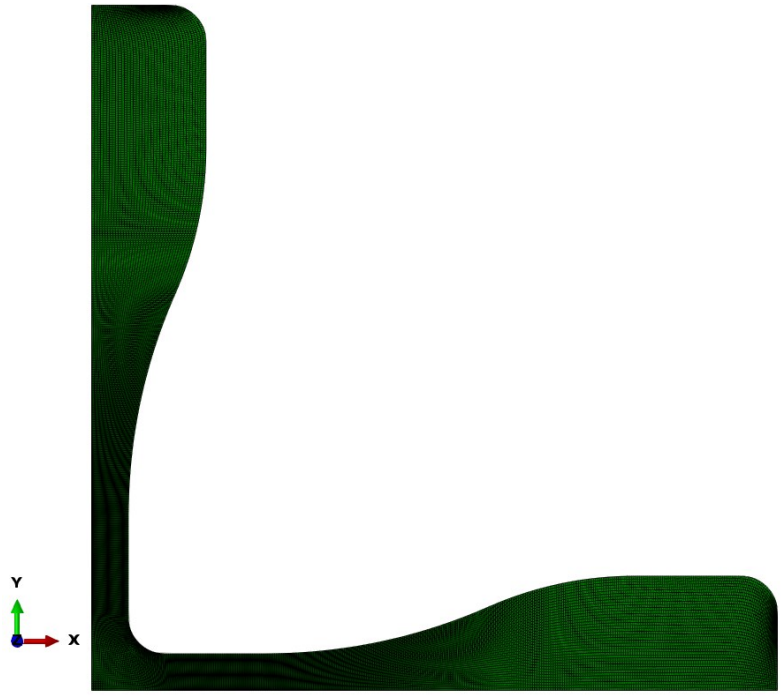

Figure B-4: Cruciform biaxial extension represented by a mesh size of 0.1mm.

The localization problem is totally evident when the responses of global displacements represented by Figure B-5 are compared to the equal biaxial strains of Figure B-6 evaluated in the center for each mesh size.

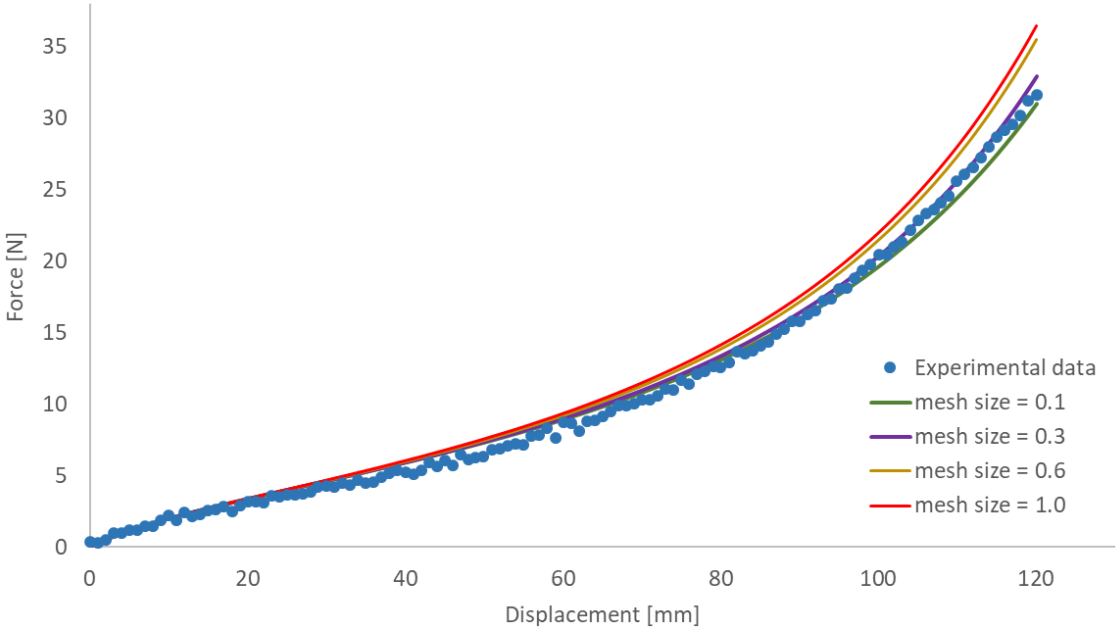

Figure B-5: Global displacement response according to force for different mesh sizes.

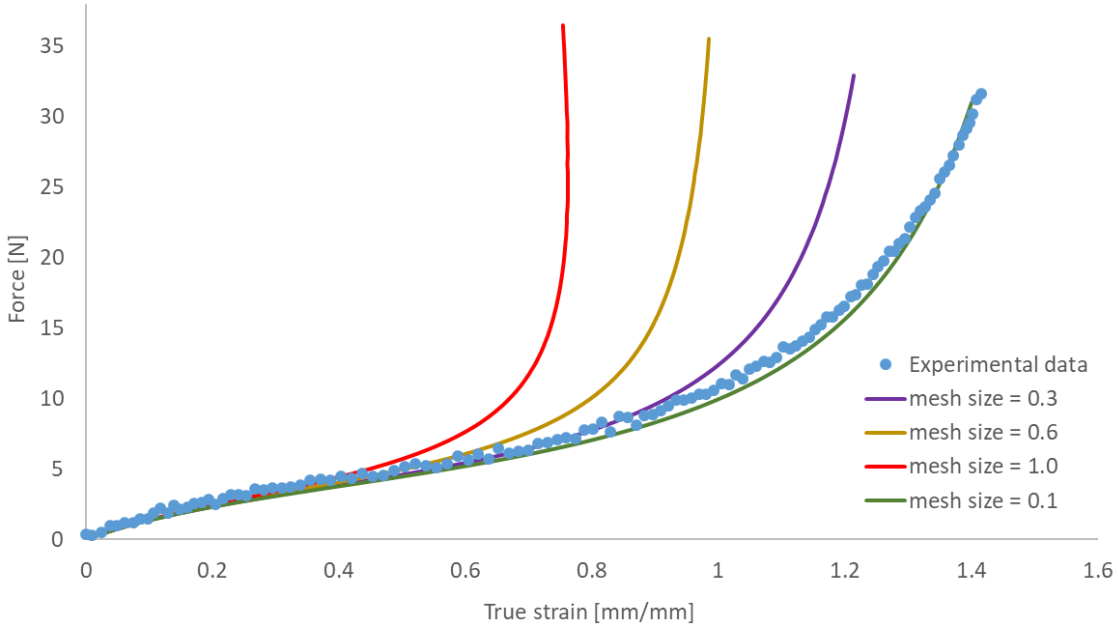

Figure B-6: Localized true strain response according to force for different mesh sizes.

It is possible to note that, the localized strain response starts to show a great increase in the difference between evaluated mesh sizes from values higher than 40% of true strain, that is, approximately 50% of nominal strain and equivalent to 24mm of global displacement. But, on the other hand, because overall stiffness is less affected by this phenomenon the difference between each mesh size response becomes greater only after 70mm of displacement and even this way this difference is not too significant.

The mesh dependency problem can also be analyzed by the history of the total artificial strain energy (ALLAE). This is a more quantitative approach since it is the total energy dissipated to control hourglassing deformation. It contains both viscous and elastic terms; however, since the viscous term is usually predominant, most of the energy that goes into artificial strain energy is non-recoverable (SIMULIA, 2016).

One way to determine if ALLAE is representing excessive values, is to compare it to the other internal energies. Since the material of the proposed study is based on the hyperelasticity theory a comparison with the total elastic strain energy (ALLSE) becomes more appropriate. Thus, from Figure B-7 the ratio between artificial strain energy and elastic strain energy is represented over the global displacements.

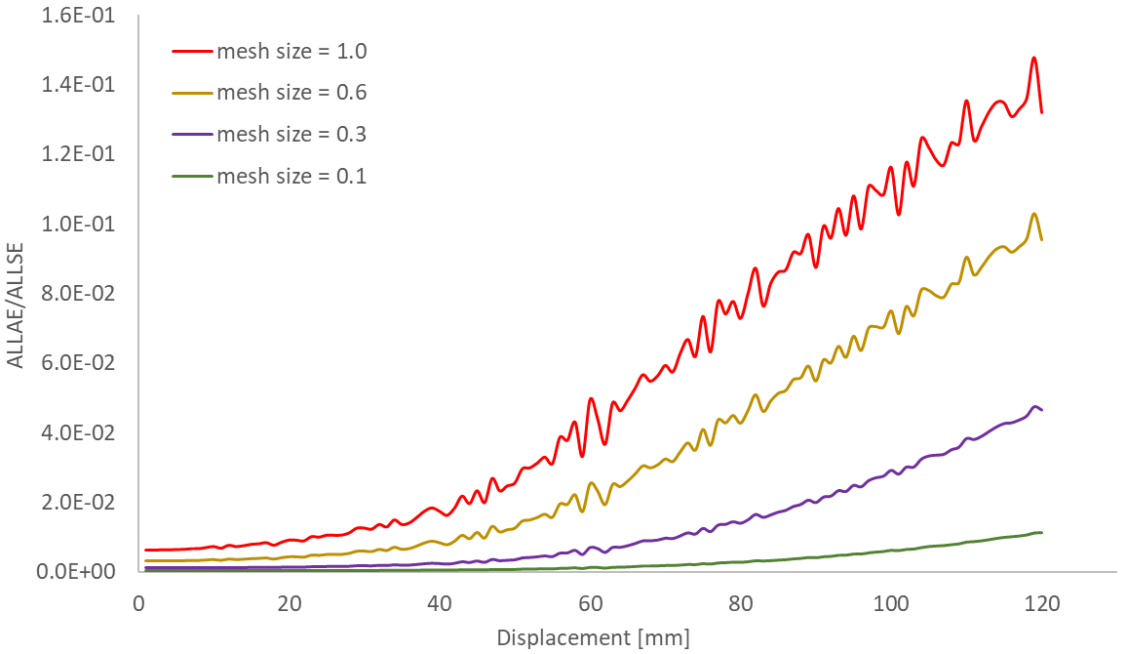

Figure B-7: Raelation between ALLAE and ALLSE over the global displacements

Finally, considering that mesh dependency describes a solution which appears to follow the mesh nodal positions, the final deformed shapes are respectively depicted in Figures B-8 to B-11 according to the adopted mesh size (1.0, 0.6, 0.3, 0.1 mm).

Through the pictures, it is possible to see the effect of the displacements following the mesh due to hourglassing. For this reason, the coarser the mesh the greater will be the artificial strain energy going into controlling hourglassing deformation and consequently the lower will be the localized strains around the center as shown in Table B-1 compared to experimental test.

Table B-1: Final equal biaxial true strains according to the mesh size and experimental test.

	Mesh size: 1.0mm	Mesh size: 0.6mm	Mesh size: 0.3mm	Mesh size: 0.1mm	Experimental test
Central true strains	75.89%	102.39%	123.15%	140.19%	141.51%

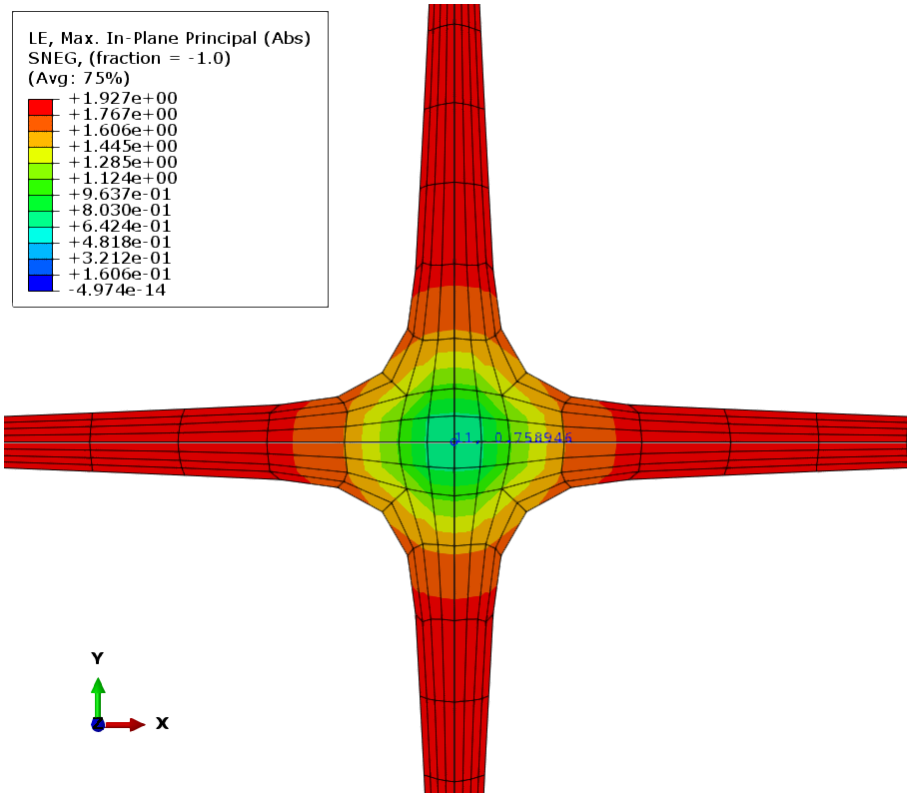

Figure B-8: Equal biaxial true strain distribution modeled with a mesh size of 1.0mm.

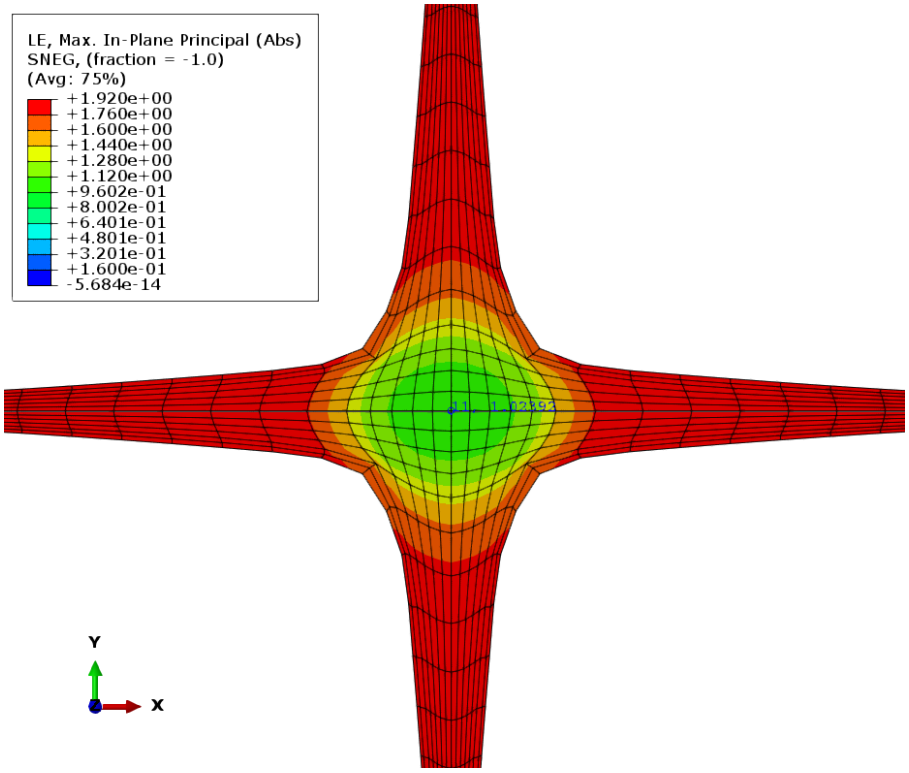

Figure B-9: Equal biaxial true strain distribution modeled with a mesh size of 0.6mm.

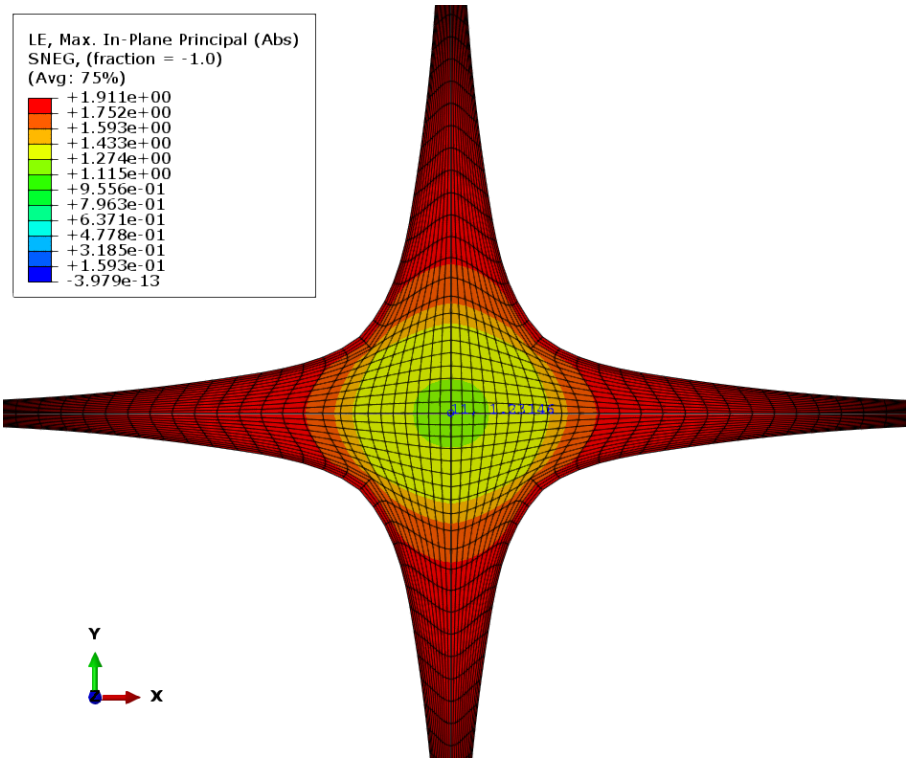

Figure B-10: Equal biaxial true strain distribution modeled with a mesh size of 0.3mm.

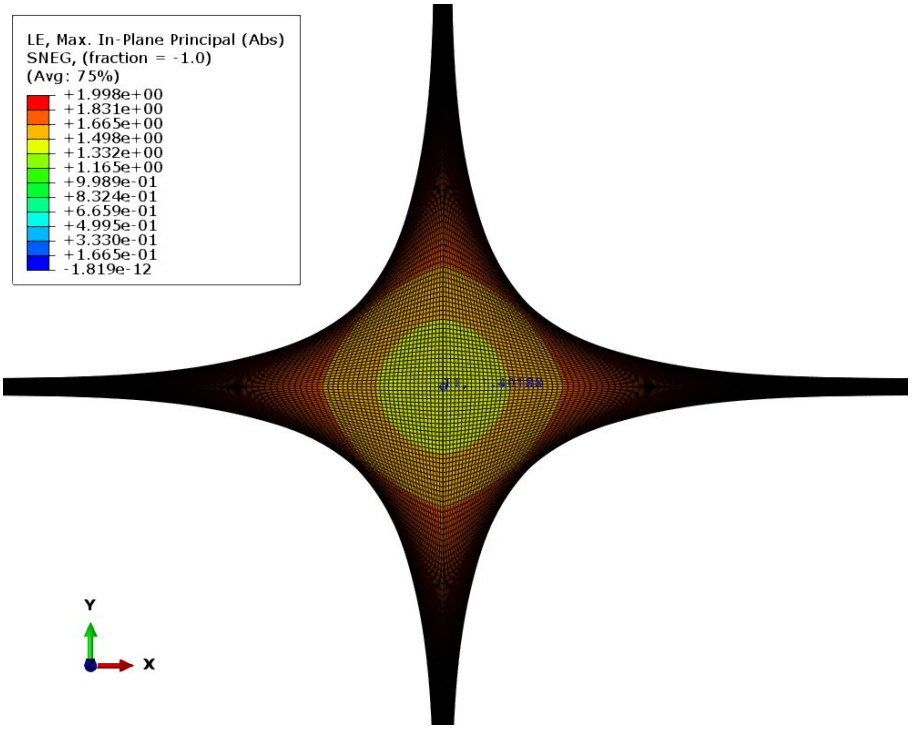

Figure B-11: Equal biaxial true strain distribution modeled with a mesh size of 0.1mm.

APPENDIX C

SIMPLIFIED RUBBER BUSHING UNDER AXIAL LOADING

In order to initiate the studies, the first simulations have been performed on a rubber bushing component with a simpler geometry. This component is also manufactured by Vibtech, where the load-deflection prototype curve could be obtained as well. Some studies involving optimization techniques have also been performed.

The FEA was performed using the commercial software Abaqus®, and the axisymmetric formulation was applied due to the rotational symmetry of the model. The metal parts were modeled by using the 3-node linear triangle axisymmetric elements (CAX3) and the rubber pad by using the 4-node bilinear quadrilateral axisymmetric elements with the hybrid formulation and constant pressure (CAX4H). The final model with its refined mesh and boundary conditions is shown in Figure C-1 (LALO and GRECO, 2017).

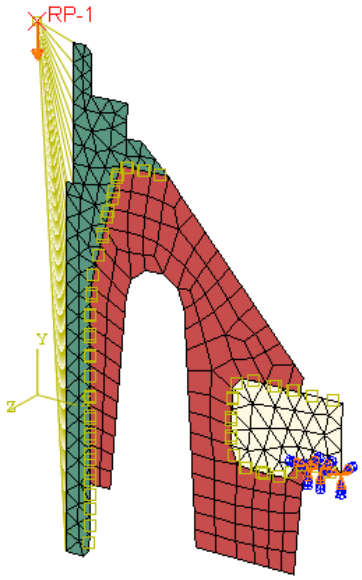

Figure C-1: Rubber spring finite element model (axial section).

Initially, the constitutive modeling was implemented based on a relationship obtained from literature between rubber Shore-Hardness and first order Mooney-Rivlin model with two coefficients. These values are listed according to Table C-1, and do not cover all types of rubber, they are just an approximation based on uniaxial extension test for some rubbers with Poisson' ratio very close to 0.5, that is, nearly incompressible. For this reason, it can be used as a reference (ALTIDIS and ADAMS, 2005).

Table C-1: Mooney-Rivlin model with two coefficients.

Source: Adapted from Altidis *et al.* (2005).

Shore-A	Young's Modulus (E)	Shear Modulus (μ)	C_{10}	C_{01}
[º]	[N/mm^2]	[N/mm^2]	[N/mm^2]	[N/mm^2]
55	3.207	0.956	0.382	0.096
58	3.811	1.089	0.436	0.109
60	4.268	1.185	0.474	0.118
65	5.616	1.465	0.586	0.147
70	7.289	1.839	0.736	0.184

The final results showed that the rubber section undergoes large strains but it still keeps the reasonable shape, without excessive distortion. According to Figure C-2 it is possible to compare the undeformed (a) and deformed shape (b). The maximum displacement value occurs around the metal axle, more exactly at the point where the concentrated load is applied.

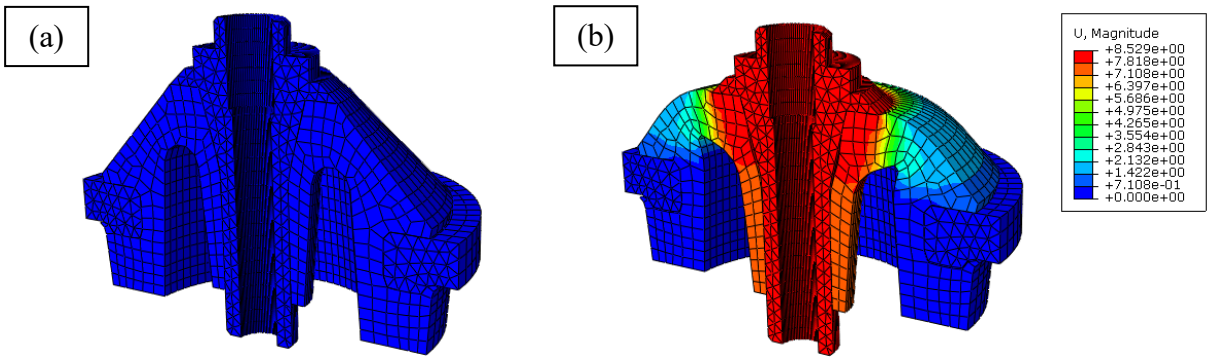

Figure C-2: Rubber bushing deformation under axial load (a) undeformed shape; (b) deformed shape.

The comparison among experimental data and curves obtained by FEM simulation for the Mooney-Rivlin constitutive model is presented in Figure C-3.

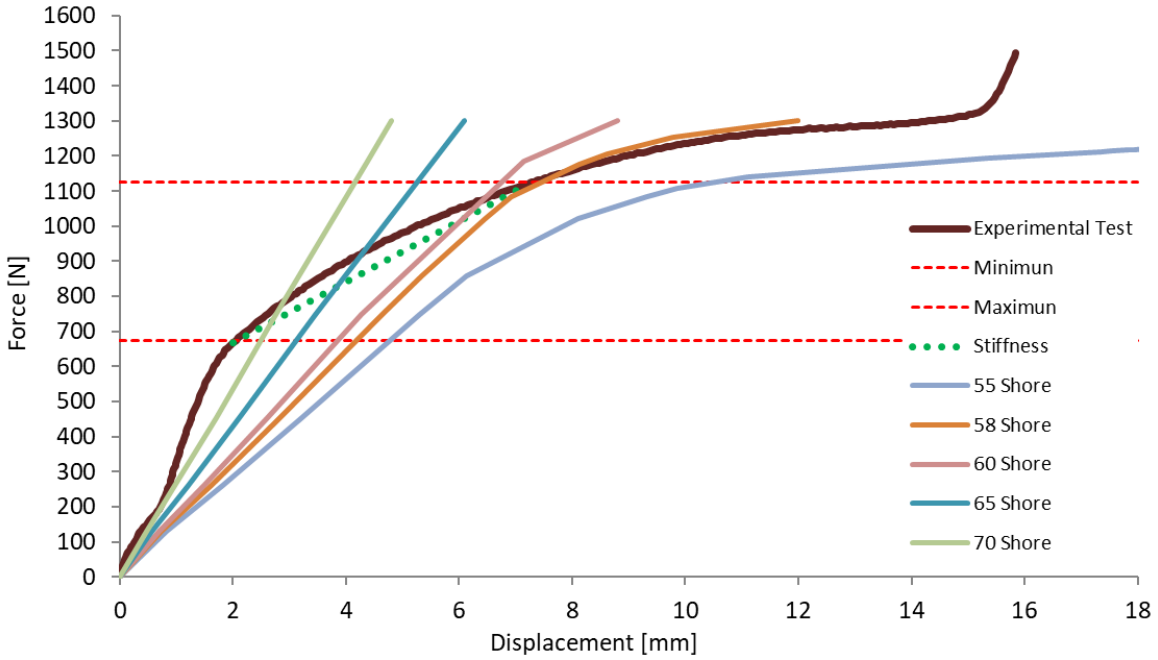

Figure C-3: Bushing behavior comparison with prototype experimental data and Mooney-Rivlin models based on shore hardness.

Then an optimization study was also performed by testing nine algorithms types. From the algorithms tested, the one which best fits the prototype experimental curve was the MMFD (Modified Method of Feasible Directions) initially implemented by Vanderplaats (1984). The Yeoh constitutive model was used for material description, once that it deals with large strain rates. Through the graph shown in Figure C-4 it is possible to compare the axial stiffness of the component with the curves obtained by the optimization methods tested.

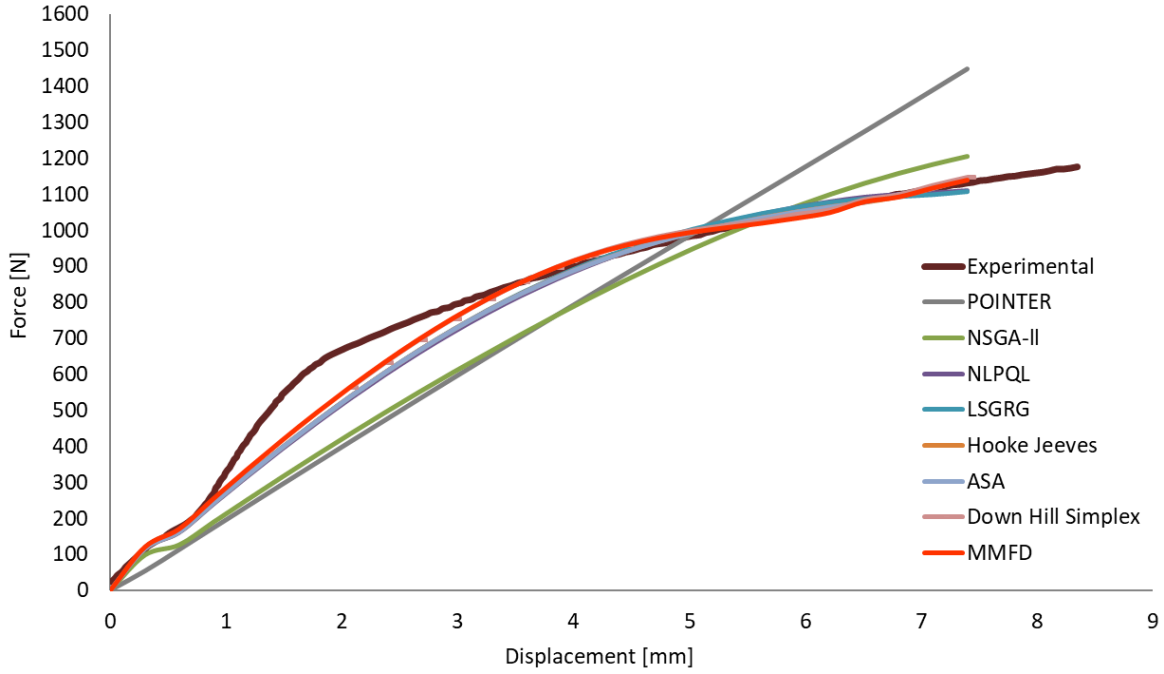

Figure C-4: Bushing behavior comparison with prototype experimental data and Yeoh models based on optimization algorithms.

In the case where optimization algorithms are used, the adjustment becomes better, however the prototype test data will always be necessary for the material characterization, aiming as an objective function minimizing the error between the curves computed by the area difference. Therefore, for a more accurate calibration without accessing prototypes test data, experimental tests based on simple specimens and considering some states of deformation should be performed, mainly for the biaxial extension.

During the optimization process, the material constants should be defined as design variables in which their values change throughout the analysis. Each optimization algorithm tested resulted in a set of Yeoh constants taking into account the deviatoric and the hydrostatic parts of the stress tensor. The final values obtained as design variables basically depend on the search method implemented by each algorithm and can be found in Table C-2. Since the MMFD method provided the best result, it is highlighted in the gray color.

Table C-2: Final material constants obtained by optimization process for Yeoh model.

Optimization Algorithm	Total Run	C10	C20	C30	D1	D2	D3	Error - Area Diff
POINTER	59	4.133	-1.955	15.577	16.078	-5.781	-4.908	787.189
NSGA-ll	237	1.200	-1.145	7.654	0.707	-7.215	0.800	506.561
NLPQL	123	2.796	-2.300	0.080	1.403	-0.609	1.075	179.391
LSGRG	152	2.840	-2.100	0.080	1.400	-0.600	1.585	169.478
Hooke Jeeves	352	2.840	-2.116	6.392	1.400	-0.600	8.539	143.506
ASA	940	2.840	-2.110	6.390	1.400	-0.600	8.530	144.436
Down Hill Simplex	452	2.649	-1.428	5.335	1.121	-0.473	11.769	106.526
MMFD	513	2.638	-1.421	5.383	1.110	-0.462	11.760	104.938